Data storage and processing using magnetic nanowires

By

Simon G Bance

A thesis submitted for the degree of

Doctor of Philosophy

Engineering Materials,

The University of Sheffield.

June 2009

Abstract

This thesis contains data from micromagnetic simulations that investigate new methods for data storage and processing on the nanoscale using ferromagnetic nanowires.

First I consider a magnetic memory, domain wall trap memory, which could compete with a number of existing devices that are currently in widespread use. Domain wall trap memory exhibits a 90% lower coercivity over traditional MRAM designs because, instead of remagnetizing a rectangular or oval magnetic free layer by moment rotation or domain nucleation, an existing domain wall is moved along a structured nanowire to remagnetize part of the wire. I determine the fields for de-pinning, switching and expulsion of domain walls in memory cells to show that the margins between them can be sufficiently large for reliable operation. The nudged elastic band method is used to show that domain wall trap memory is thermally stable at room temperature.

The second part of the thesis examines spin waves in ferromagnetic nanostructures, particularly rectangular thin-film wires, where exchange spin waves dominate. Spin wave logic devices have been proposed as a replacement for traditional silicon-based electronic logic for a range of applications. I show that is is possible to reduce spin wave reflections with boundary conditions of increased Gilbert damping constant and investigate the effects of geometry and material parameters on spin wave propagation. I go on to examine the effects of edge notches, roughness and bends on the quality of spin waves, finding that a nanowire with periodic roughness can be considered a type of magnonic crystal, with frequency band gaps corresponding to the spin wave frequency modes. It is shown that magnetic nanowires are highly suitable for use as spin wave waveguides in spin wave logic devices.

Thanks & acknowledgements

I would like to thank my supervisor, Thomas Schrefl, for giving me the opportunity to study for this PhD in a challenging, friendly and fun environment. His words of encouragement and advice helped me through some stressful times and he often taught me to see things from a more relaxed point of view. I greatly appreciate the opportunities for travelling to exciting places and really enjoyed presenting my work to the wider community.

I have been very lucky to work in such a great research group, where I was always made to feel an important member. Thank you to all of the members of the group for their help, especially Gino Hrkac, Alex Goncharov, Julian Dean, and Asif Bashir.

A big thank you to my secondary supervisor, Dan A. Allwood, for always being available to discuss my results and for helping me decide what to do next.

For support, encouragement and technical assistance I would like to thank the members of the Sheffield Centre for Advanced Magnetic Materials and Devices (SCAMMD), especially Mike R J Gibbs, Matt Bryan and Swaraj Basu.

Much credit must be given to our collaborators at the University of Glasgow who designed, tested and fabricated many of the domain wall trap MRAM cells that I investigate in this thesis. In particular Craig Brownlie, Stephen McVitie and John Chapman, who helped with the publication of my first peer-reviewed article. Craig was a great help as much of what I have done follows on from his experimental work, and he has always been willing to provide indispensable insight into the understanding of our combined results.

For fruitful discussion and inspiration I thank our friends at Vienna Technical University (TUWIEN) especially Dieter Suess, Josef Fidler and Werner Scholz (now Seagate).

Thank you to Claudio Serpico (Dipartimento di Ingegneria Elettrica, Università di Napoli "Federico II") and Massimilliano D'Aquino (Università degli Studi di Napoli "Parthenope") for being such great hosts during our visits to Naples for the PLoCH project meeting and later during the HMM '07 conference.

Thank you to the Engineering and Physical Sciences Research Council (EPSRC) for funding my studies.

Finally I would like to thank my family and friends for their very welcome support throughout my studies.

Contents

CHAPTER 1

Background & motivation

The original work contained in this thesis concerns two areas of research interest. In both cases, a magnetic nano-device is investigated as the potential replacement for one or a number of existing technologies that play critical roles inside modern computers.

Firstly, domain wall trap magnetic random access memory (DWT-MRAM) is a proposed "universal" memory device, which could one day replace solid-state memory devices such as SRAM and DRAM. DWT-MRAM technology could also give high enough storage densities to threaten the position of the non-volatile magnetic hard disk drive (HDD) and Flash memory.

Secondly, spin wave logic devices and spin wave bus circuits have been proposed to perform logic calculations and transport data inside and between the central processing unit (CPU).

This chapter provides an overview of the computer architecture into which the proposed devices would be introduced. For the purpose of comparison a history of previous technologies is presented alongside a summary of the current technologies that DWT-MRAM and spin wave computers would be competing with. An overview of the aims and requirements for successful memory technologies is provided.

1.1. "A computer in every home"

Magnetic materials and devices have played an integral part in the history and development of modern computers. This thesis outlines a number of areas where they can play a further part in the future of computing, introducing new functionality and improving performance beyond the limits of today's technologies. Until the 1970s, electronic computers were big machines that each filled a whole room and only existed for a few specialized roles. Industrial, academic, military and space research are a few of the areas where computers were used to perform repetitive numerical calculations at speeds orders of magnitudes faster than ever before. Then, in the 1970s, microcomputers with processors based on integrated circuits (ICs) were introduced, making personal computing within reach of small businesses and home users. Today, microprocessor devices are increasingly being introduced into objects where they previously had no

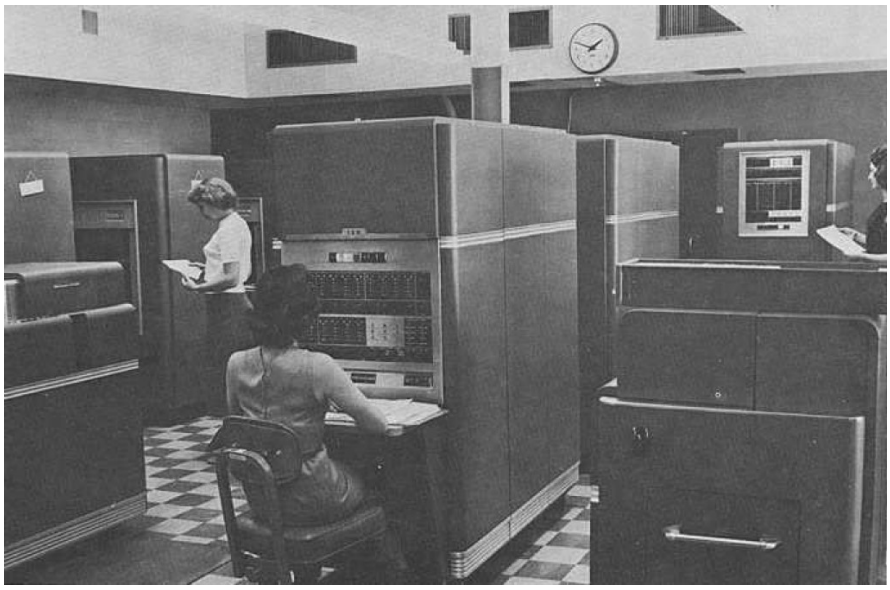

FIGURE 1.1. The IBM 650 Magnetic Drum Calculating Machine, created in 1953. The machine is considered to be the world's first commercial computer to generate any meaningful profit. Output was presented using a display panel of bi-quinary light indicators. Long term memory storage was provided by the IBM 727 Magnetic Tape Unit, while short term memory was stored using the magnetic drums. Magnetic core memory was also used, as part of the IBM 653 High-Speed Storage Unit. (Image: IBM Archives).

place. These days, there is more computing power contained within the average mobile telephone or automobile than was available to the Apollo Guidance Computer (AGC) that helped guide astronauts to the moon in the late 1960s [**1**].

1.2. Computer architecture

Computers work by processing data using an orderly list of actions, according to a set of instructions known as a computer program. Virtually all computers can be envisaged as being constructed from six distinct units or sections [**2**] (Figure 1.2):

(1) Input unit. Data and programs are received by the computer so that other units can use them for processing. Typical input devices are keyboards and mice, although many others exist such as scanners, network connections and microphones.

(2) Output unit. The information that has been processed by the computer can be displayed or otherwise made available for use outside the computer via output devices. Data is most commonly displayed on a monitor, printed on paper, used to control

other external devices or sent over a network connection. Today's multimedia computers have a wide range of devices for data output, for instance speakers for audio data and vibrating "rumble packs" inside gaming joypads.

(3) Memory unit. The main short-term system ("primary") memory stores data from an input source, making it available for processing. Computer programs are stored in the memory while they are being processed. System memory is therefore fast, but is also volatile and loses data when it is switched off.

(4) Arithmetic and logic unit (ALU). The ALU performs arithmetic calculations such as addition, subtraction, multiplication and division as well as bit-wise logic operations such as AND, NOT, OR and XAND, and bit-shifting where items in memory can be moved by a specified number of bits. In most modern computers the ALU is built into the CPU.

(5) Central processing unit (CPU). The CPU is the part of the computer that coordinates and supervises all of the other distinct units. For example, it coordinates the input and output devices and tells that ALU what logic operations to perform on a set of input data.

(6) Secondary storage unit. The secondary, long-term memory device stores data for later retrieval and is non-volatile, meaning data is not lost when the power is switched off. Secondary storage devices normally have slow access times and low cost per data bit, meaning they are cost-effective for storing large amounts of data but not fast enough for use as the main system memory. The most common such device in use today is the hard disk drive (HDD), although with the falling cost and increasing density of flash memory, solid state disk drives are becoming more common as an alternative to HDDs.

All of these components communicate via a series of electrical connections, which are often visible as a collection of wires and follow a range of well known standards. In computer terminology, a "bus" is a data connection between components of a computer, or between multiple computers, allowing them to communicate using electrical signals. Examples of well-known bus types found internally and externally within modern desktop personal computers include PCI [**3**], USB [**4**], Firewire [**5**], SCSI [**6**] and SATA [**7**].

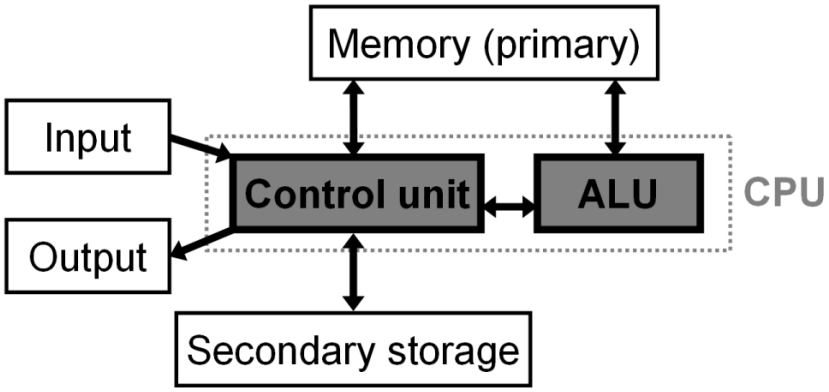

FIGURE 1.2. Computer architecture, consisting of the six main logical units that make up virtually all computers.

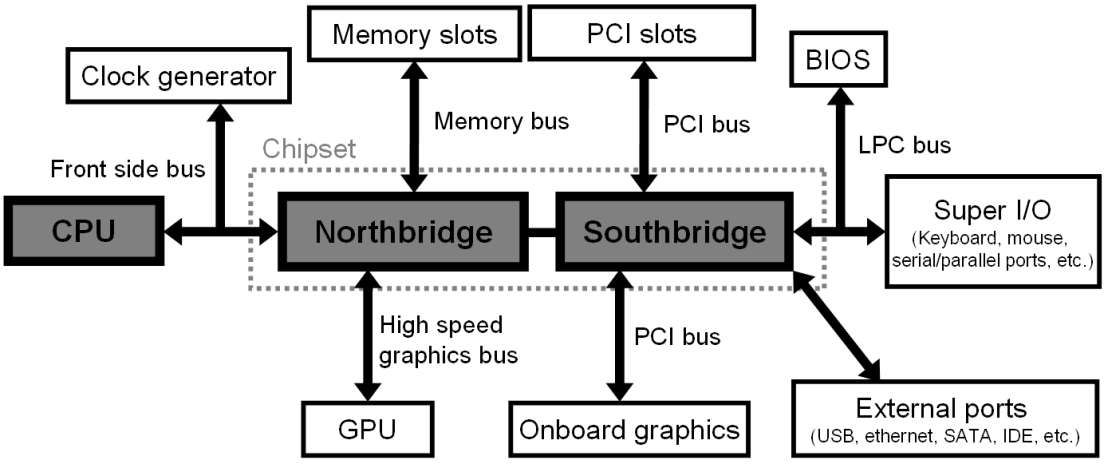

FIGURE 1.3. Typical arrangement of the CPU and chipset architecture showing the network of bus connections between distinct component devices. The so-called Northbridge connects the slots for system memory and the graphics processing unit (GPU) to the chipset. The Southbridge connects everything else, including PCI slots, BIOS ROM and external hardware devices. A number of different bus standards are used, with the fastest being the front side bus and the high speed graphics bus.

Inside an integrated motherboard, the distinct components communicate via a number of bus connections. Two of the most important examples of system bus are the front side bus (FSB) that carries data between the CPU and the memory controller hub and the memory bus that carries data between the memory controller hub and the system memory slots (Figure 1.3). The CPU is connected to the chipset via the FSB. The chipset consists of memory controller hub called the "Northbridge", and an I/O controller hub called the "Southbridge".

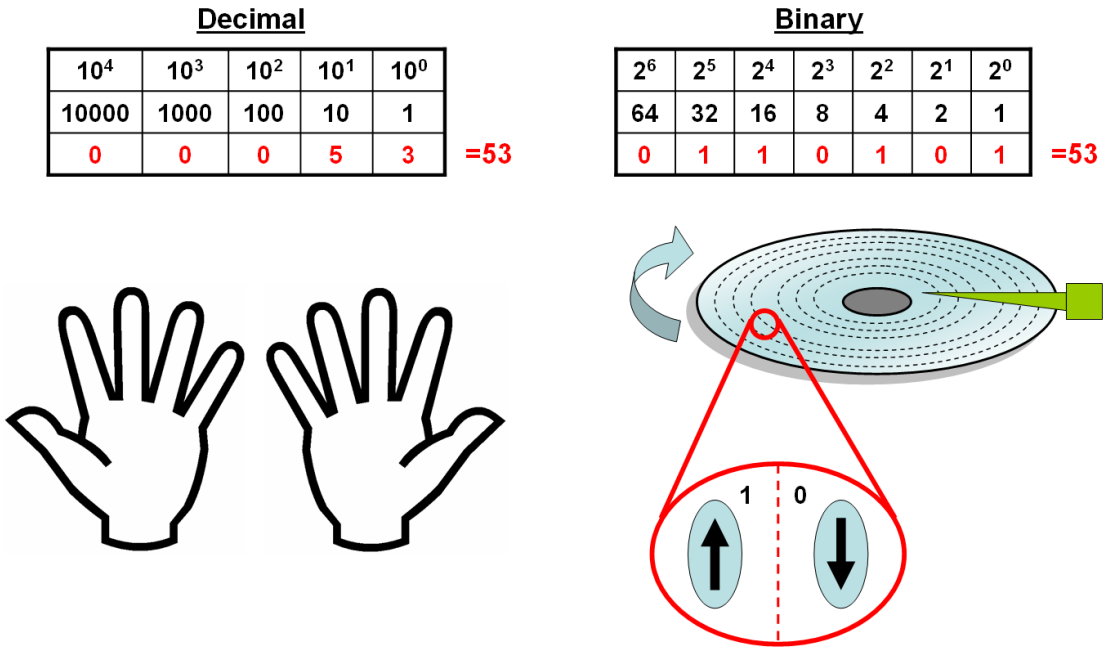

FIGURE 1.4. Comparison between the decimal and binary number systems. The decimal system is based on the powers of the number 10 and originates from the fact that humans have 10 digits on their hands for counting. The binary system is based on the powers of the number 2 and can be represented using systems constructed from units each with two distinct states. In the example here, the decimal number 53 is written in binary code as "110101". In a hard disk drive, a common device for long term data storage, data bits exist on the form of magnetic islands on the disc surfaces. They are magnetized in one of two directions to signify a "1" or a "0".

1.3. Computer memory

1.3.1. Binary counting system. Inside a computer, data is stored as a series of ones and zeros known as binary code. Traditionally, most human cultures count using base ten, which is natural as we have ten digits in total on our hands. In a computer, numbers are counted using base 2, which can be represented by a system with two possible configuration states; true or false, 1 or 0. Any number can be represented by a series of columns that represent the number of units in powers of 2 (Figure 1.4). In magnetic data storage, the two states are represented by the alignment of a magnetic data "bit". Alphabetic characters are stored by assigning a particular number to them.

1.3.2. Short term and long term memory. In a modern computer there are two main types of memory; long term, which is usually stored on a hard disk drive (HDD), and short term, which is stored in the system random access memory (RAM). The long term memory

is non-volatile so that information is not lost even when the memory device is switched off. However, read-write access times for long term memory devices such as HDDs are very slow. This means that they are not suitable for use as the main system memory; a separate, faster memory is required for this job. Before an instruction can be processed by the CPU is must be read from the slow, long term memory and stored in the much faster short-term memory.

Long term memory is typically of much higher storage density, and cheaper per storage capacity. This makes the distinct arrangement of long and short term memories inside a computer optimal with today's technology; we can have fast computers with lots of room for storing large amounts of data for an affordable price.

RAM is so-called because any data bit in the device can be read or written regardless of which one was accessed previously.

1.3.3. Modern memory technologies. We continue with a summary of modern memory devices, in order to assess their advantages and disadvantages and to justify out requirements for new replacements. A brief description of a number of historic computer memory technologies is presented in Appendix A.

1.3.3.1. *Primary storage.* Most modern personal computers use solid-state RAM as their primary short term method of data storage, with a magnetic hard disk drive acting as the secondary device for permanent storage. Solid-state memory cells store binary data by collecting and retaining electrical charge. The first solid-state RAM chip using MOS technology was discussed in the mid-1960s **[8, 9]** and since then solid-state memory has become prevalent. There are two main types of MOS RAM, called static RAM (SRAM) and dynamic RAM (DRAM), and we now take a brief look at each type.

SRAM (Static Random Access Memory) works using bi-stable latch circuitry as the storage cell **[10]**. Four transistors are used to make up two cross-coupled inverters (Figure 1.5a). A number of additional transistors are then required to control access to a storage cell during read and write operations. The data does not need to be periodically refreshed, as is the case with DRAM, meaning that power consumption in SRAM is generally lower. However, data is still lost when the device is unpowered. The term "random access" indicates that any data bit in the device can be read or written regardless of which one was accessed previously. SRAM areal density and cost are limited by the high number of transistors per data bit. The relatively large cell area is approximately $40F^2$, where F is the minimum feature geometry in the fabrication

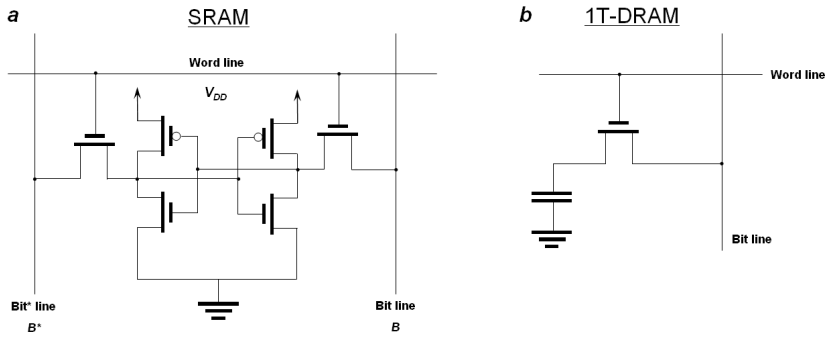

FIGURE 1.5. Circuit diagrams illustrating the components and layouts of typical (a) SRAM and (b) DRAM cells.

process [**11**]. This means that SRAM is too expensive to use as the large, main system memory but instead occupies areas like the fast cache memory inside the CPU where its fast access times, typically 25 nanoseconds, are most useful.

DRAM (Dynamic Random Access Memory) is the type used for the main memory in most modern desktop computers. A 1-TDRAM (One-transistor DRAM) uses just one transistor and one capacitor (Figure 1.5b). The information needs to be refreshed approximately once every millisecond because charge from the capacitors leak through the pass transistor over time. This increases power consumption. Since each DRAM bit is constructed from only one transistor and one capacitor the cells are much smaller than in SRAM, leading to higher areal densities. Cell size is usually around $10F^2$ [**11**]. Read and write times are moderate, with typical access times of around 60 ns.

Memory densities have increased rapidly since the early days of computing, doubling approximately every two years, whereas the speeds at which the memories work have remained relatively constant. In the 1990s the speed of SRAM and DRAM was considered a potential bottleneck when compared to the much faster speeds of CPUs being developed. If the front side bus (FSB) that connects the CPU to the system memory is slow then the CPU will have to wait for significant amounts of time to retrieve data from the memory. The cache SRAM is built into the CPU to help alleviate this problem. It is much faster than the system memory and allows the CPU to continue working. The cache memory stores data that has been accessed recently a number of times, so that commonly accessed data is readily available and does not need to be retrieved using the memory bus each time. Many modern processors include multi-level caching, with different types of cache for particular tasks. Because cache memory is so expensive, the amount that can be included in a CPU is severely limited by cost. This is

particularly true for budget processors. In recent years the progress in CPU speeds have slowed and the CPU-memory bottleneck has not proven to be as critical as had been feared.

1.3.3.2. *Secondary storage.* Flash memory is a specific type of EEPROM (Electrically Erasable Programmable Read Only Memory) that is erased and programmed in large blocks, hence it is not technically a form of random access memory and is not very suitable for use as system memory in a computer. However it is non-volatile and exhibits low power consumption so it is ideal for longer-term data storage use in portable devices that run from battery power. The four largest areas of flash memory uptake have been in removable memory cards (used in devices such as cameras), USB flash drives, MP3 players and portable or wireless devices such as mobile phones and PDAs. Removable Flash memory cards exist in a wide range of industrial standards and form factors, for instance Memory Stick [**12**], SmartMedia and Compact Flash [**13**]. Flash memory consists of a collection of individual cells that work by storing charge in a floating gate transistor. The amount of charge in the gate corresponds to the 1 or 0 of a binary data bit. Flash usually comes in one of two types; NOR or NAND. NAND flash uses tunnel injection for writing and tunnel release for erasing.

In NOR flash a cell resembling a MOSFET transistor with two gates stores charge on a floating gate that is electrically insulated from the control gate (Figure 1.6). This charge can be held stable for years and, because it partially screens the electric field from the control gate, the threshold voltage of the cell is modified. This threshold voltage determines the conductivity of the MOSFET channel, allowing a method for determining the state of the cell with a voltage being applied to the control gate. NAND flash typically has a cell size of $4F^2$, while NOR is typically $10F^2$ in size. Therefore NAND flash is more suitable for high-density data storage and is mostly used in MP3 players, digital cameras and digital video cameras. NOR flash is suitable for storing and executing program code because of faster initial read times and is used mostly in mobile telephones. Flash offers fast access times because erasing in large blocks speeds up the otherwise slow erase cycles when writing data. Therefore it is faster than standard EEPROM, although slightly slower than DRAM. It is cheaper to manufacture than byte-programmable EEPROM. Flash is physically quite robust because there are no moving parts inside, unlike traditional hard drives.

A disadvantage of NAND flash devices is their limited write endurance that make them unsuitable for use as main system memory inside a computer, which would involve large numbers of write events. NOR flash is more suitable for random access operations. Typically, each block

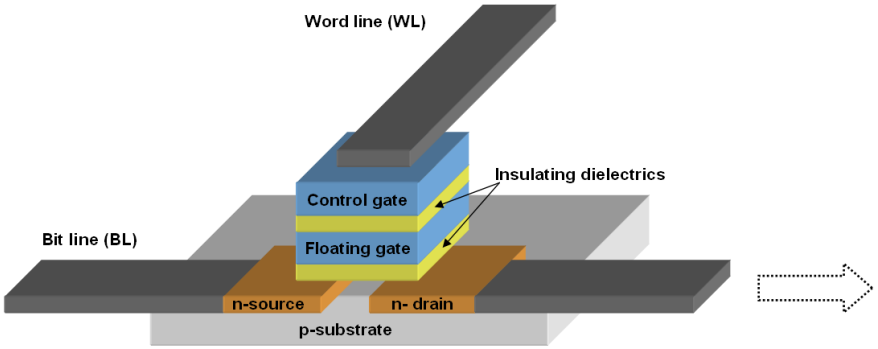

FIGURE 1.6. Schematic drawing of a typical flash memory cell. Electric charge is stored at the floating gate, and the amount of charge present determines the binary output status. Orthogonal electrical connections known as bit and word lines control read and write operations to the individual flash cells, which are arranged in an array architecture inside the device.

can survive around 100,000 program/erase cycles. Techniques to combat this problem include making sure that the amount of usage is spread evenly across all memory blocks, and that bad blocks are well managed. The voltages required for programming and erasing flash are high meaning power consumption is large. Reading from flash, however, only needs low voltages and has unlimited durability. Flash memory is still more expensive per byte than hard disk storage, particularly for larger form factors, but solid state drives to replace ordinary HDDs have started to appear on the market. These are currently much more expensive but capacities are beginning to be comparable and for some customers the promise of higher durability due to the lack of moving mechanical parts is attractive **[14]**. Most Flash memory cells are of single-level cell (SLC) design, where only one bit of data can be stored. Some later designs are multi-level cell (MLC) meaning that that a number of values can be stored, as various amounts of charge can be stored in the floating gate.

The Hard disk drive (HDD) is essentially one or more disk-shaped platters that are covered with granular thin-film magnetic media (Figure 1.7). The grains are essentially exchange decoupled, allowing independent magnetization orientation of neighbouring grains. Regions of the disk surface, containing a collection of grains, can be remagnetized in one of two uniaxial directions by a write head that hovers just above the disc platter, which spins at speeds up to 15,000 rpm. The write head also operates as a read head, using magnetoresistance phenomena to detect the orientation of the stray magnetic field emanating from the disk regions. Since floppy disk drives became largely obsolete in the early 21st century the HDD has become the only magnetic storage device that is widely used in modern personal computers. The first

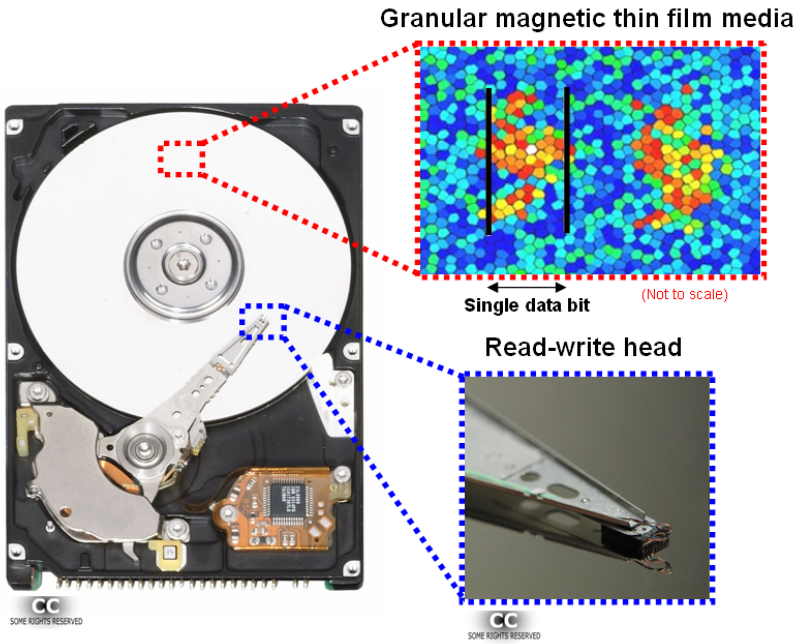

FIGURE 1.7. The internal workings of the magnetic hard disk drive (HDD), a mass-storage device. Ths spinning disc platters each have a GMR read-write head hovering above their surface as they spin at great speed. The head follows circular data tracks made up of regions of distinct magnetization, representing the data bits (Images: Composite from public domain).

commercial magnetic hard disk drive was included in the IBM 305 "Random Access Method of Accounting and Control" (RAMAC) in September of 1956. 50 disks each of 24 inch (0.61 m) diameter stored at total 5 Mbytes of data. The most recent HDDs have areal densities of around 500GB/sq.in meaning their 2.5" disks can store up to a total of 1.5TB of data. A number of different standardised form factors exist for hard drives, which cater for a range of applications **[15]**, the smallest being for hand-held devices such as MP3 players. The HDD faces a number of challenges in order to maintain its market position. The cost of Flash memory has reduced drastically allowing it to become competitive as high-capacity non-volatile storage. HDDs are not as physically robust as solid state memories due to the internal moving parts. The HDD is a technical triumph when one considers the precision required for the internal workings of the device, but due to its mechanical nature reliability is often a major issue with many parts such as motors and actuators likely to fail over the device lifetime. Although the HDD is the strongest candidate for storing large amounts of data, for instance in archiving, many home and business consumers are willing to pay a premium for safer solid state drives (SSDs) and it is expected that prices for these will fall even more in years to come.

Magnetic tape, constisting of a coating of iron oxide (Fe_2O_3) powder on a long paper strip, was invented in 1928 by a German, Fritz Pfleumer for recording and playback of audio signals. Later the paper was replaced with plastic for improved flexibility, strength and durability. One of the first examples of magnetic tape being used for computer data storage was in the UNIVAC1 computer in 1951 [**16**]. Stand-alone tape units such as the IBM 701 reel-to-reel tape drive, released in 1952, were installed as part of larger complete computer systems. Cassettes were introduced later in order to contain the tape itself and aid usability. The tape works in a similar way to the magnetic hard disk drive (HDD) but, instead of a rotating disk with a granular thin film, the iron oxide-coated tape is wound across a read-write head linearly. A popular format, Digital audio tape (DAT) systems, originally designed for high-quality audio recordings, provide extremely large storage capacities for periodic backup operations of computer networks. The length of the tape can be very long meaning the total data capacity is large but the nature of the device means that access times can be slow. Tape memory is actually classed as off-line or "tertiary" storage, which is stored as a permanent archive and accessed when required. Tape-based data storage is popular for use with automated library archives. The tape has proven to have long data retention and robustness, better than that of HDDs, which are the only size-comparable method of storage for comparable cost.

Combined compact disc read only memory (CD-ROM) and digital versatile disc read only memory (DVD-ROM) drives are commonly found in modern computer systems as a convenient method of removable storage and data archiving. Originally invented in the late 1970s for storing audio, the 12cm diameter removable compact discs (CDs) contain a spiralling track of pits that are read as binary data using the relative reflectivity of incident laser light to the areas with no pits [**17**]. The pit tracks in a typical CD are 150nm deep and 500nm wide, separated by 1100nm. Recordable drives for home users were introduced in the 1990s and use laser light to imprint data onto special photo-sensitive dyes. The CD standard has a data capacity of 700 MB. DVD discs improve on this with closer, smaller pit tracks and use of laser light of shorter wavelengths, to be able to store 4.7 GB per DVD layer. DVDs are popular for storage of high-quality video and advanced multi-layer versions have increased their capacity further. Recently the next generation of high definition optical disc formats [**18, 19, 20**] has entered the market, with Blu-ray winning out commercially over its rival, HD-DVD. Blu-ray discs can store 25GB on a single layer, with double-layer discs available.

For the first time in 2008 more than half of personal computers sold were portable laptop

computers, as opposed to desktop computers. There has also been a significant shift towards ultra-portable laptop designs [**21**], often forsaking an internal optical drive to reduce size, weight and cost. Ownership of an optical drive has become significantly less crucial, and the availability of most software and other data as an internet download has reduced the need for distribution of physical CD-ROMs or DVD-ROMs for installation.

1.3.4. Future memory. MRAM is proposed as a universal memory to replace and improve on existing primary and secondary storage solutions. As a random access memory (RAM) it can compete with DRAM for speed and for areal density [**11**]. As a high-density non-volatile memory it has comparable density to Flash and should work at similar speeds with unlimited read and write durability. We continue with a look at the principles and design of MRAM in chapter 3.

MRAM is not the only type of universal memory currently being researched. Various solid-state solutions are being pursued, including the non-volatile NVSRAM [**22**] and battery-backed SRAM (BBSRAM), which is a form of SRAM that relies on battery power to retain data and thus provide a form of non-volatility [**23**]. Ferroelectric RAM (FRAM) is designed like standard SRAM but instead of a dielectric layer it includes a ferroelectric layer that allows non-volatility [**24, 25**]. Spin torque transfer RAM (STT-RAM) is currently being developed by TDK and IBM, and is a variation on MRAM where instead of a magnetic field a spin-torque current is used for remagnetization of an oval magnetic tunnel junction (MTJ) cell [**26**]. Racetrack memory is a form of magnetic memory where magnetic domain walls are encoded into a wire [**27**], but many technical issues remain to be solved such as domain wall annihilation and inconsistent domain wall velocites.

1.4. Processor and bus

1.4.1. Logic gates for computer operations. Three basic logic gates, AND, OR and NOT, can be combined to perform all possible logic functions and operations required by computers. Some of these combined operations are so common that they have names and symbols of their own, such as NAND, NOR and exclusive-OR ("XOR"). Two of the most common logic gates, NAND and NOR can each be built from four transistors (Figure 1.8) [**28**].

The XOR gate, which gives positive output when we have positive input for either of its two inputs, but not both ("A or B but not both"), can be constructed in a number of ways (Figure

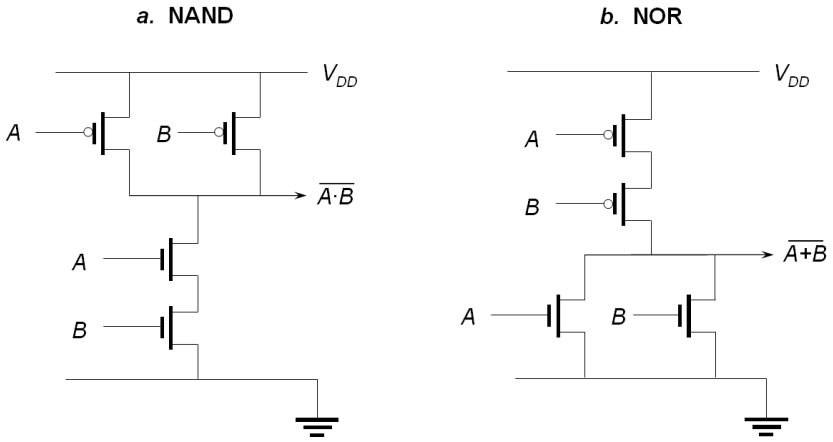

FIGURE 1.8. NAND and NOR logic gates each built by combining two n-channel "pull-down" transistors and two p-channel "pull-up" transistors.

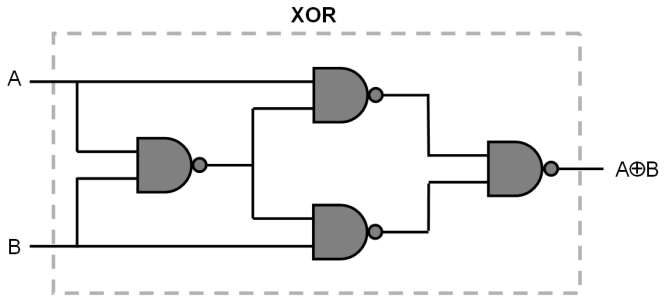

FIGURE 1.9. An exclusive-OR logic gate can be constructed in a number of ways from a collection of the basic logic gates. The simplest way is to use four NAND gates.

1.9). Firstly, one OR gate, two NOT gates and two AND gates are used. However, in most applications this is a cumbersome arrangement. Instead it is possible to use four NAND gates. This makes it cheaper and easier to wire together for use on a printed circuit board (PCB), for instance, as now instead of requiring three different types of gate we use all of the same type.

By combining logic gates we can perform arithmetic operations such as addition, subtraction, multiplications and division. For example, an adding circuit can be built from two AND gates, two XOR gates and one OR gate.

1.4.2. History of processors. A brief history of computer processors is presented in Appendix B.

1.4.3. Processor and bus limits. The continued size reduction of CMOS devices cannot continue along the current trend, and is likely to end by 2019 [**29**]. The reasons for this relate to fundamental and practical limits of transistor operation and manufacturing methods. To

increase the areal density of transistors on an IC chip, wires and components are made smaller and are positioned closer together. As the dimensions of a MOSFET are scaled down, the internal operation voltages must be scaled with it. This reduces the ratio between operation voltage and electron thermal voltage, which is constant at room temperature and equal to k_BT/q where k_B is the Boltzmann constant, T is temperature and q is the electron charge [**30**]. The thermal diffusion of electrons leads to higher source-to-drain leakage currents [**30**].

Scaling a MOSFET requires a reduction in the thickness of the gate oxide. If this is scaled to the thickness of a few atomic layers then quantum mechanical electron tunneling can occur through the oxide layer. The resulting gate leakage currents further degrade the performance of the transistor. As size is decreased further the inability to sufficiently dissipate this heat becomes a real limiting factor.

Manufacturing difficulty increases as transistor size is reduced. Lithographic techniques for manufacturing CMOS ICs have been scaled down well below the wavelength of visible light [**31**] and now extreme ultraviolet (EUV) light is used. This has required new approaches and innovative solutions to overcome subsequent barriers to further scaling. Future integrated circuits will need to make use of technologies other than CMOS.

Another limit of CMOS performance is the so-called *interconnect problem* or *interconnect bottleneck*, which some believe to be the most significant speed bottleneck for CMOS CPU and memory design today [**32**]. The interconnect problem is "the problem of unprecedented high density of interconnections operating at extremely high speeds and carrying high current densities" [**33**]. It is concerned with the limited bandwidth, latency and power of the electrical connections inside the CMOS architecture [**34**] when scaling down to nano-scale device architectures. As components can be made smaller and smaller the power and data connections to them from other components and from external devices must be made smaller and more closely packed too. This can lead to high crosstalk between different parts and excessive heating from the increased current densities. Efforts to reduce the problem by using better-performing materials, such as copper instead of aluminium can only improve matters to an extent. Further ideas, such as optical or superconducting interconnects have proven to be unsuitable for many high-level applications or difficult to scale down for general use.

1.4.4. Future processors. The major problems outlined above are common to all CMOS processing circuits, which work using electronic signals. In order to overcome these problems

new technologies for information processing and transport could be developed that are based on something other than the manipulation of electronic charge. In one example self-assembling nano-layers have been suggested **[35]** to build smaller and smaller transistors and interconnects. A truly fundamental limit in the distant future for transistor and circuit scaling is the size of individual atoms.

In order to provide a technological framework to extend the scaling of information-processing, spin wave logic and spin wave bus devices have been proposed. This is presented in more detail in Chapter 3.

1.5. Summary

The history of computer device and architecture design has shown that phenomenal increases in computational performance have been achieved through innovative and creative research and development. The driving force behind the earlier innovation came largely from military, research and commercial industrial application but later home consumers became an important factor. A number of current technologies require replacement if the growth trend in computing power and storage is to continue. Two of these new technologies are domain wall trap MRAM (DWT-MRAM), which is a candidate for universal memory in a wide range of applications and spin-wave logic gates with spin wave bus, which could revolutionize CPU design and push computer processing power past the not too distant limits of CMOS. The motivation for this thesis is to address these technologies and assess their abilities to fulfil the roles for which they have been proposed.

CHAPTER 2

Introduction to domain wall trap memory

2.1. MRAM

MRAM (Magnetic Random Access Memory or Magneto-resistive Random Access Memory) is a binary data storage concept that was first suggested in the late 1980s as a non-volatile replacement for conventional solid-state RAM [**36**]. An MRAM cell consists of a magnetic tunnel junction (MTJ) that contains a number of thin film layers, including a fixed layer and at least one free layer. As well as non-volatility, MRAM exhibits unlimited read-write endurance and fast read-write times and requires low supply voltages (Table 2.1).

2.1.1. MTJ structures. An MTJ generally contains a thin dielectric layer between the fixed and free layers, through which an electrical tunneling current can flow. The effective resistance experienced by the current, is measured as a fractional change called the magneto-resistance (MR), which depends on the alignment state of the free layer and is represented by equation (2.1).

$$R_1 = R_0 \left(1 + MR\right) \tag{2.1}$$

R_1 is the effective electrical resistance of the anti-parallel state and R_0 is the effective resistance through the parallel state. Realignment of the free layer creates a change in resistance

TABLE 2.1. Comparison of performance attributes for MRAM and its main competitors. In all areas MRAM performs well, meaning that it could one day take its place as a "universal" memory, replacing a number of existing technologies.

	SRAM	DRAM	Flash	MRAM
Read time	Fast	Moderate	Moderate	Moderate-fast
Write time	Fast	Moderate	Slow	Moderate-fast
Cell size	Large	Small	Small	Small
Voltage	Low	Moderate	High	Low
Non-volatile	No	No	Yes	Yes
Write endurance	High	High	Low	High

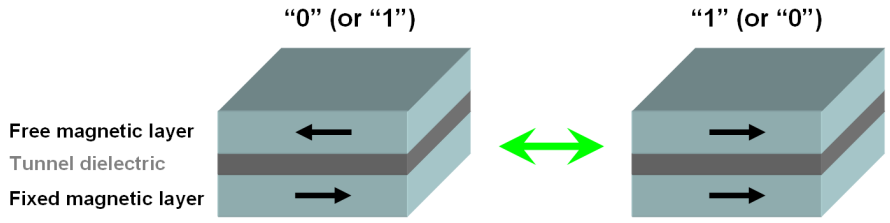

FIGURE 2.1. Standard design (not to scale) for a "Stoner-Wohlfarth MRAM" MTJ. The relative orientations of the free and fixed layers lead to two distinct states – parallel and anti-parallel – which correspond to varying electrical resistance through the multilayer structure. These represent the two binary data states of 1 and 0 (the choice is arbitrary).

which is larger when the free and fixed layers are anti-aligned and lower when they point in the same direction. This phenomenon is called tunneling magneto-resistance (TMR).

The most common MTJ contains a single free layer. This free layer, often made of permalloy, has a magnetic easy axis of polarization that is defined by its shape, and this is aligned parallel or anti-parallel to the easy axis of the fixed layer. The two different states can be inferred by the change in magneto-resistance through the stack. This information is interpreted as a "1" or "0" – a binary bit of data. MRAM cells are designed in a variety of shapes, including ovals and rectangles [**37, 38**]. The free layer can be magnetized arbitrarily into either direction using an external field. Since the free layer is sometimes assumed to switch by Stoner-Wohlfarth reversal [**39**] this standard, traditional design of MTJ is often referred to as "Stoner-Wohlfarth MRAM" (SW-MRAM). There is much evidence to suggest that MRAM elements actually switch by non-uniform reversal mechanisms [**40**].

Standard MTJs are faced with a number of technical problems. To fully select a bit for programming or erasing both the corresponding "bit" and "word" lines for the particular MTJ cell must be on (c.g. Section (2.1.3)). But this means that many other cells in the device experience "half-select" fields from the current lines [**41**]. Often the margin between half select and full select is small, meaning that switching can sometimes be overcome by thermal activation in half-selected cells. This problem is exacerbated by distributions in cell size and the presence of cell defects, both of which can be results of manufacturing [**42**]. Traditional MTJs experience significant error rates, which limits their implementation to small array sizes and short lifetimes [**41**].

2.1.2. Toggle MRAM. In order to overcome the significant error rates associated with Stoner-Wohlfarth MTJs an improved MTJ scheme known as "toggle MRAM" (Figure 2.2) was

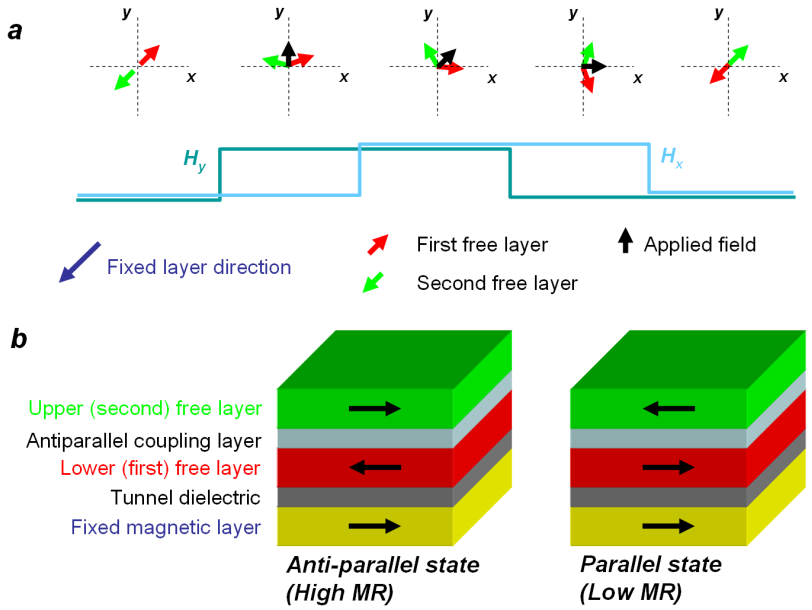

FIGURE 2.2. Schematic representation of a "Toggle MRAM" MTJ. It differs from traditional Stoner-Wohlfarth MRAM in that there is an additional free magnetic layer. The two free layers are separated by an anti-parallel coupling layer that ensures they are oppositely magnetized. Toggle MRAM overcomes some of the problems associated with previous MTJ designs by enlarging the separation between half-select and full-select fields. (Image adapted from [**37**])

suggested by Savtchenko [**43**]. This newer design incorporates an additional free layer that is separated from the other by an anti-parallel coupling layer so that the two free layers are oppositely magnetized at equilibrium, due to their dipole fields. The MTJ state is toggled by exposing it to a similar write line and bit line control sequence. Initially the applied field, $H = H_x + H_y$, points at a 45° angle to both free layers but both free layers attempt to align with the field, perturbing their directions. The field rotates, forcing the free layers to rotate with it, until pointing along the x-axis.

Toggle MTJs are much more tolerant of so-called "half-select" fields and of the stray magnetostatic fields from adjacent cells, because the free layers together have no net magnetic moment. Therefore it is more suitable for higher packing densities. One disadvantage is that at the end of switching the free layer has rotated 180° from the initial state, regardless of the initial state. The device must therefore be read at the start of the write cycle and only toggled if the initial state is different to the state of the incoming data.

2.1.3. MRAM architectures. There are two well-known approaches for MRAM architecture (Figure 2.3). The first, "cross-point" (XPT) architecture, consists of an array of wires

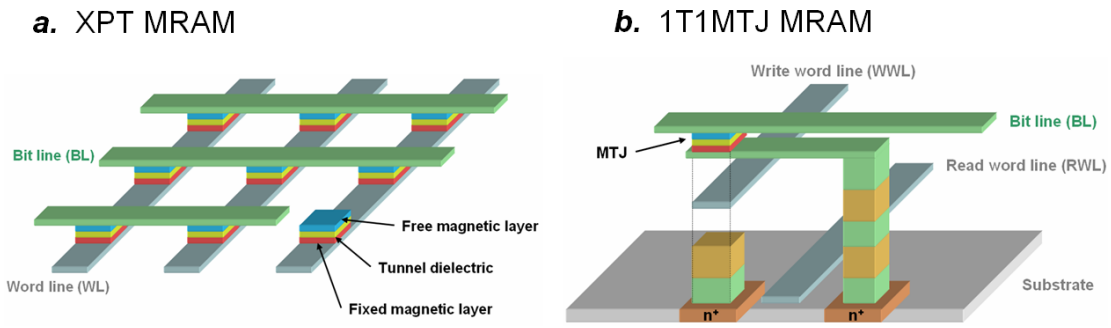

FIGURE 2.3. The two most widely used MRAM architecture designs; (a) XPT MRAM uses a single word line and a single bit line for each MTJ, which sits at the junction between the cross-over point of the two lines. In this way an array of cells is constructed. Unfortunately, the XPT arrangement suffers from bit-rate errors originating from half-select fields. (b) The "one-transistor-one-MTJ" (1T1MTJ) arrangement uses a field effect transistor (FET) as the read word line for each MTJ cell so that only one MTJ can be selected for writing at once. Although packing density is reduced the absolute read signal is much improved.

with an MTJ cell at each junction. The MTJ sits inside a rectangular region between two overlapping wires, the "word" and "bit" lines, that perform the read task by measuring the electrical resistance and the write task by generating an inductive field. This architecture exhibits high packing density and stacking is possible since no contact is made between the MTJ and the silicon substrate [**37**]. However, there are high current losses because each MTJ is associated with a resistance. Increasing the effective resistance of each individual MTJ helps but also lowers the absolute signal value. Performance is further degraded by the other MTJs along the same bit lines as the selected cell, and the current through these interferes with the read signal.

The second MRAM architecture scheme is called "one-transistor, one-MTJ" (1T1MTJ), where every MTJ is connected in series with an n-type FET (field effect transistor). The gate of the n-FET is used as the read word line (RWL) to select a particular cell for read operations, meaning that current losses are reduced. The absolute read signal is much higher than in XPT MRAM, therefore the effective resistance of each MTJ can be lower. However, due to the configuration, packing density is reduced.

2.1.4. Scaling of MTJ size. The size of each MRAM cell design is determined fundamentally by the minimum feature size that can be produced. Magnetic thin film elements can be patterned using various techniques. Electron beam lithography (EBL) with lift-off [**44**] is a popular method within research and development due to its ease of use and low cost for small

sample batches. However, EBL is not suitable for scaled-up production and ultimately some form of masked lithography would be required for full-scale device production. These technologies also have the advantage that they are present in a highly mature form within a number of closely-related industries such as semiconductor and solid-state memory production [**9**].

Critically, conventional MRAM scaling is limited because a decrease in element size must be accompanied by an increase in material coercivity, so that the superparamagnetic limit is avoided. [**45**]. This means that as MRAM areal density increases the write voltages required to switch the element polarization might become very high.

Spacing between neighbouring cells can also be an important factor when the MTJ has a finite magnetic moment, as magnetostatic fields from neighbour cells alter the effective field and lead to a spread in the switching field strength. Patterned media elements are usually designed with large enough cell-cell spacing so that they do not interact magnetostatically, but this increase reduces the areal density. Toggle MRAM avoids this problem somewhat since the combined upper and lower free layers have no total magnetic moment, except for briefly during toggling.

2.1.5. MRAM overview. MRAM has the potential to be a "universal" memory device as it possesses all of the important attributes that are required for a wide range of memory applications. In particular, fast read-write access times make it ideal for use as non-volatile computer system memory and high data densities make it suitable for high density secondary data storage. Since it uses lower power consumption than, say, Flash memory, it suitable for mobile devices running on battery power.

Traditional MRAM is limited by a number of problems that relate to the switching process in the free magnetic layer. There are a number of different mechanisms for realignment of the free magnetic layer. Domain reversal rarely proceeds via Stoner-Wohlfarth domain rotation but more likely follows nucleation and growth of a second domain, due to the size and shape of the cell, as well as material parameters [**40**]. In a typical MRAM the usual reversal process involves the nucleation of a new domain, complete with domain walls, which require the system to overcome a large energy barrier. This means that high field strengths are required, leading to higher energy consumption than might otherwise be the case. In addition, the switching process is not completely reproducible because domain nucleations can occur at different positions in the magnet each time. As a result the switching field varies.

The main challenges facing MRAM technology are to limit switching field variation by utilizing a reproducible switching mechanisms and to lower device voltages that depend on the coercivity of the switching element. Reducing the size of MRAM cells that are designed from discrete shapes causes an increase in coercivity, which is detrimental to the possibility of scaling to higher memory densities.

2.2. Domain wall trap MRAM

2.2.1. Introduction. In order to address the difficulties found with conventional MRAM a different approach known as DWT-MRAM (Domain Wall Trap MRAM) has been suggested [**45, 46**]. In DWT-MRAM, instead of a whole magnetic element being remagnetized during switching, a domain wall moves between two stable positions, remagnetizing the region of the MRAM cell through which it has travelled (Fig. 2.4). The applied magnetic field strength, H, required to de-pin a domain wall from the stable positions (closely related to the coercivity) is significantly lower than that required to nucleate a new domain wall [**45**]. The strength of the magnetic field generated by an electrical current through a conductor is proportional to the current amplitude, so lower currents can be used in the bit and word lines during program and erase operations [**47**]. This should lead to MRAM devices with lower power consumption.

Another advantage of DWT-MRAM over traditional Stoner-Wohlfarth MRAM is that the switching mechanism in DWT-MRAM should be more reproducible, allowing for consistent switching fields. This will depend on the ability to control the domain wall motion precisely and on the pinning sites for the domain wall.

2.2.2. General principles. A domain wall memory cell contains two magnetic domains that are separated by a 180° domain wall. The cell includes two domain wall traps, which are stable positions for the domain wall to sit at. Depending on the domain wall position, the magnetization of the middle region of the cell is aligned in one of two directions, which signifies a binary bit of data – a “1” or a “0”.

The stable configurations can be overcome by large thermal energies according to the Arrhenius-Néel law (Figure 2.5). Thermal stability of meta-stable micromagnetic configuration states is discussed in detail in Chapter 4.

2.2.3. Existing literature . The idea for a DWT-MRAM cell was first suggested in a paper by McMichael and co-workers [**45**], in which 2.5nm thick permalloy elements are modelled

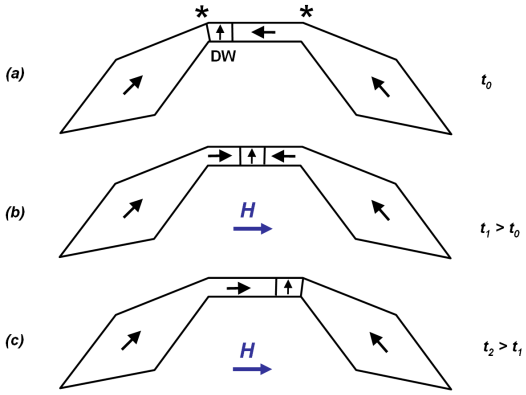

FIGURE 2.4. Domain wall memory works by using an existing domain wall to remagnetize a magnetic nanowire instead of nucleating a new domain wall for each switching event. A domain wall (DW) finds meta-stable positions at one of two domain wall traps (*). This reduces the coercivity (switching field) of the cell, allowing lower voltages to be used. The switching mechanism should also be more reproducible than total cell remagnetization [**46**].

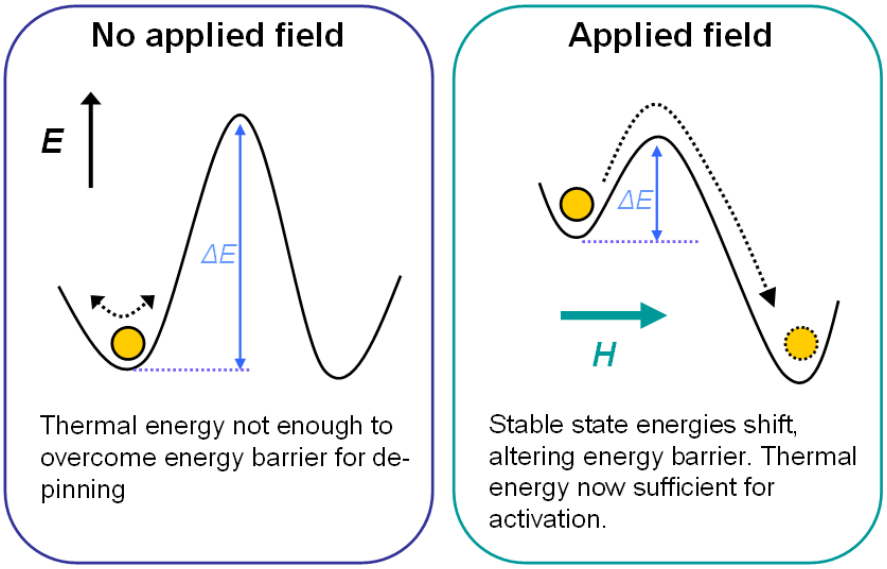

FIGURE 2.5. The domain wall memory has two stable "domain wall trap" positions, between which the domain wall is moved to switch data bit output from "0" to "1" and vice versa. In zero external field the memory should be thermally stable, meaning that the energy barrier for switching is much larger than thermal energy at room temperature. By applying a field in a given orientation we alter this energy landscape (in particular, Zeeman energy increases altering the balance of energies in the magnetic system) and make it favourable for switching to occur.

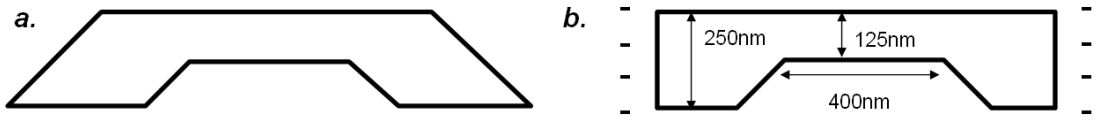

FIGURE 2.6. Example of domain wall trap memory as specified in [**45**]; (a) The shape of the domain wall trap (DWT) memory cell, (b) typical dimensions of the DWT cell. In [**45**] the authors use the finite difference (FD) method with surface charge boundary conditions that reduce the size of the simulation (b).

using the finite difference (FD) method. The authors investigated the relationship between coercivity and the element shape and size during switching to show that, for rectangular elements and domain wall trap (DWT) memory cells of comparable total area, the DWT cells showed around 94% lower coercivity. In this instance, the current amplitude in the write lines was 6% and the power 0.6% of the amount required to switch the rectangular element.

The domain walls were stable at the trap positions because there the domain wall angle is reduced, leading to a reduction in exchange energy. Instead of a 180° domain wall, as when the domain wall is at the centre of the trap, when positioned at either trap the domain wall angle is actually reduced to 135°, resting at the interior corner of the trap. A de-pinning field of 3.2 mT (32 Oe) is reported for moving the domain wall from one of the traps. The switching process of the rectangular element included two domain walls in motion, which explains the higher coercivity of the system. The authors also discovered that switching times for a given applied field above the critical switching field were almost twice as fast for the DWT cells as for the rectangular cells.

Using the finite difference (FD) method has a number of disadvantages. The diagonal boundaries in the triangular section of the cell (Figure 2.6b) cannot be accurately reproduced by square FD elements and so some precision in the experiment is lost. The authors chose to include surface charge boundary conditions to imitate a wire of infinite length (Figure 2.6b) but this means the pointed shape of the wire ends (Figure 2.6a) are not represented in the simulation. It is well known that the shape of a nanowire, including parts not directly involved with switching, can affect the switching mechanism [**48**]. With the angled ends the magnetization configuration at the ends of the wires would certainly be angled differently to the infinite wire case. A discussion on the FD method is presented in Chapter 4.

Brownlie and co-workers investigate a number of permalloy ($Ni_{80}Fe_{20}$) DWT structures (Figure 2.7) using Lorentz microscopy with a transmission electron microscope (TEM) [**46**]. The structures are produced using electron beam lithography (EBL) and the lift-off method

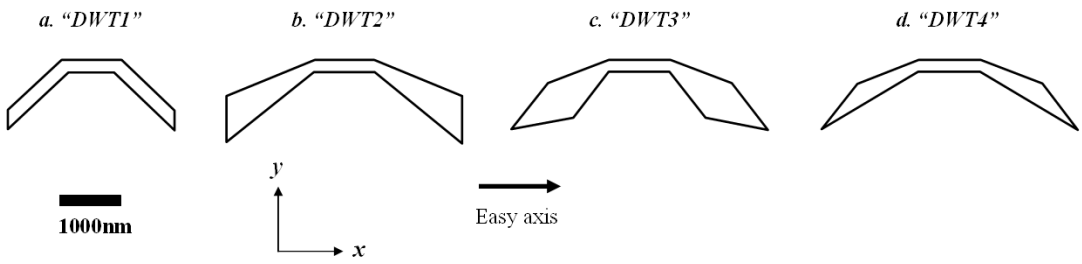

FIGURE 2.7. Some DWT cell designs from [**46**]; (a) DWT1 is a simple example where wire width remains constant throughout; (b)-(d) later examples use widening of the wire to increase the margins between the depinning field and the "expulsion field" required to push the domain wall out of the structure.

[**44**]. Domain walls are nucleated by applying a saturating external magnetic field some small angle away from the perpendicular of the long axis of the wire. The angle is chosen to control the position of the domain wall in the cell. The authors find that, for the given geometries and measurements, vortex domain walls occur 99% of the time and transverse walls only 1%.

The domain walls form in one of five positions; at the centre or slightly to either side of either trap position (2.8). It is necessary to design the wires with sufficient shape anisotropy at the ends so that domain closures do not inhibit the formation of domain walls in the specific desired trap position. The domain walls can be moved between the ends of the element using an applied magnetic field that is a few tens of Oersteds in magnitude. Detailed analysis of different domain wall types in each DWT cell show that the domain wall type affects the switching field and sometimes hinders the possibility of switching taking place at all.

Importantly, in some of the structures switching is not reproducible. Domain walls sometimes change to a different type under an applied field. This could result in a spread of switching fields that would be detrimental to device operation. The authors find the DWT3 design (Figure 2.7c) to be the most suitable for device applications due to low switching field, high domain wall stability and high resistance to domain wall expulsion. The DWT1 design (Figure 2.7a) is found to be particularly unsuitable.

The switching fields required to move a vortex domain wall back and forth between the ends of the middle section is not symmetrical due to the chirality of the vortex wall. When a vortex moves between ends it does not change chirality and so with respect to the axial symmetry of the switching region the interaction between the wall and the trap geometry is unequal.

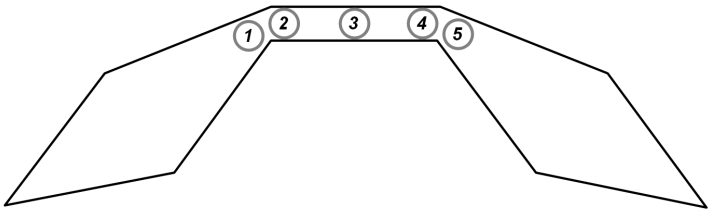

FIGURE 2.8. The five domain wall positions observed by Brownlie and co-workers [**49**] when a saturating field had been used to nucleate a vortex domain wall in the "DWT3" DWT-MRAM cell.

2.3. Domain walls in magnetic strips

Aside from DWT-MRAM, there is substantial literature in existence concerning domain wall dynamics in magnetic nanostructures. Here we review some important work that covers some of the fundamental concepts required to understand head-to-head domain walls in ferromagnetic nanowires.

2.3.1. Head-to-head domain wall configurations. Magnetic domain walls are the boundaries between distinct regions of a magnet where the internal magnetization in each individual region is effectively uniform [**50**]. Over the finite width of the domain wall the magnetization angle rotates between that of the two neighbouring domains. The main driving force behind the formation of distinct magnetic domains is internal containment of surface charges and the corresponding reduction in the magnetostatic energy term. Early works by Barkhausen [**51**], Bloch [**52**], Landau & Lifschitz [**53**], Neél [**54**], Kittel [**55**], among others, contain theoretical predictions and experimental evidence for the existence of domain walls.

It is possible to differentiate between a so-called Bloch wall, where the magnetization rotates through the plane of the wall and a Neél wall, where the magnetization rotates in the plane of the wall (Figure 2.9). The Bloch wall therefore exhibits surface charges while the Neél wall does not. These are the two basic domain wall types seen in ferromagnetic thin films. Bloch walls usually occur for larger film thicknesses, while Neél walls occur in film thickness below a certain size. In $Ni_{80}Fe_{20}$ permalloy this Bloch to Neél transition occurs at around 35nm [**56**].

The domain wall width for Bloch walls is dependent on the exchange and anisotropy energy terms and is approximated by $\delta_{Bloch} = \pi\sqrt{\frac{A}{K_1}}$, where A is the exchange constant and K_1 is the uniaxial anisotropy constant, while the width of a Néel wall depends on the exchange, anisotropy and magnetostatic energy terms and is given by $\delta_{Neel} = \pi\sqrt{\frac{2A}{\mu_0 M_S^2}}$, where μ_0 is the magnetic permeability of free space and M_s is the saturation magnetization.

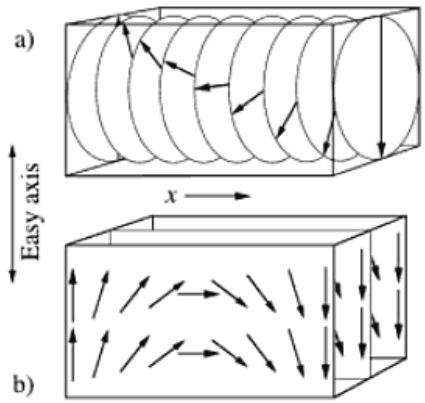

FIGURE 2.9. Bloch and Néel domain walls. (a) In a Bloch domain wall the rotation of the magnetization inside the domain wall, between the two magnetic domains, occurs through the plane of the thin film. (b) In a Neél wall the rotation occurs "in-plane". (Image taken from [**50**]).

Nanowires usually contain 180° domain walls since the domains are magnetised in one of two directions parallel to the long axis of the wire. Domain walls of 45° are common in magnetic closure domains, which can exist at the ends of nanowires or in larger multi-domain ferromagnets [**50**]. McMichael & Donahue [**57**] use finite difference (FD) simulation [**58**] to investigate domain wall structures in thin $Ni_{80}Fe_{20}$ strips with widths up to 500 nm and thicknesses up to 64 nm. The authors find that the type of head-to-head domain wall present in a permalloy strip nanowire is related to the wire width and thickness and the exchange length of the material. A phase diagram is constructed using the critical thickness T_{crit} and width W_{crit} at which a single vortex configuration and a transverse configuration are equally stable. Transverse domain walls have a lower energy when $T_{crit}W_{crit} \approx 130A/\mu_0 M_s^2$ [**57**]. Nakatani and co-workers [**59**] use a more precise micromagnetic method to numerically calculate a refined phase diagram. In addition they recognise the existence of a further domain wall type; the asymmetric transverse wall.

2.3.2. Domain wall motion. There is a large amount of existing literature on domain wall motion in ferromagnets owing to the huge interest in the use of domain walls in logic devices and memory. Domain walls generally move in the direction of an applied field that is oriented in the positive or negative direction with respect to the long axis of the wire. Domain wall velocity is important because if it is slow it could become a bottleneck for operation speeds in domain wall memory devices. The velocity of domain wall motion is different for different domain wall

types [**60**]. Vortex domain walls exhibit lower velocities than transverse domain walls due to the energy losses associated with the out-of-plane vortex core [**59**].

Early theoretical and numerical results were reached by Walker [**61**], Dillon [**62**] and Schryer & Walker [**63**] where domain wall motion under a d.c. applied magnetic field is found to fall under two distinct regimes. Below a critical field value $H_0 < H_w$ the domain wall motion is linear with the field. Above the critical field the domain wall is subject to a phenomenon, now known as "Walker breakdown", where its motion becomes oscillatory with respect to time and its position along the wire. Walker breakdown originates from the change in domain wall width and angle that results from the applied field. As the applied field increases the domain wall width decreases and the domain wall rotates with respect to the wire. At H_w (the Walker breakdown field or Walker field) this angle reaches a tipping point, where domain wall motion can be reversed altogether inducing the oscillatory motion. Walker breakdown has since been observed experimentally [**64, 65**] and in more complex simulations [**66**].

Suppression of Walker breakdown can be achieved on application of a transverse field [**67, 68**]. Glathe and co-authors [**68**] experimentally find strong influence on the domain wall motion from transverse fields above and below H_w. In particular, domain wall velocity below H_w is greatly increased due to stabilising of the internal structure of the domain wall.

Parkin and co-workers suggest a new type of memory that encodes data using a series of domains along a nanowire [**27**]. In "racetrack memory" read/write operations take place at one position of the wire, so the domain walls must be pushed through the wire using spin-torque currents [**69, 70, 71, 72**]. At present the technology faces a number of serious problems. For instance, to avoid data corruption all of the domain walls must travel at the same speed. This does not happen because crystal imperfections and edge roughness in the wires affect domain wall motion [**73**]. If the imperfections can be removed then domain wall velocity is improved 1000 times meaning racetrack memory could perform significantly faster than HDDs. Racetrack memory could potentially store huge amounts of data as its design could allow it to be fabricated in a 3-dimensional form.

2.3.3. Domain wall pinning. Domain walls can be pinned at a certain position inside a nanowire by local imperfections in the material parameters and geometry. This happens because the inhomogeneities produce local energy minima, making it energetically stable for the domain

wall to be present. Material imperfections are inherently hard to control, whereas geometric nanoconstrictions such as notches can be designed and fabricated with good accuracy.

A number of methods exist to calculate the pinning potential or the depinning field associated with a nanoconstriction. Kläui and co-authors [**74, 75, 76**] investigate domain wall pinning at nanoscale contrictions in permalloy nanostructures using low-temperature magnetoresistance measurements. Alongside high-resolution Scanning Electron Microscopy (SEM) images it is shown that vortex domain walls, occurring in thicker ferromagnetic ring structures, are repelled by notched nanoconstrictions and pinned to sites adjacent to the notches. Transverse domain walls, which occur in thinner structures, are pinned by the notch potential itself. The difference comes from the internal spin structures of the domain walls and their relative alignments to the magnetization in the nanostructure, which is perturbed by the notch.

Backes and co-workers [**77**] use simulation based on a Heisenberg model, alongside holographic imaging techniques, to find a faster than linear relation between the width of a ferromagnetic nano-ring and the width of the domain wall that it can support. For similar reasons, domain wall motion is inhibited by edge roughness in ferromagnetic nanostructured devices, increasing the coercivity in nanostructured elements with edge roughness [**78**]. Nakatani and co-workers suggest that domain wall motion could be enhanced by deliberately engineered edge roughness, to suppress Walker breakdown [**79**].

Asada and co-authors [**80**] use micromagnetics to simulate the bidirectional pinning of Bloch-like domain walls at a step in the thickness of a ferromagnetic thin film. They show that the de-pinning field required to de-pin the domain wall from the step increases with decreasing film thickness and varies according to the direction towards the step.

2.3.4. Multi-level cell storage. DWT-MRAM is able to function as a multi-level cell (MLC) device by containing more than two domain wall trap positions (Figure 2.10). This was first suggested by McMichael and co-workers [**45**]. A DWT device can contain a number of domain wall traps connected in series to represent a counting system of higher order than binary. For instance, eight traps would allow eight meta-stable positions for a domain wall, and this could be used for storage of numbers using the "base 8" counting system.

An alternative use for domain wall trap "chains" is to aid increased packing density of the standard binary DWT cells. By aligning and connecting the chains correctly it is possible to avoid problematic magnetostatic fields that exist at the ends of the standard DWT cells. These

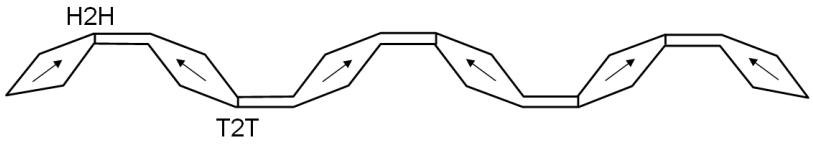

FIGURE 2.10. Domain wall trap memory chains, which could be used for multi-level storage (more than one bit of data) or as a way of efficiently packing single-bit cells on a substrate.

fields could otherwise interact with neighbouring cells, aligning the magnetic spins anti-parallel to the field and modifying the behaviour of the cells.

Brownlie and co-workers [**49**] fabricate a series of "domain wall chains" where every other DWT segment in the chain is inverted upside down. By applying a field to the whole chain head-to-head (H2H) and tail-to-tail (T2T) domain walls are formed, one in each segment. Under an applied field along the chain's long axis these H2H and T2T domain walls move in opposite directions and when two domain walls meet they annihilate. To generate a single domain wall in the structure is possible in an MRAM architecture consisting of bit and word lines, but the authors were unable to create sufficiently precise local fields inside the microscope.

2.4. Other domain wall applications

Aside from memory applications a number of devices exist, or are proposed to exist, that make use of domain walls and domain wall motion. The beauty of these devices is that they can often be lithographically fabricated to arbitrary specification, so a wide number of designs can be envisaged. Allwood and co-workers demonstrate a number of domain wall logic devices including diodes [**81**], shift registers [**82**] and logic gates [**83**].

A domain wall diode can be constructed by combining a ferromagnetic wire and a triangle (Figure 2.11). When a domain wall approaches the diode from the left it meets a low pinning potential due to the small step in wire thickness, but if it approaches from the right hand side the step in size is associated with a much larger pinning potential and the domain wall cannot pass though. It is hoped that by combining these and other individual components domain wall circuitry could replace electronic circuits in a number of applications.

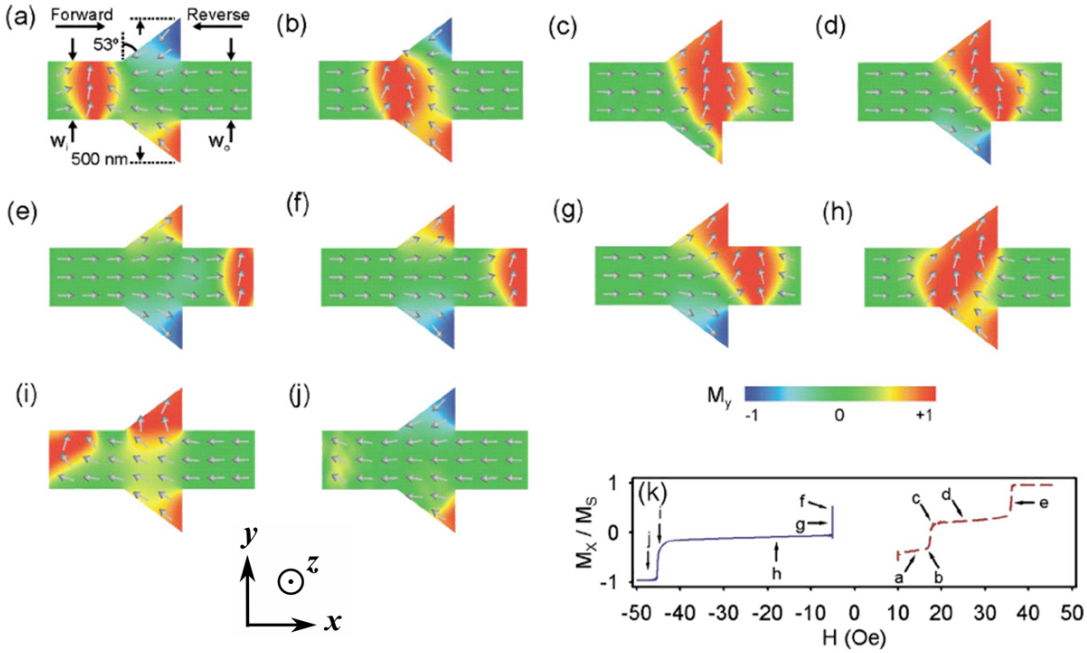

FIGURE 2.11. Simulation results demonstrating a DW diode. The domain wall is first moved in the forward direction and then the reverse direction using applied fields. The field strength to pass the diode is higher in the reverse direction due to an increase in the pinning potential (figure adapted from [**84**]).

CHAPTER 3

Introduction to spin wave nano-devices

As described in Chapter 1, many experts expect CMOS CPU technology to hit hard physical barriers to performance within a single decade. This has motivated the invention of some exciting new technologies, many of which are still in the early phases of development, but could one day replace CMOS. In this chapter we introduce the idea of using magnetic spin waves to transport data inside a computer, via a spin wave bus, as well as demonstrating how spin waves can be used to perform logic calculations. We discuss the advantages and disadvantages of the proposed devices and provide a review of important spin wave theory and significant existing literature.

3.1. Overview of spintronics

Before we enter into a discussion of spin wave theory we introduce the field of spintronics ("spin electronics"), of which spin wave research is a subset. In a traditional electronic circuit an electrical current travels around a closed loop consisting of a conducting medium and various functional components such as resistors, capacitors, inductors and transistors. The electric current is a flow of electric charge, which in metals is usually made up of freely mobile electrons, but in other materials can also consist of ions or pseudo-particles such as electron "holes" [**85**]. From these basic building blocks very complex circuitry can be constructed, culminating in the highly complicated microprocessors that we take for granted today.

Traditional electronics is successfully described by the classical theories developed by such pre-eminent scientists as Ampère, Faraday, Joule and Maxwell [**86**]. One of the most significant ideas of quantum physics is that fundamental particles such as photons, electrons (both leptons) and quarks have a quantum mechanical property known as "spin", which is a fundamental quantity, like charge. Along with the electron orbital angular momentum, it is the electron spin angular momentum, which has no classical equivalent, that determines so much of magnetic behaviour. Unlike classical angular momentum, these are quantized and can only take certain values for electrons within an atomic orbital.

The quantization of the electron orbital angular momentum inside an atom determines the available electron shells around the atomic nucleus. Since they are fermions, electrons are subject to Pauli's exclusion principle [**87**], which leads onto the arrangement of orbital electrons inside the aforementioned electron shells and the resulting periodic table of elements [**88**].

In traditional electrical circuits the quantum mechanical electron "spin" is ignored. In spintronics, however, the spin degree of freedom is utilized, either in addition to the charge or alone. When we speak of "spins" (for instance in micromagnetics) we are usually referring to the magnetization at the individual lattice points. This is a conventional manner of speaking in the magnetics community [**88**].

Giant magnetoresistance (GMR) was discovered independently by two research groups [**89, 90, 91**] in the late 1980s. When electrical current passes through a multilayer of ferromagnetic thin films, the resistance experienced by the current alters depending on the relative alignment of the layers. This is related to a reduction in the spin-dependent scattering of the carriers [**92**]. By designing such a GMR device it is possible to detect minute differences in magnetic field strength.

The most important consequence of GMR is that it became possible to design and build more sensitive read heads to measure the magnetization of individual data bits on a HDD platter surface (see Chapter 1). This allowed the use of smaller read-write heads and smaller bit sizes, resulting in higher areal densities and the continuation of the increasing trend of higher HDD data capacities [**93**]. A GMR "spin valve" typically consists of one fixed magnetic layer, pinned by a hard magnetic layer on one side and separated from a free magnetic layer on the other side by a non-magnetic spacer layer (Figure 3.1).

Another way that electrical current and a ferromagnet can interact is through the spin-torque effect and the closely related spin polarization effect. When an electrical current is applied through a ferromagnet the spins of the carrier electrons interact with the orbital electron spins that define the magnetic polarization, via the spin-orbit interaction. In this way the carrier electrons can become spin-polarized (Figure 3.2). Spin-polarization occurs over distances through the ferromagnet of the order of one or a few nm. A spin-polarizer is essential for a spintronics device as a source of spin-polarized current.

The magnetization of the spins inside the ferromagnet can be modified by the spin-torque effect [**71, 72**]. The spin-torque effect can be represented by an additional "Slonczewski" term in the LLG equation [**71, 94**] for numerical simulations. Spin-torque currents are an essential

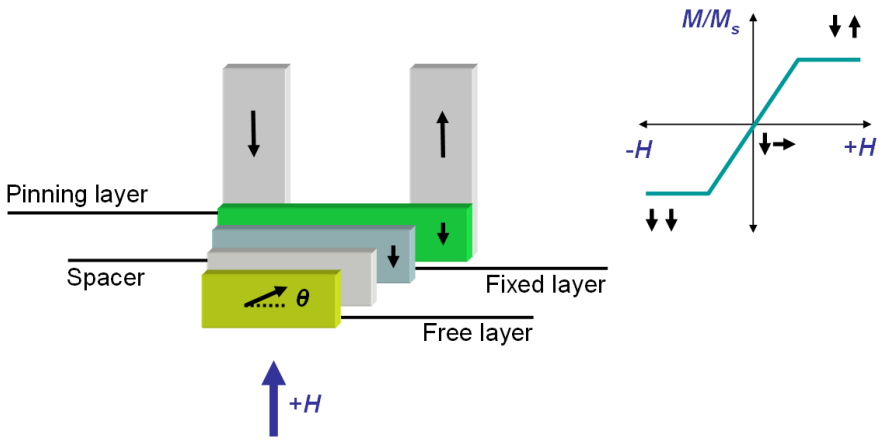

FIGURE 3.1. Schematic of a GMR spin valve. The fixed layer is pinned by a ferromagnetic layer. The free layer is able to rotate under the influence of an applied magnetic field. The difference between the orientations of the fixed and free layers determines the electrical resistance through the multilayer stack.

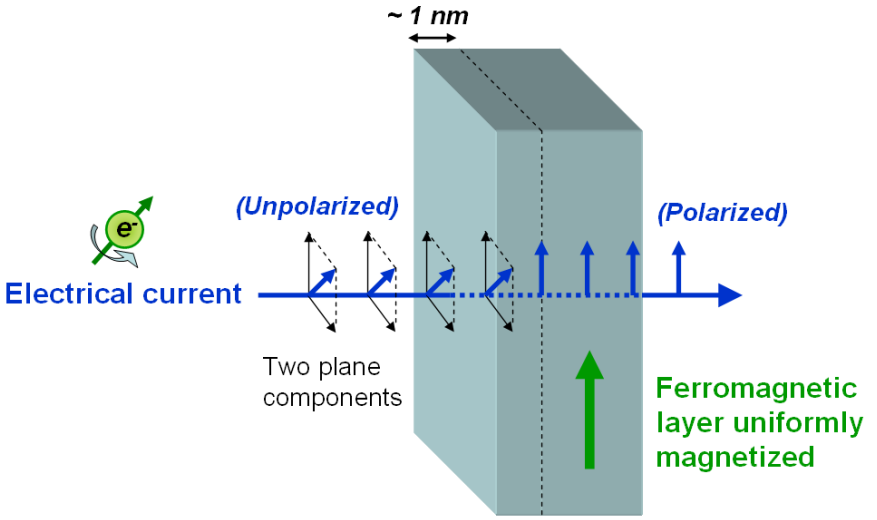

FIGURE 3.2. A schematic representation of the process of spin polarization of an electrical current. The spins of the unpolarized electrons have two components in the film plane. As they pass through a small distance of the uniformly magnetized ferromagnetic layer the spin is polarized in the magnetization direction.

part of spintronics as they provide an important link between conventional electronics and spin-utilizing devices. A domain wall, for instance inside a ferromagnetic nanowire, can be moved by a spin-torque current.

A more detailed discussion of the theory of spin-torque and spin-polarization can be found in the references provided.

3.2. Spin wave theory

3.2.1. Background. Spin waves are propagating disturbances in the ordered internal magnetization of a magnetic system. The term 'spin waves' usually refers to magnetic waves that have a wavelength much greater than the lattice parameter of the crystallographic ferromagnet through which they propagate [**95**]. The concept of a spin wave was invented by Bloch [**96**] and spin wave theory is covered comprehensively by Kittel's "An Introduction to Solid State Physics" [**85**].

Spin wave modes inside a ferromagnet contain contributions from both the short-range exchange interaction and the long-range magnetostatic or "dipole-dipole" interaction. These spin waves are hence sometimes referred to as "exchange-dipole" spin waves. The quantum mechanical exchange interaction results from overlapping electron wavefunctions [**88**], directly affecting nearest-neighbour spins, which adjust their polarization in an attempt to align along the same direction. Indirectly, the exchange interaction has a slightly longer-distance effect on the magnetization due to secondary perturbations. The range of its effect on the magnetization of spins is called the exchange length, and can be calculated from material parameters (Chapter 2).

At different length-scale regimes one of these terms can dominate (Figure 3.3) [**95, 97**]. For large wavelengths of typically a few hundreds of nanometres and above the magnetostatic spin waves dominate in their overall contribution over the exchange spin waves [**98**]. In very long wavelength regimes the spin waves are often referred to simply as "magnetostatic waves" in the literature because the contribution from exchange is minimal. A much larger volume of work exists regarding magnetostatic waves (MSWs) than for "exchange" spin waves. The main reason for this is the relative difficulty in detecting and measuring exchange spin waves, which require experimental techniques on a very small length scale and with very short temporal resolutions.

Many experimental papers exist where yttrium iron garnet (YIG), a material ideal for work with magnetostatic waves because it displays long magnetic relaxation times [**99**], is used as a

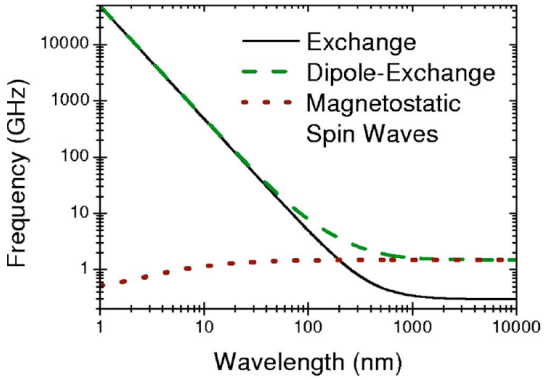

FIGURE 3.3. Dispersion relations of dipole-exchange spin waves inside a 5nm thick YIG film. At smaller wavelengths, as found in nano-devices, the exchange contribution dominates over the magnetostatic so that they can be considered "pure exchange" spin waves (figure taken from **[97]**).

propagation medium for microwave (wavelengths from 1mm to 1m) electromagnetic radiation **[98, 100, 101, 102, 103]**. A number of magnetostatic wave (MSW) applications are discussed by Ishak **[104]**. For example, delay lines that rely on MSWs being many times slower than electromagnetic waves to propagate.

For wavelengths below a few hundred nanometres the exchange term heavily dominates, since the sample dimensions are comparable to the exchange length. Spin waves in nanostructured devices, where at least one of the dimensions is on the nanoscale, can usually be approximated as pure exchange due to their short spin wave wavelengths **[105]**.

Spin waves share many behavioural characteristics with other more well known oscillatory systems. For instance spin waves can reflect, refract and disperse when encountering edge boundaries, defects or other features **[106]**. Some of these effects may present useful outcomes; for instance a head to head domain wall can be used to shift spin wave phase by a controlled angle for logic calculations **[107]**. At other times, wave effects can be detrimental to a device. Spin wave frequency modes are dependent on the specific device geometry and material parameters. The resonant frequency of spin waves inside a nanowire of rectangular cross-section with thickness T and width W can be calculated analytically using the Kittel formulation (Equation 3.2). This formulation assumes that spin waves originate purely from the exchange interaction and thus is valid for small length scales.

$$f_{res} = \frac{\gamma \mu_0}{2\pi} \left[\left(H_{ext} + (N_y - N_x) M_s \right) \times \left(H_{ext} + (N_z - N_x) M_s \right) \right]^{\frac{1}{2}} \tag{3.2}$$

N_x, N_y and N_z are demagnetizing factors that originate from the geometry of the wire (Equations 3.3, 3.4, 3.5). Generally, the internal demagnetizing field, H_d, which subtracts from an applied field, H_a, is inversely proportional to the magnetization of the sample, with the combined demagnetizing factors providing the constant of proportionality so that $H = H_a - H_d = -NM$. The demagnetizing field originates from surface poles that form at the ends of a magnetized material of anisotropic geometry. Inside ferromagnetic nanostructures, spatial confinement at nanometre length scales becomes important in determining spin wave behaviour. Equation (3.2) considers this spatial confinement by including the demagnetizing factors in three dimensions. In thin films the spatial confinement is in one dimension meaning that the demagnetizing factors dominate in the plane of the film. In thin-film nanowires spatial confinement exists in two dimensions so that $T \ll W \ll L$ and the demagnetizing factor along the length of the wire dominates. The dimensions of the crosssection of the wire are represented by the width, W, and the thickness, T, while the length of the wire, L, is the largest measurement and runs along the long axis of the wire. If the wire sits in the $x-y$ plane with x the long axis, and z pointing out of the wire plane (the thickness of the wire is measured along the z-axis) then the demagnetizing factors are given by equations (3.3), (3.4) and (3.5). Spin waves propagating along a soft wire travel along the $\pm x$ directions and can be measured by the transverse magnetization, $\boldsymbol{M}_y$.

$$N_x = 0 \tag{3.3}$$

$$N_y = \frac{2T}{\pi W} \tag{3.4}$$

$$N_z = 1 - \frac{2T}{\pi W} \tag{3.5}$$

3.2.2. Artificial spin wave generation. Spin waves originate from a localized disturbance in an ordered ferromagnet. At finite temperatures so-called "thermal spin waves" are present, but these are typically of low amplitude and too incoherent to have use in practical applications. In order to generate spin waves artificially, a localized disturbance can be produced

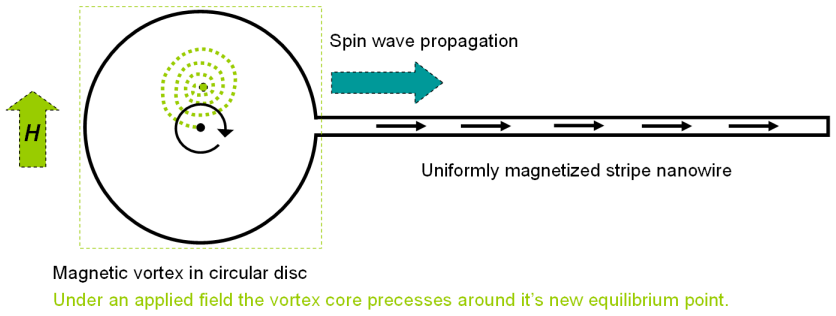

FIGURE 3.4. Vortex core method for artificial spin wave generation. By applying an external field to the nanodisc the vortex core is forced into a new equilibrium position, off-centre in the disc structure. Before it reaches this new equilibrium the core spirals into the equilibrium position in damped precessional motion. The precessing vortex core periodically disturbs the magnetization of the disc, and this disturbance propagates into the attached nanowire. By applying a pulsed magnetic field it is possible to induce sustained oscillations of the vortex core.

using a number of methods:

(1) Induction. An external magnetic field can be induced by an electric current in a strip-line, much the same as a word or bit line in an MRAM device. This induced external field perturbs a localized region of the sample, introducing an increase in Zeeman energy into the system, which is dissipated by releasing spin waves into the system before equilibrium is reached. One method to produce very sharp field pulses is to use a laser beam on the insulating semiconductor layer between strip-line sections so that a current pulse is discharged [**108**]. This current pulse then induces a response in the ferromagnetic layer of the thin-film sample.

(2) Vortex core oscillation. The position of a vortex core inside a circular nanodisc is perturbed by an external field, and precesses around its new position before reaching equilibrium (Figure 3.4). This periodic precession disturbs the magnetization of the entire disc and the disturbance propagates into the connected strip nanowire as spin waves. The method provides some control of spin wave properties but is not field-programmable for frequency.

(3) Spin-torque current. A spin-torque current can be applied through a region of a magnetic nanowire to alter the polarization. This localized perturbation, when introduced over a finite time interval of the order of picoseconds, generates spin waves that propagate into the rest of the sample.

When producing spin waves by applying a localized oscillating magnetic field, standing spin waves of a particular frequency can be excited. Spin wave amplitude will be largest when the drive freqency, f_d, of the applied field matches the spin wave resonant frequency, f_{res}, of the ferromagnet. By sweeping through a range of f_d and looking for measured amplitude variations it is possible to find the eigenmodes in the frequency response of the system. Applying a single field pulse, or switching on and holding, or switching off a previously "on" localized field will result in a broadband spin wave packet, which contains a distribution of spin wave frequencies and a main frequency peak corresponding to the f_{res} of the sample ferromagnetic structure. Hertel and co-workers demonstrate a simulation method for generating a broadband spin wave packet in magnetic nano-structures where a region of a nanowire is arbitrarily set to a different magnetization orientation from the bulk of the sample. On relaxation, the perturbed region aligns to the effective field, $\boldsymbol{H}_{eff}$, of the sample via damped precession, with the excess internal energy dissipating as spin waves [**108**].

An experimental observation of spin wave amplitude in a magnetic nanostructure will measure the thermal spin waves that result from the finite thermal energy. This can be useful because it removes any influence on the spin waves from an external stimulation and allows the natural frequency modes to be examined closely. Jorzick and co-workers [**109**] investigate spin wave wells in rectangular micrometer sized elements, measuring the thermal spin waves using Brillouin light scattering (BLS) [**110**].

3.3. Spin wave devices

3.3.1. Spin wave interferometer. Hertel and colleagues demonstrated a proof-of-concept spin wave interferometer [**107**] that uses a branching nanowire to split a coherent beam of spin waves and recombine them to produce constructive and destructive interference (Figure 3.5). Spin waves that pass along a wire that contains a head-to-head domain wall experience a phase shift $\triangle\Phi = \frac{\theta}{2}$, which is proportional to θ, the angle of rotation of the domain wall. For example, a 180° domain wall (the authors use a transverse domain wall in a 36nm wide, 6nm thick permalloy strip wire) induces a phase shift of 90° , or $\frac{\pi}{2}$ radians.

A local non-uniformity in the magnetization can be created not only using a domain wall but with an applied magnetic field. An analytical investigation by Vasiliev and co-workers [**97**] for a YIG waveguide interferometer suggests that certain profiles of the local non-uniformity allow total transmission of spin waves while inducing the large phase shifts required for a functioning

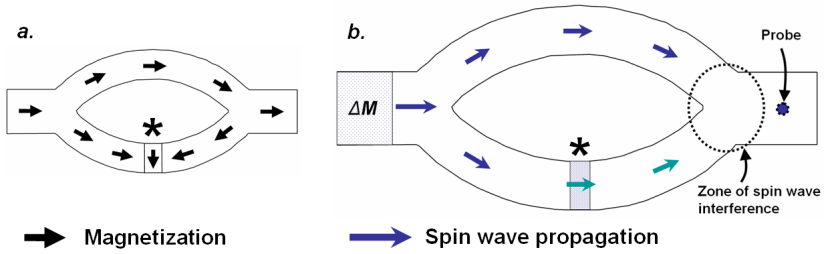

FIGURE 3.5. A spin wave interferometer. Spin waves are generated at one end by perturbing the magnetization direction by a small angle (denoted "$\Delta \boldsymbol{M}$"). A domain wall (*) in one branch acts as a phase shifter on the spin waves that pass through that branch. The spin waves from each branch then recombine, with the phase shift producing interference [**107**].

logic device. Spin wave interference has been observed by Choi et al [**106**] in a simulation reminiscent of the famous "Young's double slit" experiment [**111**]. Spin waves from an oscillating vortex core pass though a nanowire waveguide, with a branch splitter and into a bulk film. The spin waves from these two point sources then refract and propagate through the ferromagnetic film before meeting and producing constructive and destructive interference patterns.

3.3.2. Spin wave logic and spin wave bus. Spin wave logic with a spin wave bus is suggested as a replacement for traditional transistor logic circuits. The idea for spin-wave logical gates is suggested by Kostylev et al [**112**], using a 5 μm thick YIG waveguide, and Khitun & Wang [**113, 114**] who propose a nano-scale ferromagnetic thin film as a waveguide, as part of a nanoscale computational architecture using a spin wave bus. A cellular non-linear network (CNN) is a promising architecture for future computer systems, which consists of a multi-dimensional (2 or higher) array of identical cells. Each cell is able to communicate with surrounding cells locally and within a finite radius [**114, 115, 116**].

A CNN can be built using broadly different materials and cell designs. In fact a simple CNN can be constructed from simple objects such as snooker balls, but the practical uses for this kind of network are limited, and so most CNNs in use today are constructed using silicon-based cell designs. Two-dimensional CNNs are now widely used [**117**] to perform powerful tasks such as image processing [**118, 119**] and motion detection [**120**]. Among many other uses they are also able to solve partial differential equations, model sensory-motor organs and analyze 3-D surfaces.

A spin wave CNN can be built using an array of standardized cells that sit above a ferromagnetic thin film. The thin film acts as a bus between the cells, and allows them to communicate

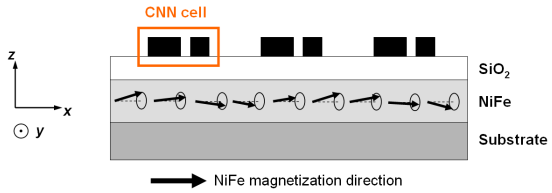

FIGURE 3.6. A spin wave CNN system, utilizing a ferromagnetic NiFe thin film as the spin wave propagating medium (the spin wave "bus"). The CNN cell, consisting of an asymmetric coplanar strip (ACPS) transmission line generates and detects spin waves by electromagnetic induction from a current pulse.

using spin waves that propagate through the ferromagnet in two dimensions. Each cell acts as a spin wave source (output) and a spin wave receiver (input). This can be achieved using an asymmetric coplanar strip (ACPS) transmission line [**114**].

The spin wave CNN overcomes the interconnect problem (Section 1.4.3) by communicating via magnetic induction (Figure 3.6). There is no electrical interconnect between the cell and the ferromagnetic medium required. Spin waves are generated by passing electrical current through the lines of a cell, and via Faraday induction the resulting magnetic field creates a perturbation in the magnetization of the underlying NiFe layer; a spin wave source.

Logic functions can be performed by utilizing the constructive or deconstructive interference that occurs when two spin waves are combined and are measured. A voltage pulse through a CNN cell generates a spin wave packet. If the pulse is inverted then so is the spin wave packet. In a cellular network, three cells arranged in a line as part of a larger array are required to perform an AND logic operation (Figure 3.7a). The outermost cells (numbered 1 to 3) generate spin wave packets, which propagate outwards through the ferromagnetic film in two dimensions. The superimposed spin wave packets are measured by the central cell (numbered 2). If both spin wave packets have positive polarity then the combined amplitude is above the (carefully selected) reference voltage, V_{ref}. If one or both of the spin wave packets are of negative polarity then the measured voltage at cell 2 is below V_{ref}. Any output voltage measured above V_{ref} is interpreted as a logical output of 1, whereas below V_{ref} the logical output is 0. This is consistent with the traditional logic truth table for an AND gate (Figure 3.7b). By varying the reference voltage, Khitun and Wang also proposed similar devices for NOT and OR logic calculations [**29**].

The spin wave bus and logic system does have some inherent drawbacks; magnon-magnon and magnon-phonon scattering leads to significant amounts of damping so that the relaxation

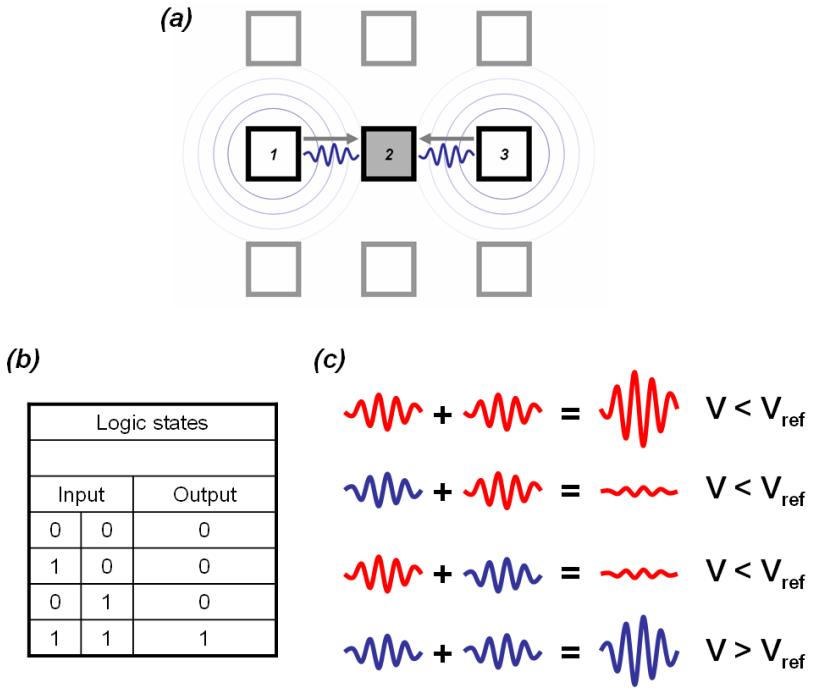

FIGURE 3.7. A spin wave cellular non-linear network (CNN) working as an AND logic gate. A reference voltage is chosen for comparative analysis with the measured output voltage. The only instance where the output is greater in amplitude than the reference voltage is for two "true" inputs, which constitutes an AND function.

time of spin waves is of the order of nanoseconds at room temperature and attenuation occurs quickly [**121**]. Additionally, the group velocity is relatively low (about 104 m/s) meaning that signal propagation is slow [**121**]. These two factors combine to restrict spin wave bus operation to short distances, up to a few tens of micrometres. However, spin wave buses are still capable of providing a useful alternative to CMOS systems as some specific logic functions and algorithms can be performed more easily and using fewer components.

3.4. Spin wave reflections

In order to limit computational costs during micromagnetics simulations, the model is often limited to a sub-region that approximates a much larger device. Intelligent use of boundary conditions can improve the accuracy of the approximation. For instance, McMichael & Donahue use boundary conditions to approximate an infinitely long nanowire [**45**]. However, this technique sometimes means that the boundaries of the geometry are much closer to the areas of interest inside the model. In a simulation involving spin waves, the spin waves may not be able to damp

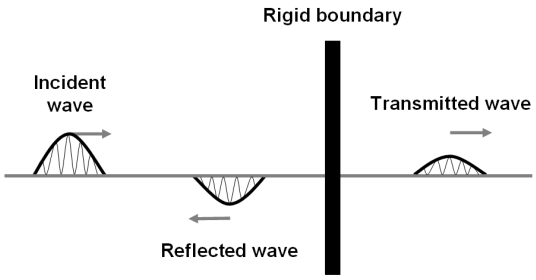

FIGURE 3.8. Schematic representation of reflection and transmission of an incident wave packet at a rigid boundary. The sum of all the amplitudes is zero.

out before reflecting from the boundaries, as would have been the case with a much larger geometry. These reflections can interfere with the incident spin waves and complicate interpretation of the SW properties. Constructive and destructive wave interference can be detrimental to micromagnetics results. Hrkac and co-workers have investigated standing waves generated by point contacts in circular nano-pillar spin-torque oscillators [**122**]. They have found that spin waves reflecting from the boundaries interfere with the incident waves to destroy the standing wave patterns.

For mechanical waves incident on a rigid boundary we have $A\cos(k_1x - \omega t) + B\cos(k_1x + \omega t) = C\cos(k_1x - \omega t)$ where A is the amplitude coefficient of the incident waves, B of the reflected waves and C of the transmitted waves (Figure 3.8). Note that the reflected wave is inverted in amplitude with respect to the incident wave. For perfect reflection, with no transmission, this becomes $f(\omega, t) = A\cos(k_1x - \omega t) + B\cos(k_1x + \omega t)$.

Spin wave reflections have been addressed for the case of MSWs in YIG. Physical additions to the bulk YIG film using recording tapes, ferrite powders [**123**], soft iron rods [**124**], permalloy bars [**125**] and GaAs thin films [**126**] have been made to absorb MSWs and stop reflections.

3.5. Magnonic crystals

A magnonic crystal is a material with magnetic properties that are periodically modulated at the nanometer scale (Figure 3.9). They can act as a medium for spin wave transport where the periodic internal structure can introduce frequency band gaps to spin wave propagation.

Band gap phenomena are observed in a wide range of scientific disciplines, for instance photonics [**127**], plasmonics [**128**] and semiconductor physics [**129**]. A band gap is a range of frequencies ω over which there are no propagating real solutions of Maxwell's equations for any wavevector $\boldsymbol{k}$.

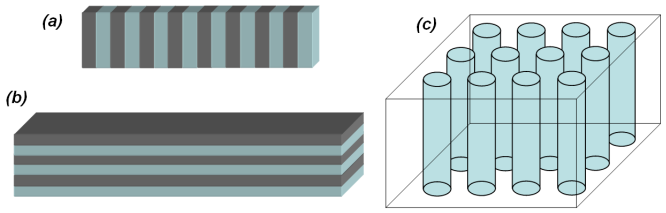

FIGURE 3.9. Examples of magnonic crystals: (a) a nanowire with longitudinal periodicity; (b) a nanowire with transverse periodicity; (c) a two-phase nanopillar matrix. Materials that could be used in these structures include an Fe/YIG matrix since both of these are known to effectively transmit spin waves [**131**]. NiFe permalloy could also be used.

Krawczyk and co-workers formulated frameworks that describe forbidden frequency regions for magnon propagation in magnetic nanostructures with three dimensional periodicity [**130**] and in layered composite materials [**131**]. Kruglyak and co-authors have presented a theoretical derivation of the spectrum and damping of spin waves in a cylindrical periodically-structured magnetic nanowire, a type of cylindrical magnonic crystal [**132**].

Gorobets and Reshetnyak [**133**] investigate the reflection coefficients of bulk spin waves from ferromagnetic multilayers (including a single barrier) with periodically modulated parameters of the exchange interaction, the uniaxial magnetic anisotropy and the saturation magnetization; a type of magnonic crystal. They show that spin wave reflection depends on the spin wave frequency as well as interfacial coupling parameters and internal structure of the unit cells.

We will investigate periodicity not in material parameters but in geometric features, namely periodic edge roughness in strip nanowires.

3.6. Summary

Magnetic spin waves in magnetic nanostructures usually have wavelengths small enough so that we can approximate their behaviour to pure exchange spin waves. Spin waves can be used to transmit and process data in a cellular non-linear network (CNN). This could be used to overcome some of the fundamental barriers to continued performance that are faced by the current generation of CMOS-based computers.

Spin waves themselves are propagating disturbances in the ordered magnetization of a magnetic medium and do not require electrical current to work, avoiding many of the problems associated with scaling down CMOS in size, such as resistive heating and leakage currents.

In later chapters we use micromagnetics to assess the quality and behaviour of spin waves in magnetic nanowires and their ability to function in useful spin wave devices. We investigate methods for tuning spin wave properties and the effects of the magnetic medium on the spin wave propagation.

CHAPTER 4

Finite element (FE) micromagnetics

The differential equations that govern magnetic phenomena can only be solved analytically for certain special cases. Normally a numerical solution is required for greater accuracy with real world problems. In this chapter we describe how the finite element and boundary element methods are used to model dynamic magnetic systems of arbitrary design and materials. We also describe a method for finding saddle points and minimum energy paths in the energy configuration space of a magnetic system. This enables us to estimate the thermal stability of memory storage devices such as magnetic random access memory (MRAM).

4.1. Micromagnetic background

4.1.1. Overview. Micromagnetics is a continuum model for understanding dynamic magnetic processes at sizes between the nano-scale and the meso-scale, a domain that encompasses many devices such as iron oxide magnetic recording tape, hard drive read-write heads, patterned media and magnetic nanowires. In this sense, micromagnetics bridges the gap between our understanding of the quantum mechanical origins of magnetism [**88**] and the macrosopic equations of Maxwell [**134**], giving a theory that is capable of conveniently solving sophisticated problems. The resulting theory, relying on classical physics, largely ignores quantum mechanics because to consider objects of such size from quantum first principles would involve numbers of particles so large as to be impossible with even the fastest computers. Computational micromagnetics provides a convenient tool to study ultra-fast dynamic processes, such as switching (Figure 4.1) and precessional motion. Micromagnetics finds its origins in papers by Landau & Lifschitz involving calculations on domain walls [**53**]. Later work by Brown [**135**] discusses the theory in greater detail.

4.1.2. Equation of motion. The effective field, $\boldsymbol{H}_{eff}$, exerts a torque on the magnetic dipole moment of the electron spin $\boldsymbol{m}$ equal to $\boldsymbol{m} \times \boldsymbol{H}_{eff}$ causing the magnetic moments to precess. The torque is equal to the temporal rate of change of the angular momentum of $\boldsymbol{m}$,

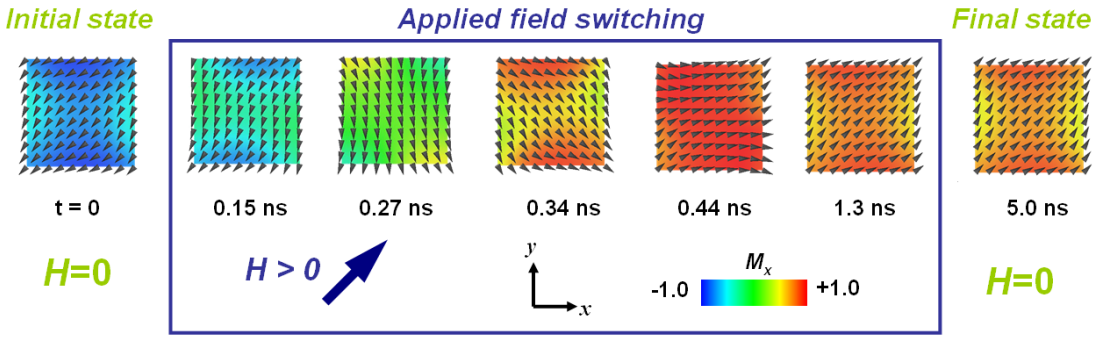

FIGURE 4.1. A micromagnetics simulation of the remagnetization of a 100 nm wide thin-film permalloy square element under an applied field with strength 0.014 T. The initial magnetization configuration is of the stable remanent state. Application of the field opposite to the direction of magnetization results in rotational reversal in less than 1.3 ns. In this example the dimensionless Gilbert damping constant is set to $\alpha = 0.1$.

which is equal to $\boldsymbol{m}/\gamma$ according to quantum theory, where γ is the gyromagnetic ratio of the system (4.6).

$$\frac{\partial}{\partial t}\left(\frac{\boldsymbol{m}}{\gamma}\right) = \boldsymbol{m} \times \boldsymbol{H}_{eff} \tag{4.6}$$

When $\boldsymbol{m}$ is aligned with $\boldsymbol{H}_{eff}$ there is no torque and the system is in equilibrium. In reality a viscous damping term must be included to properly describe the route to equilibrium and this is proportional to the rate of change of $\boldsymbol{m}$, $\partial\boldsymbol{m}/\partial t$ with a constant of proportionality, η. This dissipative term is added to the effective field to give the Gilbert equation of motion (4.7).

$$\frac{\partial}{\partial t}\left(\frac{\boldsymbol{m}}{\gamma}\right) = \boldsymbol{m} \times \left(\boldsymbol{H}_{eff} - \eta\frac{\partial \boldsymbol{m}}{\partial t}\right) \tag{4.7}$$

We can rewrite this in a more convenient notation (4.8) by introducing the dimensionless Gilbert damping constant $\alpha = -\gamma\eta \mid \boldsymbol{m} \mid$, which keeps the magnitude of the magnetic moment constant.

$$\frac{\partial \vec{m}}{\partial t} = -\mid \gamma \mid \boldsymbol{m} \times \boldsymbol{H}_{eff} + \frac{\alpha}{\mid \boldsymbol{m} \mid}\boldsymbol{m} \times \frac{\partial \boldsymbol{m}}{\partial t} \tag{4.8}$$

Equation (4.8), often referred to as the Landau-Lifschitz-Gilbert (LLG) equation, now contains a precessional term related to the torque caused by the local effective magnetic field on the magnetic moments, so that the magnetic moments precess around the field in a circular motion. A damping term causes this precessional motion to dissipate energy and damp towards equi-

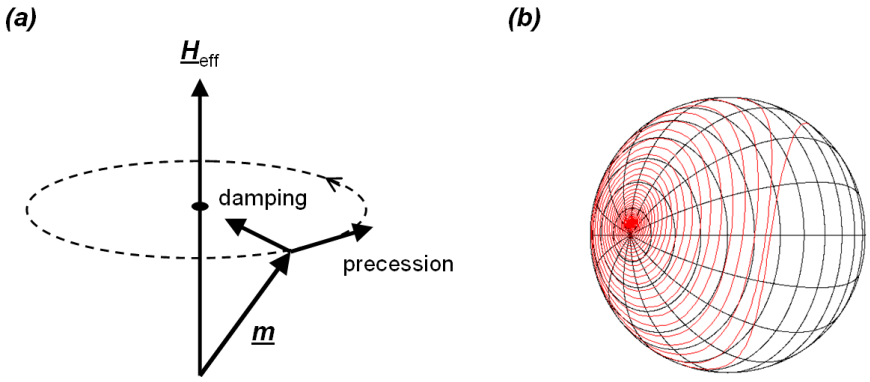

FIGURE 4.2. (a) Schematic representation of the dynamic LLG equation of motion. The magnetic moment m reaches equilibrium by undergoing damped gyromagnetic precession towards the effective field H_{eff}. (b) A spherical 3-D plot of the magnetization during reversal of an ellipsoidal magnetic element under an applied field.

librium by aligning with the field. The LLG equation is a partial differential equation (PDE) in space and time, which describes the physical path of the magnetic moment, $\boldsymbol{m}$, towards equilibrium, which is illustrated in Figure 4.2.

4.1.3. Balance of energies. The internal magnetization configuration inside a ferromagnetic material results from the process of energy minimization inside the material. The total Gibbs free energy, E, is an integral sum of four main energy terms (Figure 4.3), which compete during minimization and lead to the different characteristic behaviours observed in magnetic microstructures (4.9).

$$E = E_{Exchange} + E_{Magnetostatic} + E_{Anisotropy} + E_{Zeeman}$$

$$E = \int \left(A \left[\sum_{i}^{x,y,z} (\Delta \boldsymbol{u}_i)^2 \right] + K_1 \left[1 - (\boldsymbol{u} \cdot \boldsymbol{a})^2 \right] - \frac{J_s}{2} (\boldsymbol{u} \cdot \boldsymbol{H}_s) - \boldsymbol{J}_s (\boldsymbol{u} \cdot \boldsymbol{H}_{ext}) \right) dV \tag{4.9}$$

where A is the exchange constant, $\boldsymbol{u}$ is the unit vector parallel to the magnetic moment $\boldsymbol{m}$, K_1 is the uniaxial anisotropy constant, $\boldsymbol{a}$ is the anisotropy directional vector, $\boldsymbol{J}_s$ is the magnetic induction. $\boldsymbol{H}_s$ is the demagnetizing field and $\boldsymbol{H}_{ext}$ is the external field. Magneto-elastic energy is neglected, since it is negligible in the systems being investigated throughout this thesis.

Exchange energy. The first term inside the integral on the right hand side of Equation (4.9) is the exchange term. The exchange interaction between spin moments is quantum me-

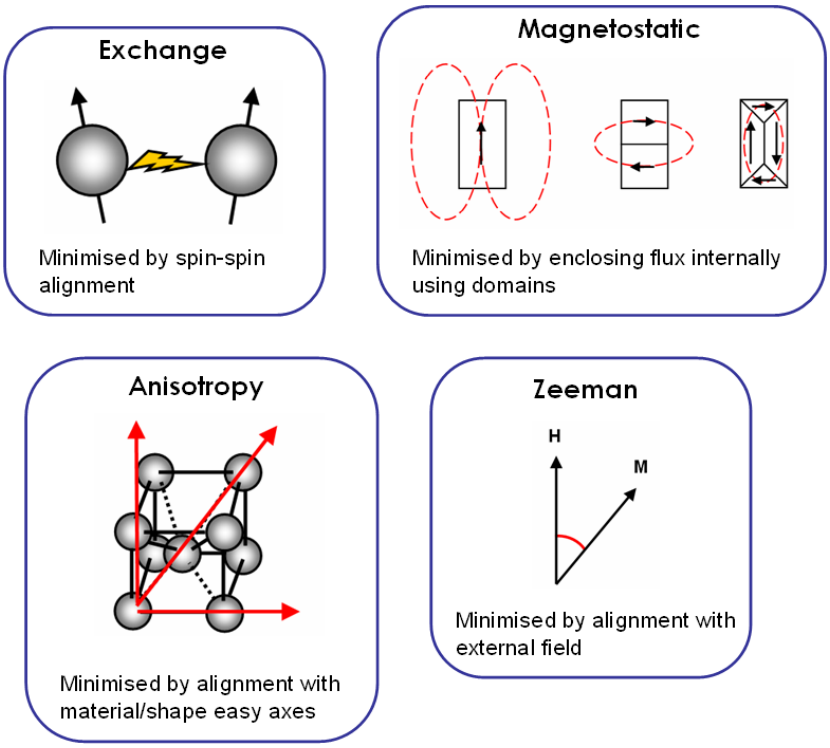

FIGURE 4.3. The energy terms that contribute to the total Gibbs free energy inside a ferromagnet. Minimization of the total Gibbs free energy leads to the magnetization configuration in the sample.

chanical in origin and much stronger than any spin-spin interactions via their dipolar magnetic fields. It is a short-range interaction and results in alignment of nearest-neighbour spins. The exchange energy in a magnet is minimized when all spins that are exchange-coupled together are aligned, so exchange forces the magnet towards a uniform magnetization. The exchange length, L_{ex}, is defined as the distance over which the magnetization, $\boldsymbol{M}$, changes due to the short-range exchange interaction and is an important characteristic length scale for a magnetic material. The spin deviation percentage follows a bell curve distribution around a local perturbation, and the exchange length is measured from the centre of the perturbation to the point where the spin deviation angle, γ, is one third of the maximum value (Figure 4.4) [**136**].

Magnetostatic energy. The second term, representing the magnetostatic self-energy, originates from the classical interactions between magnetic dipoles. Real samples are of finite size and the edge boundaries lead to surface charges, with an accompanying demagnetizing field. It is minimized when all of the stray field flux from the structure is diverted through the magnet

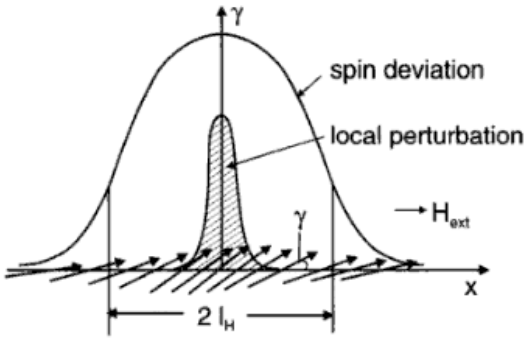

FIGURE 4.4. Definition of the exchange length (here denoted "L_H") as the distance, through exchange, of spin deviation from a local perturbation by an external field, H_{ext}. Image taken from [**136**].

internally. This is achieved by splitting the magnetic structure into a number of oppositely aligning domains, each containing many microscopic magnetic moments.

In thin magnetic films, domain walls may be charged, with the divergence of the magnetization being non-zero. These volume charges are a source of magnetic fields in thin film geometries.

Anisotropy energy. Real magnetic materials are not isotropic. Magneto-crystalline anisotropy is caused by the spin-orbit interaction of the electrons. Since these orbital electrons are associated with fixed positions in the crystallographic structure the internal atomic arrangement gives rise to well-defined crystallographic "easy" axes, which the spins prefer to align with. The Anisotropy energy term is minimized when the magnetization is aligned with an easy axis of the system.

Zeeman energy. The Zeeman energy is the energy of interaction between a magnetic moment and an applied field. The Zeeman energy in a magnet increases when there is a large angle between spin moments and an external field. It minimizes when the moment and the field are in alignment. As a result the moments attempt to reach alignment with the field in order to achieve energy minimization.

$\boldsymbol{M} = \boldsymbol{m}/V$ is the magnetization of the sample and is the magnetic moment per unit volume, where V is the total volume of the sample. The effective field is proportional to the negative partial derivative of the total Gibbs free energy density, E/V, with respect to $\boldsymbol{M}$ (3.5).

$$\boldsymbol{H}_{eff} = -\frac{1}{\mu_0 V}\frac{\partial E}{\partial \boldsymbol{M}} \tag{4.10}$$

Similarly, the effective field is a sum of contributions from the exchange field, magnetosttaic field, anisotropy field and Zeeman field (4.11).

$$\boldsymbol{H}_{eff} = \boldsymbol{H}_{Exchange} + \boldsymbol{H}_{Magnetostatic} + \boldsymbol{H}_{Anisotropy} + \boldsymbol{H}_{Zeeman} \tag{4.11}$$

4.1.4. Shape anisotropy. Another form of magnetic anisotropy is related to the shape of the magnet, but actually originates from minimization of the magnetostatic energy. The shape anisotropy, otherwise known as the magnetic dipolar anisotropy, is particularly important in thin films because of the restricted geometry. Magnetic surface charges are contained within the sample to avoid stray field, meaning that the magnetization tends to run parallel to the edge of the sample. In thin films this means that the magnetization is constrained into the film plane very strongly to avoid the presence of surface charges pointing out-of-plane. The shape anisotropy energy is minimized when the magnetization aligns with the longer axis of symmetry in a sample of asymmetrical shape; when the angle between the shape long axis and the magnetization is zero (4.12) [**137**].

$$E = \frac{1}{2}\mu_0 M_s^2 \cos^2\theta \tag{4.12}$$

A ferromagnetic nanowire has reduced size in two dimensions (with one or both of these in the nanoscale regime) and one long dimension that is much larger in size. This "long axis" is the easy axis in materials such as permalloy ($Ni_{80}Fe_{20}$) where magneto-crystalline anisotropy is low enough to be considered insignificant.

Shape anisotropy is a very useful concept for explaining magnetic structure but is not a fundamental energy contribution so is not included in calculations.

4.2. Finite element method (FEM)

4.2.1. Introduction. The finite element method (FEM) is a numerical technique for approximating partial differential equations to solve science and engineering problems. It works well for geometrically complex objects because arbitrary shapes can be approximated accurately with a well-constructed finite element mesh. The technique was first successfully applied in the

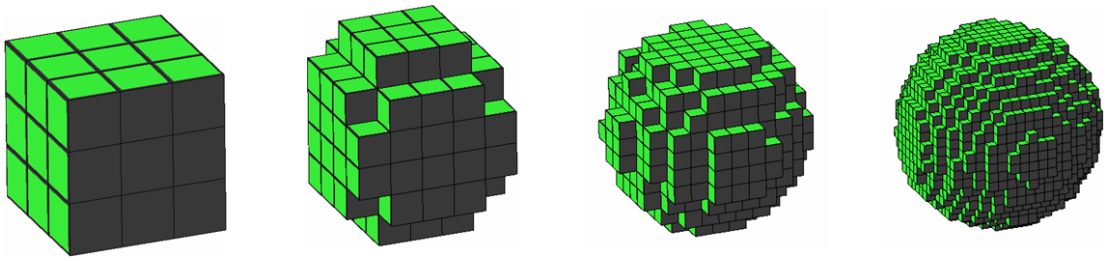

FIGURE 4.5. Discretization of a sphere using regular cubic finite elements. Decreasing mesh size (left to right) increases the accuracy of representation of the spherical shape.

field of structural analysis and has since become a powerful tool, used over a wide array of technical disciplines. As modern computers have developed, processing power has increased rapidly. FEM is an important technique within computer modelling, and it is in recent years that it has been used to solve some very complex problems in micromagnetics.

By modelling complex structures as smaller constituent pieces (Figure 4.5), FEM allows one to change the problem into a form that can be solved numerically. Partial differential equations (PDEs) that describe the system variable in a complex system can be discretized in space and time to obtain a collection of simpler localized mathematical descriptions that can be solved more readily.

4.2.2. Space discretization. If we represent a one dimensional (1D) field using a polynomial expression such as $u(x) = a + bx + cx^2 + dx^3$ then we are required to go to high orders for an accurate fit. However, going to higher orders of a polynomial introduces oscillations that are unacceptable **[138]**. Instead, we split the field into a series of piecewise low-order linear functions that exist inside subdomains of the parent domain Ω (Figure 4.6). In order that the approximation is continuous across the subdomain boundaries we introduce linear basis functions that act as weighting functions on the nodal parameters. The linear basis functions vary between 0 and 1 and combine to preserve the values of u at each node point. Higher orders of continuity are sometimes used so that $\partial^n u/\partial^n x$ where n is the order number is continuous over the element boundaries. 2D and 3D basis functions can be constructed as products of 1D basis functions **[138]**, allowing us to approximate more complex 2D and 3D fields. After discretization, a magnetic moment is positioned at each node on the irregular finite element grid.

The Gilbert equation describes a continuum model of micromagnetics. The FEM subdivides

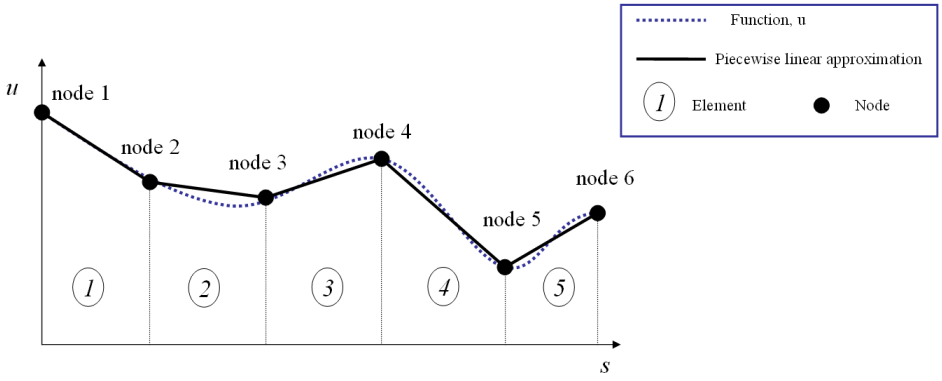

FIGURE 4.6. Discretization of a 1D field $u(s)$ where s is a measure of distance along the x-axis, using a piecewise linear approximation. The approximation is first-order continuous across the element boundaries.

it into computational cells. We interpolate the magnetization vector using piecewise linear functions. The result is a tetrahedral finite element mesh where, using a box scheme, we assign one magnetic moment to each node. Discretization in space of the Gilbert equation integration leads to a stiff system of ordinary differential equations (ODEs), one at each node point. Using (4.9) and (4.10) the magnetic moment and the effective field can be calculated at each of the node points.

4.2.3. Solution of ODEs. We solve our system of ODEs numerically using the software package CVODE [**139**]. CVODE is a general purpose software package written in the C programming language [**140**] for solving initial value problems for stiff and non-stiff ODEs. CVODE is able to use a number of different linear multi-step methods [**141**] such as the variable coefficient Adams-Moulton and backwards differentiation formula (BDF) methods [**142**]. Multi-step methods refer to several previous function values to improve accuracy over single-step methods, which refer to just one previous value. Linear multi-step methods use a linear interpolation of the previous values.

4.2.4. Calculation of magnetostatic field using the boundary element method (BEM). Generally, the boundary element method (BEM) is a numerical technique similar to FEM where instead of meshing the entire domain only a mesh of the boundary is required. This greatly reduces the size of the mesh in comparison, reducing computing costs. The BEM solves linear partial differential equations that have been formulated as integral equations. The BEM is difficult to implement and cannot solve all linear problems [**138**]. It has difficulty solving non-linear problems. For these reasons, FEM is the preferred method for many problems.

Combining FEM and BEM into a hybrid technique allows us to take benefits from both [**143, 144, 145**]. We use FEM inside the magnet and calculate the stray field using BEM. The boundary conditions for the magnetic field at infinity are mapped onto equivalent boundary conditions on the surface of the parent domain, Ω. This removes the requirement for a discretized volume mesh outside of Ω, drastically reducing the overall model size.

Because FEM uses irregular grid structures we cannot use traditional fast Fourier transform (FFT) methods to compute the magnetostatic interaction. Instead we proceed by introducing a magnetic scalar potential $H_d = -\nabla \boldsymbol{U}$, which is related to a number of boundary conditions for the problem. Inside the magnet $\nabla^2 \boldsymbol{U} = \nabla \boldsymbol{M}$, outside the magnet $\nabla^2 \boldsymbol{U} = 0$ and at the magnet boundary $\left(\nabla \boldsymbol{U}^{in} - \nabla \boldsymbol{U}^{out}\right) \cdot \boldsymbol{n} = \boldsymbol{M} \cdot \boldsymbol{n}$ where $\boldsymbol{n}$ is the surface normal at the boundary. These three equations are solved using the hybrid FEM/BEM method.

4.2.5. Time integration. In order to solve our stiff system of ODEs we use higher order backward differentiation formula (BDF) methods for the time integration. BDF methods are more efficient than explicit time integration schemes in systems with high levels of exchange coupling. Since BDF methods are implicit methods we must solve a non-linear system of equations at each time step. For solving the LLG equation BDF methods of order 2 prove to be most efficient [**146**].

Time discretization must take care of the intrinsic timescale, which is commonly determined by the Larmor frequency, ω (4.13). This frequency is usually on the order of GHz, meaning that time steps must be on the order of picoseconds to properly resolve the dynamic precessional motion of spins.

$$\omega = \gamma \boldsymbol{H}_{eff} \tag{4.13}$$

4.2.6. Characteristic length scales. In micromagnetics a number of important limits must be considered when choosing mesh size. The resolution of the finite element mesh is the maximum size of the finite elements and, in order to obtain sufficient resolution, is chosen to be smaller than the minimum feature size that could occur during solution of the PDEs of the system. In zero-temperature micromagnetics two typical lengths are important, and these correspond to the two basic types of domain walls that can occur. Domain walls are

typically considered to be the smallest features, with the smallest spatial distance for a rotation of magnetization, that occur in nanomagnets.

(1) $\delta_{Bloch} = \pi\sqrt{\frac{A}{K_1}} = \pi L_{ex}^{Bloch}$ is the domain wall width of Bloch type domain walls, which corresponds to the Bloch exchange length, L_{ex}^{Bloch} and a factor of π.

(2) $\delta_{Neel} = \pi\sqrt{\frac{2A}{\mu_0 M_s^2}} = \pi L_{ex}^{Neel}$ is the domain wall width of Néel type domain walls, which corresponds to the Néel exchange length, L_{ex}^{Neel} and a factor of π.

The smallest of these two values is usually taken as the minimum possible feature size in a micromagnetics simulation. In $Ni_{80}Fe_{20}$ permalloy the Néel exchange length, $L_{ex}^{Neel} = 5.7$ nm and the corresponding domain wall width $\delta_{Bloch} = 17.9$ nm are usually quoted, by convention, as the required mesh resolution. Rave and co-workers argue that discretization lengths in FE micromagnetics must be comparable to the exchange length of the material [**147**], however this will of course depend on the specific discretization and solution methods used. Linear interpolation techniques can be utilized to smooth out changes in magnetization between FE mesh points, which is the approach taken with our micromagnetics code.

Although in bulk permalloy the anisotropy constant, K_1, is measured as negligible, an effective shape anisotropy value is used in its place to calculate the Bloch wall width, as described in detail by Porter & Donahue [**148**].

In section 6.5 we perform simulations to investigate the relationship between FE mesh size and the propagation of spin waves.

4.2.7. Finite element mesh. The first step in FEM is to generate our test structure and discretize it spatially. The sub-element type used depends strongly on the specific problem. In two dimensional (2D) modelling triangular or rectangular elements are used. For three dimensional (3D) problems tetrahedral or cubic elements are used. The rectangular and cubic sub-elements often suit less complex structures, or structures that are themselves cubic in nature (Figure 4.7a). Triangular and tetrahedral elements suit more complex or irregular shapes, particularly those with curved surfaces (Figure 4.7b) because they allow an irregular grid arrangement that can be better adapted to the geometry of the sample.

The meshing task is usually performed by specialist software, which uses an algorithm to mesh surface and volume elements by a variety of schemes. The results presented in this thesis were obtained using FE meshes generated in GiD [**149**], a "personal pre- and post- processor" software package.

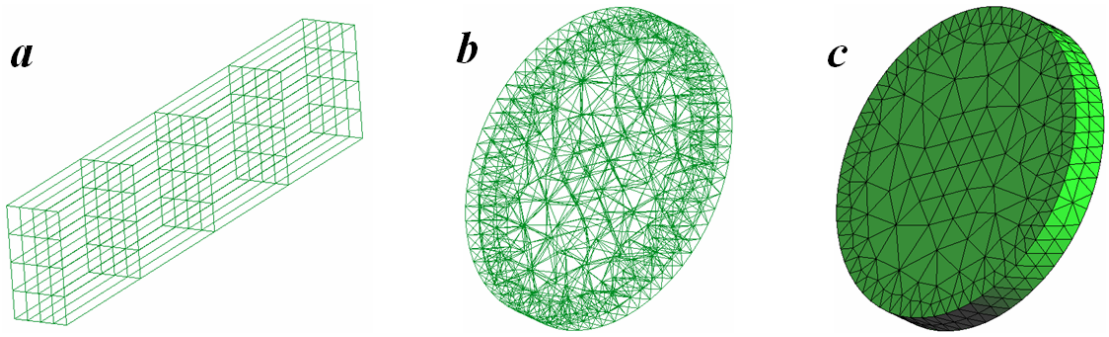

FIGURE 4.7. Rectangular meshing (a) is suitable for rectangular structures, whereas triangular meshing (b) is suitable for more complex structures with smooth boundaries. Here (c) shows the surface mesh of (b), a circular disc.

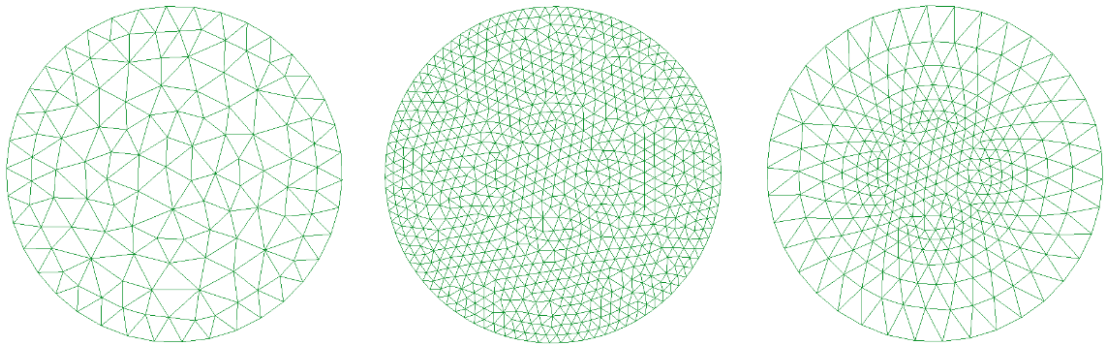

FIGURE 4.8. Coarse, fine and adaptive finite element meshes of a circular disc. A higher number of mesh elements results in higher accuracy but is accompanied by greater processing costs. An adaptive mesh is a compromise as it allows one to use a finer mesh in more important parts of the structure while sacrificing accuracy in less important parts. Here we model a circular magnet with a vortex core at the centre.

4.2.8. Mesh size and adaptive meshes. By using a larger number of sub-elements to approximate a test object we increase the accuracy of reproduction (Figure 4.8). However, the gains in accuracy that come with a fine mesh are accompanied by a trade-off in computational costs, so an arbitrarily fine mesh size is impractical. An adaptive mesh can be used to increase the mesh detail in areas of importance, while sacrificing accuracy elsewhere. For instance, a fine mesh size below the characteristic length could be used to resolve the area around a stationary domain wall, with coarser meshing making up the rest of the model.

4.2.9. Summary of alternative techniques. Other numerical and analytical techniques exist, with respective advantages and disadvantages that render them suitable for specific problems. The Stoner-Wohlfarth theory [**39**] treats magnetic domains as single particles with homogeneous internal magnetization. Therefore it is useful for the treatment of single-domain fine

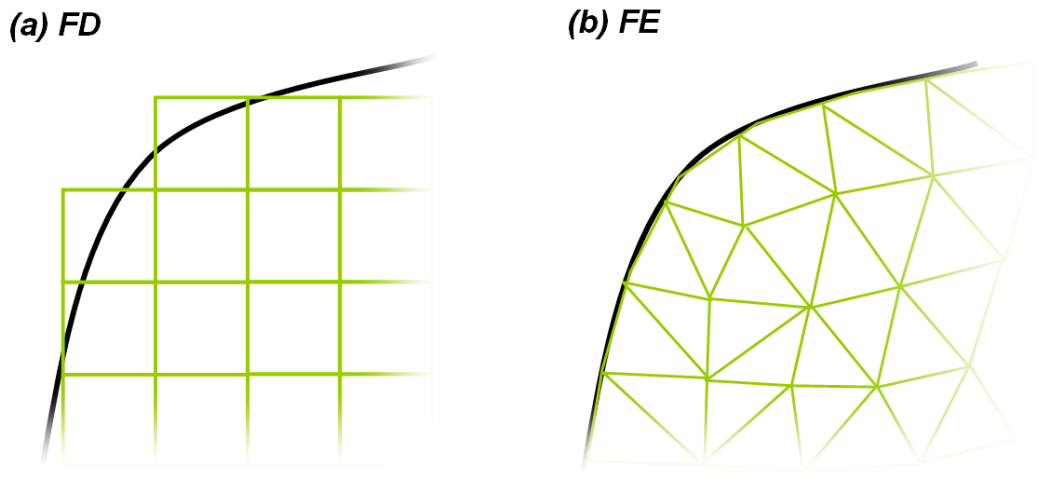

FIGURE 4.9. Finite element (FE) analysis is often better than the standard finite difference (FD) method at modelling objects with irregular shapes. In this simple example the regular grids of FD (a) cannot reproduce the shape accurately whereas the irregular triangle FE mesh (b) is capable of more precision.

particles with no internal inhomogeneity. However, this limits the technique to only the simplest of cases, and does not provide the required complexity for analysing routine problems such as switching processes and domain wall motion; such topics are now being routinely investigated using FEM [**150, 151**].

The finite difference (FD) method [**152**] uses a regular grid for discretization and is a common tool for solving problems that involve partial differential equations in many areas of science and engineering. Apart from the meshing differences, the technique is quite similar to FEM. However, a regular grid is not as capable of accurately representing irregularly shaped objects as FEM, which can use irregular grids (Figure 4.9). Techniques have been developed recently to tweak FD methods, so that they work for edges that are not aligned with the grid. These require some advanced treatment of the boundaries and are not yet commonly used [**153, 154**]. Standard FD methods are widely used in micromagnetics, for instance in the popular OOMMF micromagnetics code OOMMF [**58**].

The finite volume (FV) method [**152**] is younger than FD and FE methods. The model is discretized into volumes, as with 3-dimensional (3-D) FE modelling, but a structured mesh is not usually a requirement. Boundary methods can be applied non-invasively since the values of the conserved variables are averaged across the volume of the element as opposed to being located at nodes or on surfaces. FV methods are widely used to solve problems of fluid dynamics

and heat flow.

4.3. Nudged elastic band method

4.3.1. Outline. The nudged elastic band method is a technique for finding saddle points and minimum energy paths (MEPs) in the energy configuration space of a magnetic system. This enables us to assess the thermal stability of memory storage devices such as magnetic random access memory (MRAM). At each step in a FEM/BEM micromagnetic simulation we calculate the total Gibbs free energy, E, from the magnetization configuration.

Often we would like to calculate the MEP over the energy landscape between two magnetization configurations of a magnetic system. However, this is not usually a straightforward problem and requires sophisticated path refinement methods, which we will now briefly discuss.

4.3.2. Thermal stability. A system within a local energy minimum can be stimulated by thermal energy. If the thermal energy available is comparable to the height of the local energy barrier then it can be overcome, leading to spontaneous switching. The thermal stability of a system can be estimated using the Néel-Arrhenius meta-stable lifetime equation (4.14) according to the Neél-Brown theory [**155**].

$$\tau = \frac{1}{f_0} \exp\left(\frac{E_B}{k_B T}\right) \tag{4.14}$$

Here τ is the meta-stable lifetime, f_0 is the so-called attempt frequency, E_B is the local energy barrier, k_B is the Boltzmann constant and T is temperature. The probability of the occurrence of a significant event is directly proportional to the exponential of the temperature. f_0 depends on material parameters, such as anisotropies, damping, and shape but can only be calculated analytically for simple switching events, such as uniform rotation under a field parallel to the easy axis. For general situations, estimates for the attempt frequency are made that may vary widely between different authors. Normally it takes values between $f_0 = 10^9$Hz and $f_0 = 10^{10}$Hz [**156**].

A memory device is often considered stable if it must overcome an energy barrier larger then 23 $k_B T$. According to the Arrhenius-Néel equation, thermal activation overcomes a barrier of $23 k_B T$ (with $T = 300$ K) within a time of 1 s if the attempt frequency is 10^{10} Hz . If the energy barrier corresponds to $E_B = 38 k_B T$ then $\tau = 37$ years (Figure 4.10).

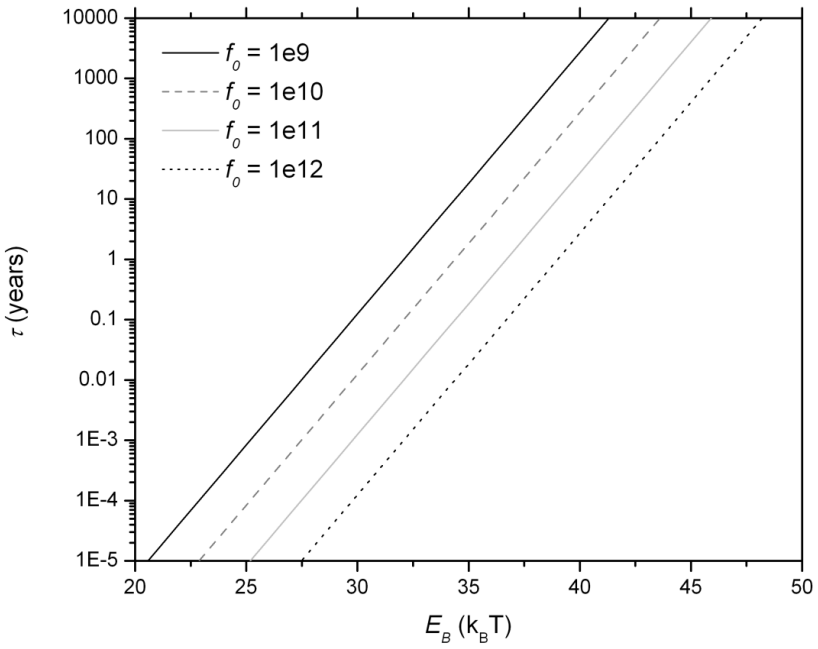

FIGURE 4.10. A plot of the Néel-Arrhenius law, which relates the thermal stability lifetime to the energy barrier between states. The plot is given for a selection of different values for the attempt frequency f_0.

It is possible to simulate thermal processes using stochastic methods, but these occur on very short timescales that are much smaller than the timescales involved with rare switching events, which can have half-lives of a number of years. This disparity between time-scales makes stochastic simulation of dynamic micromagnetic phenomena such as a switching event too computationally expensive. Therefore, a more suitable method is to calculate the energy barrier related to the event and then use the Néel-Arrhenius law to estimate thermal stability.

4.3.3. Method. Our path is represented by a sequence of indexed magnetization configuration images $\boldsymbol{M}_k$ where $k = 1, 2, 3, ..., n$. Our opening guess for the path between the initial magnetization state $\boldsymbol{M}_i = \boldsymbol{M}_1$ and the final magnetization state $\boldsymbol{M}_f = \boldsymbol{M}_n$ makes an interpolated straight line in configuration space. Each image $\boldsymbol{M_i}$ is a node along the path (Figure 4.11). At each timestep the gradient of the total Gibbs free energy, $\triangle E$ is calculated. The node is then adjusted by moving it down the gradient to a lower E. This process continues until the MEP is found when at every node $\triangle E$ is pointing along the path, represented by equation (4.15) where $\boldsymbol{t}$ is the nodal tangent unit vector of the path.

$$(\nabla E(\boldsymbol{M}_k)) \times \boldsymbol{t} = 0 \qquad k = 1, n \tag{4.15}$$

for $k = 1$, n (1.19)

An iterative scheme is used to find the MEP [**156**]. The images are adjusted parallel to $-\triangle E$ and normal to the path (4.16).

$$\boldsymbol{D} = -\{\nabla E(\boldsymbol{M}_k) - (\nabla E(\boldsymbol{M}_k) \cdot \boldsymbol{t})\,\boldsymbol{t}\} \tag{4.16}$$

Within the MEP, where $\boldsymbol{D}$ is the component of the gradient of the total Gibbs free energy, E, that points perpendicular to the path direction, the energy is stationary for any degree of freedom perpendicular to the path.

A stiffness factor is introduced to the path connecting the images [**157**]. This can be modified arbitrarily to control the separation between neighbouring images, in order to achieve a realistic path. If the stiffness is too low then images can move in a highly independent manner and diverge from the true MEP. The nudged elastic band (NEB) method can be qualitatively likened to the tensioning of a long rope over a range of mountains (Figure 4.12).

The path finding scheme is represented by a system of ODEs (4.17).

$$\frac{\partial \boldsymbol{M}_k}{\partial \boldsymbol{t}} = \boldsymbol{D}(\boldsymbol{M}_k) \qquad k = 2, n-1 \tag{4.17}$$

The system of ODEs is solved using the CVODE software package [**139**]. The initial guess for the path is helped by choosing initial and final states that are temporally as close as possible within the event of interest. For instance, if we hope to find the energy barrier for depinning of a domain wall from a potential well in a magnetic nanowire then we could take the states just before and just after depinning for A and B respectively. However, if we take the final state much later in the event, such as when the domain wall moves further along the wire, we may experience a higher number of intermediate meta-stable states and the path iteration might make less favourable choices. Reducing the time between the end states also speeds up the NEB calculation.

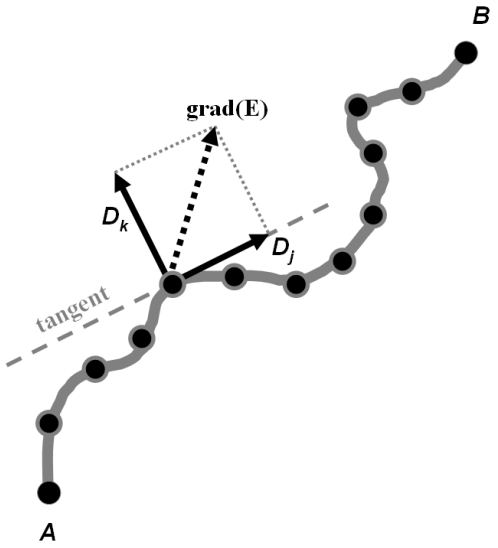

FIGURE 4.11. Schematic representation of the optimization method for a path between an initial state, A, and a final state, B. The path is split into a number of segments recorded by their nodal points. $\boldsymbol{D}_k$ is the component of the gradient of the total Gibbs free energy E that points perpendicular to the path direction. When $\boldsymbol{D}_k$ equals zero the node is said to be on the minimum energy path. If $\boldsymbol{D}_k$ is finite then the position of the node is moved down along the slope towards lower E.

4.4. Summary

Finite element analysis is a versatile technique that can be used to model and simulate objects of complex geometries and has proven benefits over other discretization methods. In FE micromagnetics the boundary element (BE) method can be incorporated to calculate stray fields.

Considerations must be made for minimum mesh size in order to accurately resolve the smallest features in the magnetization of the sample, which are determined by the domain wall widths for the material.

The nudged elastic band (NEB) method can be used instead of expensive stochastic methods to calculate energy barriers between states and approximate thermal stabilities.

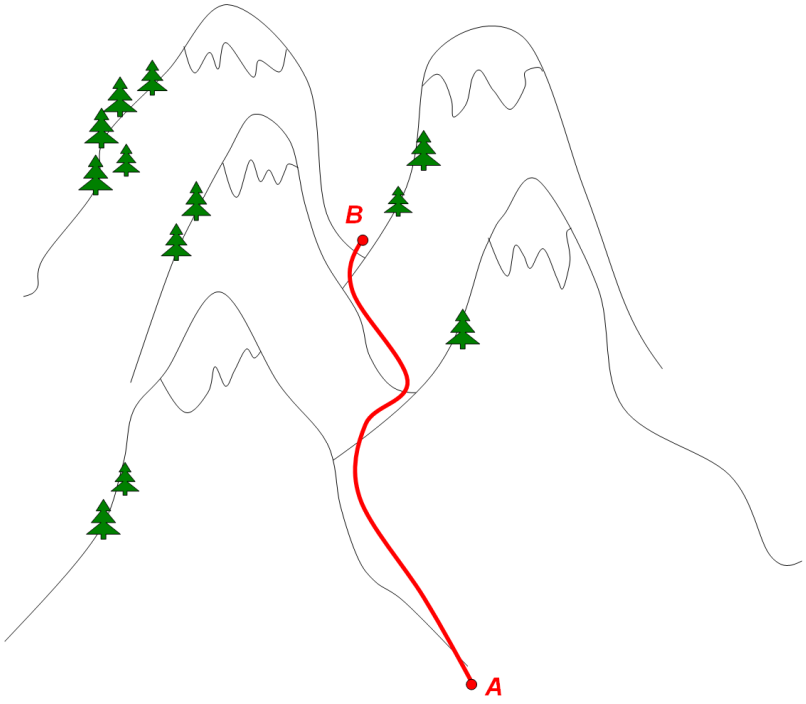

FIGURE 4.12. The minimum energy path (MEP) is analogous to a rope being tensioned over a mountainous range. In this analogy, the height of the mountains with respect to the Earth's surface are equivalent to the Gibbs free energy in configurational space.

CHAPTER 5

Domain Wall Memory

In this chapter we investigate the fundamental behaviour and reliability of a number of domain wall trap (DWT) memory cell designs by assessing their switching mechanisms and thermal stability, using zero-temperature finite element micromagnetics and the nudged elastic band method. Hence it is possible to determine whether these devices can be a competitive alternative to commercial products such as solid state RAM and FLASH systems.

5.1. Details of method

5.1.1. Nanostructure geometry. Figure 5.1 shows four designs for DWT memory cells. These cells are based on thin film nanowires of various shape. The permalloy (Table 5.1) wires contain two "trap" positions where a potential well is able to pin a head-to-head domain wall inside the wire. An external field can then be used to manipulate the domain wall by de-pinning it and moving it through the wire to the other trap position. This switching between the two traps realigns the magnetisation in the mid-section of the wire. In the wires shape anisotropy dominates their remanent configuration states, and the magnetization will align left or right along the long axis.

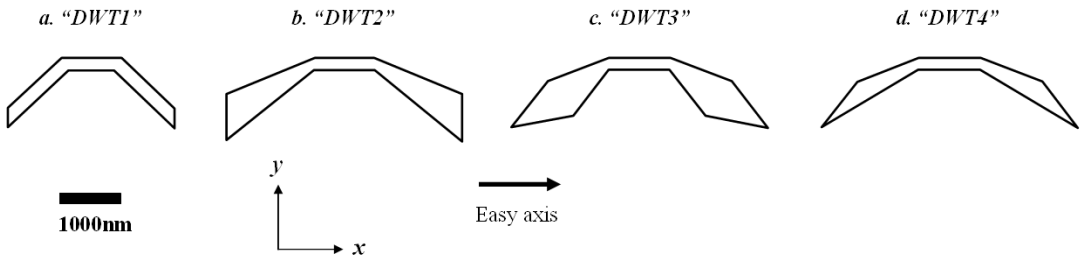

FIGURE 5.1. Some DWT cell designs from [**49**]; (a) DWT1 is a simple example where wire width remains constant throughout; (b)-(d) later examples use widening of the wire to increase the margins between the de-pinning field and the domain wall expulsion field required to push the domain wall out of the structure.

Parameter	Symbol	Value	Units
Exchange constant	A	1.3×10^{-11}	J/m
Magnetic induction	J_s	1.0	T
Magneto-crystalline anisotropy constant	K	0	J/m^3
Gilbert damping constant	α	0.02	1
Curie temperature	T_c	869	K
Exchange length	L_{ex}	5.7	nm

TABLE 5.1. Material parameters of $Ni_{80}Fe_{20}$ permalloy (Py), which have been used in our FE simulations, in S.I. units.

5.1.2. Finite element model. Throughout this work finite element models have been constructed from tetrahedral finite elements. The meshing task is performed on a user-defined wireframe geometry by a specialist third party software package called GiD [**149**]. Adaptive meshing has been used in models where a fine mesh is required for sufficient mesh resolution around important regions of interest, but where other parts of the structure are less significant (Figure 5.2). This ensures accuracy while minimizing the total finite element model size. In order to resolve a domain wall the mesh size must not be larger than the domain wall resolving length, which is 17.9 nm in permalloy. The domain wall memory cells contain feature sizes up to 2000nm, meaning that model dimensions are large for finite element simulations.

5.2. Remanent state preparation

5.2.1. Formation of domain walls by initial configuration. We want to test realistic structures with realistic micromagnetic configurations. We specify the initial magnetization configuration by splitting the model into distinct grains, each of which has uniform internal magnetization (Figure 5.3a). The model and the specified magnetization data can then be used as the input state for further micromagnetics calculations. During this simulation a stable configuration is quickly reached, as the forced configuration is energetically very unfavourable. Within a few nanoseconds the states shown in Figure 5.3b are reached. Because we don't need to consider the time-dependent dynamics of the problem a high damping constant can be chosen to speed up the simulation. The forced configuration should be chosen carefully for the desired outcome and to avoid some other close but less favourable meta-stable configurations.

There are a number of domain wall types that can form inside the memory cell structures (Figure 5.4). The one that is present will be determined by the balancing of energy terms inside the sample to minimize its total Gibbs free energy. In a particular wire, each domain wall type possesses a different domain wall energy, meaning that some domain wall types are more

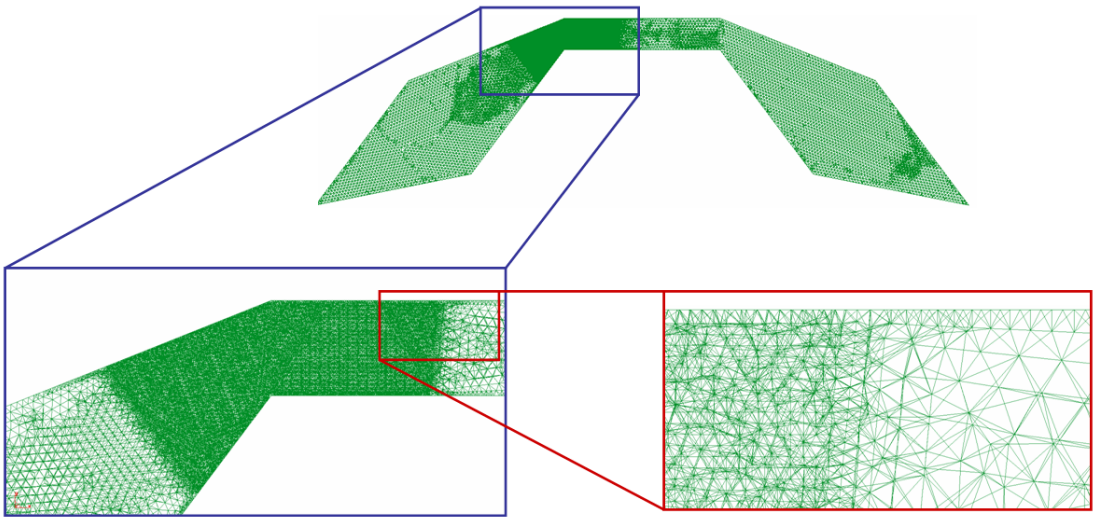

FIGURE 5.2. A 2D projection of the 3D adaptive tetrahedral finite element mesh for the "DWT3" domain wall trap memory cell design. In this instance the model is intended for use in an experiment where the domain wall is expected to stay positioned in the vicinity of the left hand domain wall trap position. Thus the mesh size is fine (5nm) in this important section of the model, so that the domain wall is accurately resolved. In permalloy the domain wall resolving length is 17.9 nm since the exchange length is 5.7 nm so in theory we are able to use a mesh size as large as 17.9 nm and still obtain accurate results. A coarser mesh size is sufficient to resolve larger features in magnetization.

energetically favourable than others. Particularly important is that a transverse domain wall (TDW) is more stable when the wire width is small, whereas in larger wires a vortex domain wall (VDW) is favourable [**59**]. Increasing wire dimensions further will eventually lead to multiple domain structures, but this does not concern us here.

5.2.2. Formation of domain walls by saturation field. Brownlie and co-workers [**49**] were able to form domain walls at specific positions in their DWT-MRAM cells using a strong external magnetic field. Although they were not able to produce a field strong enough to saturate the magnetization of the sample, the fields were strong enough to form a domain wall at a specific position by remagnetizing parts of the cell. The maximum field strength inside the TEM was roughly 7000 Oe (0.7 T).

We recreate this experiment but arbitrarily use a saturating field, with our FE simulation methods. The DWT3 memory cell is chosen and the homogeneous state is arbitrarily chosen as the initial input state. A very strong, ramped external field with peak amplitude $\mid H \mid = 10$ T is applied to saturate the sample, with the field vector angle from the y axis, θ, specified over a range of values, each angle used for a single simulation. This field value is larger than would be

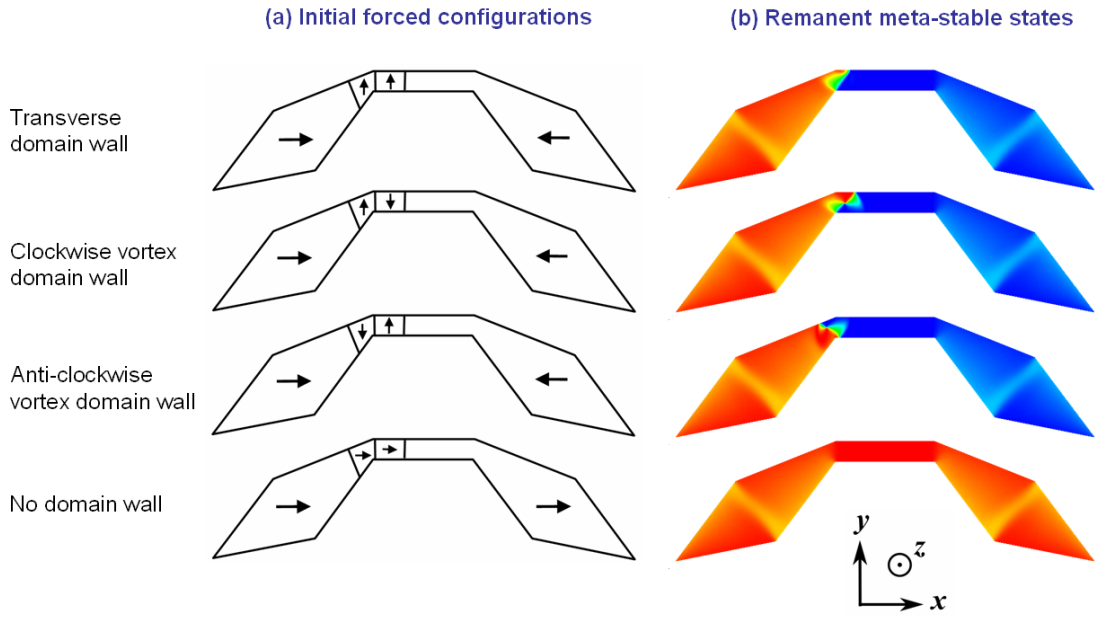

FIGURE 5.3. Method for setting up head-to-head domain wall configurations in a magnetic nanowire DWT-MRAM memory cell. The cell structure (here DWT3 is used) is split into a number of regions, referred to as "grains", which can be individually assigned an initial (uniform) magnetization orientation. During a relaxation simulation the FE micromagnetic code finds the meta-stable remanent state after a few nanoseconds. In some examples a desired configuration is too energetically unstable to form. Here, a transverse domain wall has formed but is highly unstable, due to the large width of the wire. The unstable nature is suggested by the contorted shape of the domain wall, and can be confirmed by energy barrier calculations and analysis of the total configurational energies of the different meta-states.

possible in a real experiment but for modelling purposes it is acceptable. The field is held at its maximum value before being released to zero over a period of 1 ns. The sample is then allowed to reach a stable magnetization configuration under zero field for 10 ns. Field angles are chosen as θ = -45 $^\circ$, -40 $^\circ$, -35 $^\circ$, -30 $^\circ$, -25 $^\circ$, -24 $^\circ$, -23 $^\circ$, -22 $^\circ$, -21 $^\circ$, -20 $^\circ$, -19 $^\circ$, -18 $^\circ$, -17 $^\circ$, -16 $^\circ$, -15 $^\circ$, -14 $^\circ$, -13 $^\circ$, -12 $^\circ$, -11 $^\circ$, -10 $^\circ$, -9 $^\circ$, -8 $^\circ$, -7 $^\circ$, -6 $^\circ$, -5 $^\circ$, -4 $^\circ$, -3 $^\circ$, -2 $^\circ$, -1 $^\circ$ and 0 $^\circ$. The results are summarised in Figure 5.5 as categories of observed final configurations.

When $\theta \leq$ -22 $^\circ$ the angle is too far off-centre, meaning that if a domain wall is formed it occurs to the left of the trap, and outside of any useful position. Effectively we obtain a homogeneous magnetization. Often when a domain wall forms here it is expelled from the structure completely.

Within the range -20 $^\circ$ $\leq \theta \leq$ -10 $^\circ$ a clock-wise vortex forms at the left hand trap position. This scenario covers a conveniently wide range of values, although one exception was observed

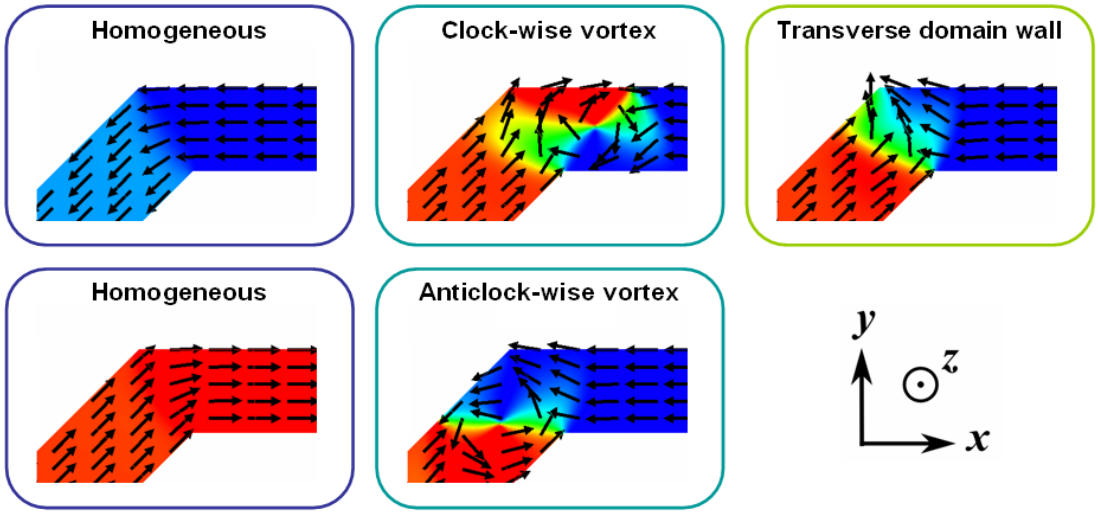

FIGURE 5.4. The possible stable magnetization configurations at domain wall traps in a domain wall memory device (DWT1 design). Which one of these is present depends on the history of the sample but is strongly related to the size of the sample. Domain wall energy is directly proportional to its surface area, so widening the nanowire will alter which configuration is most favourable. As a general rule, increasing wire size will increase the probability of a vortex wall being the most stable. The domain walls do not always form or sit in exactly the same positions, a fact which has important consequences for device behaviour.

at -12 $^\circ$, where a type of transverse wall is formed. For this transverse wall the internal wall structure is different to other transverse walls observed during the simulations, with the internal magnetization following the in-plane rotational characteristics of the clock-wise (CW) vortex. In this sense it is convenient to refer to it as a "clock-wise transverse" domain wall.

For -9 $^\circ$ $\leq \theta \leq$ -4 $^\circ$ an anticlock-wise (ACW) transverse wall remains at the left hand trap position after removal of the saturation field. This is also a sufficiently large angular range to be useful and reproducible in an experiment. The internal magnetization of the domain wall is in alignment with the external field vector.

Over the range -3 $^\circ$ $\leq \theta \leq$ -1 $^\circ$ an anticlock-wise (ACW) vortex forms in the centre of the memory cell, away from the trap, between the centre of the wire and the trap. As the negative angle becomes closer to zero the distance to the centre of the wire tends to reduce. At $\theta = 0^\circ$ a vortex is formed at the centre of the wire. In this instance the vortex is clock-wise but this is arbitrary, as the symmetry of the problem provides no reason for a choice between the two rotational orientations.

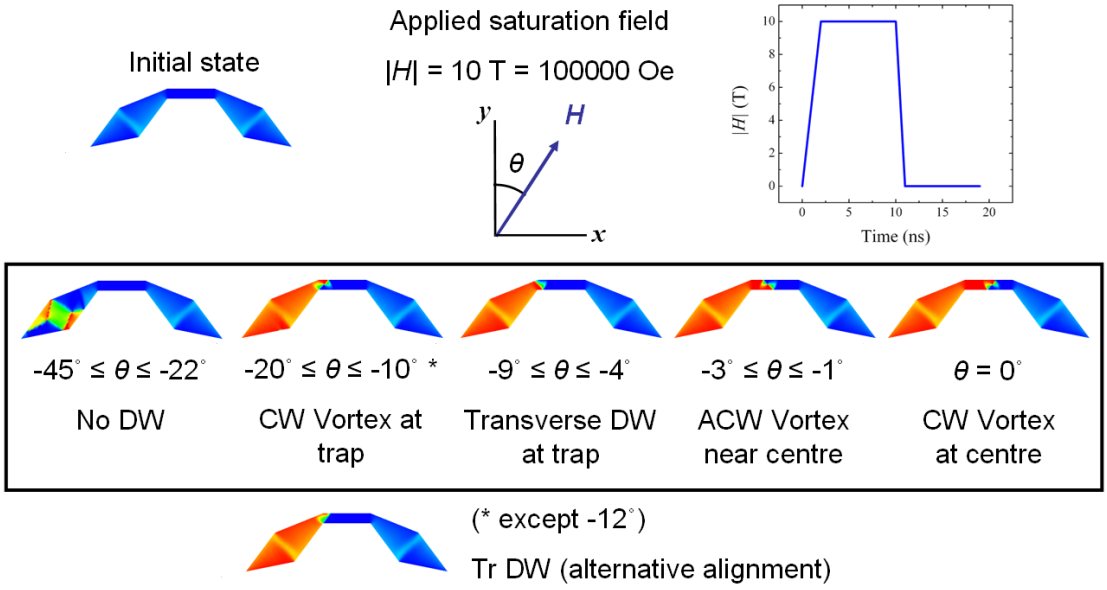

FIGURE 5.5. Forming domain walls at the traps in a DWT-MRAM cell (DWT3). Applying a saturation field (here we use an arbitrarily high field for simulation purposes) and then relaxing this field results in a number of configurations, which depend on the angle of the field. Between -20° and -10° a clock-wise vortex domain wall is formed at the desired trap position, apart from one case where a transverse wall is formed.

The simulations were also performed for a number of positive angle values. Due to the symmetry of the cell geometry similar results were observed.

The implication from these results is that it is possible to form a domain wall at a specified trap position or at the centre of a DWT-MRAM cell by applying a saturating external magnetic field. Furthermore, it is possible to specify a vortex or transverse domain wall. However, the type of vortex wall is dependent on the field angle.

Figure 5.6 shows two examples of detailed magnetization data for the memory cell as a function of time after the saturation field is released. With the field in place the magnetization of the sample completely follows the field vector direction. As the field is removed the magnetization is influenced by the shape of the wire and immediately begins to follow the shape anisotropy in the cell. Because of the shape of the wire, particularly the angles made between the different sections, the magnetization finds a stable state with a head-to-head domain wall at the left hand trap. The difference between obtaining a vortex and a transverse domain wall may be a result of the former forming inside a wider section of the nanowire, where a vortex wall is much more energetically favourable. In the narrower, middle section of the wire a vortex is also more energetically favourable than a transverse wall, but the difference is smaller and

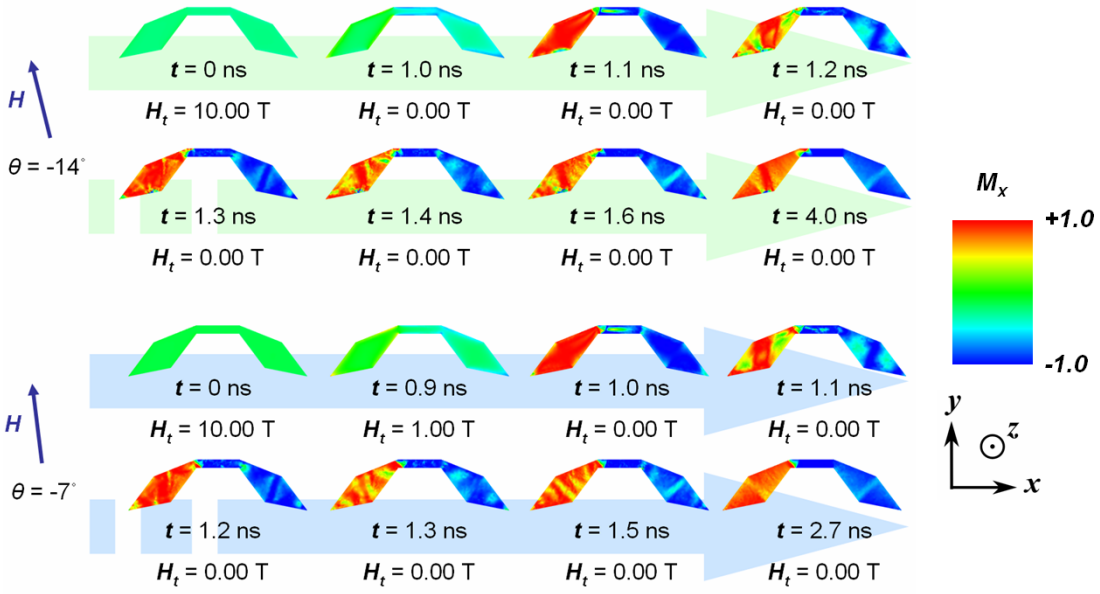

FIGURE 5.6. Detailed temporal magnetization data for the release of a saturating field with specified angles in order to form a domain wall. The amount of time, t, since release of the saturating field from its maximum value and H_t, the instantaneous applied field strength at time t are given.

the internal wall structure aligns with the applied field producing a transverse wall instead.

It is reported by Brownlie and co-workers that field strengths in the TEM were not high enough to saturate the sample copmpletely, but that fields were strong enough to form a domain wall by remagnetization of one side of the cell. This could affect the domain wall type formed and is likely to increase the chances of a vortex domain wall (VDW) being present. It is also reported that the DWT3 cell requires the lowest field strength to form a DW, after beginning with an initial homogeneous state.

5.2.3. Remanent state internal energies. We determine the internal energies of the domain wall memory cells quantatively, using the energy term data from our finite element calculations, and compare this data for all of the main magnetization configurations.

From hysteresis data (Section 5.3) it is clear that during normal operation the vortex domain walls do not actually exist at position 1 (we defined the five domain wall positions in section (2.2.3)), as was initially suggested, so we adjust our method for defining the domain wall position (Figure 5.8). The relative difference in energies of the three domain wall states show that the clock-wise domain wall state is always the most stable at the left hand trap. Figure 5.7 shows a plot of the respective total Gibbs free energies, exchange energies and demagnetization energies

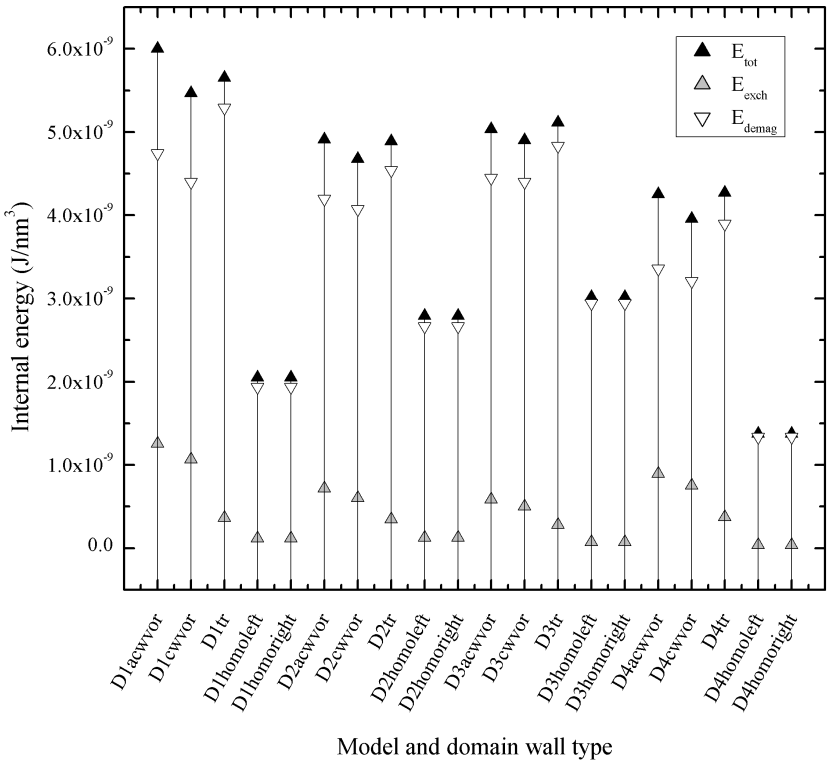

FIGURE 5.7. Internal energies for model and domain wall types, where the anticlock-wise vortex is in position 2, as would be the more likely case between switching events. The total energy and important energy contributions for the different domain wall memory cell designs are plotted for the different domain wall types; anticlock-wise vortex ("acwvor"), clock-wise vortex ("cwvor"), transverse ("tr"), homogeneous ("homoleft" and "homoright").

of the anticlock-wise vortex, clock-wise vortex, transverse domain wall, and homogeneous states for the four DWT-MRAM cells (c.f. Figure 5.1). For each cell design the homogeneous states have by far the lowest internal energy, with exchange being particularly insignificant, since the whole sample is magnetized with the length of the wire. In all cases, the most energetically favourable state for each design is the homogeneous magnetization, where no domain wall is present (Figure 5.7). With an effectively uniform magnetization throughout the sample the exchange energy is minimized, and due to the wire-like shape there are only minimal surface charges, leading to a low demagnetization energy. Due to symmetry in the geometry the energies are the same for both magnetization directions, left ("homoleft") and right ("homoright").

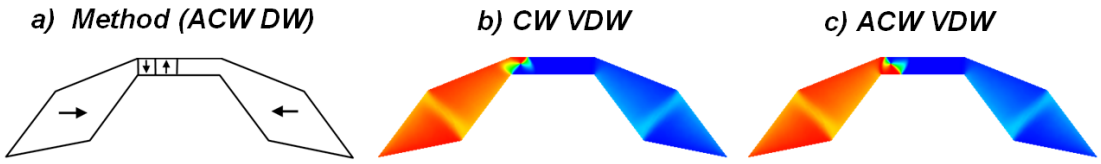

FIGURE 5.8. The positions of (b) the clock-wise vortex domain wall and (c) the anticlock-wise vortex domain wall during normal operation of the D3 memory cell design. Both domain walls exist in the central section of the wire and do not pass into the left or right hand sections. This is confirmed by $\boldsymbol{M} - \boldsymbol{H}$ hysteresis loop simulations. In order to accommodate this finding we adapt out method of DW formation by moving the position of the defined grains in the FE model (a).

5.3. Hysteresis loop measurements

In order to design useful energy barrier simulations we first obtain some $\boldsymbol{M} - \boldsymbol{H}$ loops to determine the domain wall behaviour during controlled switching events. Starting with a clock-wise vortex domain wall at position 2 we apply a slowly ramping external field parallel to the x-axis, the long axis of the cell (Figure 5.9). The field takes 40 ns to ramp from 0 Oe to the maximum value for each loop direction. The coercive field, H_c, is equivalent to the field strength required for switching, and is specifically defined as the $M = 0$ intercept.

However, the minor loop is not symmetrical around the origin. This asymmetry was reported in experimental data by Brownlie and co-workers. In the $-x$ direction (when starting with an ACW vortex at the position 4) the $\boldsymbol{M} - \boldsymbol{H}$ path appears smooth, whereas in the $+x$ direction it appears to be more rectangular. This asymmetric switching behaviour is explained as a difference in the pinning potentials for CW VDWs and ACW VDWs, as well as a central potential well due to magnetostatic effects. Due to symmetry a vortex domain wall experiences different pinning potentials at the two different trap positions since it does not change chirality during switching. This is described in more detail in section 5.6.1.

It is clear from Figure 5.9 that during the normal switching process of the memory cell the vortex domain walls do not pass the traps and do not settle at positions 1 or 5. The field required to traverse the trap and expel the domain wall from the central region is larger than the switching field. This means that for any further simulations we should initialize the ACW vortex at position 2 on the left hand side, and the clock-wise vortex at position 4 on the right hand side (due to symmetry). The hysteresis loop slopes before DW switching takes place since M_x is measured for the whole of the cell. Rotation of the magnetization occurs before the moment of switching, particularly in the end regions of the cell.

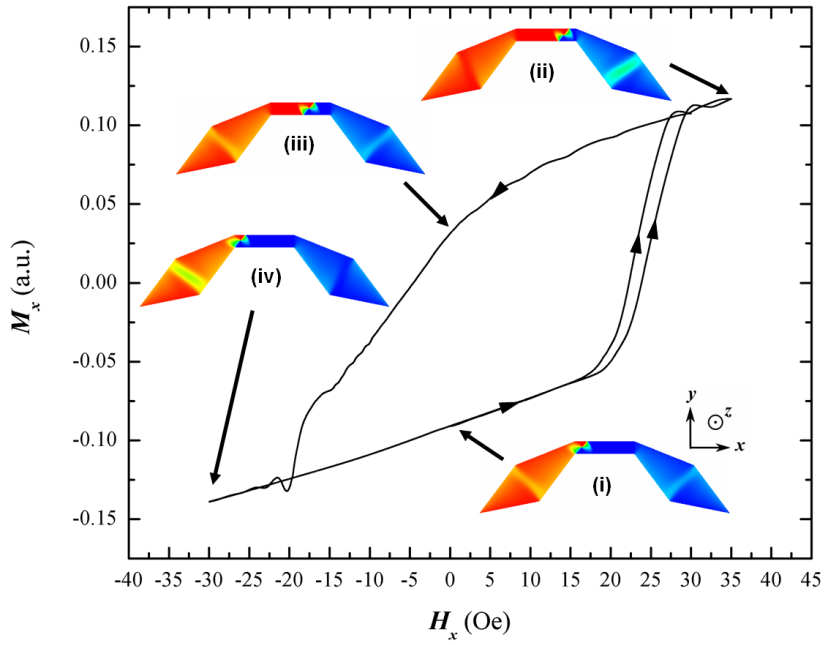

FIGURE 5.9. Asymmetric minor hysteresis loop data for the clock-wise vortex domain wall in the DWT3 memory cell. An important result here is that after switching ($+\boldsymbol{H_x}$) the domain wall stays in the central portion of the cell, at position 4. It does not pass the trap and move to position 5. This means that under normal working conditions the anticlock-wise vortex wall (note the symmetry) should not be modelled at position 5 (or 1 by symmetry) but at 4 (or 2 by symmetry) when held at a domain wall trap.

5.3.1. Coercivity measurements. We assess the coercivity of switching for the DWT3 cell at various scaled dimensions in comparison to simple rectangular elements that are geometrically identical to the central region of the nanowire memory cell. The length and width of the cells and rectangles are scaled and keep a 5:1 ratio, while the thin film thickness is held constant at 20 nm.

From Figure 5.10 it appears that the $\boldsymbol{M} - \boldsymbol{H}$ loops for the rectangular elements are symmetrical around the origin. The loops are rectangular in nature, which is ideal behaviour for a memory element. There is no evidence to suggest that the switching mechanisms are irreproducible, but edge roughness and thermal fluctuations are not considered. Edge roughness can introduce small pinning potentials to the edges and surfaces of the cell geometry which can inhibit domain wall motion and domain rotation. Depending on the magnitude of these complications the switching fields could vary between different cells.

We compare the coercivity measurements for the rectangular elements with those for the DWT-MRAM cell (Figure 5.11), which we estimate by performing LLG simulations to find the

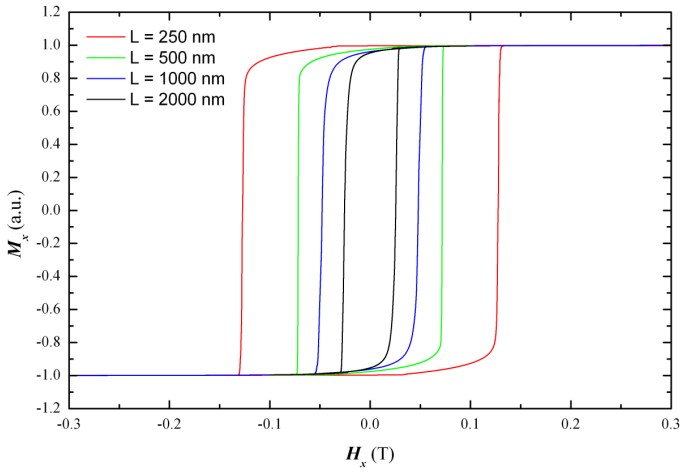

FIGURE 5.10. $\boldsymbol{M}-\boldsymbol{H}$ hysteresis loop data for rectangular permalloy thin film elements of thickness 20nm and length, L, to width, W, rations of 5:1. Scaling down the size increases the coercivity of switching (see Figure 5.11). For W = 50 nm, L = 250 nm the coercive field is around 0.125 T (1250 Oe), and for W = 200 nm, L = 1000 nm it becomes around 0.05 T (500 Oe). The typical maximum field strength that can be generated inside a TEM, for instance, is around 0.07 T (700 Oe).

switching field. The switching coercivity for the DWT3 cell is roughly an order of magnitude lower than for the rectangular cell for all sizes.

5.4. Domain wall phase diagrams

5.4.1. DWT-MRAM phase diagram. We construct a phase diagram of domain wall types for a range of sizes and thicknesses of the DWT3 MRAM cell. So that we do not distort their shape, we scale the in-plane geometry exactly. W is the width of the middle section of the cell, W. In two separate simulations for each model we attempt to set a vortex and transverse domain wall at the centre of the wire and find the remanent magnetization configurations. For each value of T the remanent state total energies for the two cases are plotted against W to find their crossover value. These critical values of W, W_{crit}, are plotted against T in Figure 5.12. We expect that for smaller dimensions the transverse domain wall will be favoured over the vortex, as reported by Nakatani and co-workers [**59**] and McMichael & Donahue [**57**]. As the dimensions of the wires increase the vortex wall energy should approach the transverse wall energy until a crossover region where the vortex becomes more energetically favourable. This information is important for the design of domain wall motion devices: If we are working in

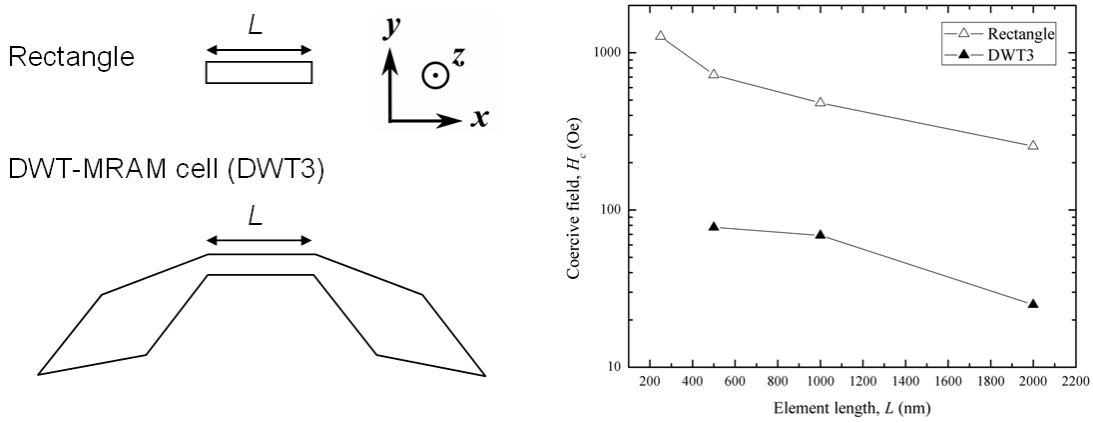

FIGURE 5.11. Comparison between the coercive fields of switching H_c for rectangular permalloy elements ($L : W$ ratio 5:1, $T = 20$ nm) and DWT-MRAM cells where the central rectangular region is of identical dimensions ($L : W$ ration 5:1, $T = 20$nm). For the rectangles H_c is estimated from the $\boldsymbol{M} - \boldsymbol{H}$ hysteresis loop. For the DWT-MRAM cells the coercivity is a factor of 10 lower than for the rectangles of equal L.

a regime close to the transverse-vortex crossover region then our specified domain wall may become unstable, resulting in unpredictable device behaviour.

Figure 5.12 displays a clear trend separating the two phase regions where transverse domain walls and vortex domain walls respectively are the most energetically stable configurations.

Previously such domain wall phase diagrams have been constructed for a number of nanostructures including nanowires, but not for DWT-MRAM cells. In the next section we attampt to reproduce such nanowire domain wall phase diagrams in order to validate our method and compare the results with those for the memory cell.

5.4.2. Rectangular nanowire phase diagram. We construct a phase diagram of domain wall types for a range of nanowire widths and thicknesses. Keeping the $L : W$ aspect ratio constant at 10:1 we scale width, W, and thickness, T, of the permalloy strip over a range of values. In two separate simulations for each model we attempt to force a vortex and a transverse domain wall configuration at the centre of the wire and find the resulting remanent configuration. The final total energies for the three cases are then compared to find the configuration with the lowest energy.

We plot total Gibbs free energy, E_{tot}, against W for each specific value of T, for both the VDW and TDW configurations. The crossover point between the two plots enable us to estimate the critical width, W_{crit}, where the TDW and VDW Gibbs free energy are equivalent.

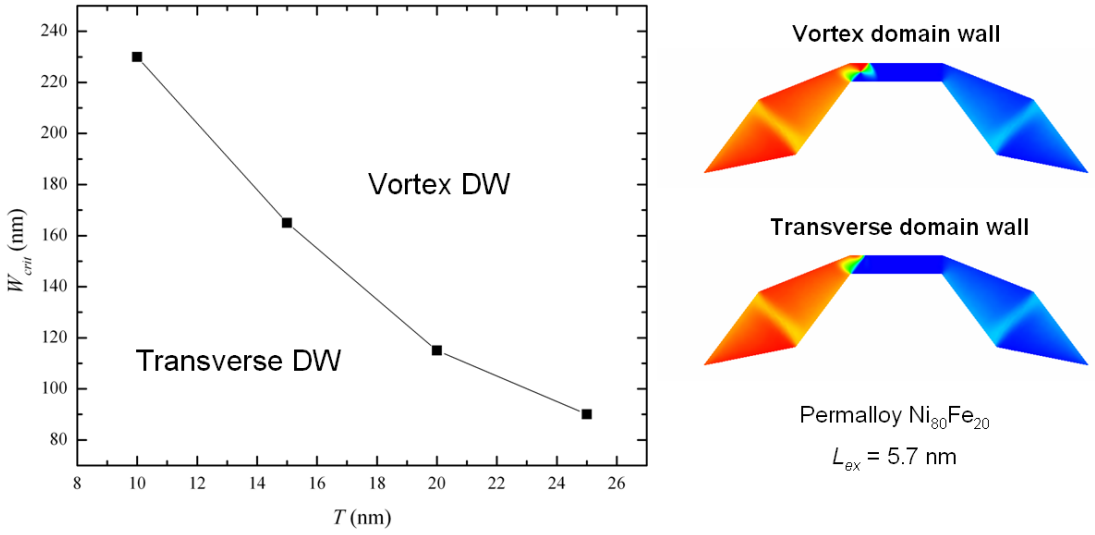

FIGURE 5.12. Phase diagram showing the most energetically favourable domain wall configuration (vortex or transverse) for widths W and thicknesses T of the scaled cell. The line separating the phases is calculated from the crossover points of the vortex and transverse E_{tot} vs W plots for a number of T values. Thus the data points represent the critical values of W where E_{tot} is equal for the vortex and transverse domain wall configurations for a specific value of T.

Figure 5.13 shows the values of W_{crit} as a function of T, with data from Nakatani et al [**59**] and McMichael & Donahue [**57**] for comparison. The plot defines two regions in a phase diagram with each region defining the range of wire dimensions where a different DW configuration is most energetically stable.

Figure 5.13 agrees remarkably well with the existing literature, with our data sitting between the other two data sets. This fact might be explained as follows; our original data is obtained from wires with L/W ratio or 10:1. Nakatani et al used wires of minimum calculation region length 2000 nm, suggesting that the total wire length is well in excess of a 10:1 ratio. McMichael & Donahue [**57**] use wires with L/W ratio 4:1 and artificial end boundary conditions to approxmiate an infinite wire length. For low wire aspect ratios we find that domain walls did not stay in their specified position along the wire but often moved off-centre, possibly altering the internal energy contributions (see section 5.5 for further discussion on this). Using longer aspect ratios reduces this domain wall displacement.

We also compare our rectangular nanowire data (Figure 5.13) to the plot for the DWT3 cell (Figure 5.12). The critical widths for the memory cell are higher for each particular T by typically around 25% of the nanowire value, suggesting that a TDW that is pinned at the DW

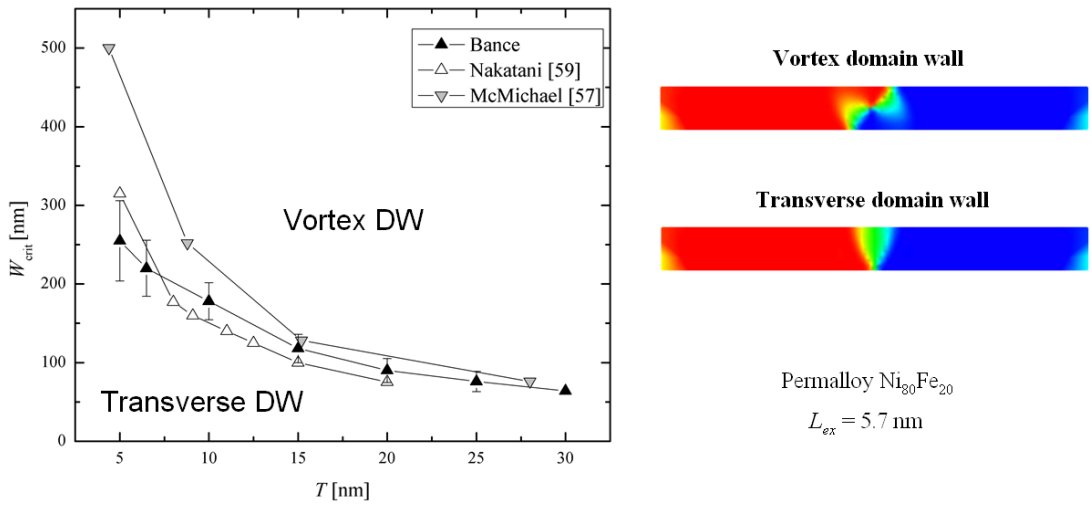

FIGURE 5.13. Domain wall configuration phase diagram for a rectangular permalloy nanowire. The line represents the critical wire width, W_{crit}, for thickness T where the total Gibbs free energy for the VDW and the TDW are equal. Either side of this line lie regions where one of the two DW types become energetically favourable and stable.

trap is energetically favoured up to larger wire dimensions than for an un-pinned DW inside the rectangular nanowire. This is a result of the angle in the wire as the two sections that join at the position of the domain wall are not aligned along the exact same axis. This influences the internal structure of the domain wall, so that the tendency is for a transverse domain wall to occur. This asymmetric angular influence also explains why the transverse domain wall is observed in experiment with its internal magnetization only oriented in one direction [**49**].

The range of values of T and W over which Figure 5.13 provides information is not chosen arbitrarily. In order to compare E_{tot} for the TDW and VDW both configurations must be reached during simulation, but for many dimensions at the extremities of the value ranges this was not possible. For instance, for the much larger values of W and T the TDW is not stable enough to form. At lower dimensions the CW vortex configuration does not appear as a possible meta-stable state, since it would require increasingly higher energy than the TDW state as the dimensions decrease. As T increases, W_{crit} is reduced; however, for the larger values of T in our sample range W_{crit} approaches T so that wire dimensions no longer represent a strip nanowire. As a result, an upper limit on the value of T is reached. This implies that for thicker wires (~ 30 nm and above) the TDW configuration is never possible for any value of W. This roughly corresponds to the transition dimension for Néel and Bloch walls (Chapter 2).

5.4.3. Rectangular nanowire phase diagram with applied field. We perform simulations to find the total Gibbs free energy of stable domain wall states in rectangular nanowires over ranges of values of T and W while applying a transverse field in the plane of the film (Figure 5.14a). The field strength is varied for the values H = -0.010, -0.005, 0, +0.005, +0.010 T. As for previous phase diagram compositions, the critical value of W, W_{crit}, is calculated from the crossover of the E vs T plots for the transverse and vortex DW states (an example is shown in Figure 5.14b).

The plot shows an increase in the supported nanowire sizes for favourable transverse domain wall states with more strongly positive field strength (Figure 5.14c). As the field becomes more strongly positive, aligned with the internal magnetization direction of the TDW, it supports the wall by providing a reduction in Zeeman energy in comparison to a VDW, where part of the DW is oppositely aligned to the field. As the field becomes more strongly negative, opposing the internal magnetization direction of the transverse wall, the TDW becomes less stable, and W_{crit} for each T is reduced in size.

If we extrapolate to higher values of T, W_{crit} becomes close to T. In reality, these measurements no longer represent a thin-film nanowire, where usually $W \gg T$. Thus, we disregard those simulation where T approaches W. We check the magnetization data to confirm that the values taken for energy are from the correct domain wall configurations in the nanowires of each size.

5.4.4. Rectangular nanowire phase diagram with modified anisotropy. The domain wall phase diagram for rectangular nanowires is recreated where the uniaxial magnetocrystalline anisotropy constant, K_1, is modified for three cases; zero anisotropy, $K_1 = 10000$ J/m^3 with $\theta = 0^\circ$ and $K_1 = 10000$ J/m^3 with $\theta = 90^\circ$ (Figure 5.15). θ is usually defined as the angle between the magnetization, $\boldsymbol{M}$, and the crystallographic easy axis. Here the angle is measured from the x axis, in the wire plane, parallel to the long axis. The changes in the anisotropy constant shift the VDW-TDW boundary; for $\theta = 0^\circ$ the boundary falls on higher values of W and for $\theta = 90^\circ$ we observe lower values of W for each T.

Magnetization data for the three different anisotropy settings are presented in Figure 5.16 for different nanowire dimensions. The domain wall structures are altered significantly so that the domain walls are narrower when the anisotropy runs along the length of the wire ($\theta = 0$) and are wider when the anisotropy is transverse to the wire length ($\theta = 90$).

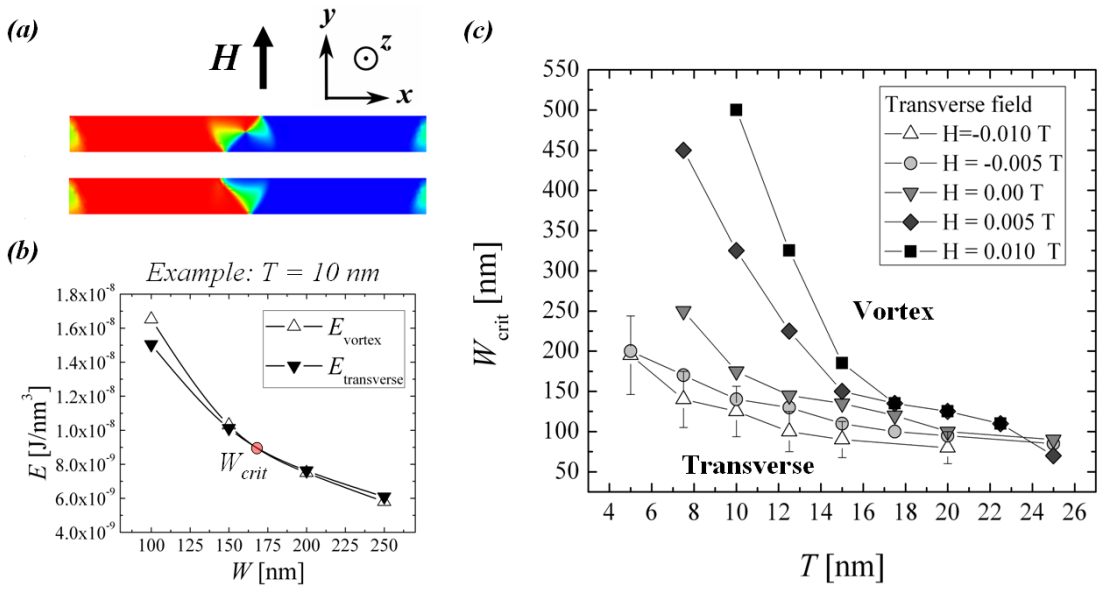

FIGURE 5.14. Domain wall phase diagram for rectangular nanowires showing regions of transverse and vortex domain wall favourability, for a range of transverse applied fields. (a) Schematic showing the direction of the transverse applied field. (b) Calculating W_{crit} for the case of $T = 10$ nm and $H = 0$ .00 T. (c) The final phase diagram containing plots of W_{crit} vs T.

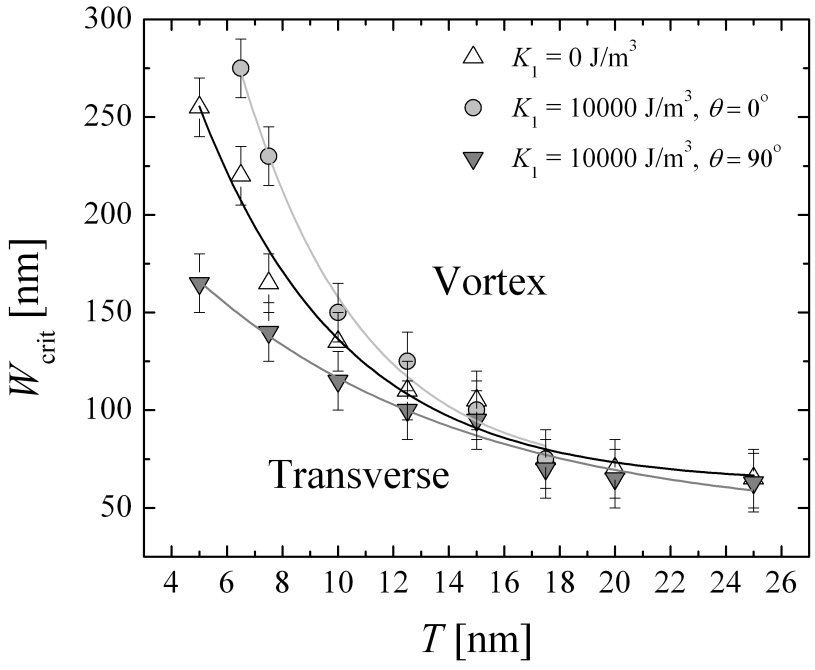

FIGURE 5.15. Domain wall phase diagram for rectangular nanowires with modified magneto-crystalline anisotropy constant, K. Error bars reflect the human error of estimating the value of W_{crit}.

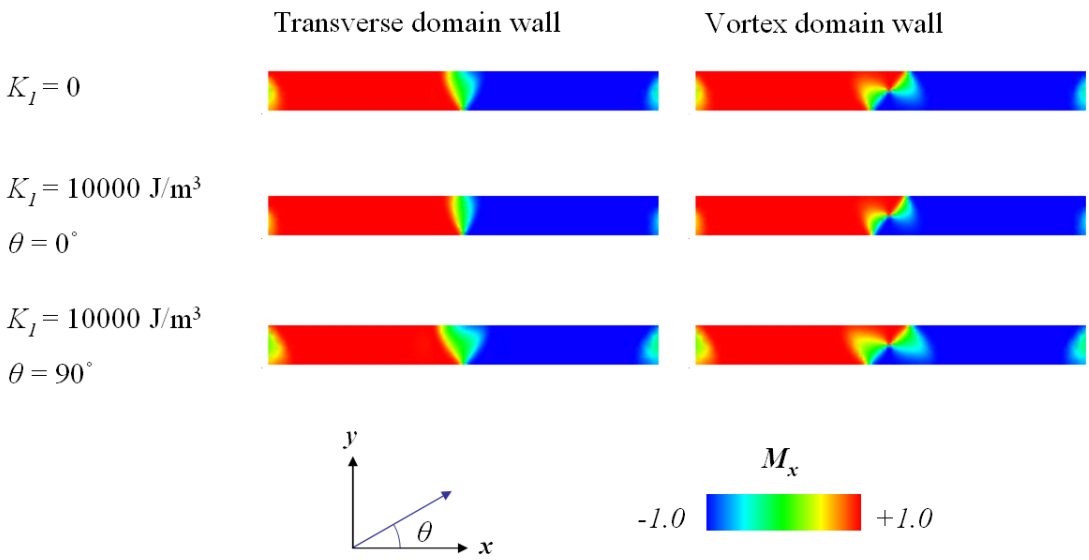

FIGURE 5.16. Magnetization data for nanowires (T = 10 nm, W = 150 nm) with different anisotropy modifications.

When $\theta = 90^\circ$ the anisotropy is parallel to the internal magnetization of the domain walls, stabilizing them and increasing their widths. In the vortex wall the internal magnetization is symmetrical about the centre and since the anisotropy is uniaxial it works along both directions. In the vortex wall, the DW widening is accompanied by a reduction in exchange energy, as the internal change in magnetization occurs over a larger area. For this reason we see a shift in the TDW-VDW boundary so that VDWs are dominant for smaller wire dimensions than the case for no anisotropy.

Where $\theta = 0^\circ$ this argument is reversed, with a decrease in domain wall width that results in an increase in exchange energy for the VDW configuration. This makes the TDW arrangement more stable and shifts the TDW-VDW boundary upwards.

5.5. Internal energy and domain wall displacement

In some preliminary simulations, which had lead onto the successful investigation culminating in Figure 5.13, the domain walls are shifted in their position. To assess the effect of this domain wall displacement on the internal energy of the sample we perform some controlled simulations to plot the percentage difference in E_{tot} as a function of the displacement of a transverse domain wall. The results, shown in Figure 5.17 suggest that there is no obvious correlations between E_{tot} and DW displacement, with other factors such as variations in the internal domain

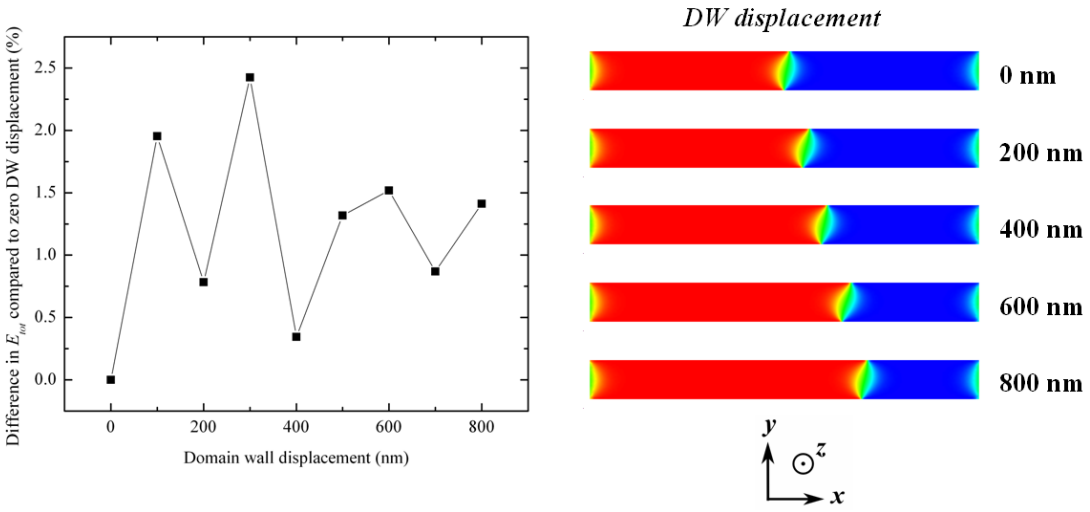

FIGURE 5.17. The percentage change in total energy E_{tot} of a strip nanowire (L = 4000 nm, W = 400 nm, T = 20 nm) as a function of the domain wall displacement from the centre. There appears to be no clear correlation, with other factors such as internal structure of the domain wall having a greater effect on the value of E_{tot}.

wall structure having greater influence. The average difference in E_{tot} is found to be 1.3 % away from the value for zero displacement, meaning that our phase diagram showing the most stable domain wall type for different nanowire measurements can be considered to be accurate.

5.6. Domain wall de-pinning field, switching field and expulsion field

Domain walls can be expelled from a nanowire or a DWT memory cell by a strong magnetic field. For controllable, non-destructive switching of the DWT-MRAM the de-pinning and switching fields must be lower than the expulsion field. An alternative approach would be to apply a precisely timed switching field that is used to move the wall from the initial stable trap position and then turned off before the wall passes the second trap position. However, this is more technically difficult and it is much more practical to design a device with large margins between the switching field and expulsion field.

We calculate the de-pinning field for each of the DWT-MRAM cells (Figure 5.1) and DW types by measuring the minimum field strength at which the domain wall leaves the left hand (LH) trap and moves along the cell, to the right. A probe positioned 200nm left of the centre of the cell will measure a change from a negative to a positive value for the $\boldsymbol{x}$-component of the magnetization, $\boldsymbol{m}_x$, allowing the investigation to be controlled autonomously by a Python [**158**] script, focussing down onto the minimum de-pinning field to a specified degree of accuracy. We

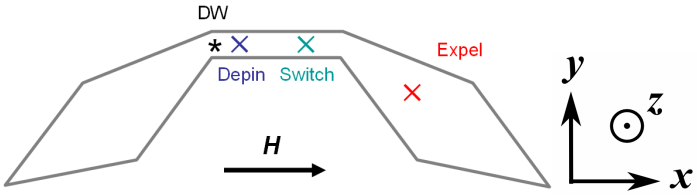

FIGURE 5.18. Method for measuring the minimum de-pinning, switching and expulsion fields in the four DWT memory cells. The domain wall (DW) is initially at the left hand trap position. An external field is applied along the long axis ($+\boldsymbol{x}$). Three probes measure for a reversal of the local magnetization, which indicates that the domain wall has passed their position.

define a de-pinning field as one where the DW de-pins and does not later return to the LH trap position. For accuracy, the field is applied for a number of nanoseconds and then after it is removed the simulation is allowed to continue for a further 4 ns, ensuring that equilibrium is reached.

In a similar fashion the switching field is calculated by using a probe that is positioned 200nm to the right of the centre of the cell to detect the lowest field strength where the DW is de-pinned and moves past the probe, settling to the right of the centre. This method ensures that we are measuring the switching field and not the de-pinning field.

The expulsion field is calculated by placing a probe in the RH side section of the wire and measuring the minimum applied field required to move the domain wall past the probe. The method, including all three probes is illustrated in Figure 5.18.

Figure 5.19 displays minimum field values for de-pinning, switching and expulsion for the four DWT cell designs with CW and ACW domain walls. Data for the transverse domain wall is omitted in all cases as its instability makes it unsuitable for switching applications at these dimensions. The data suggests that the field margins for switching in DWT2 and DWT4 are too small to support reliable switching. In DWT3 the field margins are sufficiently high for reliable switching in both directions.

We observe that the field margins for DWT1 are not significantly smaller than for the DWT2 and DWT4 cell designs. DWT1 has no geometric widening in the side regions, which are added to the other cells in order to increase the expulsion fields. The unexpectedly large margin, particularly for the ACW VDW could be purely down to the difference in angle between the applied field and the easy axis (due to shape) in the side regions of the cell. In all cells, de-pinning fields are consistently larger for the CW than for the ACW VDW. This supports our

results from other simulations that the pinning potential is stronger for the CW VDW.

The DWT3 de-pinning and switching fields do not match the values seen in the hysteresis loop for switching. These differences are unlikely to be a result of changes in the FE models, all of which contained sufficient mesh density and identical geometries. We suggest that these processes, particularly the domain wall de-pinning process, are more complex than they first appear and cannot be simplified to simple criteria relating to the specific probe positions. For instance, small changes in our definition of when the domain wall depins make a difference in the measured de-pinning field. A domain wall can still be influenced by the pinning potential after it begins moving so we must define de-pinning as an event when, after removal of the field, the domain wall does not move back to the trap position. The different position of each DW type relative to the trap complicates matters further, which we discuss in the next section.

We plot the x-plane magnetization of the sample, M_x and the Zeeman energy term E_{Zeeman} as functions of the external field, H_x, in Figure 5.20 for the de-pinning (and eventual switching) of a CW VDW in the DWT3 cell. The peak in E_{Zeeman} occurs at around 30 Oe, corresponding to rotation of the side region that is magnetized in opposition to the field. The magnetization changes abruptly at around 100 Oe, corresponding to the beginning of domain wall motion, leading to switching of the domain wall position to the second trap. Up until switching, the plot of M_x appears mostly linear with applied field, due to the rotation of the magnetization in the whole sample. This is particularly prominent in the DWT3 cell, where the side regions are large and have reduced shape anisotropy compared to some of, say, DWT1 or DWT4. The side regions clearly affect the switching fields, explaining why the DWT3 cell exhibits suitable field margins during operation.

The lower de-pinning and switching fields that are seen in experimental data can be explained by the effects of thermal energy. In our simulations the domain wall motion is field driven with no thermal energy. Experimentally, the applied field changes the energy landscape and reduces the energy barrier between the pinned and de-pinned configuration states. This increases the probability that a switching event will occur, according to the Neel-Brown law 4.14. Due to the very long measurement times, on the order of seconds, used in experimental measurements [**46, 49**] switching events become very likely during the application of the applied field, as thermal energy becomes comparable to the de-pinning energy barrier.

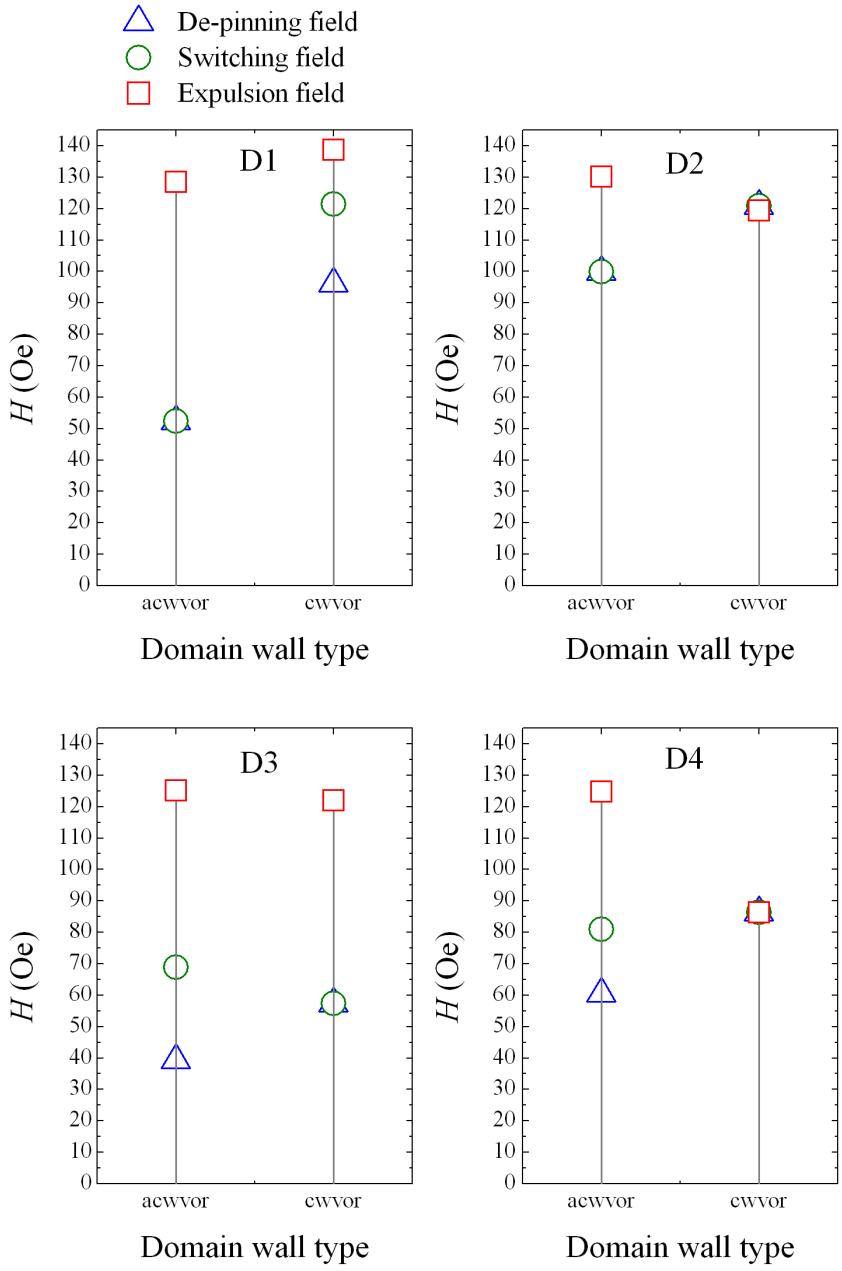

FIGURE 5.19. De-pinning field, switching field and expulsion field strengths for anticlock-wise vortex ("acwvor") and clock-wise vortex ("cwvor") domain walls in the four memory cell designs. Transverse domain walls have been omitted as their in-stability leads to DW type swapping to vortex domain walls during switching. The DWT3 ("D3") cell design exhibits the largest field margins between switching and expulsion, as well as the overall lowest switching fields for both domain wall types.

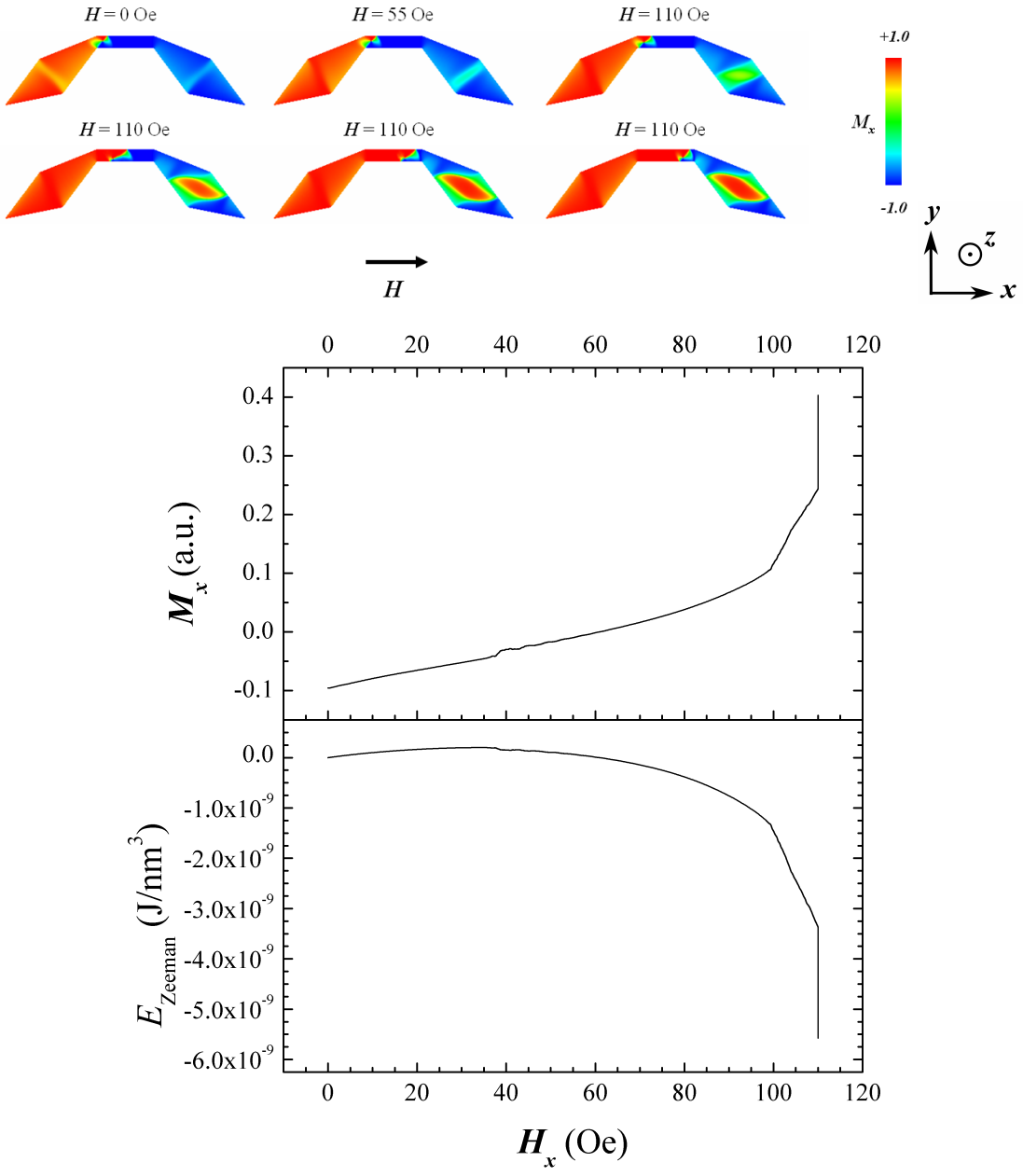

FIGURE 5.20. (Top) Magnetization data for the D3 cell during de-pinning of a clock-wise vortex domain wall with a maximum field of 110 Oe. The de-pinning and switching fields are much higher than have been measured experimentally **[46, 49]**. (Bottom) Plots of M_x and the E_{Zeeman} as functions of the external field, H_x show that sudden de-pinning occurs at around 100 Oe, and switching at 110 Oe.

5.6.1. Explanation of relative de-pinning field strength for opposite vortex chirality. The switching field for the ACW vortex domain wall is higher than that for the CW vortex for all memory cell designs (apart from DWT1). The difference must be explained using a combination of the symmetry of the memory cell, the asymmetry of the internal vortex structure and the relative orientation with an applied field. The remanent states for the two vortex configurations at position 2 are shown in Figure 5.21. The CW vortex sits closer to the domain wall trap position, where the nanowire is angled. The ACW vortex sits further away from the trap and appears to be less strongly influenced by the trap. The reasons for this difference relate to the relative magnetization angles in the memory cell and parts of the vortex structure.

A domain wall is pinned by the angle of the domain wall trap because when it is positioned at the trap the actual domain wall angle is reduced. This is accompanied by a reduction in the exchange energy, which lowers the total Gibbs free energy, so that the trap behaves as a potential well. A vortex domain wall inside the nanowire memory cell is "asymmetric" about the y-axis, leaning off-centre. If we consider the vortex as a combination of two transverse domain walls that are joined together with a vortex core then it is clear that one of these pseudo-transverse domain walls (labelled "C" in Figure 5.21) will be closer to the trap than the other. As can be seen from Figure 5.21 the relative magnetization of the "transverse" region is opposite for the CW and ACW cases. The left hand region of the wire (labelled "A" in Figure 5.21), to the left of the trap, has magnetization oriented along the $+x$ direction but since it is angled it contains a $+y$ component also. If the region of the domain wall closest to the trap is aligned with $+y$ then the region ("C") is expanded due to the influence of the side region ("A"). This is the case for the CW vortex. If region "C" is aligned with $-y$, as with the ACW vortex, then it is in opposition to the side region and so the wall shrinks in size. For the CW vortex the effect of this increase in the size of region "C" is that the reduction in the domain wall angle from the structure geometry and the corresponding decrease in exchange energy is large. For the ACW vortex the opposite is true, so the exchange energy reduction is smaller. For these reasons the domain wall trap acts as a stronger pinning potential well for the CW vortex than for the ACW vortex. This explains why the CW vortex state (at the left hand trap) has lower total Gibbs free energy and why the de-pinning field is higher.

In the DWT3 cell the observed minimum switching field is higher for the ACW VDW, which is explained by the presence of a central pinning potential. The central pinning potential in the memory cell affects the ACW VDW more strongly than the CW VDW because of the

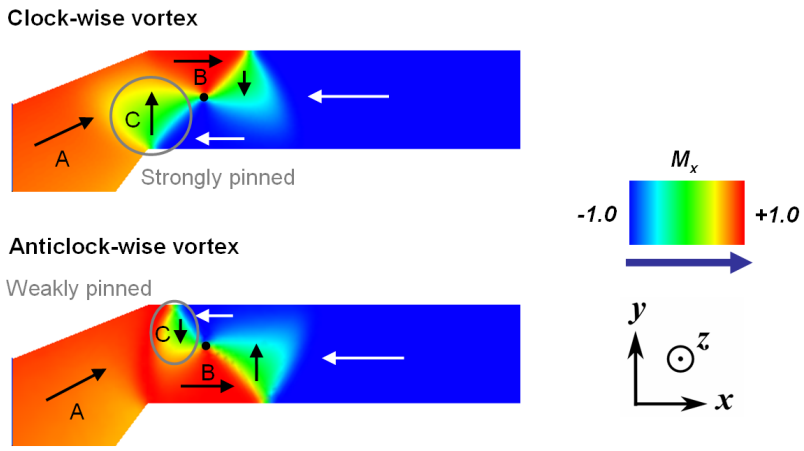

FIGURE 5.21. Visualization of the magnetization data showing the enlarged "C" region in the domain wall internal structure for the CW VDW. This region is magnetized upwards and neighbours the angled left hand section of the wire, which has an upward magnetization component. The opposite is true for the ACW VDW when at the left hand trap, and the "C" region shrinks. The size of the "C" region determines the exchange energy reduction for the domain wall, and so the CV VDW is more strongly pinned. Of course, at the right hand trap position the situation is reversed due to symmetry, and there the ACW VDW is more strongly pinned.

internal domain wall structures. The applied field enlarges parts of a domain wall that are in like alignment with it, and in the two different DW chiralities these enlarged regions are pointing in opposite directions; down and up, respectively Figure 5.22. The side regions of the wire are pointing in opposite directions along the long axis (x) but both have an upwards component. Thus the enlarged upwards portion of the ACW VDW experiences a potential well at the centre of the wire when it is in like alignment with the stray magnetostatic field from the sides. The CW VDW instead sees a small potential barrier, but this does not appear to affect the switching fields so significantly.

5.6.2. Domain wall de-pinning. In order to switch the domain wall memory cell we remagnetize the central part of the cell by moving the domain wall from one trap position to the other. This requires an initial de-pinning of the domain wall from a potential well using an external magnetic that must be stronger than the minimum de-pinning field. We manipulate our domain wall position by applying an external field to the whole sample.

The field strength required for switching will depend on the material properties, cell shape and size, field angle and the existence of domain wall pinning defects. We test for the switching field by introducing a static field, which is ramped up over a period of ten or more nanoseconds

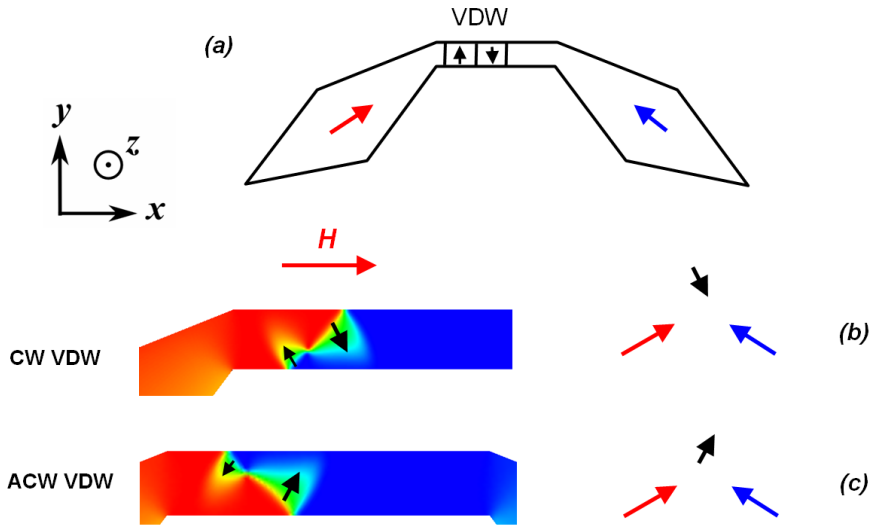

FIGURE 5.22. The central pinning potential in the memory cell affects the ACW VDW more strongly than the CW VDW because of the internal domain wall structures. The applied field enlarges parts of a domain wall that are in like alignment with it, and in the two different DW chiralities these enlarged regions are pointing in opposite directions; down and up, respectively. The side regions of the wire are pointing in opposite directions along the long axis (x) but both have an upward component. Thus the enlarged upward portion of the ACW VDW experiences a potential well at the centre of the wire when it is in like alignment with the stray magnetostatic field from the sides. The CW VDW instead sees a small potential barrier, but this does not appear to affect the switching fields so significantly.

and finally ramped down to zero. Slow introduction and removal of the applied field is important because a fast increase would take the system out of dynamic equilibrium, changing the energy landscape and altering the measured value.

5.6.3. De-pinning of CW VDW. We investigate the de-pinning process of a CW VDW from the left hand trap position of the DWT3 MRAM cell (Figure 5.23). Corresponding temporal plots of the total Gibbs free energy and the contributing energy terms are shown in Figure 5.24. An external field, $\boldsymbol{H}$, is slowly introduced along the long axis of the wire, in the direction that we desire the domain wall to travel. At first the domain wall is stable at the potential well. As the external field increases, but is still too low for switching, the Zeeman energy term increases. As the external field strength increases further the domain wall de-pins from the potential well and accelerates as the distance from the potential well becomes larger. The internal domain wall structure becomes altered as the internal magnetization aligns with the applied field and the expanding domain ($M_x > 0$), resulting in the vortex core being pushed downwards. This

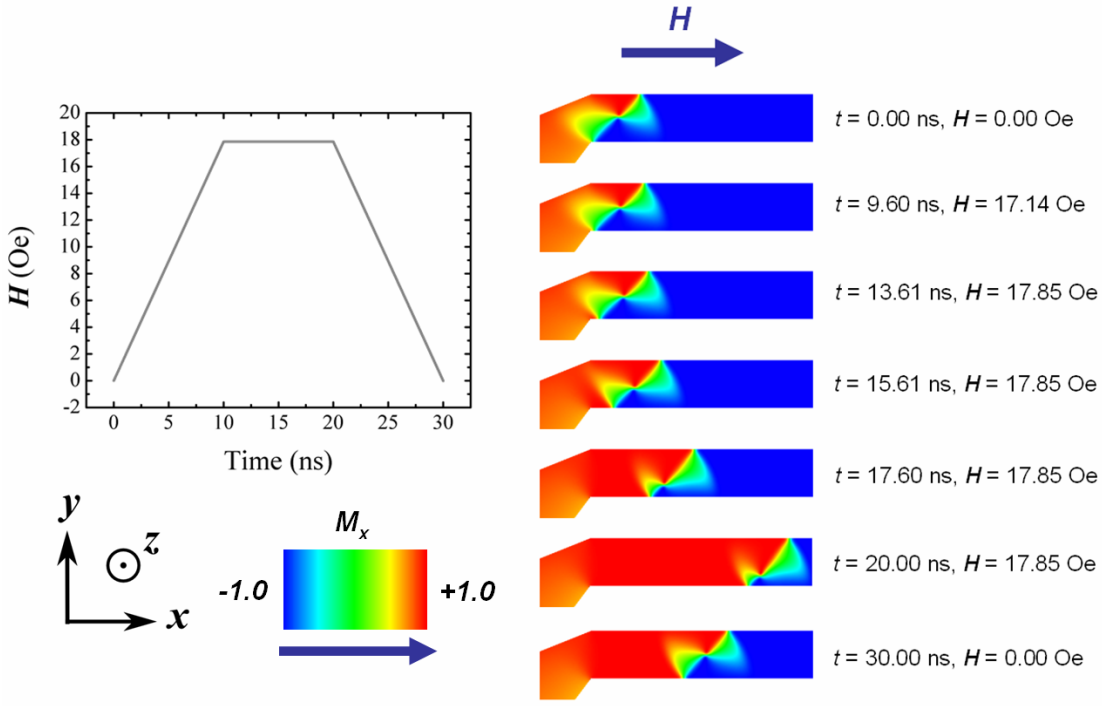

FIGURE 5.23. De-pinning of a clock-wise vortex from the left hand domain wall trap in the DWT3 memory cell. As the external field strength increases the domain wall de-pins from the potential well and accelerates. The internal domain wall structure becomes altered as the internal magnetization aligns with the applied field and the expanding domain (red), resulting in the vortex core being pushed downwards. This increases the internal demagnetization energy by revealing further surface charge at the edge of the wire. A slight peak in the exchange energy at around 21 ns is the results of the applied field being ramped down.

increases the internal demagnetization energy by revealing further surface charge at the edge of the wire.

A slight peak in the exchange energy at around 21 ns corresponds to the removal of the applied field and a readjustment of the energy terms to reach energy minimization. The excess energy that is left behind as the field strength is reduced is observed in the form of spin waves, evident as oscillatory ripples in some of the energy plots. The actual moment of de-pinning is considered the moment when the total energy passes its peak. The peak is overcome and the energy gradient becomes negative as soon as de-pinning has occurred. The CW VDW continues to approach the RH trap position but as the field strength does not reach the switching field value it does not become pinned. After the field is released the domain wall returns to the centre of the wire where it sits. The centre of the wire contains a shallow energy minimum since the shape of the wire introduces stray field from both ends, creating a small potential well.

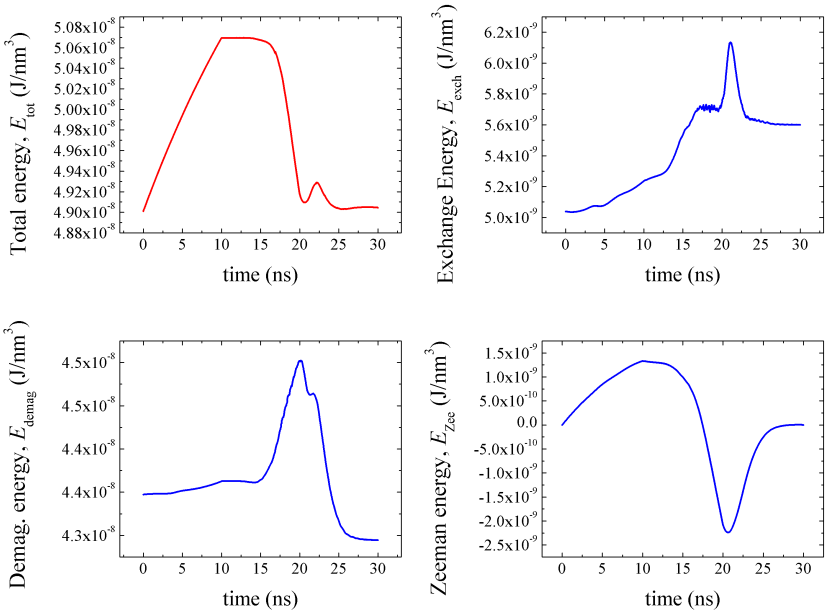

FIGURE 5.24. Temporal plot of the total Gibbs free energy and contributing energy terms for the de-pinning of a clock-wise vortex in the DWT3 memory cell (Figure 5.23). The balancing of these energy terms determines the final magnetization configuration of the sample. The Zeeman energy peaks at around $t = 10$ ns, which corresponds to the instance when the domain wall first starts de-pinning from the trap position.

5.6.4. De-pinning and switching of ACW VDW. In this next example, the ACW VDW (Figure 5.25, Figure 5.26) de-pins from the left hand trap position at higher applied field strength than the CW VDW and its motion through the cell is inhibited by the potential well that is a result of the stray field from the side regions of the cell. At this point the applied field is still increasing in magnitude, and when it reaches the switching field the DW can overcome the central potential of the cell and continue towards the RH trap. The field is also strong enough to push the DW all the way to the trap where it becomes pinned by the trap potential well. Since the field ramp time for all of the simulations is the same, regardless of the peak field strength, the field ramp speed is faster. For simulations like this one where the peak field strength is large we see some oscillatory behaviour from precession of the lattice spin moments as the rate of change of the applied field vector is comparable to the precessional motion of the spins.

Temporal plots of the total Gibbs free energy and the significant contributing energy terms for an ACW vortex DW at the left hand trap of the DWT3 cell are given in Figure 5.26. The initial rise of the Zeeman energy is far less pronounced than in the case of the CW vortex since

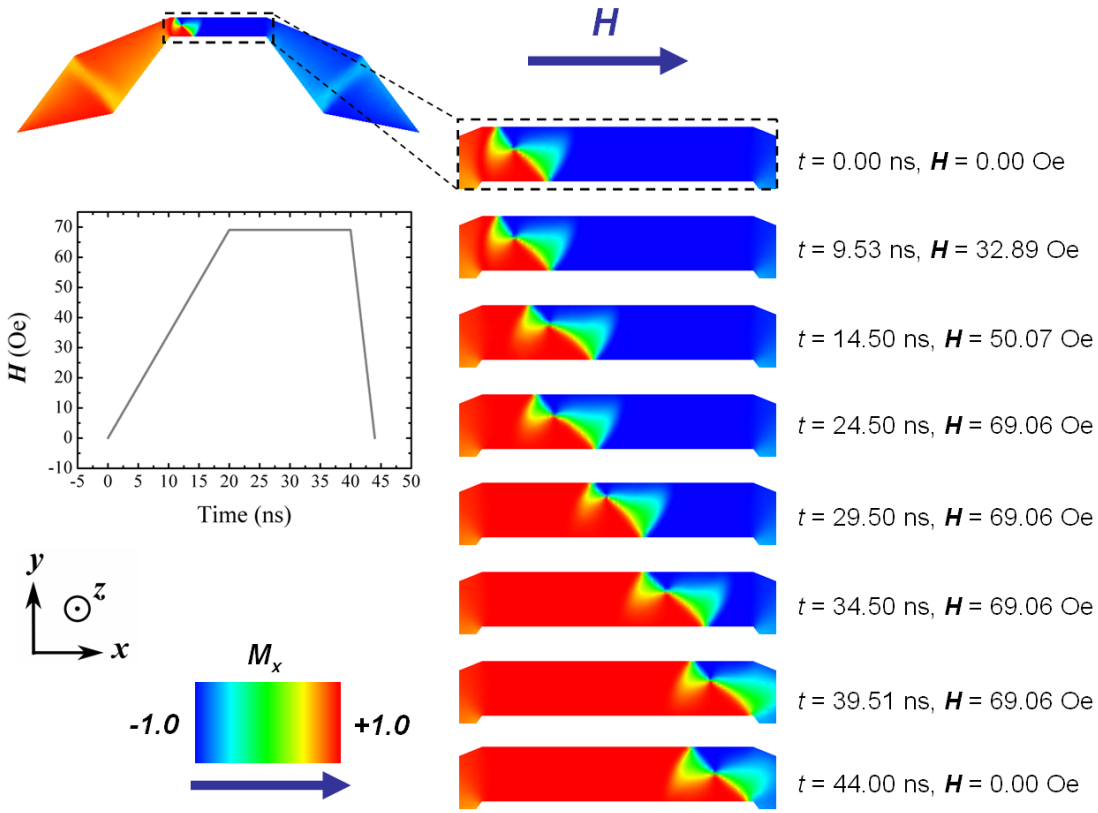

FIGURE 5.25. De-pinning and switching of an ACW vortex domain wall from the left hand trap of the DWT3 memory cell. The actual pinning potential at the trap is not strong and so the de-pinning field is low, however further domain wall motion along the length of the wire is inhibited so that the switching field is considerably higher.

the pinning potential is much weaker and domain wall de-pinning occurs at a much lower field strength. DW motion is inhibited along the wire and this is reflected in the many features of the plots. Since the field strength is higher than in the example for the CW VDW, magnetization rotation in the RH side section of the wire is more pronounced, which changes the strength of the pinning potential at the centre of the cell and makes the potential asymmetric. Therefore the ACW VDW in this example is less strongly held by the potential.

5.6.5. De-pinning and morphing of TDW into CW VDW. In this example for the transverse DW (Figure 5.27 and Figure 5.28) the applied field strength is above the de-pinning field but below the switching field so the domain wall de-pins and is then caught by the central potential well. However, before the final state the TDW changes to a CW VDW. The TDW state is meta-stable and less energetically favourable stable than the VDW for these cell dimensions.

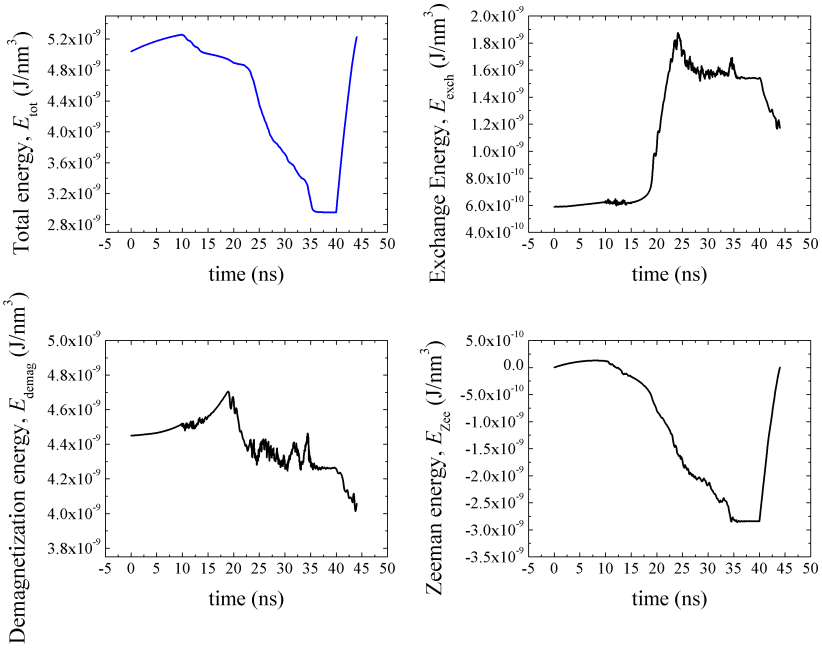

FIGURE 5.26. Temporal plots of the total Gibbs free energy and the significant contributing energy terms for an ACW vortex DW at the left hand trap of the DWT3 cell. The initial rise of the Zeeman energy is far less pronounced than in the case of the CW vortex since the pinning potential is much weaker and domain wall de-pinning occurs at much lower field strength. DW motion is inhibited along the wire and this is reflected in the many features of the plots.

The excess energy from the de-pinning step is sufficient to overcome an energy barrier associated with the nucleation of a vortex core from the top edge of the wire. As the CW VDW moves along the wire the region of its internal structure that is in alignment with the applied field expands and stretches. In this example the domain wall is almost able to momentarily change back into a TDW, before the field is removed and the stable CW VDW remains.

Temporal plots of the total Gibbs free energy and the significant contributing energy terms for a TDW at the left hand trap of the DWT3 cell are given in Figure 5.28. The change from TDW to CW VDW shows up in a competition between the exchange and demagnetization energy terms; the TDW introduces higher demagnetization energy because of the increased surface charge at the top edge of the wire and the vortex is associated with higher exchange energy due to neighbouring lattice spins being out of alignment with one another.

The change from TDW to VDW is observed in nearly all of the de-pinning simulations for TDW configurations. A second example, this time in the DWT4 cell, is given in Figure 5.29.

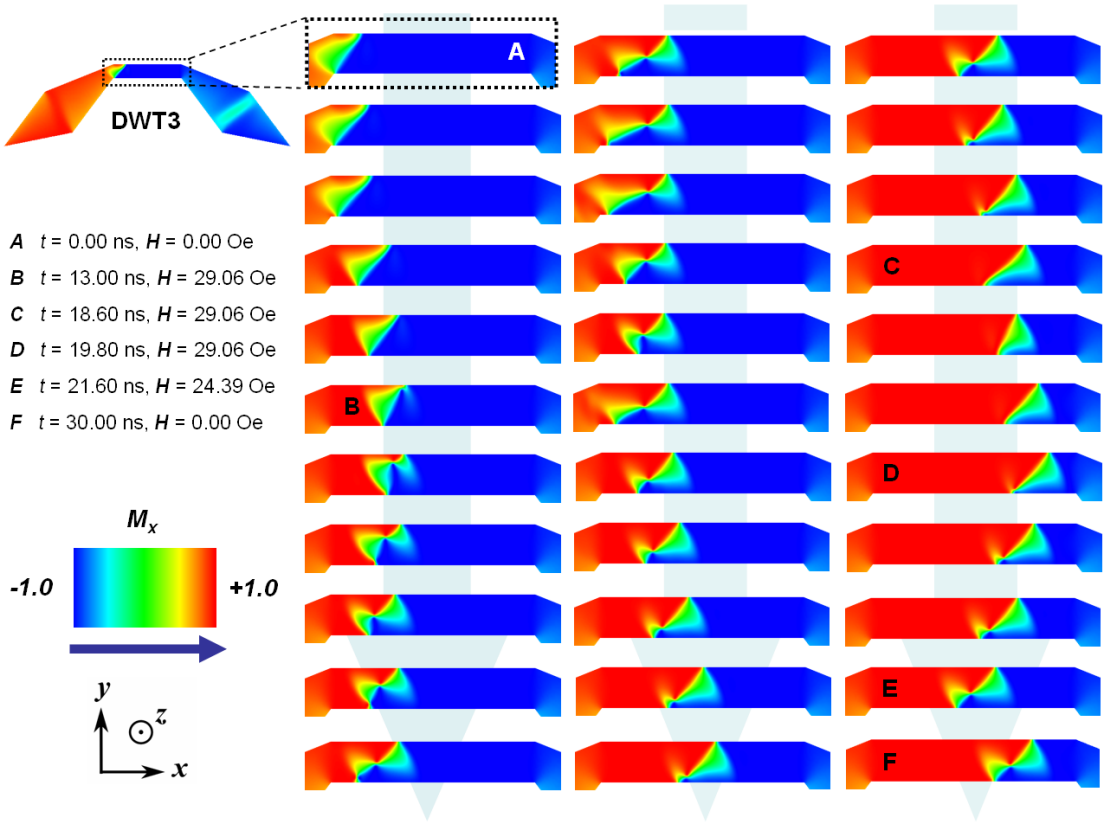

FIGURE 5.27. Time sequence images of the de-pinning of a transverse domain wall (top to bottom, left to right). Since the TDW state is meta-stable and not energetically preferable over the VDW for these geometric dimensions, the excess energy required for de-pinning is enough to overcome an energy barrier associated with the nucleation of a vortex core from the top edge of the wire. As the CW vortex moves along the wire the region of its internal structure that is in alignment with the applied field expands and stretched. In this example the domain wall is almost able to momentarily change back into a TDW, before the field is removed and the stable VDW remains.

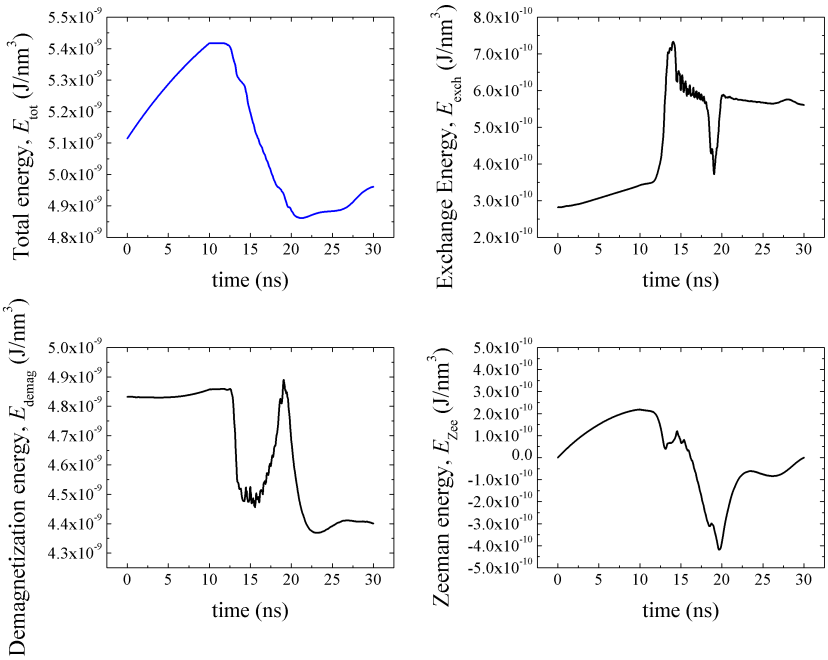

FIGURE 5.28. Temporal plots of the total Gibbs free energy and the significant contributing energy terms for a TDW at the left hand trap of the DWT3 cell. The oscillation between VDW and TDW shows up in a competition between the exchange and demagnetization energy terms; the TDW introduces higher demagnetization energy because of the increased surface charge at the top edge of the wire and the vortex is associated with higher exchange energy due to neighbouring lattice spins being misaligned. The total energy plot, however, is relatively smooth.

5.7. Switching of domain wall types by rotating field

We have already demonstrated the phenomenon of TDWs changing into VDWs under a d.c. external field, and this supports experimental evidence reported by Brownlie and co-workers [**46, 49**]. Now we investigate whether using a rotating field, with defined amplitude and frequency, can provide greater control in changing between different domain wall types. Rotating fields are often used to control domain walls in 2D nanowire circuits [**81, 82, 159, 160**].

In order to effect a change in domain wall type we apply a rotating in-plane magnetic field of defined frequency and amplitude (Figure 5.30). These two parameters are adjusted to construct a phase diagram of possible outcomes. After the field has completed a specified number of rotations it is removed and the sample is allowed to relax to a stable (or at least meta-stable) magnetization configuration. This damped relaxation usually takes a few nanoseconds. We then determine the magnetization configuration that remains in the structure.

The rotating field allows the total Gibbs free energy of the system to be increased with

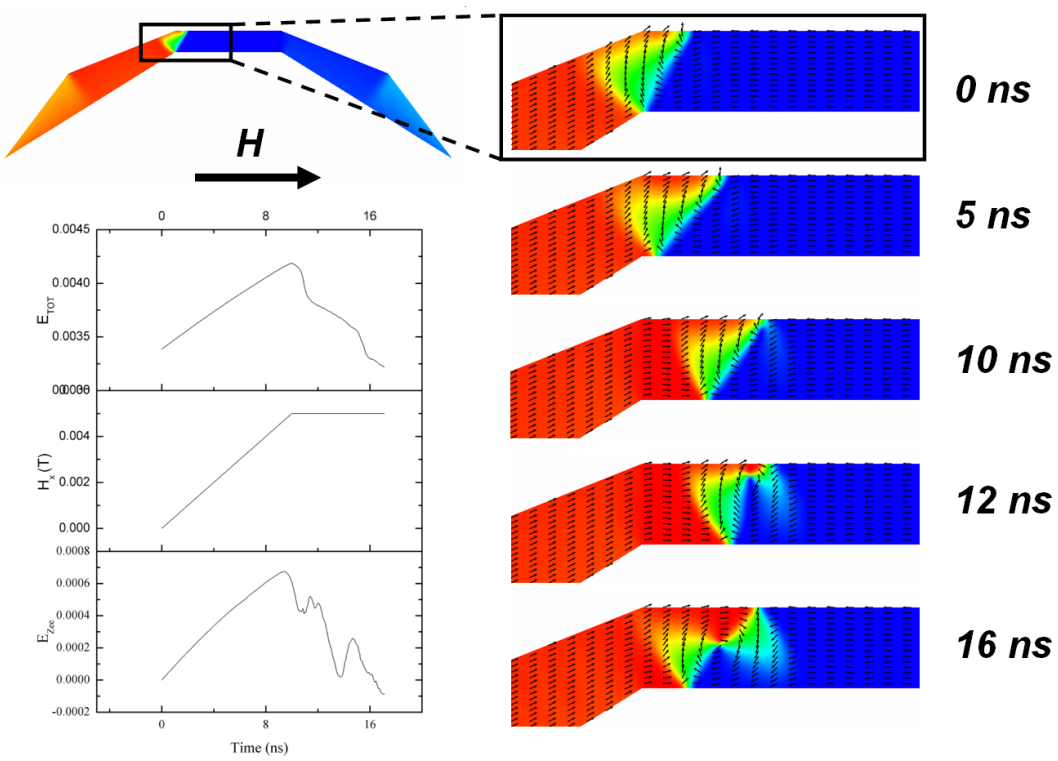

FIGURE 5.29. DWT4 transverse wall de-pinning under a ramped $H_x = 50$ Oe field. In this instance the transverse domain wall is less energetically favourable and therefore less stable than the clock-wise vortex, and the excess energy after de-pinning is enough to overcome the energy barrier for a transverse-to-vortex transition. It is this process that makes transverse domain walls unsuitable for use in our memory cell designs. A predictable and reproducible switching mechanism is essential for correct device operation.

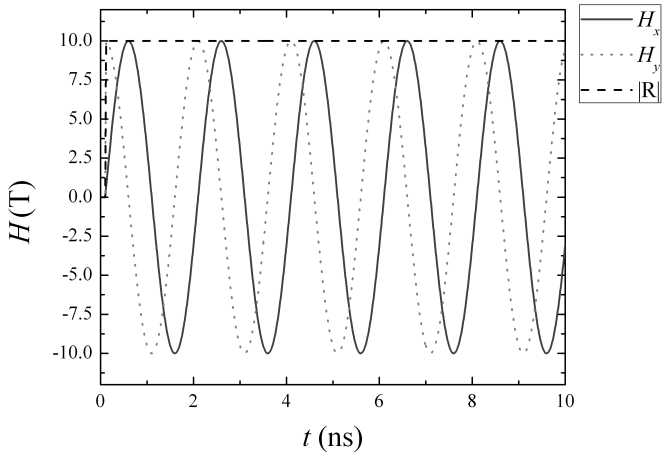

FIGURE 5.30. Rotating magnetic field using sinusoidal field components. This allows the field amplitude to remain constant.

a field that, when time-averaged, has no specific in-plane orientation. The increased internal energy may be enough to overcome specific energy barriers between meta-stable configurations with different domain walls. The rotations may allow a coupling between the rotation frequency and the natural resonant frequency of the magnetic material. The natural frequency of the DWT1 cell is measured during relaxation to remanence from a state of forced magnetization. The y-plane magnetization of the sample, M_y, is plotted against time, t, after removal of the field and a Fourier transform is performed on this data to measure the natural frequency. Both temporal and frequency plots are given in Figure 5.31.

The possible outcomes for each rotating field simulation are as follows:

(1) The domain wall and the rest of the sample can remain unchanged.
(2) The domain wall type is unchanged but the domain wall has moved to a different location.
(3) The initial domain wall changes into a different domain wall type.
(4) The memory cell is damaged, so that it contains more than one domain wall or the domain wall is removed from the cell leaving a homogeneous internal magnetization configuration.

In the case of the domain wall memory cell, outcome 4 represents failure of the memory cell. Outcome 2 can represent failure if the domain wall moves to a position outside of its normal range of travel, such as outside of the central region of the cell. If the domain wall moves only slightly then it can be reset by an applied field, although data in the cell may have been lost.

5.7.1. Transverse domain wall. Figure 5.32 shows the phase diagram for an anticlockwise rotating field that is applied for two rotation periods ($N_T = 2$) to the DWT1 memory cell, which initially contains a transverse domain wall at the left hand trap. In this particular experiment the rotating field is constructed from simple linear interpolations between maximum and minimum field strengths for the two dimensions in the $\boldsymbol{x}-\boldsymbol{y}$ plane, and as such the rotating field does not hold constant amplitude. In these results we have not specified between vortex domain walls that have remained at their initial position or have moved to other parts of the central section of the wire. The plot shows distinct phase regions where a CW or ACW VDW have remained in the structure and suggests that rotating fields could be used to controllably switch between domain wall types. We do not observe any clear coupling between the magnetic resonant frequency of the cell and the phase diagram.

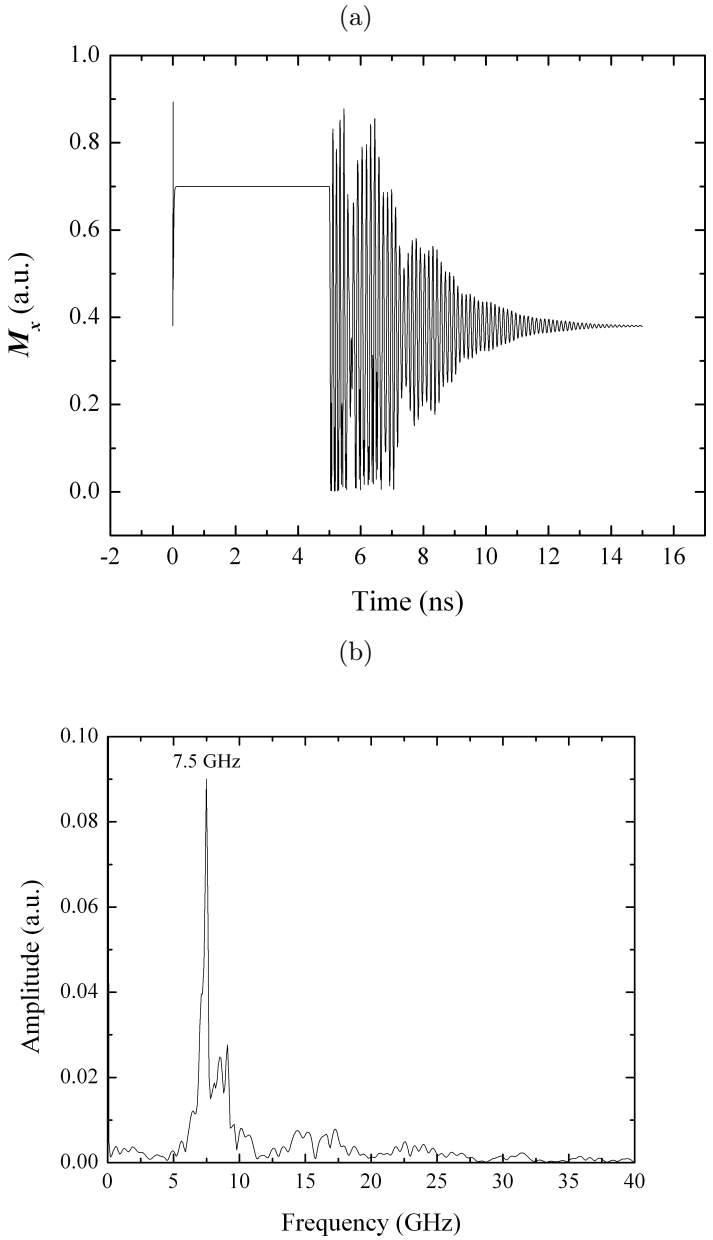

FIGURE 5.31. (a) Temporal plot and (b) frequency (FFT) plot of M_y during relaxation of the DWT1 cell. The field is applied from 0 to 5 ns. The main frequency peak, 7.5 GHz, is taken as the natural oscillatory frequency of the sample.

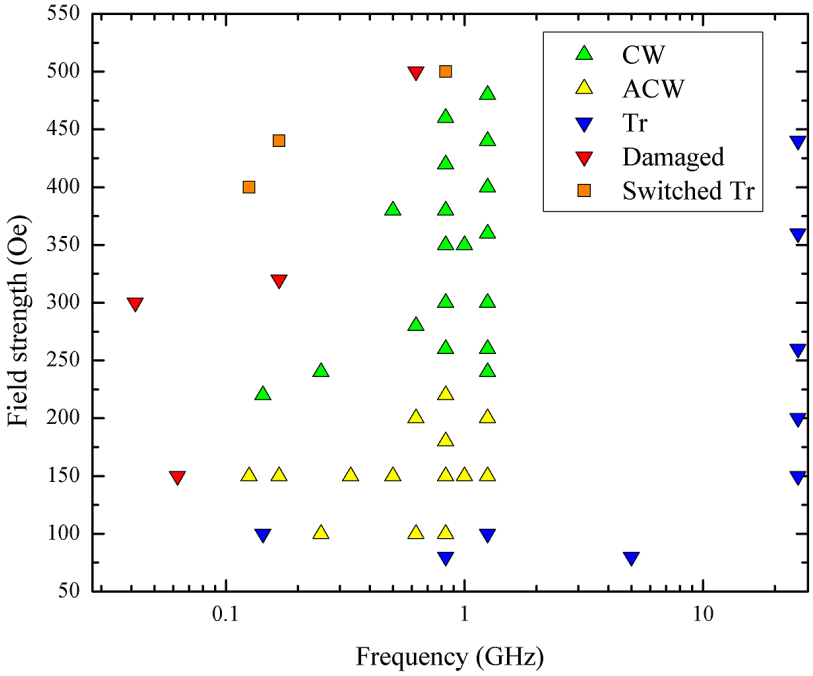

FIGURE 5.32. Phase diagram for an anticlock-wise rotating field that is applied for two rotation periods ($N_T = 2$) to the DWT1 memory cell, which initially contains a transverse domain wall at the left hand trap. After the field is removed a number of outcomes are observed. The cell may be unchanged under low fields or damaged (the domain wall is expelled or multiple domain walls form in the cell) under high fields.

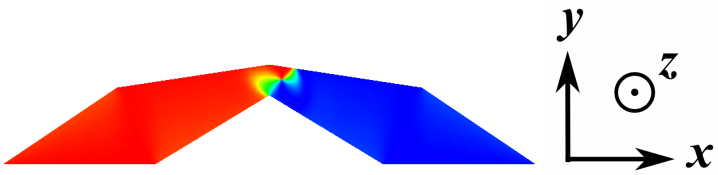

FIGURE 5.33. In order to simplify the rotating field experiment we design a model ("Q3") containing just one trap and wire widening to contain the domain wall at the trap position (total length is 3500 nm).

5.7.2. Single trap model. In order to limit the movement of the domain walls in the structure and simply focus on the changing of domain wall types we introduce a model (known as "Q3") with just one trap, including widening to avoid DW propagation into the side regions (Figure 5.33). The total length of the cell is 3500 nm.

A clock-wise rotating field is applied to the "Q3" design for 20 rotations ($N_T = 20$), starting with a CW domain wall (Figure 5.34). We observe a number of phase regions, for instance near the middle of the plot there is an area where ACW VDWs remain in the structure, but are

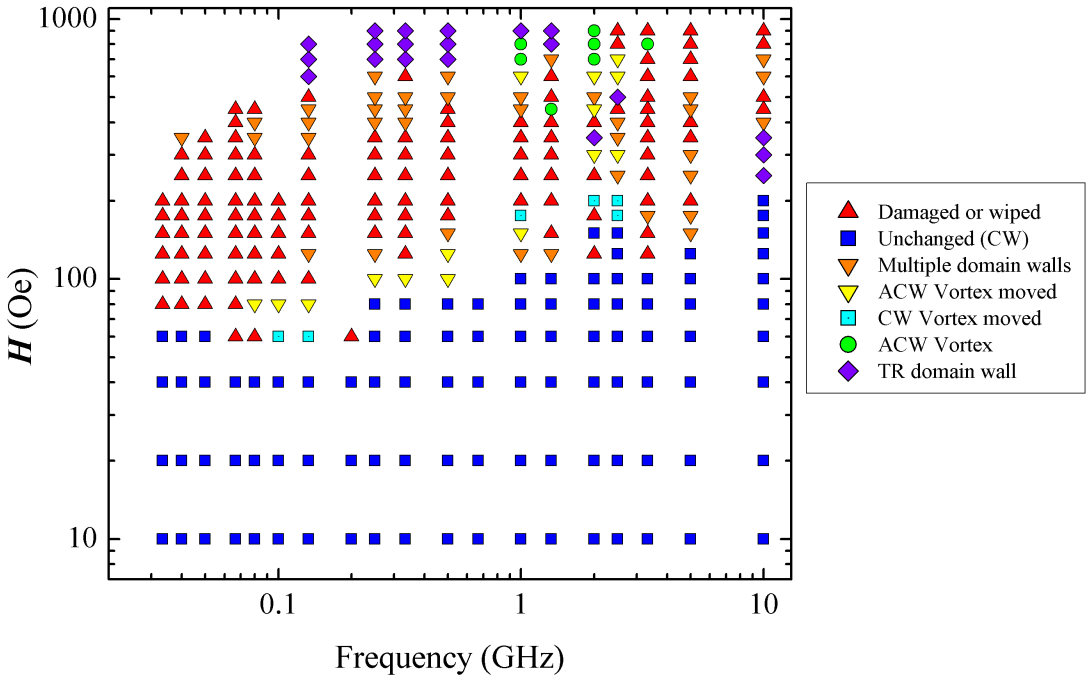

FIGURE 5.34. Phase diagram of outcomes for a series of simulations starting with a clock-wise domain wall in the "Q3" domain wall trap device and applying a clock-wise rotating field for 20 rotations.

no longer at the trap position and have moved towards the ends of the cell. In this case the domain wall could be moved back to the trap position with a d.c. field. Normally TDWs are not observed close to this region since the TDW is not energetically favourable and a transition from a vortex to a TDW is not possible without a saturating field. For lower field strengths no changes to the domain wall configuration are observed. For many higher field strengths the cell is wiped, meaning that the domain wall has been expelled completely. This requires a lower field for lower frequency as the field rotates more slowly and is acting on the domain wall for a longer period of time. For the highest field strengths, above 400 Oe, regions of TDWs appear as the strong field acts as a saturating field pointing at a specific angle, with the TDW direction corresponding to the final field direction (c.f. section 5.2.2). The widening of the structure away from the trap position is not particularly successful at stopping domain wall movement. The domain wall does not move back to the trap once a field is removed after initially leaving the trap position. However, it is possible to use a small field, oriented in the $+y$ direction, to coax the domain wall back to the trap, if so desired.

We now perform similar simulations for the Q3 model starting with a TDW at the trap

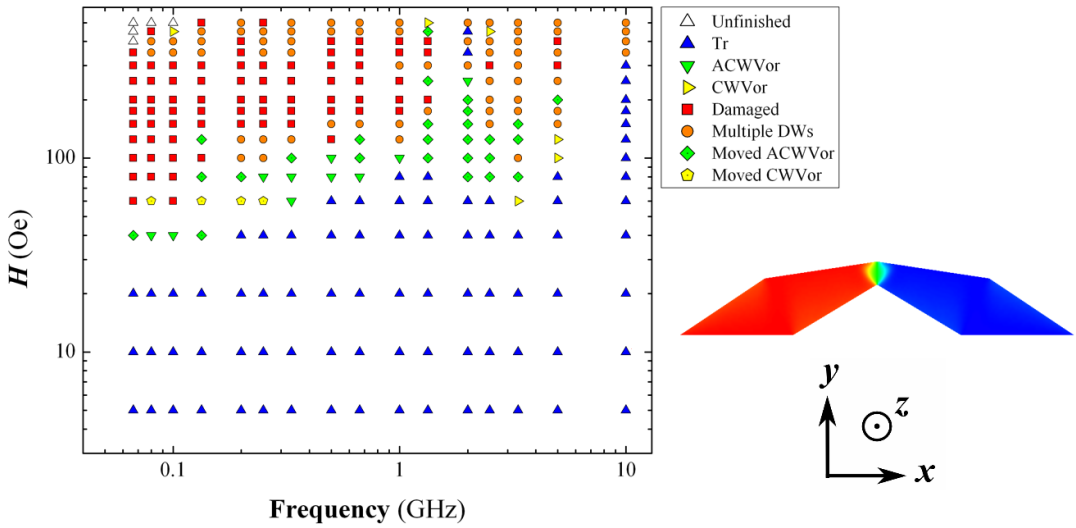

FIGURE 5.35. The phase diagram for 20 clock-wise rotations of a rotating field, starting with the "Q3" model and a transverse domain wall.

(Figure 5.35). Again 20 clock-wise rotations are used ($N_T = 20$). For low field strengths, typically below 40 or 50 Oe, we see no change in the domain wall type. Slightly higher in field strength we observe a large region containing ACW VDWs (including ones that have moved) but smaller regions for CW VDWs. The difference is a result of the field rotation direction and that the field ends up pointing in the $+y$ direction so that just before switching off it has a $-x$ component. This is more favourable for the internal alignment of the ACW VDWs.

Overall, we find that rotating fields do not provide a reliable route to switching of domain wall types because the domain walls tend to be moved from their initial position by the field.

5.8. Thermal stability

We use the nudged elastic band (NEB) method to estimate the thermal stability of a domain wall at a trap potential by calculating the minimum energy path (MEP) between two meta-stable configurations, before and immediately after de-pinning. We compute the energy barrier of the depinning process for varying external field strengths [**161**]. The zero-temperature de-pinning field for a domain wall is calculated by solving the LLG equation for increasing applied field.

We calculate a minimum energy path (MEP) with a series of 20 input images, which represent the nodes on the MEP plot. Using a series of images between the pinned and de-pinned states allows the NEB code to avoid an incorrect initial guess for the MEP, which would otherwise lead to an unrealistic MEP.

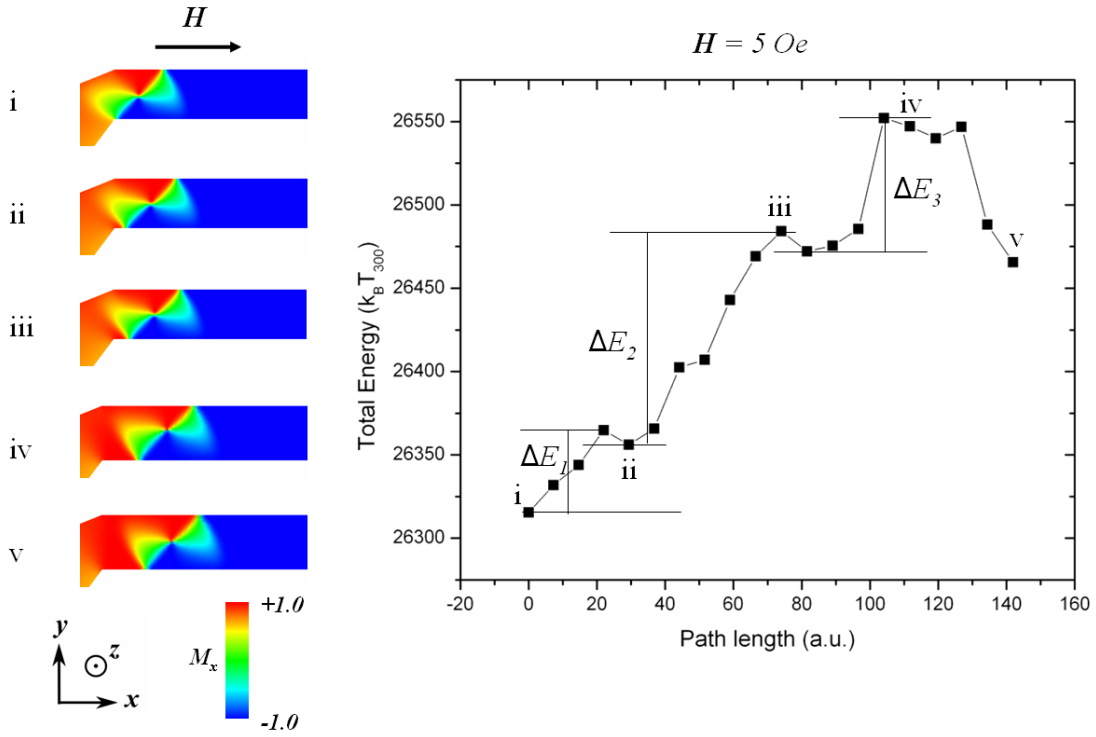

FIGURE 5.36. Example of energy barrier measurement by plotting total energy E against path length, for the DWT3 cell and a CW VDW. The magnetization images show the DW structures at the various positions indicated in the plot.

An external field is applied along the $+x$ direction, as would be for de-pinning or switching, for a range of field strengths. An example, where the field strength is $H = 5.0$ Oe, is plotted in Figure 5.36. For each field strength we measure the energy barrier, ΔE, and plot these in Figure 5.37. The definition of the energy barrier is very important. The energy plot shows a number of peaks and troughs in configuration space (path length) that correspond to rearrangements of the magnetization that occur before and during the de-pinning process. By observing the magnetization data images in Figure 5.36 we can attribute the correct barrier to the actual de-pinning movement of the domain wall. This is taken as the barrier labelled "ΔE_3" in Figure 5.36.

We plot the energy barriers as a function of applied field (Figure 5.37). ΔE decreases linearly with $\boldsymbol{H}$. According to the plot of this data the barrier vanishes at a field of about 22 Oe, which is lower than the value of 55 Oe given by LLG simulations. This might be explained by the sweep rate dependence of the coercive field. Normally, switching fields and depinning fields are large if the external field is changed quickly, because an external field changes the

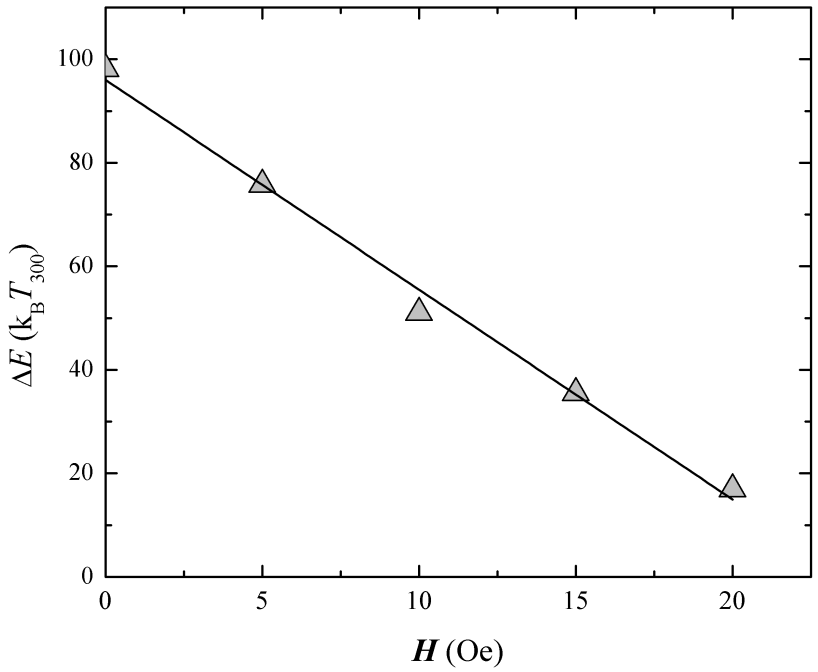

FIGURE 5.37. Energy barrier of de-pinning for the "DWT2" memory cell with a clock-wise vortex domain wall, as a function of applied field.

energy landscape before the system reaches equilibrium. Slower adjustment of the external field leads to a lower swiching field. In our LLG simulations the field is sweeped up from zero, which could account for the higher measured de-pinning field in comparison to the NEB results, where the applied field is static.

It should be noted that our choice of the energy barrier from the plot in Figure 5.37 can easily lead to the lower calculated value of the zero temperature de-pinning field when compared to the LLG results. If instead the barrier height is measured from image i to image iv as a combination of ΔE_1, ΔE_2 and ΔE_3 then the total ΔE is much larger, leading to even greater thermal stability. This different definition of the energy barrier is not unreasonable, since it is conceivable that performing the same simulations with slightly different input parameters could lead to an energy plot with fewer local minima. Additionally, it could be suggested that the probability of arriving at iv is a product of the individual probabilites of overcoming the local energy barriers. The definition of energy barrier is important and not always an obvious choice but can affect the results significantly.

In real experiments, measurement time is of the order of seconds. As an estimation of the room temperature de-pinning field we determine the field strength that corresponds to an

appropriate barrier height. According to Néel-Brown theory and using equation (4.14), thermal activation overcomes a barrier of 23 k_BT (with $T = 300$ K) within a time of 1 second if the attempt frequency is $f_0 = 10^{10}$ Hz [**155**] (c.f. Section 4.3.2). This barrier height is reached at a field of 18 Oe, which corresponds to the room temperature de-pinning field. This is slightly lower than the value of 25 ± 5 Oe measured by Brownlie and co-workers [**49**], but this small difference can easily be attributed to wire roughness and defects.

We observe that the zero field energy barrier is 96 k_BT. Thermal activation overcomes a barrier of $\Delta E = 96\ k_BT$ (with T=300 K) within a time of $\tau \sim 1.6 \times 10^{24}$ years if the attempt frequency is 10^{10}Hz. Hence, it is clear that the DWT3 memory cell is thermally stable enough for memory device applications. Since the stable lifetime is so large we can safely predict that the other cell designs, which are comparable in size and switching field strengths, would also be stable.

5.9. Summary

Our original research into domain wall trap (DWT) memory utilized finite element (FE) micromagnetics and the nudged elastic band (NEB) method to investigate a range of DWT memory device behaviour.

Hysteresis loop measurements, along with measurement of the switching fields, demonstrated an asymmetric switching behaviour for devices that contain vortex domain walls (VDWs). Simulations suggest that field margins for switching can be sufficiently large for memory devices, but depend on the design of the cell.

It is possible to form a domain wall of a specific type, at a particular trap location, by controlling the angle of a saturating field.

Domain wall memory is stable at room temperature and does not undergo spontaneous domain wall de-pinning due to thermal energy.

Because the domain wall type changes from vortex to transverse domain wall when reducing the cell dimensions it may not be possible to scale down the size of the cells. During some preliminary simulations with smaller cells, where we had scaled down the geometry in size, we observed that the TDW was unsuitable for use in a DWT-MRAM cell even when it was the most energetically favourable configuration. The TDW did not consistently sit at the trap position and during switching it was often expelled from the structure completely, suggesting that the margin between the switching field and the expulsion field was too small. We suggest that this is

because the domain wall width was comparable to the width of the cell, reducing the influence of pinning potentials at the trap position and allowing it to pass through the widened side regions easily.

The coercivity of switching for the DWT3 cell was shown to be a factor of 10 smaller than that for a rectangular wire, a major advantage over more traditional MRAM designs.

Domain wall phase diagrams were produced to measure the range of dimensions where the transverse and vortex domain walls were respectively the most energetically favourable configuration state. This was performed for the DWT3 cell, as well as rectangular nanowires. The data for the nanowires matched well with existing results from the literature. The experiment was extended for a series of transverse field strengths and a variety of types of magneto-crystalline anisotropy, both of which were able to stabilize domain walls in the wires and shift the TDW-VDW phase boundaries.

We found that rotating fields do not provide a reliable route to switching of domain wall types because the domain walls tend to be moved from their initial position by the field. However, a small d.c. field can be used to manipulate them back to the desired field. Application of a focussed rotating field inside a real MRAM cell can be achieved using the existing bit and word lines, although actually this operation is not a useful part DWT-MRAM operation. A possible application could instead be a form of memory that toggles between different domain wall type states. This itself is limited to cell sizes that can supports different types of domain walls, close to the critical size boundary.

Finally, we have used the nudged elastic band method to show that DWT-MRAM is sufficiently thermally stable for device applications, with a meta-stable lifetime of $\tau \sim 10^{24}$ years. The room temperature de-pinning field was found to be 18 Oe.

Many of these results showed good agreement with experimental data from Brownlie and co-workers [**46, 49**], with many differences being accounted for by thermal effects and fabrication characteristics of the experimental samples.

CHAPTER 6

Spin waves in ferromagnetic nanostructures

Elimination of magnetic spin wave (SW) reflections from microstructure edges could prove crucial to the success of potential spin wave logic devices. In micromagnetics the sample size is often truncated in comparison to real experimental devices as a way of reducing computation time. This leads to an increase in spin wave reflections from the sample edges, which are now spatially closer to spin wave sources and regions of measurement.

We generate spin waves in permalloy nanowires and other thin film structures, making observations on their behaviour as functions of material and applied field properties. We demonstrate the occurrence of spin wave reflections at structural boundaries and at interfaces between regions of mismatched damping constant. Reflections from these interfaces are proportional to the size of increase in damping constant. We also demonstrate the use of simple boundary conditions containing increased Gilbert damping constant or alterations in geometry for elimination of spin wave reflections.

6.1. Introduction

Spin waves generated inside a ferromagnet are associated with the dissipation of excess energy that result from a perturbation of the magnetization inside a region of the magnet and the ensuing return to an equilibrium configuration. They are of interest as information carriers in the field of spin wave logic. Here it is beneficial for their behaviour to be orderly and predictable so that device behaviour is reliable. In particular, reflections from the structural boundaries of the magnetic microstructure may cause interference. Spin waves also cause problems in micromagnetic modelling exercises where sample sizes are often constrained so that model size and thus computation time are manageable. In many real devices spin wave energy can dissipate away through the large sample without causing any interference, but in the smaller computer models the structure edges are often much closer, meaning reflections are a bigger problem.

In electromagnetic field calculations, so-called absorbing boundary conditions [**162, 163**] are used. The approximate analytical solution for the electromagnetic wave at large distances

from scattering objects is used to introduce boundary conditions that perfectly absorb incoming waves at the boundary of the computational domain. In general, a closed form is not known for spin waves at the boundaries of the computational domain of magnetic microstructures. While a rigorous way to introduce absorbing boundary conditions in micromagnetics may only be possible for special geometries, an increase of the damping may sufficiently suppress spin wave reflections in micromagnetic simulations. This method was first demonstrated by Berkov and co-workers, who simulated spin torque oscillations in point contact devices using finite sized, disc-shaped micromagnetic models to represent large area thin films with a nano-scale spin wave source in the centre [**164**]. Spin wave reflections from the sample edges would otherwise have destroyed the stable oscillations that were induced locally by a spin polarized current.

In this chapter we investigate the interaction of spin waves with edges of permalloy nanowires and disks using micromagnetic simulations. In addition we look at how spin waves pass through or are reflected from internal interfaces between materials with different Gilbert damping constants. We demonstrate simple methods to reduce spin wave reflections from structural boundaries, which can be applied during micromagnetic modelling or actual experiment. We introduce boundary conditions of increased damping constant, which hinders gyromagnetic precession and dampens out spin waves. While this is trivial to carry out in micromagnetics simulations it is also possible to modify the damping constant in some real materials using dopants, as shown by Bailey et al [**165**].

In micromagnetics, the benefit of reducing model size for management of computer resources is two-fold. Disk space usage is reduced as well as computation time. Perhaps the latter is currently more significant, allowing simulations to be performed within manageable time-scales.

6.2. Generation of spin waves

A hybrid finite element boundary element (FE/BE) method [**146**] is used to calculate the time evolution of the magnetization configuration of permalloy ($Ni_{80}Fe_{20}$) nanowires by solving the Landau-Lifshitz-Gilbert equation of motion. The nanowires are 10 nm thick and 100 nm wide while material properties are fixed as $J_s = 1.0$ T, $K = 0$ J/m^3, $A = 1.3 \times 10^{-11}$J/m. The standard value for the damping constant is $\alpha = 0.02$, except when stated (the effect of modifying the damping parameter is investigated in section 6.3.5). Spin waves are generated in a nanowire by perturbing the magnetization of a 20nm-wide region of the wire at some position along its length. This is achieved by introducing a localized external magnetic field after some

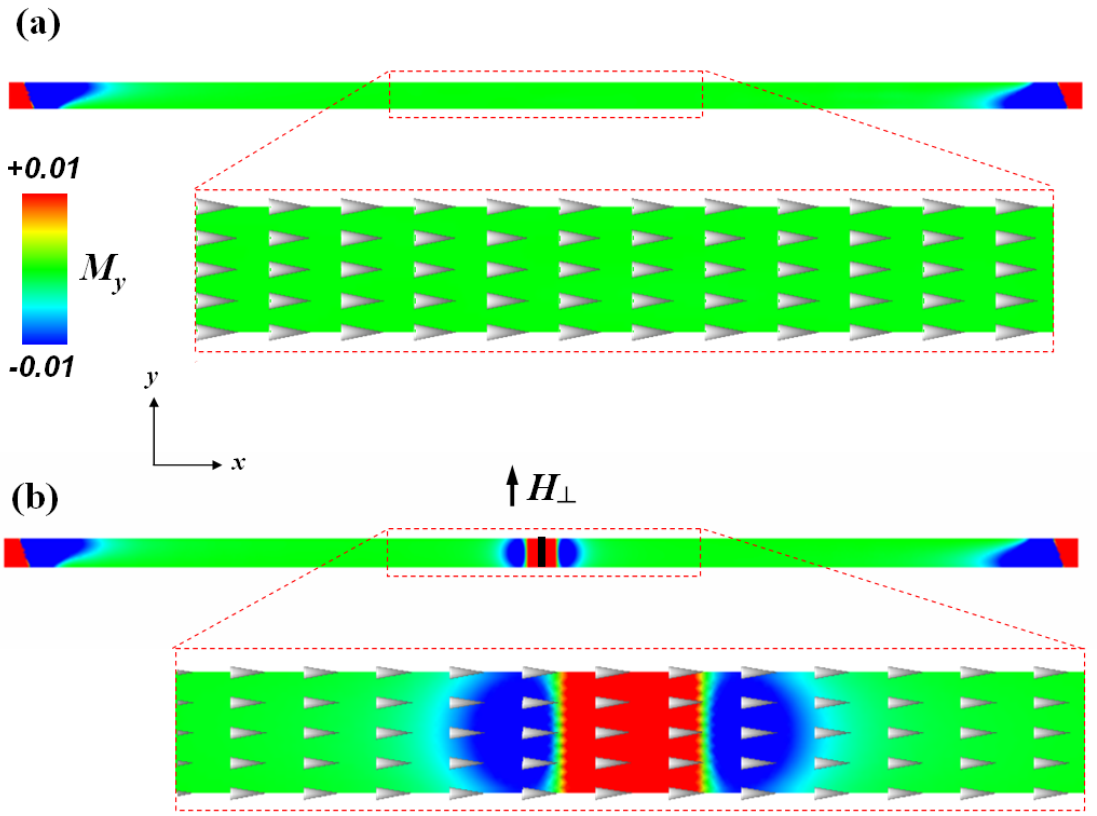

FIGURE 6.1. (a) The lowest-energy remanent magnetization configuration of a rectangular strip thin film permalloy nanowire. In most of the wire the magnetization aligns with the long axis due to shape anisotropy, so that surface charges are minimized and magnetic flux is contained internally. This minimizes the magnetostatic energy term, while the exchange term is also minimized when lattice spin moments are aligned with their nearest neighbours. At the ends of the wire exist so-called "end domains", which occur as a way of lowering the magnetostatic energy that is associated with surface charges. The end domains extend into the wire as a way of reducing the exchange term. (b) If a transverse field is applied to the middle of the wire then its influence extends outwards via exchange. Here the red region is actually around five times wider than the field region. The blue areas either side are aligned oppositely to the applied field as a consequence of the magnetostatic field from the perturbed central region.

finite time period. The external field is ramped with respect to time (the consequences of a change in ramping speed are investigated in section 6.3.3). The field is switched on after 1.0 nanoseconds and has a ramp time of 0.01 nanoseconds (10 picoseconds). The nanowire is initially magnetized along its long axis due to shape anisotropy (Figure 6.1), and the applied field is aligned transverse to this (Figure 6.2).

The system response is measured as the time-dependent transverse magnetization of the

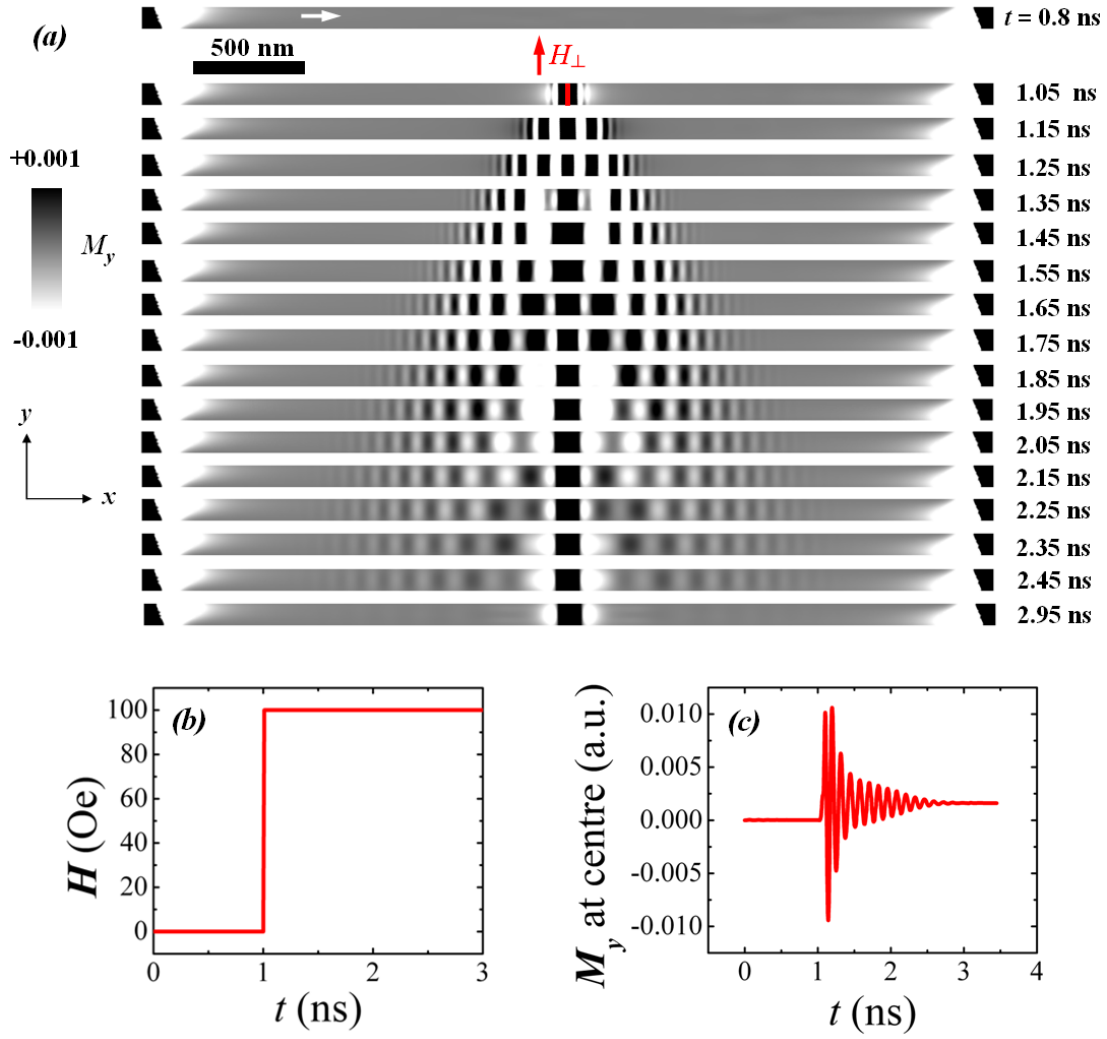

FIGURE 6.2. (a) Magnetization data showing the generation and propagation of spin waves at the centre of a 4μm long rectangular nanowire ($W = 100$ nm, $T = 10$ nm). The spin wave amplitude attenuates along the length of the wire so that the spin waves are not really large enough to be measured at all past a distance of 2500 nm from the spin wave source. After approxiately 3 ns spin waves cease to be observed and the sample reaches equilibrium. (b) Temporal profile of the magnitude of the localized applied transverse magnetic field. The applied field is switched on at 1.00 ns and ramps linearly to its final value of 100 Oe (0.01T), which is reached at 1.01 ns. The field strength is then held at a constant magnitude until the end of the siulation. (c) A probe at the centre of the wire, inside the region where the field is applied, measures the transverse component of the magnetization, M_y. The magnetization vector is perturbed only slightly and M_y peaks at just 1 %, which corresponds to a rotation angle of just 1.0°. The magnetization precesses until relaxation after around 3 ns, when M_y settles at a value of 0.0016 a.u.

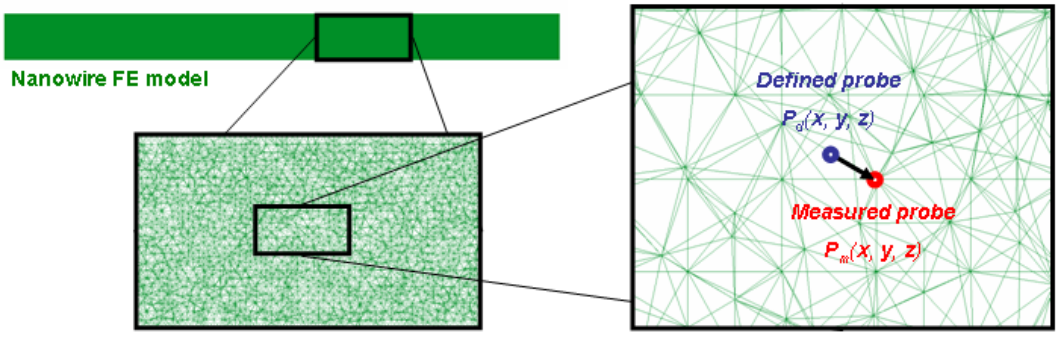

FIGURE 6.3. Method of measuring probe data for spin wave measurement. The probe position is defined arbitrarily by the user and the closest FE vertex is found geometrically. The magnetization data of this vertex is then taken as the magnetization at the defined probe position. Due to the density of the FE mesh any error introduced is minimal.

nearest FE vertex to a defined probe point some distance from the spin wave source (Figure 6.3). Because there is an element of randomness to the positions of the FE vertices (due to the meshing algorithm) it introduces an error to the probe position, which is minimized when the FE mesh density is sufficiently high. Here we use a mesh size of 5nm, which is chosen in order to properly resolve local changes in magnetization and is well below the characteristic lengths of the material (c.f. Chapter 4).

Spin waves are generated from the perturbed region at the centre of the wire and travel outwards towards each end of the wire. The perturbed region continues to precess gyroscopically after the field is ramped, and the precession itself continues to influence the rest of the sample through the exchange interaction. Thus, spin waves continue to be generated, and these naturally die out as the precession damps over time. The result is a distinct wave-packet which travels in both directions along the long axis of the wire (Figure 6.2a).

The transverse magnetization at the probe is recorded with respect to time (Figure 6.4b) and a Fourier transform of the data reveals the frequencies within the wave packet (Figure 6.4c).

6.3. Factors affecting spin wave characteristics

Being able to predict and tune the properties of our spin waves is desirable. Here we investigate the influence of a number of material and geometric parameters on SW properties.

6.3.1. Wire dimensions. We modify the physical dimensions of our standard nanowire to investigate the effects on spin wave amplitude and frequency. The nanowire width, W, is

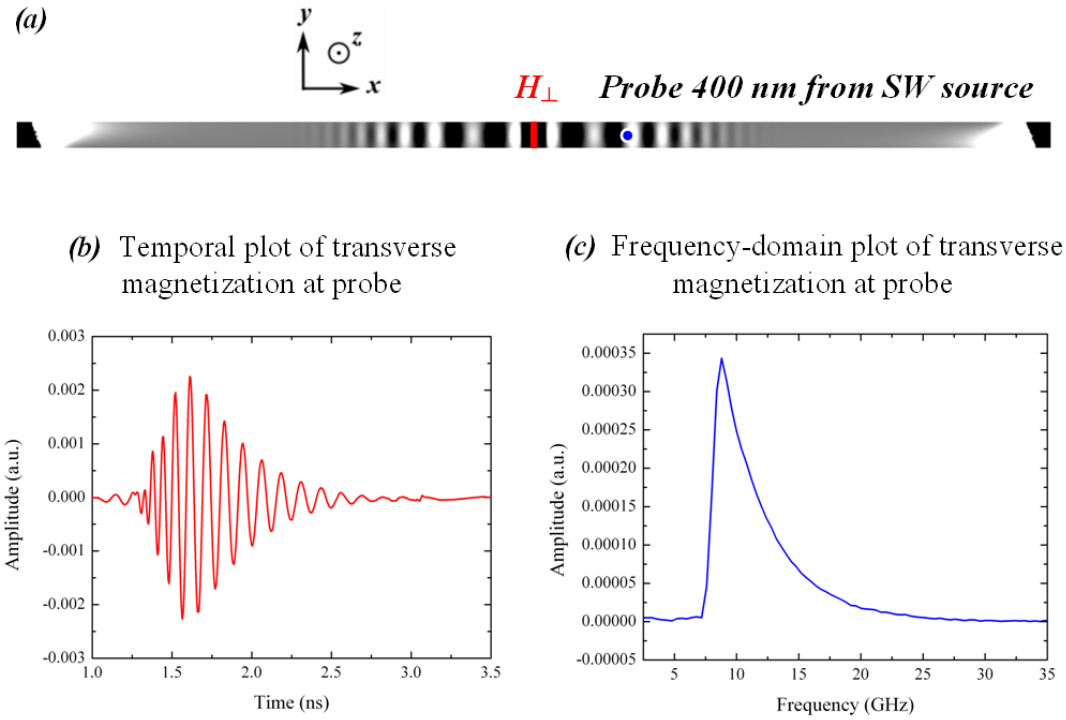

FIGURE 6.4. (a) A 100 nm wide nanowire contains a spin wave source at its centre so that spin waves propagate outwards along the length of the wire in both directions. A probe, 400 nm from the source, measures the transverse magnetization with respect to time. (b) The temporal plot of the magnetization. (c) A Fourier transform of the temporal plot gives a frequency profile of the spin waves that pass through the probe position.

altered between 60nm and 140nm while thickness, T, remains constant at 10nm (Figure 6.5a). The wire is of finite length but is long enough so that spin waves damp out well before they are able to reach the ends of the wire, thus removing the possibility of spin wave reflections. Transverse spin waves are generated in the central region by an external field of consistent geometry, amplitude and temporal profile. At a probe point 350nm away from the spin wave source the transverse in-plane magnetization is measured. The temporal data is converted to the frequency domain using a Fourier transform and presented in Figure 6.5b. We estimate the spin wave peak frequency, which corresponds to the spin wave resonant frequency of the ferromagnet in Figure 6.5c and compare with a plot derived from the analytical resonant frequency equation (3.2).

We observe that an increase in wire width, W, results in an exponential decrease in the spin wave frequency peak, f_{res}. The spin wave amplitude decreases with decreasing wire width, but this is simply because the external field is applied to a smaller area.

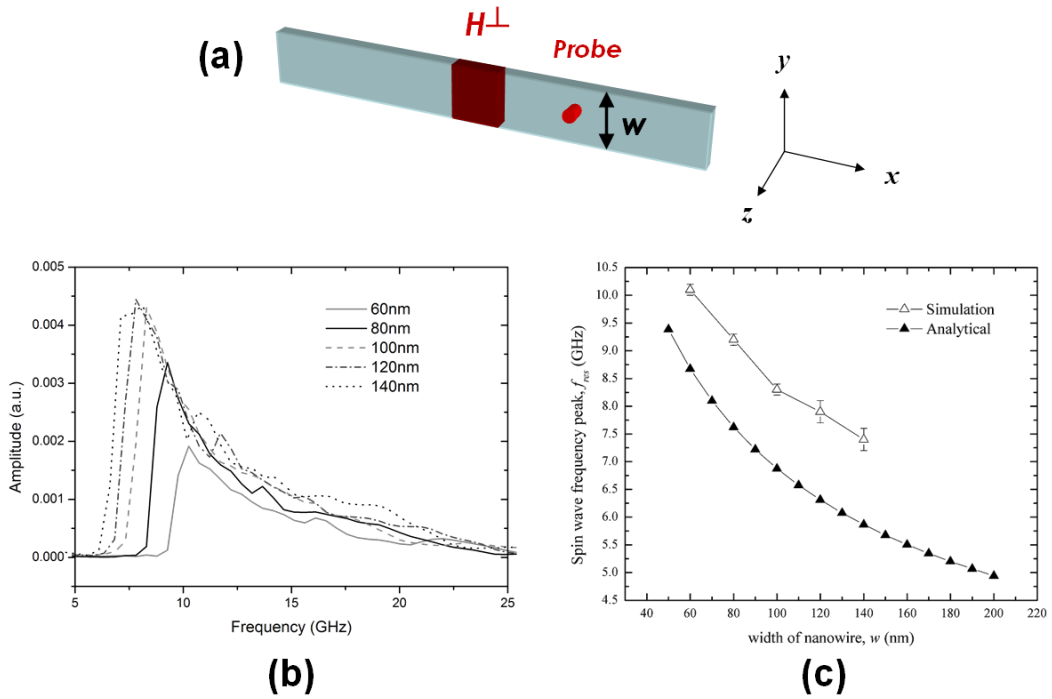

FIGURE 6.5. (a) The nanowire width, W, is varied while keeping a constant wire thickness, $T = 10$nm. (b) The result is a shift in the spin wave resonant frequency peak, f_{res}. A more narrow wire width leads to a higher spin wave frequency. (c) The variation of f_{res} with W is compared to the analytical formulation given by Kittel [**166**]. The simulation follows the same trend but the frequency is typically 1.5 GHz higher than the analytical value for a given width. The difference is due to assumptions made in the analytical solution.

The simulations agree well with the analytical solution (3.2) but over-estimate the frequency with respect to the analytical solution by around 1.5 GHz. For $f_{res} = 8.3$ GHz, whereas the analytical result gives $f_{res} = 6.8$ GHz. This difference can be attributed to a number of possible causes. The analytical solution assumes an infinitely long wire with perfectly uniform internal magnetization, whereas our FE model is of finite length and the internal magnetization is not perfectly parallal to the x axis. This difference could be particularly significant when the probe or spin wave source are positioned near the ends of the wires, where end domains locally disrupt the otherwise uniform magnetization of the wire, or near the spin wave source where the applied field perturbs the local magnetization. Additionally, the analytical solution assumes that exchange spin waves are completely dominant and disregards the effects of magnetostatic spin waves on the spin wave frequency. In the simulations magnetostatic spin waves are considered and contribute to the observed spin waves.

Wire width is clearly a very strong influence on the spin wave frequency. If nanowire spin

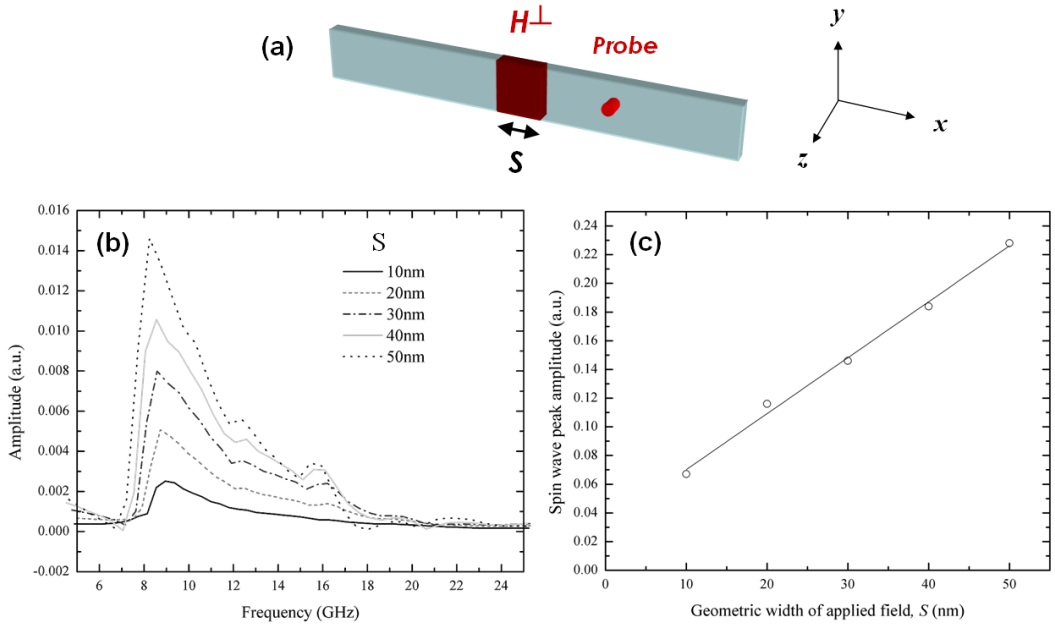

FIGURE 6.6. (a) Modifying the geometric size of the localized applied field for spin wave generation. (b) A frequency domain plot of the spin waves passing through the probe position for each value of S, the width of the applied field region. (c) The amplitude of the transverse spin waves is linearly proportional to S.

wave logic devices were to be scaled down to smaller sizes, the operational frequencies involved would increase significantly.

6.3.2. Geometry of applied field. Continuing with a localized applied magnetic field for spin wave generation we investigate the effect of changing the geometric size of the applied field by varying the length of wire over which the field is applied, S (Figure 6.6a). The wire dimensions are constant with $W = 100$nm, $T = 10$nm. Figure 6.6b shows the frequency domain plot of transverse spin wave amplitude that was obtained from the time domain spin wave amplitude data at the probe position. Increasing S increases the amplitude of the spin wave packet but does not significantly alter the frequency profile of the spin waves.

Higher harmonic modes are observed for spin waves of larger amplitude. The maximum amplitude at the spin wave frequency peak is shown against S in Figure 6.6c. The volume of the wire that experiences the applied magnetic field is $V_H = S \cdot W \cdot T$ so is linear with S. The increase in V_H means that there is increased Zeeman energy and stronger spin waves.

6.3.3. Applied field strength and rise time. We investigate the effect of field strength and field rise time on the quality of spin waves. Figure 6.7a shows the frequency domain plot

of spin wave amplitude for varying ramp speeds of the localized applied magnetic field that is used to generate the spin waves at the centre of the nanowire ($W = 100$ nm, $T = 10$ nm). The field strength is ramped linearly from 0 to 0.1 T over a time period known as the ramp time, t_{ramp}. A smaller ramp time corresponds to a faster increase in the applied field strength. For smaller t_{ramp} the spin wave amplitude increases. We explain this by referring the reader back to our earlier discussions on damped precessional motion of spins around the effective field, $\boldsymbol{H}_{eff}$ (Section (4.1.2)). If the effective field vector is modified slowly then the magnetic spins are able to stay in alignment to the field relatively easily, meaning that the Zeeman energy in the system is not drastically increased. By increasing the applied field strength quickly we modify $\boldsymbol{H}_{eff}$ at a faster rate. In this situation the damped precession of each magnetic spin moment m is relatively slow and cannot keep up with $\boldsymbol{H}_{eff}$. This increases the Zeeman energy, which is eventually dispersed as spin waves. It should be noted that if ramp speed is sufficiently slow then spin waves will be practically of zero amplitude for any applied field strength.

Figure 6.7b shows the frequency domain plot of spin wave amplitude for varying applied field maximum amplitude for constant t_{ramp}. As expected, an increased applied field strength results in larger spin waves with a sharper main resonance peak that is accompanied by a slight perceived shift in frequency. This is due to the increased field strength causing a larger disruption to the ordered magnetization inside the nanowire. Very high field strengths produce anharmonic oscillations, and strongly excite the higher order harmonics in the resonant structure, the main ones being the 2nd order harmonic that corresponds to 16.6 GHz and the 3/2 mode corresponding to 12.45 GHz (these higher harmonics are also seen for faster field ramping). Since the ramp time in these simulations is constant, the field gradient (with respect to time) is different for each field strength and the rate of increase of the field increases with increased field strength.

A strong applied field of strength $H = 0.5$ T (5000 Oe) is applied to the centre of a long wire, ramping from zero in 0.01 ns (10 ps), and the magnetization data is presented in Figure 6.8. With such a high field strength the spin waves exhibit severe distortion, with the wavefronts broken up. Although the spin waves propagate further along the nanowire length than for lower fields, the distortion limits reduce the quality of the spin waves and makes them unsuitable for magneto-logic calculations. Thus the spin wave generating applied field cannot be arbitrarily increased in strength to indefinitely increase the spin wave propagation distance.

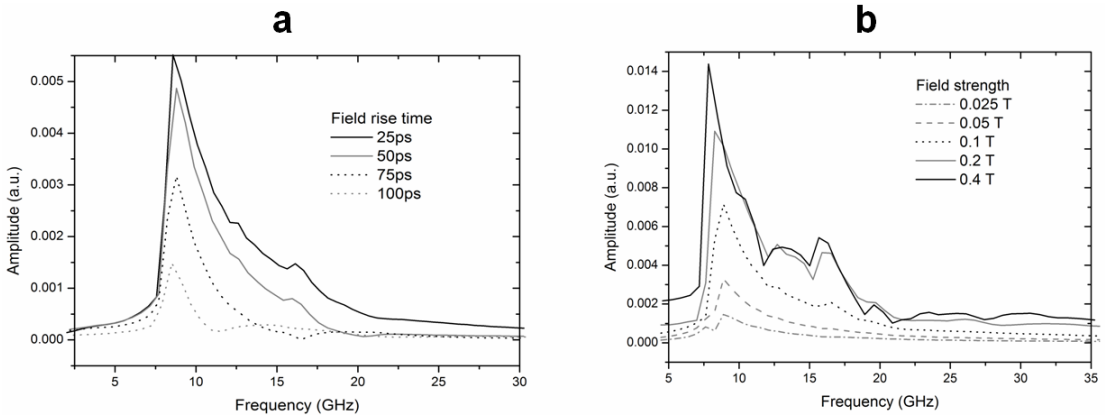

FIGURE 6.7. Frequency domain plots of spin wave amplitude (measured by a probe) for (a) varying ramp ("rise") time of the applied field and (b) varied maximum field strength. Increases in field ramp speed or field strength result in larger spin wave amplitudes as well as significant excitation of higher harmonic resonance modes.

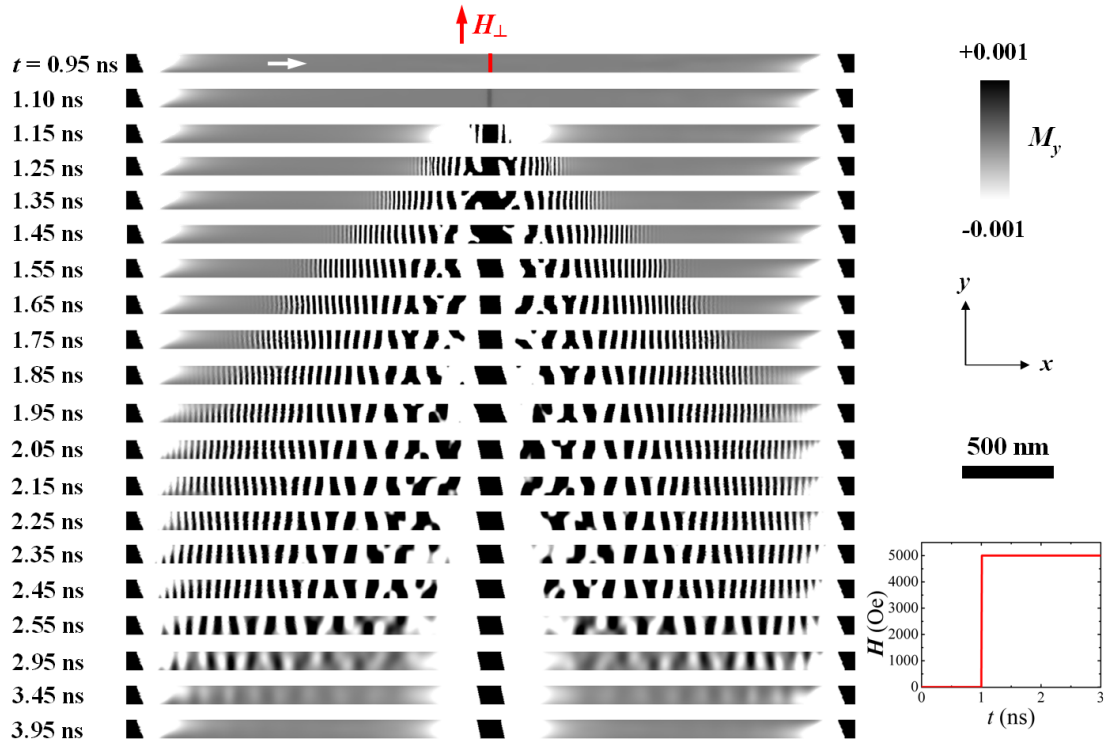

FIGURE 6.8. Spin waves generated using a very high field strength of 5000 Oe. The spin waves are of high amplitude but show large amounts of distortion, especially close to the source.

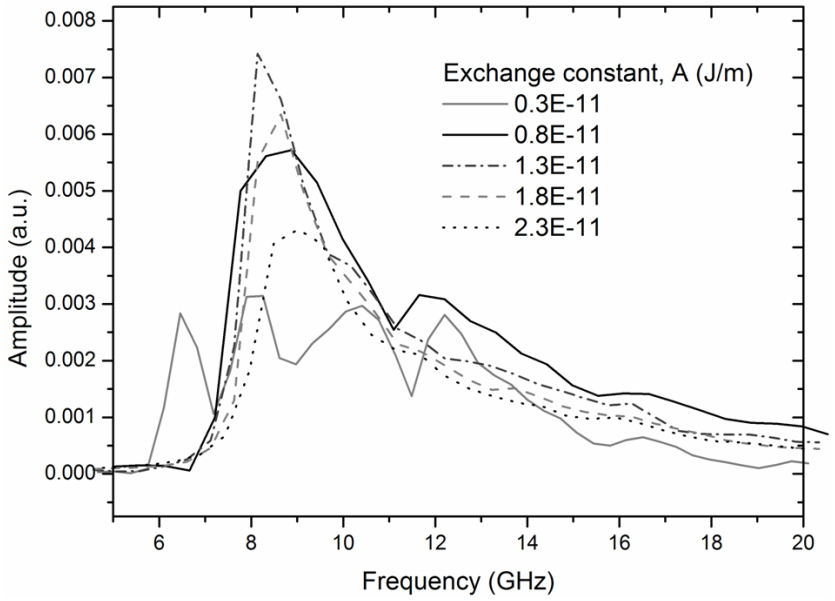

FIGURE 6.9. A spin wave amplitude plot in the frequency domain for permalloy nanowires where the exchange constant, A, has been modified from the standard value of J/m. Smaller values of A lead to spin wave packets with reduced coherence and no single frequency peak. Larger values of A result in reduced spin wave amplitudes as the spin wave energy disperses over a larger range of spin-spin exchange interactions. No significant shift in the main frequency mode is observed.

6.3.4. Exchange parameter. The exchange constant, A, is important for spin wave propagation since it determines the strength of coupling between nearest-neighbour spins (4.9). Spin waves are generated from the centre of a wire with $W = 100$ nm and $T = 10$ nm. The exchange constant, A, is modified in the range between 0.3×10^{-11} and 2.3×10^{-11} J/m (we earlier chose a standard value of $A = 1.3 \times 10^{-11}$ J/m). All other parameters are held constant.

The frequency-domain SW amplitudes measured at a probe position 350nm from the SW source are given in Figure 6.9.

Two behavioural changes are observed as A is modified. An exchange constant much lower than the standard value leads to a breaking up of the main single frequency peak, suggesting that a strong exchange interaction between neighbouring lattice spins is essential for the generation of coherent spin wave packets. This obviously agrees well with existing spin wave theory, which claims exchange as the dominant spin wave propagation mechanism in the nanoscale regime [**95**]. An exchange constant that is higher than the standard value leads to a lower spin wave amplitude. This is due to stronger spin-spin coupling resulting in a stiffer system where the energy of the oscillations is shared over a larger number of spins, dispersing over a larger volume

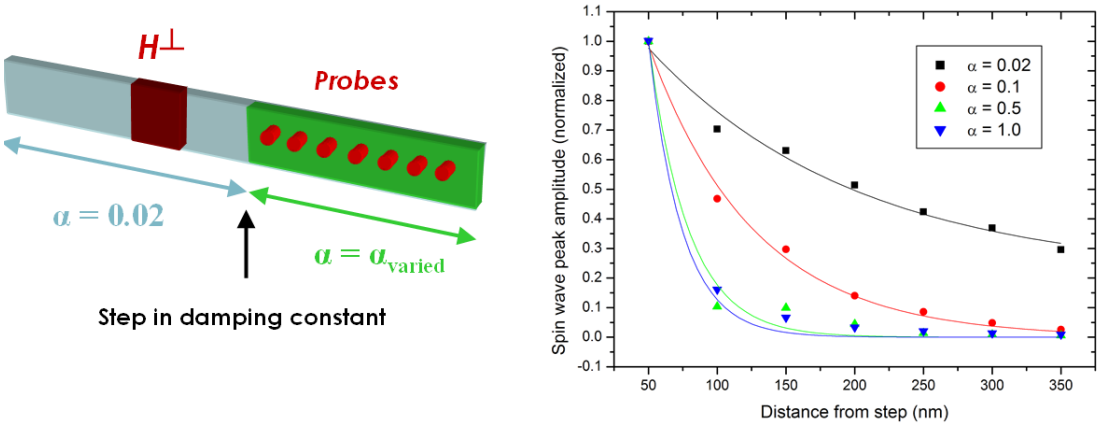

FIGURE 6.10. Attenuation of spin wave amplitude along the length of a nanowire with a damping constant step function. The data points give the maximum amplitude of spin waves passing through the probe point, at various probe distances along the wire, normalized to the value at the first probe position. Exponential decay is evident in all cases, with attenuation occurring much faster for high values of damping (exponential line fits displayed).

and leading to reduced spin wave amplitudes. Altering A does not lead to any significant shift in the main spin wave resonant frequency for the ferromagnetic nanostructure.

6.3.5. Damping constant. We now investigate the effects of modifying the Gilbert damping parameter on spin wave propagation. The attenuation of spin waves through materials of varied damping constant is measured by taking the maximum spin wave peak amplitude as it passes through a number of probe points at defined positions along the length of a nanowire. A series of wires with $W = 100$ nm and $T = 10$ nm have consistent material parameters apart from Gilbert damping constant, α, which is set to a different value in each wire.

For each wire the spin waves are generated in a region of the wire with standard damping constant $\alpha = 0.02$ and then pass through into the region with modified damping constant (we use α =0.02, 0.1, 0.5, 1.0). The probes then measure the spin wave amplitude at intervals in length after the step. By measuring the maximum magnetization deviation, which corresponds to the maximum peak amplitude of the spin wavepacket, at each probe point we can plot the spin wave amplitude as a function of distance from the spin wave source (Figure 6.10).

The spin wave amplitude attenuates with length of the wire, with faster rates of attenuation for higher damping constant. Although we expect some of the spin waves to be reflected before they pass through the damping step, it is clear that increasing the damping constant in a wire will inhibit the propagation of spin waves through it.

The line fits follow the general exponential decay formula $y = Ae^{-x/d} + y_0$ where A is the normalized initial amplitude, d is the decay constant in nm and y_0 is the y intercept. When changing α from 0.02 to 0.1 d changes from 152 nm to 71 nm. For $\alpha = 0.5$ $d = 26$ nm and for $\alpha = 1.0$ $d = 20$ nm.

6.3.6. Spin wave velocity. Spin wave velocity, $\boldsymbol{v}_{SW}$, is estimated by measuring the difference between the spin wave packet arrival times at two probe points, which are positioned a known distance apart along the length of a nanowire ($W = 100$ nm, $T = 10$ nm). This is represented in (6.18) where $\boldsymbol{r}_{12}$ is the displacement vector between the two probes, and t_{p1} and t_{p2} are the spin wave arrival times at probe 1 and probe 2, respectively (Figure 6.11). Probe 1 is closer to the spin wave source than probe 2, by definition.

$$\boldsymbol{v}_{sw} = \frac{\boldsymbol{r}_{12}}{t_{p2} - t_{p1}} \tag{6.18}$$

By taking the arrival time of the wave packet we ensure that we are actually measuring the group velocity and not the phase velocity. In a wire with measurements of $W = 100$ nm and $T = 10$ nm two probes are positioned at 300 nm and 700 nm away from the spin wave source, with a separation of 400 nm (Figure 6.11). By reviewing the transverse magnetization at each probe the spin wave group velocity is measured as approximately 816 m/s (equivalent to 1 μm/ns) . Due to dispersion it is not possible to measure the phase velocity accurately.

6.4. Spin wave reflections

6.4.1. Spin wave reflections at internal interfaces. We start to investigate spin wave reflections by determining how a step in material parameters can affect spin wave propagation. Specifically we are interested whether spin wave reflections occur at the interfaces between two regions in a nanowire that have different damping constant. In order to investigate spin wave reflections at internal interfaces in a wire we use three nanowires that are each split into two regions (Figure 6.12a-c). The first region has a standard value of $\alpha = 0.02$ and the second region of the wires have the values of α modified to 0.02, 0.1 and 1.0, respectively. We expect no reflections at the interface in the first wire, as there is no change in α, but for the other two we expect reflections at the α discontinuities. The wires have length 6000 nm, so that any reflections from the ends of the wires can be safely disregarded. For comparison, we also

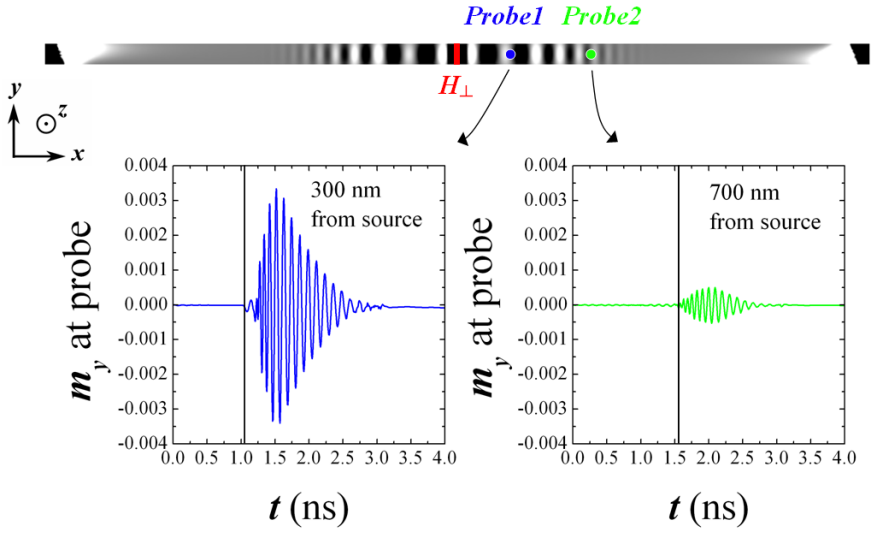

FIGURE 6.11. Calculation of spin wave velocity from simulation of a permalloy nanowire. The spin wave arrival time at Probe1 is 1.05 ns and at Probe2 is 1.54 ns. The distance between the two probes is 400 nm. From this we calculate the spin wave velocity as approximately 816 m/s.

introduce a shorter wire, which has its physical end at the positions where the other wires have the α discontinuity (Figure 6.12d).

A probe is positioned between the spin wave source and the interface to look for any differences in the spin waves that might be caused by interference from spin wave reflections at each respective interface.

In a spin wavepacket with no interference a time domain plot of the transverse probe magnetization exhibits a smooth envelope which decays after peaking as the spin waves damp out. In the frequency domain plot we see a single frequency peak and a smooth distribution around that peak. If reflections are present they will be evident in the temporal plot as a secondary wavepacket, occurring after the main packet and causing interference with the incident waves, and in the frequency plot as additional frequency peaks or even the destruction of the main frequency mode.

The results suggest that reflections can occur from abrupt discontinuities in damping constant value. The Fourier transforms of the transverse magnetization, $M_y(t)$, at the probe point are given in Figure 6.13. Reflections from the large damping step show a split in the frequency peak, which is similar to the case of the short wire where we can see interference from reflections at the physical end of the wire, albeit more prominently. The smaller damping step example shows a frequency profile that is similar to that of the long wire without a damping discontinuity,

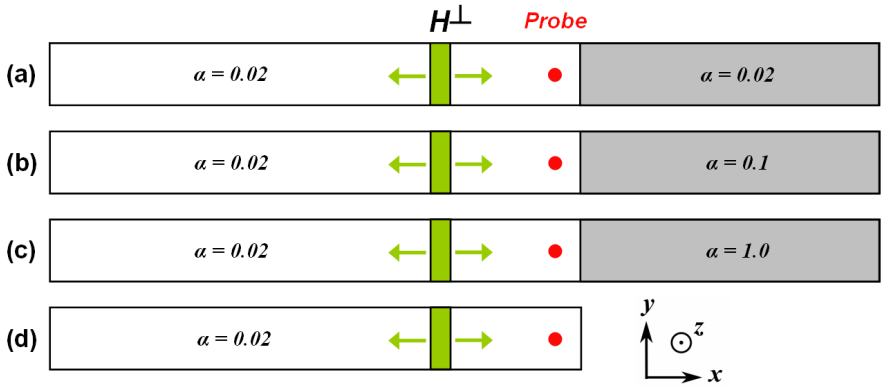

FIGURE 6.12. A test to measure spin wave reflections from an interface between two regions of a permalloy nanowire (not to scale) with different Gilbert damping constants. In (a) there is no change in α and we use this setup for reference, as we expect no measurable reflections. In (b) we introduce a moderate step size in α and in (c) there is a large step size. Setup (d) is used as a reference, where instead of an internal boundary we include a hard geometric boundary by shortening the wire. Here we expect to see very strong spin wave reflections.

where we see no reflections. We conclude that the damping constant discontinuities do produce reflections of incoming spin waves, but that these are smaller than reflections from structural surfaces and can be reduced by using small step sizes, perhaps introducing a series of small steps to increase damping constant sufficiently instead of one large step boundary conditions.

6.4.2. Suppressing spin wave reflections at nanowire ends. To test for the suppression of spin wave reflections by altering damping constant, a nanowire of length 800nm (W =100 nm, T = 10 nm) is augmented with two-step boundary conditions at either end. Each boundary augmentation consists of two 50nm wide regions, where the damping constant is increased in two steps ($\alpha = 0.1$ and $\alpha = 0.5$) to avoid reflections from the boundary that could occur at one larger step. The spin waves are generated at the centre of the wire. The probe point is a distance of 180 nm from the spin wave source.

We analyze the transverse magnetization $M_y(t)$ at the probe point in the time domain and also in the frequency domain using a Fourier transform operation. These are compared to the cases of a short wire with length 800nm and a long wire of total length 4000nm (Figure 6.14). In the short wire the end of the wire should be sufficiently close to the probe to allow large spin wave reflections, whereas in the long wire the distance is so large that spin waves should dissipate away without causing noticeable interference from reflections.

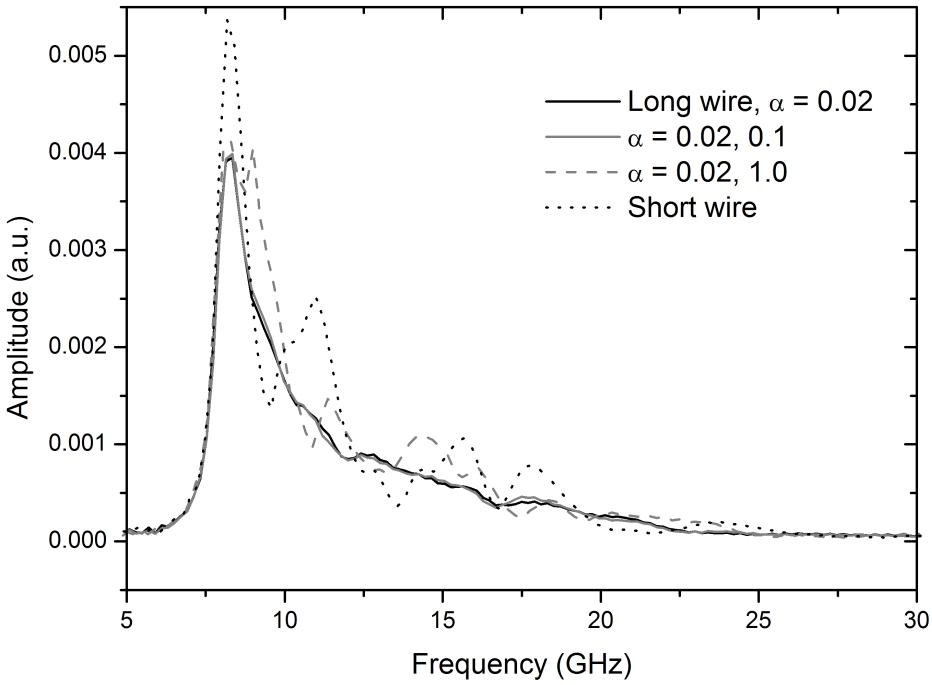

FIGURE 6.13. Test for reflections at boundaries between regions of different damping constant, α. Transverse magnetization at the probe point is compared for a long nanowire with no reflections, a short wire with large reflections and two cases where α is increased as a step function with length. For the larger step in damping constant, interference from reflections are significant, whereas for a smaller step size the interference is highly reduced.

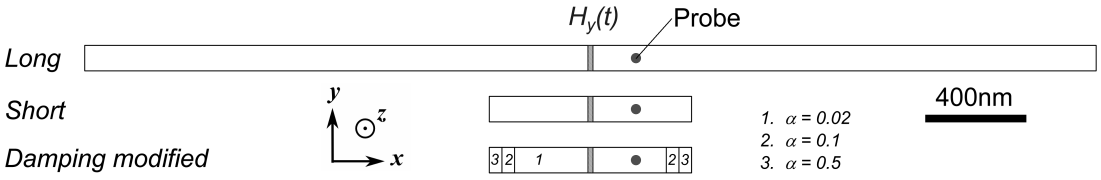

FIGURE 6.14. Schematic of the test for absorbing boundary conditions. The damping modified wire has end regions with increased damping constant, α. Spin waves are generated from the centre of the wires, where the magnetization is perturbed locally by an applied field, $H_y(t)$, that is in-plane but perpendicular to the long axis of the 10nm thick permalloy wires. A probe point is placed 220nm from the end of the short and modified wires and 1820nm from the end of the long wire. The probe measures the local transverse magnetization.

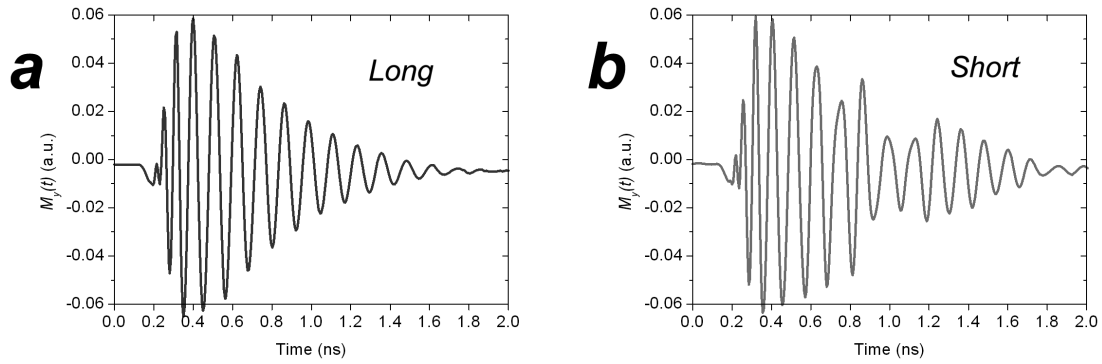

FIGURE 6.15. Probe magnetization over time for the long and short wires. The long wire has no interference from reflected waves, and hence a smooth envelope, while the short wire has interference from reflections causing multiple peaks in the envelope function.

The tests for reducing spin wave reflections from the ends of nanowires suggest that boundary conditions with modified damping constant can be successfully used. Figure 6.15 shows probe magnetization over time for the long and short wires. The distance between the probe and the end of the wire is 220 nm for the short wire and 1820 nm for the long wire.

The temporal plot for the long wire displays a simple amplitude envelope and the spin waves attenuate smoothly with only one wavepacket observed, whereas the short wire displays a more complicated envelope, with extra spin waves distorting the smooth envelope after 0.8 ns. It is possible to deduce that these extra features are reflected spin waves, moving back along the nanowire from its end and passing over the probe for a second time. There are no such reflections observed for the long wire because the spin waves undergo significant attenuation due to damping during the round trip between the probe point and wire end.

Figure 6.16 shows Fourier frequency spectra for the long and short wires as well as the wire that has been augmented with boundary conditions of altered damping constant. Interference from reflected spin waves can be seen as a break-up of the single frequency peak. The long wire shows a smooth peak, indicating no interference, and no reflected waves, while the short wire shows multiple peaks due to interference. The augmented wire, with modified damping constant sections, shows one clear, smooth peak with no significant interference, indicating that waves are not being reflected from the ends of the wire.

Tests on wires with only one single damping step in the absorbing end conditions showed that, for these wire dimensions, reflections were either too large for a large step or the increase in damping was insufficient to stop all reflections from the wire end. However, for other applications

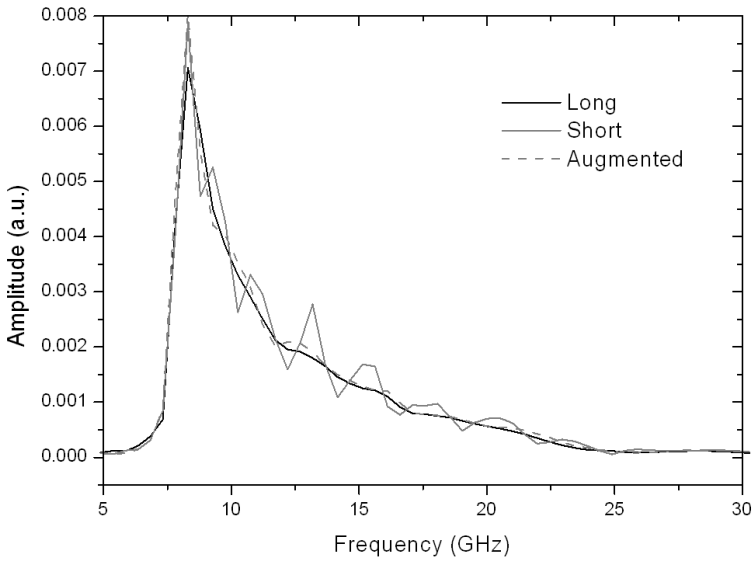

FIGURE 6.16. Comparison of probe point magnetization frequency spectra for the long, short and α-augmented nanowires. The augmented wire behaves very similarly to the long wire, with a single narrow frequency peak. This indicates that interference from reflections is drastically reduced.

a single step in damping constant may be sufficient.

6.4.3. Spin wave reflections at boundaries of disc shaped thin films. The suppression of the reflection of waves at the boundaries of disc shaped samples by absorbing boundary conditions is a commonly encountered example, for instance in finite element analysis textbooks [**167**]. Therefore we also model two-dimensional spin waves in 10 nm thick permalloy disc structures, with the spin waves generated from a 400 nm^2 spin wave source at the centre of the disc. Within this region the magnetization is moved out of plane using a highly focused out-of-plane field with strength 1000 T. This field strength is unachievable in reality but is valid for modelling purposes to generate suitably large spin waves. Here the probe measures the out-of-plane magnetization at a position 150 nm from the centre of the spin wave source. In order to avoid vortex formation an in plane field of 1 T is applied.

A disc with 200 nm radius has two concentric outer rings with increasing damping constant of 0.1 and 0.5, and respective radii of 250 nm and 300 nm. These rings act as absorbing boundary conditions to the spin waves. We compare this modified disc to a small disc and a large disc, both with no absorbing boundary conditions. We anticipate that the small disc should experience

interference at the probe point since the probe is close to the edge of the disc, whereas in the large disc spin waves should be able to dissipate away through damping. The increase in the number of volume elements in a disc scales with the square of the radius. Our large disc has a radius ten times larger than the small disc and so (if a constant mesh size is used) according to the standard equation for the volume of a cylinder contains 100 times as many volume elements. Calculation time, t, is approximated by $t \sim q \log q$ where q is the number of tetrahedral finite elements. The calculation time for the large disc is more than 100 times that of the small disc. In the disc structure two-dimensional spin waves are generated in the perturbed region at the centre and travel outwards towards the edge.

Figure 6.17 gives a Fourier plot of the out-of-plane magnetization at the probe point for the large, small and augmented discs. The large disc has a single dominant frequency peak, indicating that there is no interference from reflected spin waves whereas the small disc shows multiple peaks, indicating interference from reflections. The frequency spectrum for the disc with modified damping constant boundaries shows a peak similar to the large disc, suggesting that the boundary conditions are going some way to replicating the large disc behaviour, absorbing the spin waves so that they cannot reflect back from the edge of the disc. The increase in spin wave amplitude for the small disc might be a consequence of weaker shape anisotropy, so that magnetization can be more easily perturbed out-of-plane.

6.4.4. Suppression of spin waves by shape modifications. We perform a series of simulations on wires of length 800 nm where the ends have been modified geometrically (Figure 6.18b). A frequency-domain plot of the spin waves at a probe 200 nm from the spin wave source is given in Figure 6.18a. For comparison, we include data for a long wire, where reflections do not occur, and a short wire, where reflections are significant and interference is strongly evident in the frequency profile. None of the modified nanowires significantly reduce the levels of interference from spin wave reflections. However, the wire labelled "pro1" shows perhaps the most severe interference.

6.5. Spin waves and finite element mesh size

Spin wave propagation through a ferromagnet is affected by the material parameters. In finite element modelling we can also consider the effects of changing our model parameters, particularly the mesh size and mesh size boundaries. In large problems it is often necessary to

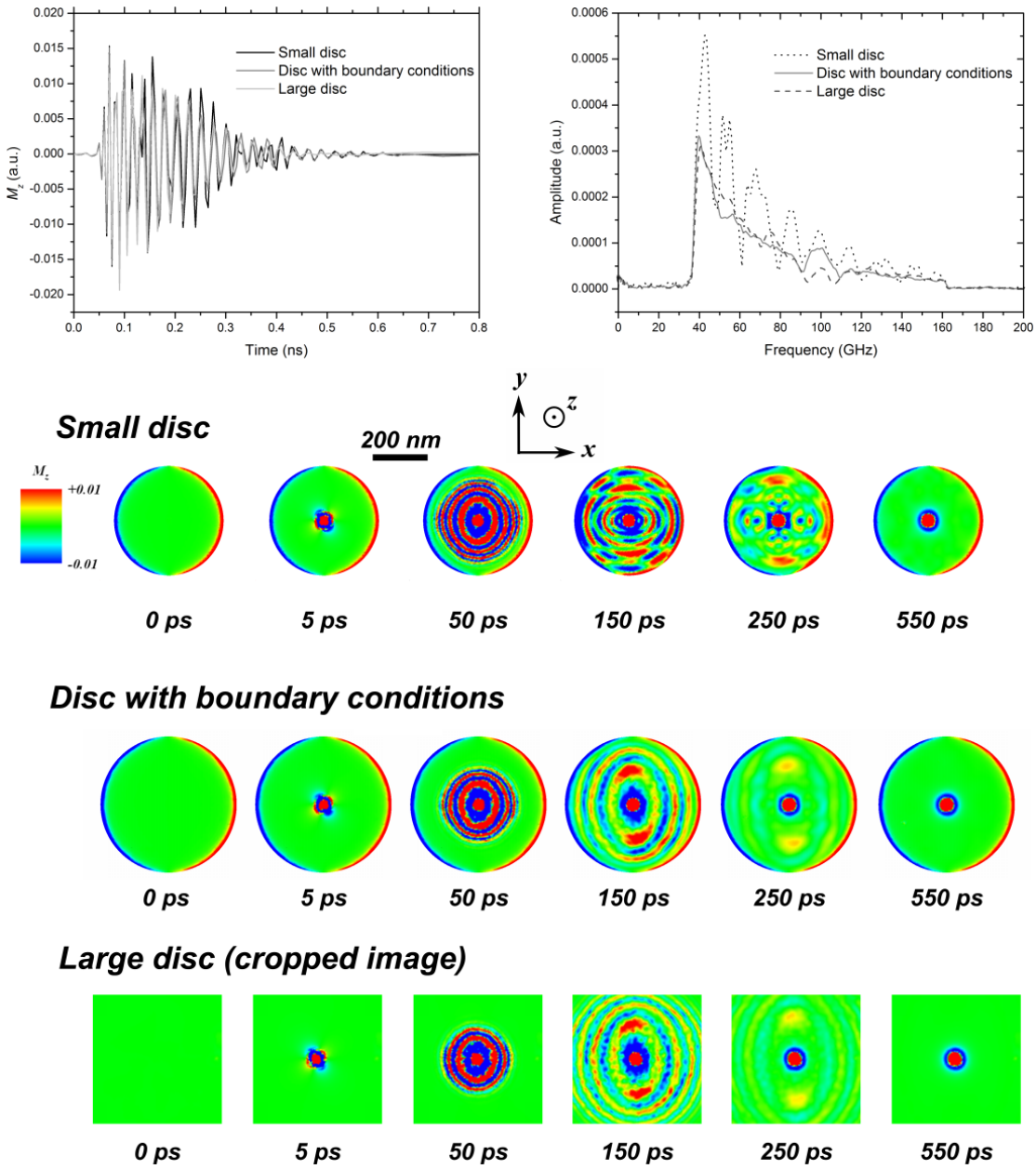

FIGURE 6.17. Frequency spectra from the disc experiment. Spin waves are generated from the perturbed region at the centre of the disc and travel out to the edge of the disc in two dimensions. The small disc shows evidence of large interference between incoming waves and waves being reflected from the edge of the disc, occurring after 80 ps. The large disc shows no such interference as the edge of the disc is too far for noticeable reflections. The α-augmented disc behaves very much like the large disc with no reflections, and very unlike the small disc with reflections, indicating that the boundary conditions are successfully damping the spin waves.

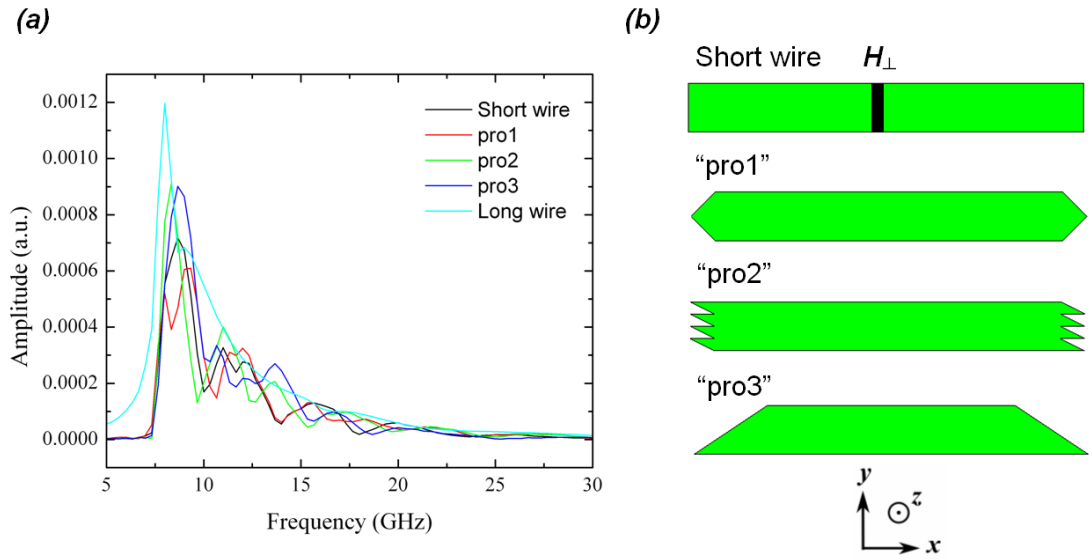

FIGURE 6.18. Investigation into the effects of edge shape modifications on spin wave reflection in nanowires. (a) Frequency-domain plots of the spin waves at a probe (200 nm from the spin wave source) show that the end modifications are not very successful in reducing interference from reflections. (b) Schematics of the wires in question.

reduce FE mesh density in order to lower the computational requirements. It is usually assumed that the mesh size needs to be smaller than the characteristic lengths of the system **[168]**, which in permalloy is around 17.9 nm (This is discussed in greater detail in Chapter 4). In our spin wave simulations we have mostly used a mesh size of 5 nm, which is well below the 17.9 nm limit.

We perform a series of simulations each for a single nanowire containing a step in mesh size at an internal boundary (Figure 6.19a). A probe positioned between the spin wave source and the mesh size step measures the transverse magnetization, which is given in Figure 6.19b along with the frequency-domain plot in Figure 6.19c. The spin waves are generated and initially propagate through a region with a mesh size of 5 nm. We observe a change in the frequency-domain plots for mesh sizes in the step region of over 20 nm. For 20 nm and 50 nm mesh sizes the envelope displays oscillatory ripples and an increase in amplitude. In this case the probe is a significant distance (400 nm) from the mesh size step and so any effect will be limited since reflected spin waves attenuate exponentially with the length of the wire through which they propagate.

A similar test is designed where two probes are used; one just 50 nm in front of a region of modified mesh size and one 50 nm after it (Figure 6.20). The mesh sizes of the modified region

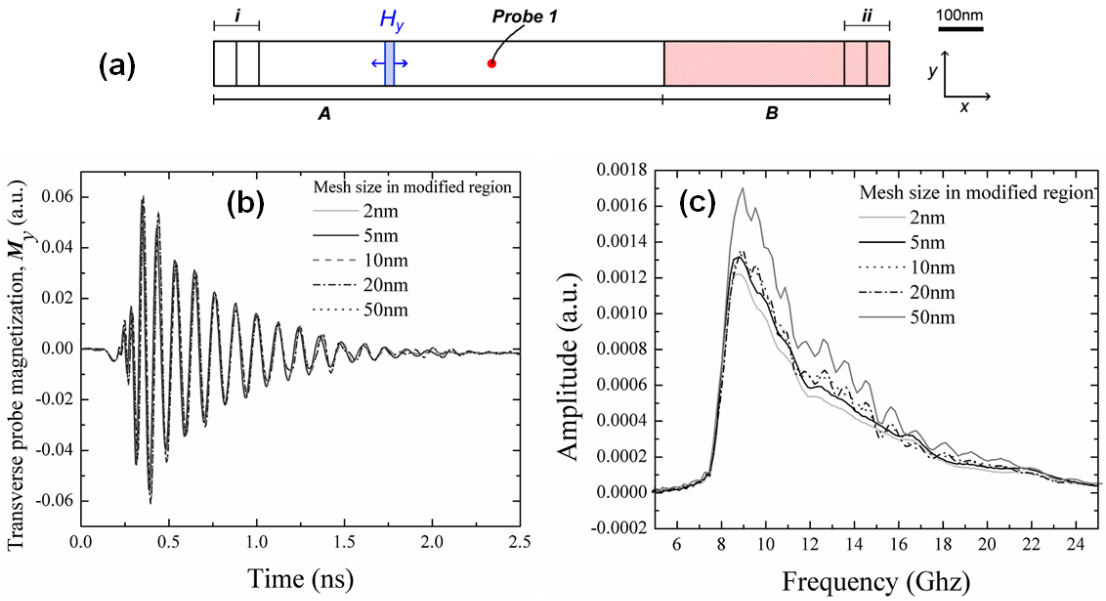

FIGURE 6.19. A probe between the spin wave source and a region of modified mesh size measures increased spin wave amplitude for large mesh sizes, indicating the presence of spin wave reflections from the mesh size step. In this case the interference from the reflected waves is minimal due to the large distances involved.

are chosen as 1 nm, 5 nm (for reference), 20 nm and 50 nm. Now the results are clearer. The first probe measures large interference for mesh sizes of 20 nm and 50 nm, which we put down to spin wave reflections from the mesh size step. Additionally, the second probe sees a huge decrease in the amplitudes of arriving spin waves, which have to propagate through the modified region, for 20 nm and 50 nm mesh size. Decreasing the mesh size in the modified region to 1 nm does not seem to greatly affect the spin wave reflection and transmission, only serving to increase the FE model size and computational costs with it.

6.6. Summary

We have investigated a number of factors affecting spin wave behaviour. Wire geometry has been determined as the most significant influence on spin wave frequency, while the exchange constant, A, strongly affects the coherence of spin waves in nanowires.

We have successfully demonstrated simple methods for reducing spin wave reflections in micromagnetic simulations, while keeping model size to a minimum along with calculation costs. These results have implications for micromagnetics as a whole, but particularly in the emerging field of spin wave electronics, where modelling of spin waves is crucial to device design, and

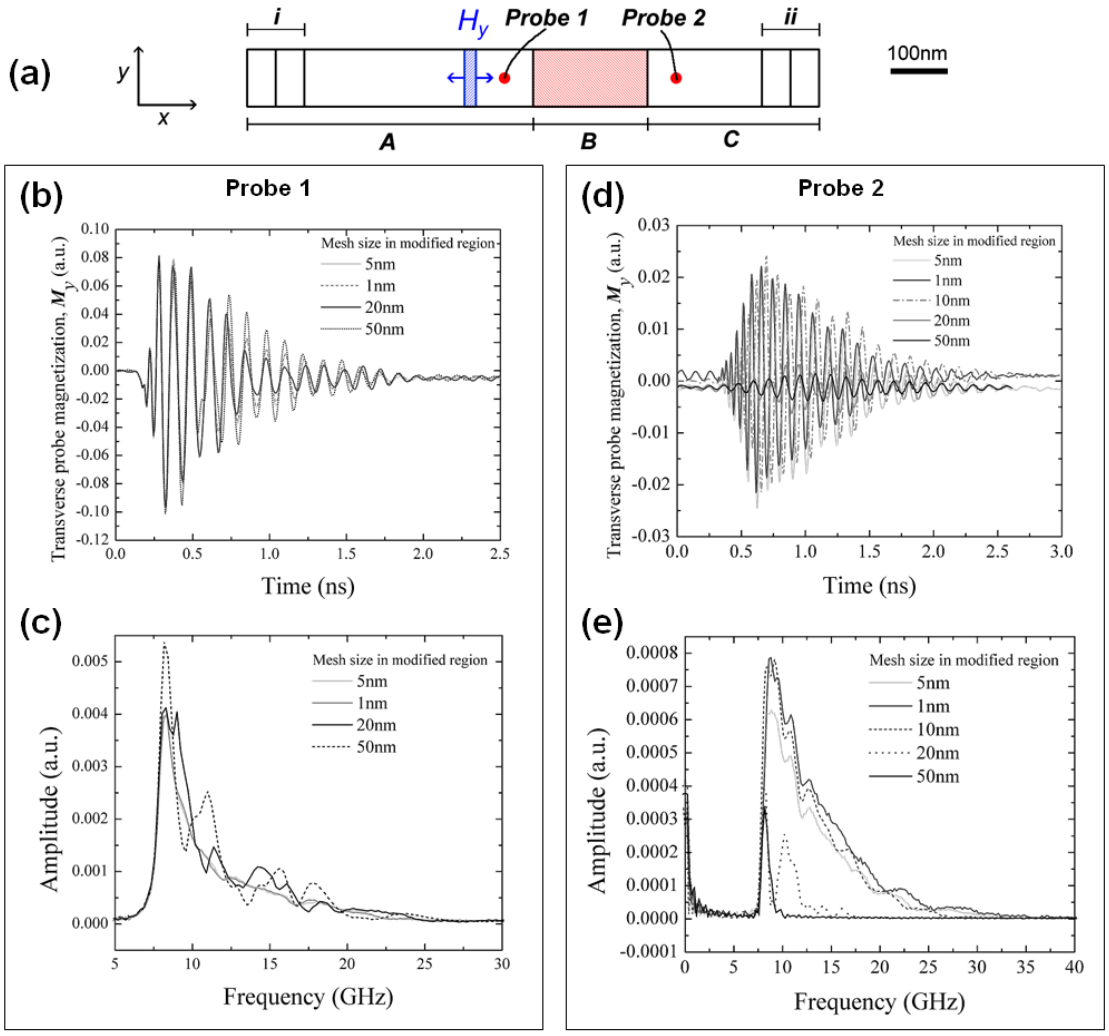

FIGURE 6.20. Test to measure spin wave reflection from and transmission through a region of modified mesh size. Mesh sizes in the modified region of 20 nm and 50 nm severely inhibit the ability of the spin waves to propagate through. Large spin wave reflections are seen at probe 1, and drastically reduced spin wave amplitudes at probe 2. For a mesh size of 1 nm, lower than the standard 5 nm size, spin wave behaviour is largely unaffected.

where spin wave behaviour inside small magnet structures must be better understood in order that they can be controlled. We are also able to exclude reflected spin waves from small-scale simulations to be able to extrapolate modelled behaviour to experiments with larger devices.

Geometric modifications were made to the ends of a series of nanowires, but did not significantly reduce spin wave reflections.

Changes in finite element mesh size have been used to confirm that the mesh size must be lower than the Bloch wall length $\delta_{Bloch} = 17.9$ for spin wave propagation.

CHAPTER 7

Spin waves in imperfect nanowires

Spin wave propagation in magneto-logic devices will depend on the properties of the transport medium. In the previous chapter we demonstrated that spin waves are affected by material parameters, but other physical and structural factors are likely to be important. In nanowire waveguides edge roughness and the presence of defects may inhibit the predictable, consistent and coherent propagation of spin waves. Edge roughness features may be tiny in relation to large devices, but in nanowires, where feature sizes can typically be 100 nm or less, they can have much bigger consequences. In this chapter we use finite element micromagnetics to investigate the effects of different types of defects and edge roughness on the propagation of spin waves in permalloy rectangular strip nanowires. We also test how spin waves can traverse bends in a nanowire, an important element in a nanowire-based spin wave logic device.

7.1. Introduction

7.1.1. Quality of real nanowires. In our finite element modelling we are able to simulate nanowires of arbitrary quality in terms of edge smoothness and the presence of defects. Experimentally, ferromagnetic thin-film nanowires of permalloy may be produced using a number of methods including focussed ion beam (FIB) milling, electron beam lithography (EBL) (with thermal evaporation) with lift-off **[49]**. The features of a nanowire are close to the limits of spatial refinement in these current techniques, and so it is difficult to create wires with perfectly smooth edges. It has previously been found from simulation that roughness introduces a spread in the switching field for a variety of magnetic nano-elements **[78, 169, 170]**. The effect of wire roughness on spin wave propagation has been far less frequently considered.

Bryan and co-workers **[171, 172]** have investigated the influence of edge roughness on magnetization switching in permalloy nanostructures (Figure 7.1). They were able to control the levels of roughness by modifying the exposure conditions of individual structures, which were fabricated using EBL followed by thermal evaporation and lift-off in acetone. In particular, the electron beam dose is reduced to produce rougher wires.

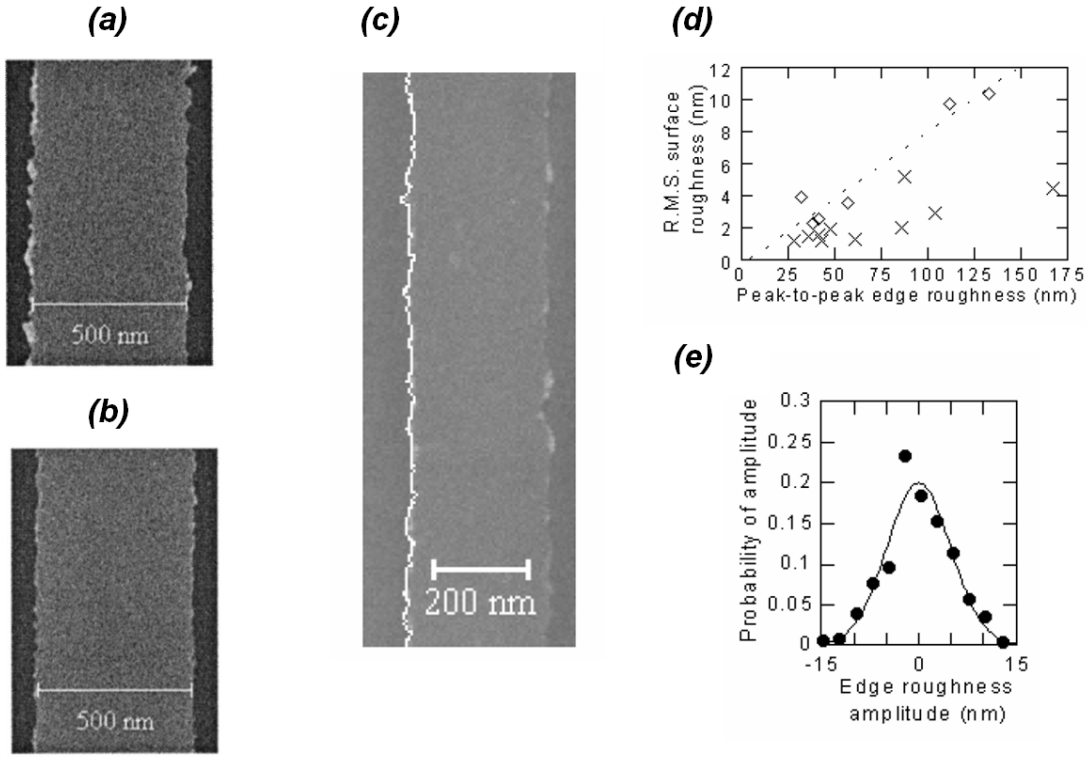

FIGURE 7.1. Bryan and co-workers [**172, 171**] fabricate permalloy wires while varying electron beam dose to produce varying levels of edge roughness. (a) A lower dose leads to higher roughness while (b) a higher dose leads to lower roughness. (c) An image of a rough wire is taken using a scanning electron microscope (SEM) and post-processed in order to trace the edge profile. (d) The trace allows measurement of the r.m.s. surface roughness and (e) the probability of roughness feature size (data for two different samples is given in each plot). (Image composite taken from [**172, 171**]).

A TEM image of a DWT cell produced by Brownlie and co-workers [**49**] exhibits edge roughness (Figure 7.2). We later use the edge profile of this image to represent realistic roughness in one of our finite element models.

7.2. Notches

One idealized model of edge roughness in nanowires is periodic, triangular roughness that is made up of a series of notches along the wire edge. Before we look at roughness we can investigate edge notches and their effect on the magnetization configuration inside the wire as well as the propagation of spin waves that encounter the notches while passing through the wire. A notch can be considered as a specific kind of physical, structural defect.

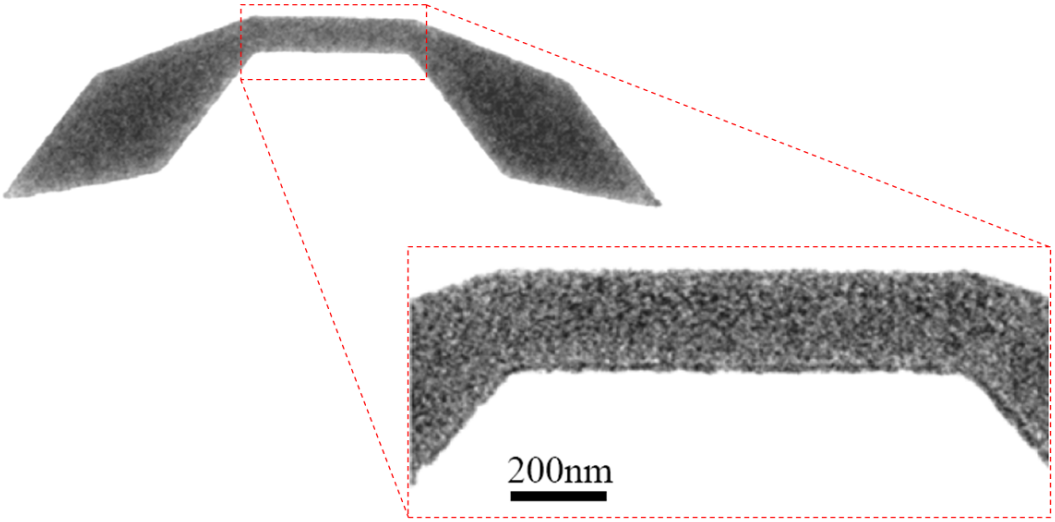

FIGURE 7.2. Example of a bright field TEM image showing edge roughness of a 200 nm wide permalloy wire (Image: Adapted from [**49**]).

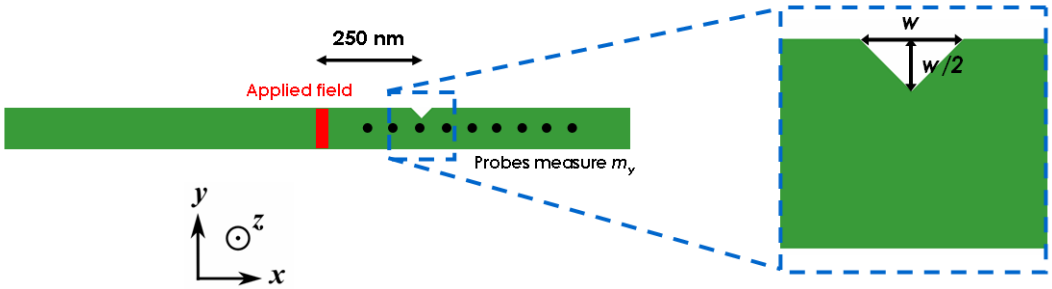

FIGURE 7.3. Test to assess the influence of a single notch of varying measurement on the propagation of spin waves through a permalloy nanowire.

7.2.1. Introducing a single notch. We apply an external magnetic field over a localized section of a permalloy rectangular wire ($W = 100$nm, $T = 10$nm) to generate spin waves which propagate along the length of the wire. The applied field vector is oriented perpendicular to the magnetization of the wire and perturbs the magnetization locally. We detect the subsequent spin waves using a series of probes that are positioned at periodic intervals of length from the spin wave source and locally measure the perpendicular magnetization.

We introduce a triangular notch with 45° angled sides and a height of half its width, which is positioned at 250 nm from the applied field, as shown in Figure 7.3. We repeat this test with notches of different size and also with no notch for referential comparison. The probe data can be compared to determine the influence of a single notch of varying size on the behaviours of the spin waves that propagate through the wire.

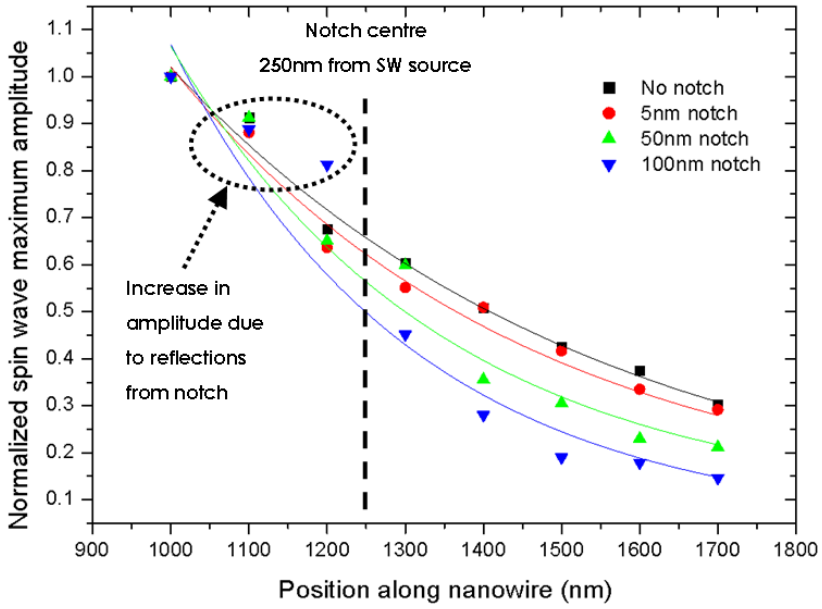

FIGURE 7.4. Plot of normalized spin wave amplitude along the wire length for notches of difference size (notch width is quoted, with the height being half this value). The reduction in spin wave amplitude at the probes placed beyond the notch position is proportional to the notch height. A 50 % reduction of spin wave amplitude at 1700 nm for the 100 nm wide notch corresponds to the 50 % reduction in wire width caused by the notch constriction.

Figure 7.4 shows a plot of the peak amplitude for the main spin wave packet as it reaches each probe, for each particular notch size. The data is normalized to the amplitude measured at the first probe. As the notch size increases there is a clear reduction in the spin wave amplitude reaching the probes positioned beyond the notch. Amplitudes measured before the notch are subject to interference effects from reflected spin waves, particularly evident in the 100 nm wide (50 nm height) notch. For the probe positioned at 1700 nm the spin wave peak amplitude for the 100 nm notch shows a 50 % decrease from the value for no notch. The 50 nm notch shows a 25 % decrease. These percentages match exactly the reduction in wire width at the notch constriction, which suggests that notch inhibits the spin waves. We observe reflections from the notch in Figure 7.4 as an increase in the spin wave amplitude for the notches closest to the notch, which increases as the notch size increases.

7.2.2. Number of notches. We now introduce a varying number of pairs of triangular notches to a permalloy strip wire (W=100nm, T=10nm). Spin waves are again generated by a localized external field and the local perpendicular magnetization is measured after some

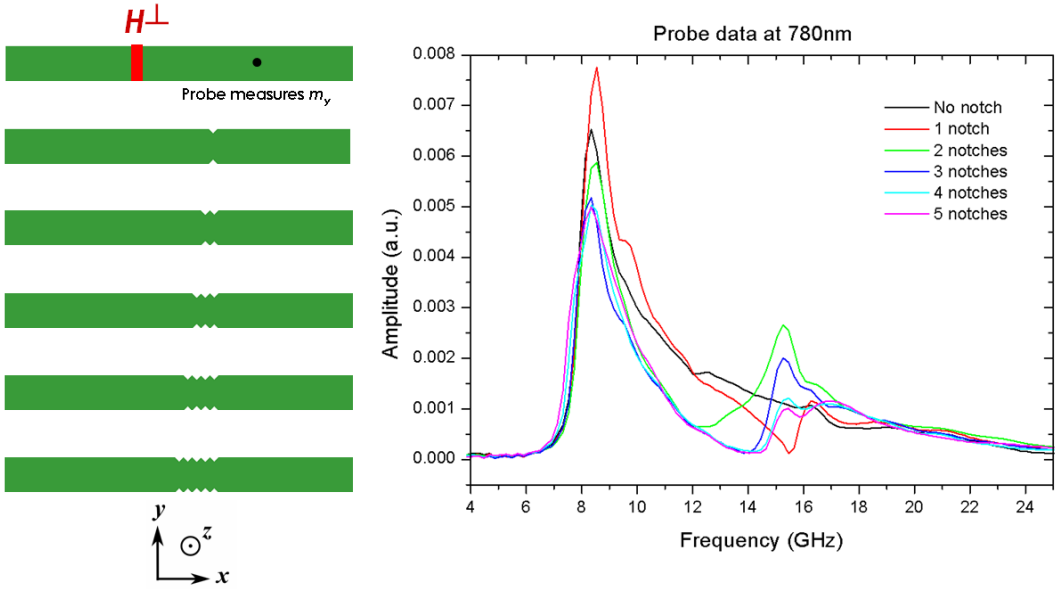

FIGURE 7.5. Introducing a series of 25 nm wide notches between the SW source and a probe. The probe measures the local transverse magnetization. Increasing the number of notches alters the spin wave amplitudes and usually reduces them.

distance by a probe. Between the applied field and the probe we start with a single notch, on both top and bottom edges, of 25 nm width and then we add an extra pair of notches for each subsequent test until the series of notches represents a length of periodic triangular roughness. The probe data can be compared to determine the influence of the increasing number of notches on the behaviours of the spin waves that propagate through the wire.

Figure 7.5 shows a schematic of the wires used and a frequency domain plot of the transverse magnetization, M_y, at the probe. The largest number of notch pairs, 4 and 5, cause a noticeable reduction in the measured spin wave amplitude. The second order frequency mode, around 16 GHz, is significant in all wires apart from the case with no notches, but is largest for the case of 2 notch pairs. This could be a result of periodicity and the exact relation between notch position and phase matching with the incoming spin waves.

Figure 7.6 contains magnetization data for the case of a single pair of notches. The magnetization around the notch is perturbed in order to reduce surface charges and minimize magnetostatic energy. This means that the area of influence of the notch extends further than the actual notch itself.

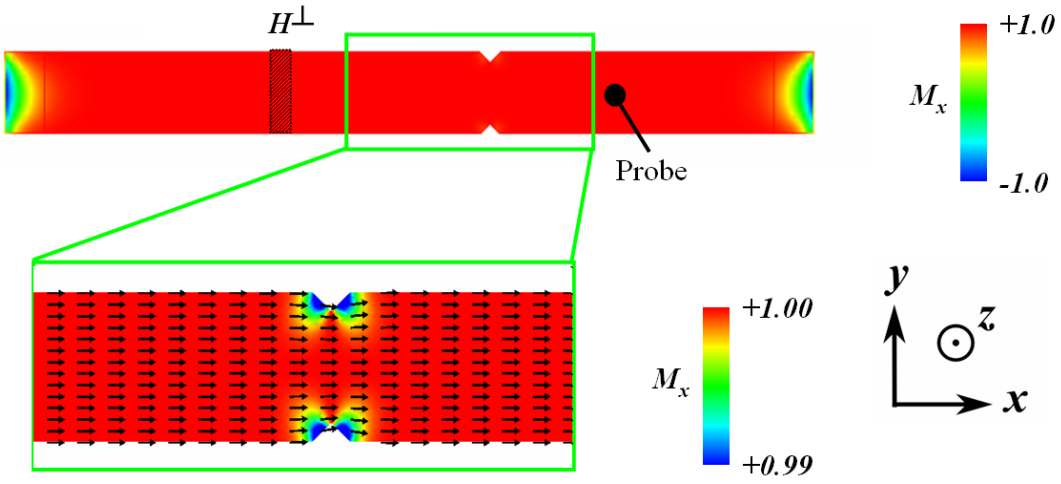

FIGURE 7.6. A rectangular thin film permalloy nanowire containing single pair of notches. Close inspection reveals that perturbation of the internal magnetization to conceal surface charge extends the influence of the notch inside the wire.

7.3. Roughness

In this section we investigate the effects of edge roughness on spin wave propagation. A number of different examples of roughness are introduced to rectangular nanowires ($L = 2000$ nm, $W = 100$ nm, $T = 10$ nm). The first wire is perfectly smooth, and is used for reference. We introduce a series of wires with triangular periodic roughness of various sizes. Once again, the notches making up the roughness have a width (5 nm, 10 nm, 20 nm) measuring twice that of their height. A random walk roughness is generated using a Python **[158]** script that takes a number of spatial interval parameters and a randomizing factor to generate a series of coordinates for the finite element model. These parameters are modified to generate the two examples shown in Figure 7.7, with the second specified to qualitatively resemble an example of characteristic roughness observed in experimental image data from Brownlie and co-workers (Figure 7.2).

We use an adaptive mesh with mesh size of 1 nm along the edges of the wire that contain roughness to ensure that all the features are correctly reproduced (Figure 7.8). This is particularly important for the 5 nm periodic roughness, as a standard 5 nm mesh would not resolve the geometric features sufficiently. Using such a small mesh size increases the number of finite element significantly and results in large model sizes.

Spin waves are generated at the centre of a wire using an external field that is applied over a 20 nm long section of the wire. The field takes 10 ps to ramp to its maximum value of 0.1 T.

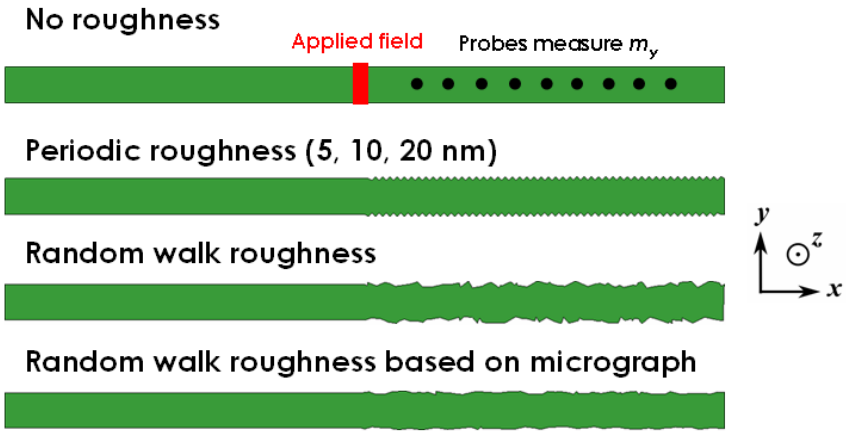

FIGURE 7.7. Examples of a smooth wire, a wire with periodic triangular roughness (the 10 nm example is depicted) and random walk roughness generated using a Python [**158**] script. The second random walk roughness is specified to qualitatively resemble realistic roughness in permalloy nanowires, taken from existing micrograph images.

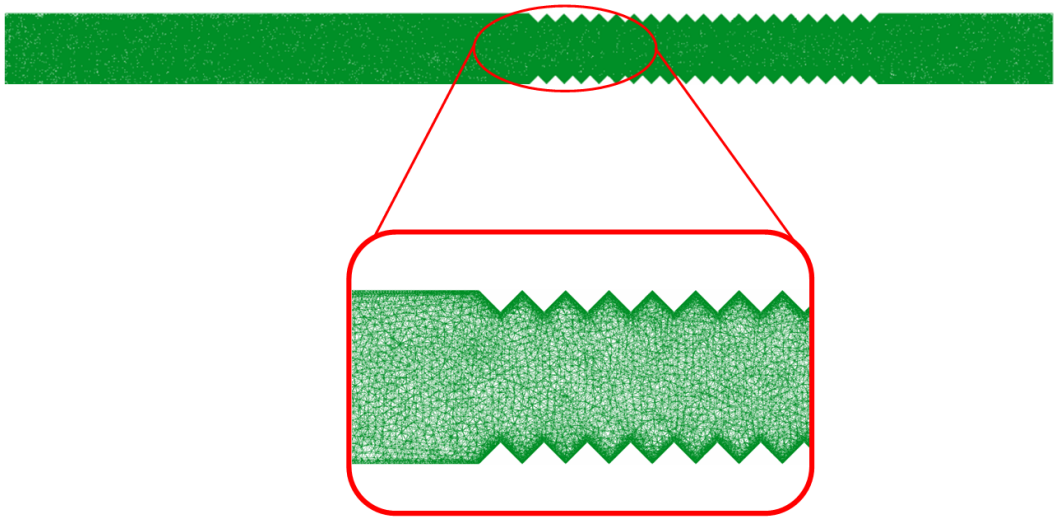

FIGURE 7.8. An example of finite element meshing for the nanowire roughness. In order to sufficiently resolve the geometric features of the roughness we find it beneficial to use a mesh size lower than the minimum feature size. For instance, in the wire with 5 nm periodic roughness an adaptive mesh with mesh size of 1 nm is used at the edge surfaces. The usual 5 nm mesh size is used for the rest of the structure.

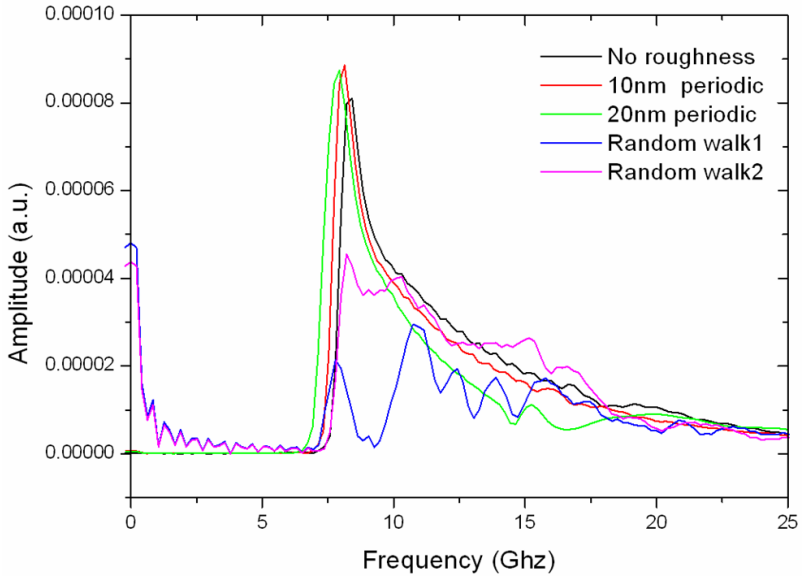

FIGURE 7.9. Frequency domain plot of the transverse magnetization data measured at a probe 650 nm from the spin wave source. The periodic roughnesses reduce the spin wave amplitudes at the probe for some frequency ranges. The randomized roughnesses break up the single main frequency peak and a number of different spin wave frequencies are measured. The overall spin wave amplitude is also reduced.

Figure 7.9 gives the transverse magnetization data at a probe (650 nm from the spin wave source) in the frequency domain. Increasing the size of the periodic roughness reduces the spin wave amplitude in some frequency ranges, due to the reduced width in the wire that accompanies larger notches. The two random walk roughness examples exhibit a large reduction in the spin wave peak amplitude. In particular, the case titled "Random walk 1", which is a coarser type of roughness, destroys the main frequency peak and instead a wide range of spin wave frequencies are measured. The overall spin wave amplitudes are also reduced by the randomized roughnesses.

7.3.1. Spin wave attenuation with distance. Using a series of probes we record the peak wavepacket amplitude of spin waves as a function of distance from the spin wave source. Figure 7.10 contains a plot of the spin wave maximum peak amplitude at each probe, normalized to the amplitude at the closest probe to the spin wave source. In this instance the example of randomized roughness is based on realistic roughness taken from a micrograph image (Figure 7.2). The nanowires contain absorbing boundary conditions at their ends, which employ a two-step increase in damping constant, to avoid any spin wave reflections.

It has previously been demonstrated by Hertel and co-workers that spin waves experience a phase shift when passing through a domain wall in a nanowire [**107**]. Furthermore, the phase

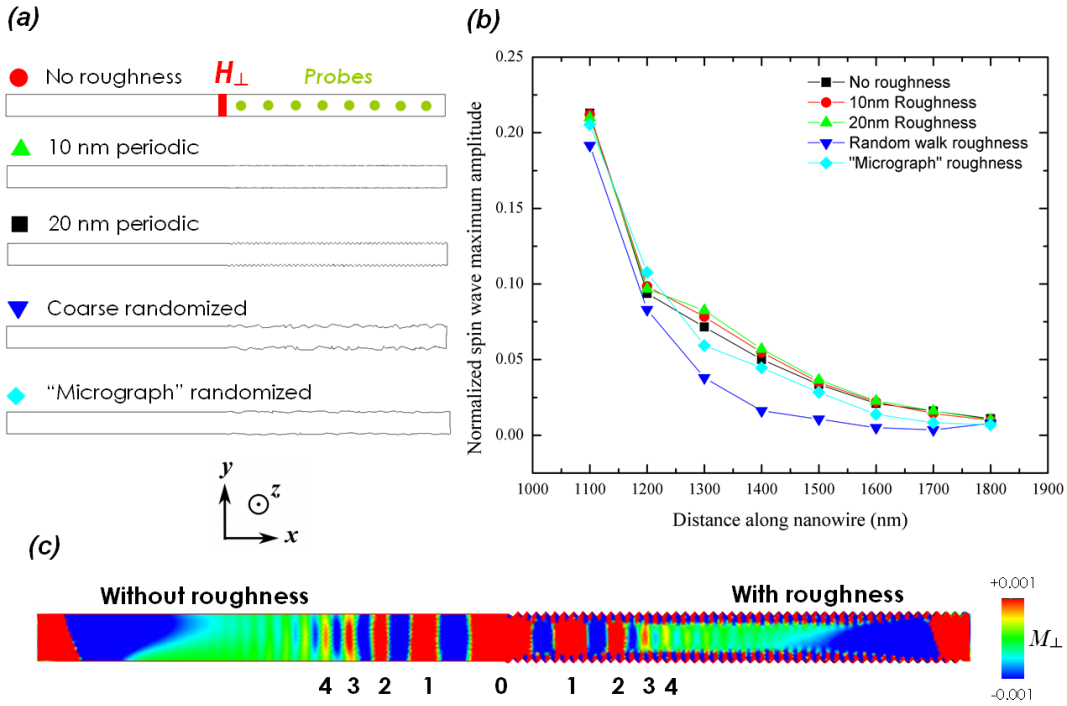

FIGURE 7.10. Spin wave attenuation with distance for nanowires with varying types of edge roughness. (a) Schematics of the models with various types of wire roughness. (b) The normalized plots of spin wave peak amplitude with distance for each roughness type. (c) A visualization of the spin waves shows that they are significantly attenuated for the 20 nm periodic roughness, perhaps even more so than shown by the numerical results since the spin waves were generated in the rough region already.

shift is proportional to the angle of the domain wall, with 360° domain wall inducing a shift of 180° (π radians) and 180° domain walls inducing a 90° ($\pi/2$ radians) shift.

Figure 7.11 shows magnetization data for a wire with an example of random walk roughness (the colour scale, for M_y at the probe, is reduced in comparison to previous figures). We observe what can be considered as small angle domain walls in the proximity of the roughness, with the angles being similar or larger in magnitude to the changes in magnetization vector that result from spin wave propagation. These small angle domain walls are not arranged uniformly across the width of the wire. We suggest that spin waves traversing regions such as this would undergo complex and non-uniform phase-shifting that would alter their frequency profile. Constructive and destructive interference is also likely to occur, altering the wavepacket amplitude.

7.3.2. Period of periodic roughness. We investigate the changes in notch period for periodic roughness without altering the notch size, which requires us to introduce separations between notches. This separation is modified in size to sweep through the periodicity of the

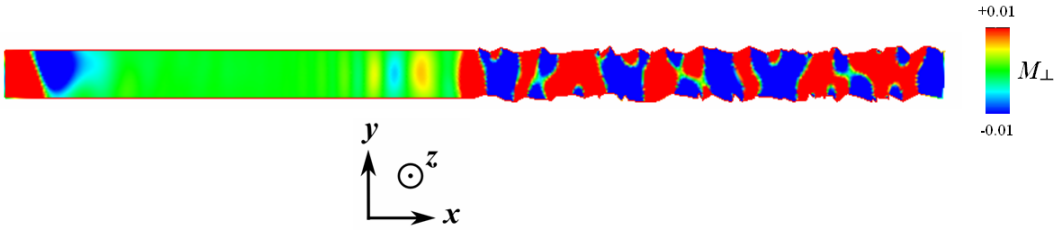

FIGURE 7.11. Magnetization (reduced scale) images of the randomized roughness show small angle domain walls, which are arranged non-uniformly and are likely to induce complex phase-shifting on incoming spin wavepackets.

roughness between 25 nm and 100 nm (corresponding to notch separations of 0 nm and 75 nm, respectively). The notch size, w, is constant at 25 nm and the length of the rough region held constant at 500 nm, with the number of notches changing to accommodate the changes in separation distance.

Without a frequency response we would expect to see a negative linear correlation between spin wave amplitude and notch separation as an increases in the number of notches in the structure would decrease the spin wave amplitude. Instead, Figure 7.12 shows a non-linear response with dips in amplitude at spatial periods corresponding to the spin wave wavelength (around 44 nm) and close to double the spin wave wavelength. We believe the periodic roughness turns the nanowire into a type of magnonic crystal, with frequency band gaps that inhibit spin wave amplitude of propagation when the notch separation is comparable to the spin wave mode wavelengths.

7.4. Bends

When using magnetic nanowires as spin wave waveguides in more complex spin wave device architectures, the spin waves might need to pass through a bend in the wire. This geometric complication might conceivably affect the spin wave characteristics, since the spin wave is being laterally confined in two dimensions. Traversing the bend in this way might introduce reflections and refraction from internal surfaces of the wire geometry.

7.4.1. Spin waves through a bend. A nanowire (W = 100 nm, T = 10 nm) is constructed with a smooth 90° bend of 100 nm inner radius. Spin waves are generated in one section of the wire and propagate outwards towards the bend. A probe is positioned after the bend to measure the transverse magnetization, which is rotated 90° in the $x-y$ plane after the

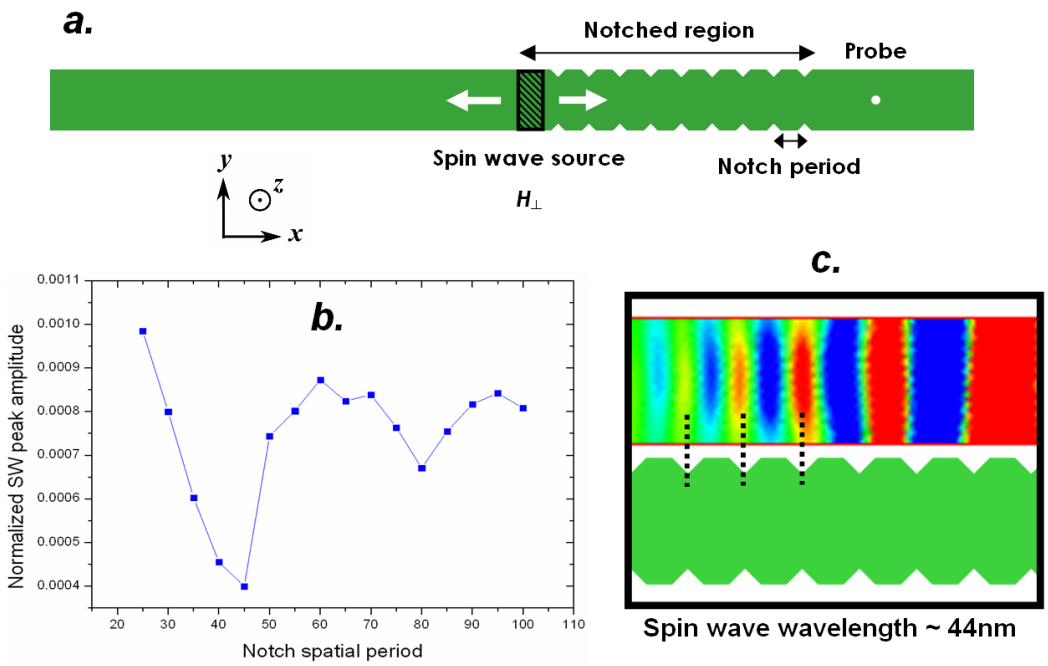

FIGURE 7.12. Investigating the periodicity of the periodic roughness in a permalloy nanowire. (b) A frequency response is observed when the separation between the notches matches the spin wave wavelength and close to twice the spin wave wavelength (c).

bend. The same simulation is performed with a straight wire for reference, with a matching distance between the spin wave source and the probe.

A frequency domain plot of the probe data is given in Figure 7.13, along with a series of images showing the magnetization at time intervals after the applied field is switched on. The frequency and amplitude of the spin wave wavepacket are not significantly modified by the bend in the wire. However, the spin wave wavefronts are rotated slightly by the bend, which could lead to readout problems in a real device, where a strip-line measures the magnetization across the width of a section of the wire.

7.4.2. Round or square bends. A similar investigation is performed for two nanowires; one with a curved 90^{o} bend (inner radius 100 nm) and one with a sharp, square-shaped 90^{o} bend. Frequency-domain probe data is given in Figure 7.14, showing that spin wave propagation is heavily inhibited in the case of the square bend. This is due to reflections of the incident spin waves from the bend and back along the wire towards the spin wave source. The reflections also cause interference that alters the frequency profile of the measured spin waves.

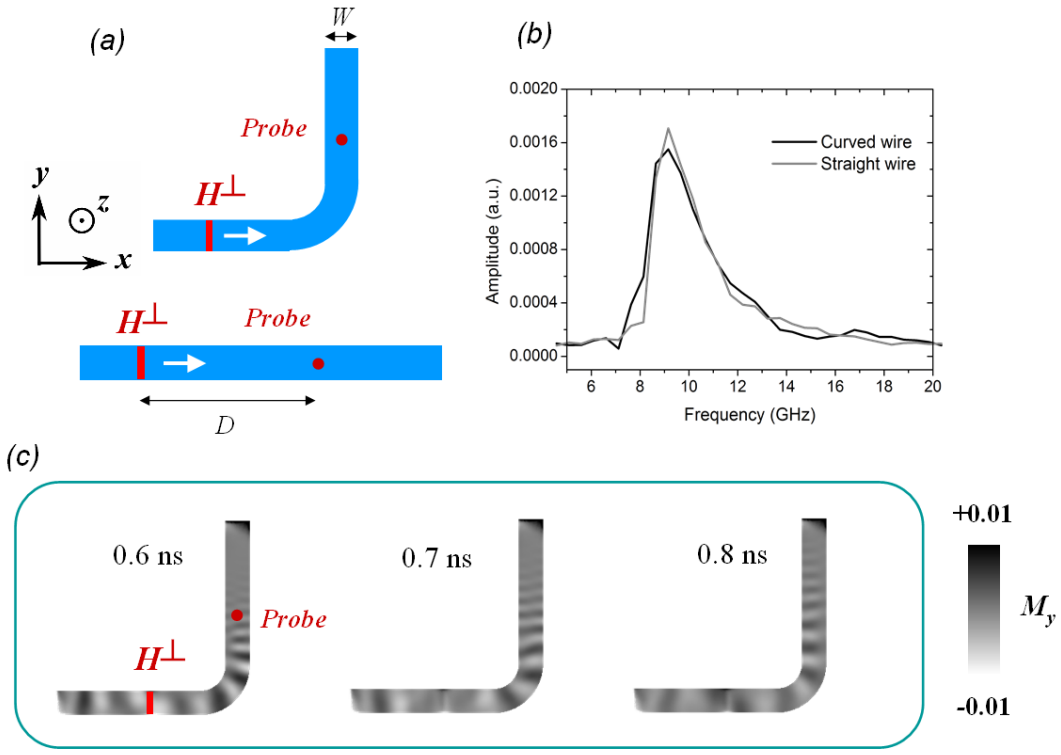

FIGURE 7.13. (a) Spin waves are able to traverse a 90º bend inside the nanowire. The inner radius of the bend is 100 nm. (b) The frequency profile and amplitude of the spin waves are largely unaltered by the bend, in comparison to a regular, straight wire. (c) Time step images of the spin waves, showing the transverse magnetization.

7.4.3. Bend radius. The inner radius of the bend r_1, which is given by the equation $r_1 = r_2 - w$ where r_2 is the outer radius and w is the wire width, is modified in size. The bend angle is 90°. Figure 7.15 contains a schematic of the structure design and a frequency-domain plot of the spin waves measured at the probe. While it appears that no large differences are observed the smallest bend radius does exhibit the lowest measured spin wave amplitudes. The frequency profiles of the spin waves in each case are not significantly different.

7.4.4. Spin waves through a double bend in a wire. A double bend is introduced as an interesting extension to the single bend test. A probe measures the transverse magnetization after the second bend. Figure 7.16 contains a schematic of the test and a temporal plot of the probe data. The spin waves eventually travel opposite to their original direction. A straight wire with matching distance between the source and the probe is also simulated for comparison.

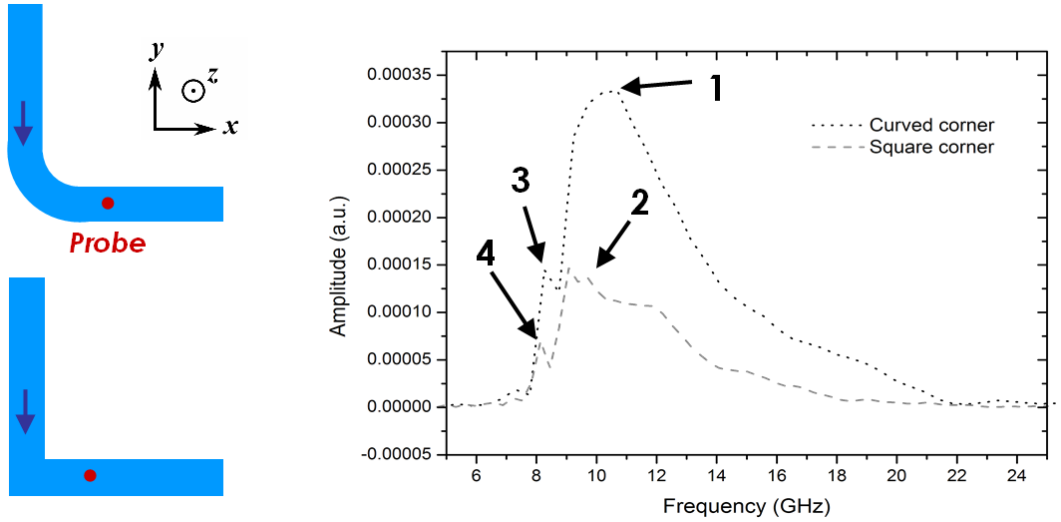

FIGURE 7.14. The spin wave source and the measuring probe are separated by two types of bend; a rounded one and a square one. In the case of the rounded bend, the spin waves are able to propagate through almost exactly as in a straight wire. For the square bend reflections occur as the spin waves meet the physical edge of the wire but also the sharp magnetization gradient that is found at the sharp change in geometry. The main frequency peak for the smooth bend (1) disappears for the sharp bend (2) and a lower frequency edge is seen more prominently (3) than before (4), possibly as a results of the increased interference from reflections.

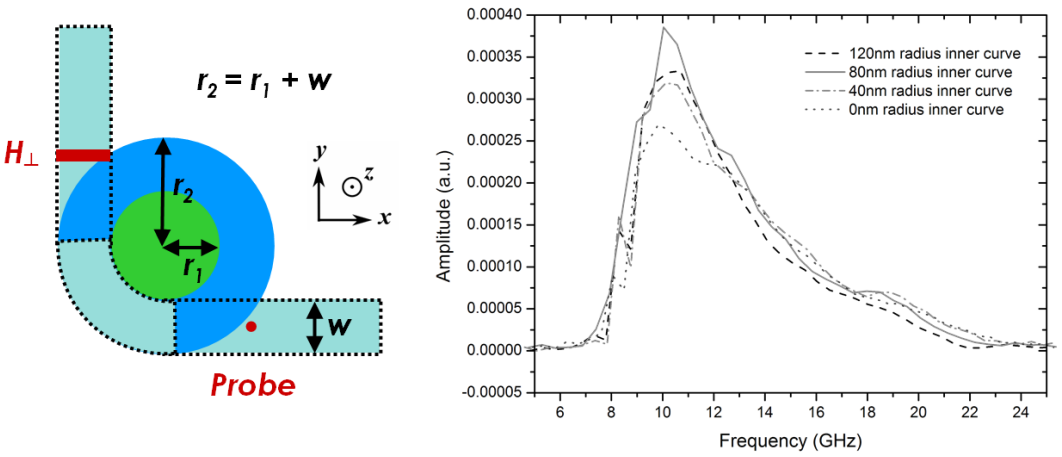

FIGURE 7.15. Tests to change the inner radius of the nanowire bend show that, while no huge differences are observed, a larger bend radius tends to allow cleaner spin wave propagation.

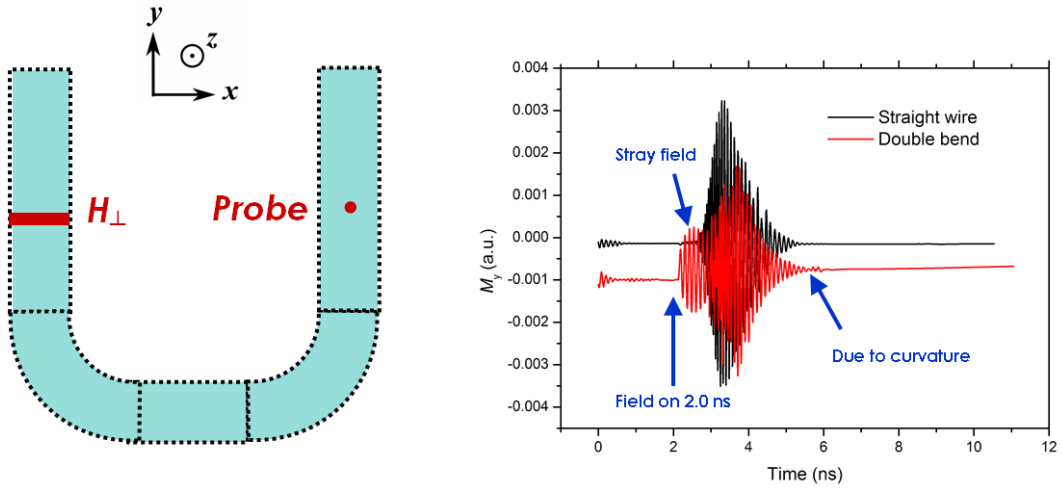

FIGURE 7.16. Spin waves passing through a double bend in a permalloy nanowire. The spin waves observed immediately at the field switch on time are a result of stray field from the nearby spin wave source, which is perturbed in its magnetization and exhibits surface charges. A spread in spin wave arrival times is a result of the curvature and could be a problem for magnetologic calculations that rely on controlled phase shifts.

Results show that the spin wave packet traverses the double bend successfully. However, the double bend data shows an earlier packet of oscillations, which occur immediately after we switch the field on and that we attribute to stray field from the spin wave source surface charges, which are sufficiently close to the probe to have influence. This leads to a reduction in the overall packet amplitude and some interference with the main wavepacket. Additionally, a spreading of the spin wave arrival times is observed. This is due to the curvature experienced by the spin waves, which travel a shorter distance at the inner curve than the outer curve of the wire, much like Olympic track athletes in a 400 metre race [**173**]. This spread could be a problem for magnetologic calculations where phase shift is used as a method of encoding logic into the spin wave packet, as the spread could induce an uncontrolled phase shift. The phase shifting in this simulation is measured using a probe that is at the centre of the wire's width, whereas in a real device the average magnetization would be measured over the entire width using a strip-line. Rotation of the spin wave wavefronts (c.f. Figure 7.13) could lead to problems in reading out the correct phase.

7.5. Summary

In this chapter we have shown that edge roughness and edge defects can significantly affect the properties of spin waves propagating in a permalloy thin film nanowire. We have seen

evidence that periodic roughness can be introduced into a nanowire to make a type of magnonic crystal, where spin wave propagation amplitude can be a function of the frequency of periodicity. This could open up a range of device applications, analogous to those found in the busy field of photonics.

It has been demonstrated that spin waves can pass through a smooth bend in a nanowire without significant loss of amplitude or coherence, although the curvature could potentially introduce phase shifting that interferes with magnetologic calculations.

We conclude that magnetic nanowires can be successfully used as components in spin wave logic devices, for instance as waveguides in larger device architectures.

CHAPTER 8

Conclusions & future work

8.1. Domain wall trap memory

In the course of this thesis I have examined the previous literature and provided new data from micromagnetic modelling concering domain wall trap (DWT) memory, which has previously been proposed as a form of universal memory to replace a range of existing devices. In particular, DWT memory could supersede Flash memory as a robust form of portable, personal storage and replace SRAM and DRAM as a computer system memory that is also non-volatile.

I have assessed the suitability of a number of DWT memory devices by fundamentally investigating a number of aspects of their behaviour. I have found that the de-pinning field for domain walls inside the DWT memory cells are different for different types of domain walls, including vortex domain walls (VDWs) of different chirality. Additionally, the switching field is different for domain walls of different types, including vortex domain walls of different chirality. These differences are a consequence of the internal structures of the domain walls and their magnetization orientations relative to other parts of the cells.

Although the hysteresis loops for the DWT memory operation are asymmetric around the origin I have found it still possible to design a working DWT memory cell, with field margins large enough to allow switching without damaging the cell spin structure permanently.

A phase diagram of domain wall configuration stability has been produced for the most reliable DWT memory design along with a similar plot for rectangular nanowires. The latter data shows excellent agreement with results from the existing literature.

As an interesting side-topic it was determined that a rotating magnetic field could sometimes be used to transform an existing domain wall into another domain wall type without moving it or using high saturation fields, and that this could be done controllably in a few cases. For instance, a transverse domain wall (TDW) was transformed into a clock-wise (CW) VDW or an anticlock-wise (ACW) VDW, but this was largely because the TDW is energetically un-favoured at the particular device sizes used.

Calculations performed using micromagnetics and the nudged elastic band (NEB) method

have shown that DWT memory cells are sufficiently stable at typical device operating temperatures for long-term data storage.

Our results, along with experimental data from Brownlie and co-workers [**46, 49**] provide compelling evidence that DWT memory can be successfully employed for data storage, although some interesting complications exist that makes the device behaviours less simple than would otherwise be expected.

So far the experimental and modelling results obtained for domain wall trap memory designs have focussed on the single free magnetic layer that would be one part of a multi-layer thin film structure. The next step would be to attempt to model or build a fully working prototype device.

8.2. Spin waves in ferromagnetic nanowires

The second major portion of this thesis considers spin waves in ferromagnetic nanostructures. Spin wave logic with a spin wave bus could form magnetic spin wave-based cellular non-linear networks (CNNs). These have the potential to perform some types of advanced logic calculations and algorithms faster and more efficiently than current computers.

Largely focussing on permalloy nanowires, spin waves have been generated by external magnetic fields and their behaviour investigated.

We have confirmed that spin wave frequency is highly dependent on geometry, agreeing with existing analytical solutions and observations, but not strongly dependent on material parameters. In addressing the problem of spin wave reflections we have found that boundary conditions containing above normal damping constant values can be included to dampen spin waves and stop them reflecting from structural boundaries. These modifications are trivial with micromagnetic simulation but increased damping in magnetic materials have been reported in the literature, where doping has been used.

Spin waves have been investigated in nanowires with various kinds of edge roughness, showing that roughness can significantly inhibit spin wave propagation by increasing attenuation along the length of a wire. However, when investigating periodic roughness made from a series of triangular notches we have observed a connection between the notch period and the spin wave wavelength. When the notch separation is equal to multiples of the spin wave wavelength a reduction in spin wave propagation amplitude is measured, suggesting that the rough wire is behaving like a type of magnonic crystal.

Spin waves can also transmit through a bend in a nanowire with little effect on the spin wave properties. This is important for magneto-logic devices where nanowires are used as the spin wave waveguides for communication between different devices and different parts of the same device.

There are many avenues for future work regarding spin waves in ferromagnetic nanostructures. In this thesis we examined how edge defects such as notches and roughness can inhibit spin wave propagation, and this could be extended to 3-dimensional defects. One might consider how a change in wire thickness, introduction of localized geometric defects or local changes in the material parameters can affect spin wave propagation .

We have shown how spin wave reflections can be reduced by applying boundary conditions with multi-step increases in the Gilbert damping parameter. Experimentally, doping could be applied as a smooth function of distance, by moving the edge of a mask. This was not chosen in our models as to introduce many material volumes can increase computation time. Such smooth boundary conditions would avoid reflections that we have shown can occur from damping steps, and could be beneficial to avoid interference in spin wave nanodevices.

Experimental research into exchange-dominated spin waves is limited by the small spatial and temporal resolutions required for precise analysis. For instance, using a probe as we have done in this thesis to measure the transverse magnetization with respect to time at a probe position is not trivial experimentally. While such fundamental testing might be difficult, to measure the voltage output of a spin wave CNN cell is, by design, possible.

Appendix A: Historic computer memory

Magnetic memory devices have often been at the cutting edge of memory technologies. We now take a brief look at a number of memory technologies that have become important at various times in history (Figure A-1.4). Years of invention are taken from various scholarly articles that often contradict each other, so due to this ambiguity the given dates are approximate.

Primary storage. Mercury delay line memory (1947) was a serial access refreshable memory used in some of the earliest digital computers in the mid-1940s [**174**]. An electrical signal is transformed into an acoustic wave that propagates to the other end of the mercury-filled tube over some finite length of time and is transformed back into an electrical signal at the other end (Figure A-1.1). In this way, data is temporarily stored in a memory and the process can be cycled repeatedly. A number of different types of delay line memory existed with different propagating media, for instance magnetostrictive and piezoelectric delay lines.

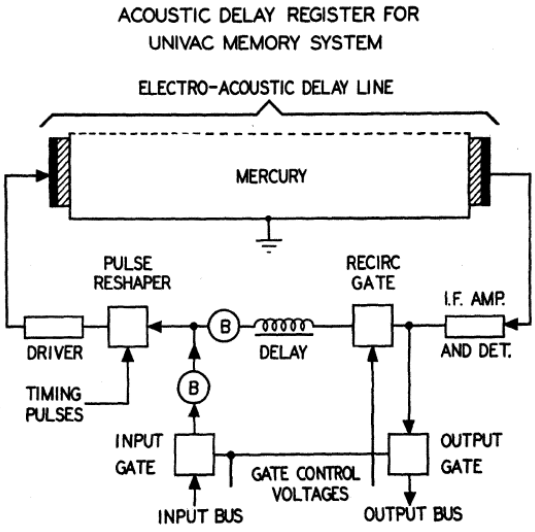

FIGURE A-1.1. Schematic representation of an early Mercury Delay Line Memory device that was used in the UNIVAC1 computer. A transducer at one end converts an electrical signal to a mechanical stress. This propagates an acoustic pulse through the mercury inside a glass tube. After a consistent delay time the pulse is converted back into an electrical signal and the process repeated. (Image taken from [**174**])

While not strictly a form of RAM, magnetic drum memory (Figure A-1.2a) is the earliest example of an electronically programmable, non-volatile primary memory device, and was notably used in IBM's first commercial business computer, the 650 Magnetic Drum Data Processing Machine or "Magnetic drum calculator" (MDC) in 1953. Magnetic drum storage was invented by G. Tauschek, a prolific Austrian inventor, in 1928 [**175**]. A metal drum was coated on the outside with a ferromagnetic recordable material. As the drum rotates a series of read-write heads along its length follow well-defined tracks around the circumference, hovering just above the drum surface without actually touching it. Often physical contact was accidentally made and the drum irreparably damaged, losing all currently stored data. Another disadvantage of the technology is that by the time the current instruction has been executed the next one has rotated around the drum and so time was lost when waiting for it to revolve back. This meant that executing programs using drum memory computers could be slow. This drum latency meant that care had to be taken with ordering of instructions.

The first RAM (random access memory) was the Williams-Kilburn CRT (Cathode Ray Tube) device invented in 1946, an example of electrostatic storage (Figure A-1.2b). Able to store 2048 bits of information, the technology was used in the Manchester Mark 1 computer [**176**] as well as the first Soviet-manufactured mainframe computer, "Strela", in 1953 and the IBM 701 "Defence Calculator" in 1952. Writing a series of dots and dashes to the CRT screen generated regions of slightly positive charge surrounded by an area of negative charge. The charge wells remain present – "in memory" – for a fraction of a second and could be immediately read by a special collector plate. This read process is destructive so data had to be reconstructed and periodically refreshed. The main disadvantage of CRT RAM was that it became unreliable with age.

CRT RAM and magnetic drum memory were later replaced by magnetic core memory (Figure A-1.4). Highly robust and resistant to radiation interference, it became central to many cold war era military applications. Introduced in 1949, it consists of a 2-dimensional grid of ferrite cores that are connected by an array or columns and rows of wiring, called bit lines and word lines. The cores can be magnetized in one of two directions, signifying a binary "1" or a "0" output, and the write process is achieved when current passes through both of the orthogonal lines at once, providing a large enough magnetic field for switching. Reading involves applying write currents in a known direction and inferring the previous state from the detection of a current pulse in the sense wire, which is associated with a flipping of states. With the

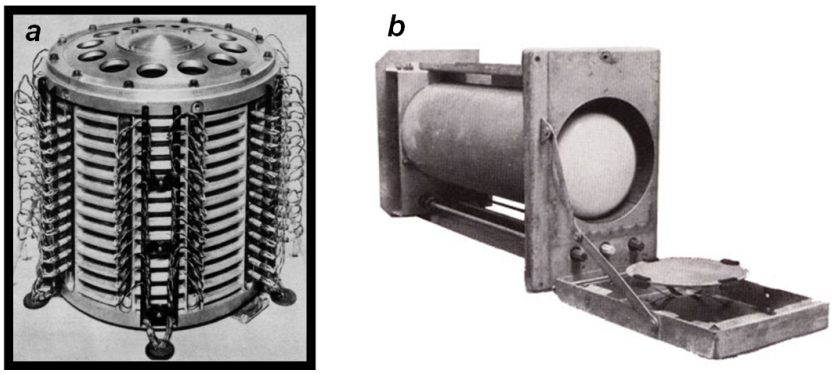

FIGURE A-1.2. (a) The drum memory system from a Polish ZAM-41 computer; (b) a Williams-Kilburn tube, the first RAM device for a computer (Images: Public domain).

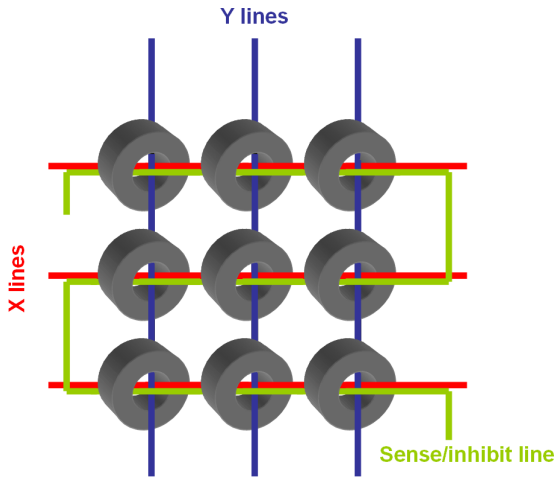

FIGURE A-1.3. Magnetic core memory consisting of a two-dimensional grid of toroidal ferrite cores interconnected by write and sense lines.

later development of solid-state metal-oxide semiconductor (MOS) RAM, core memory became obsolete due to its comparatively large size and poor performance.

Secondary and tertiary storage. If magnetism and magnetic materials have been important in the area of primary memory, then they have been utterly dominant in the realm of long-term secondary storage in modern computers. In order to have a programmable computer, where data, programs or routines are archived for later use, a form of memory storage must be utilized. A belt of perforated paper had been used by a Frenchman, Basile Bouchon, to store "programs" for a mechanical weaving machine [**175**]. In the 19th century paper punch cards had been used for the first time to store census data, and were later used for storing routines for mechanical accounting machines [**175**]. Early electric and electro-mechanical computers continued with the

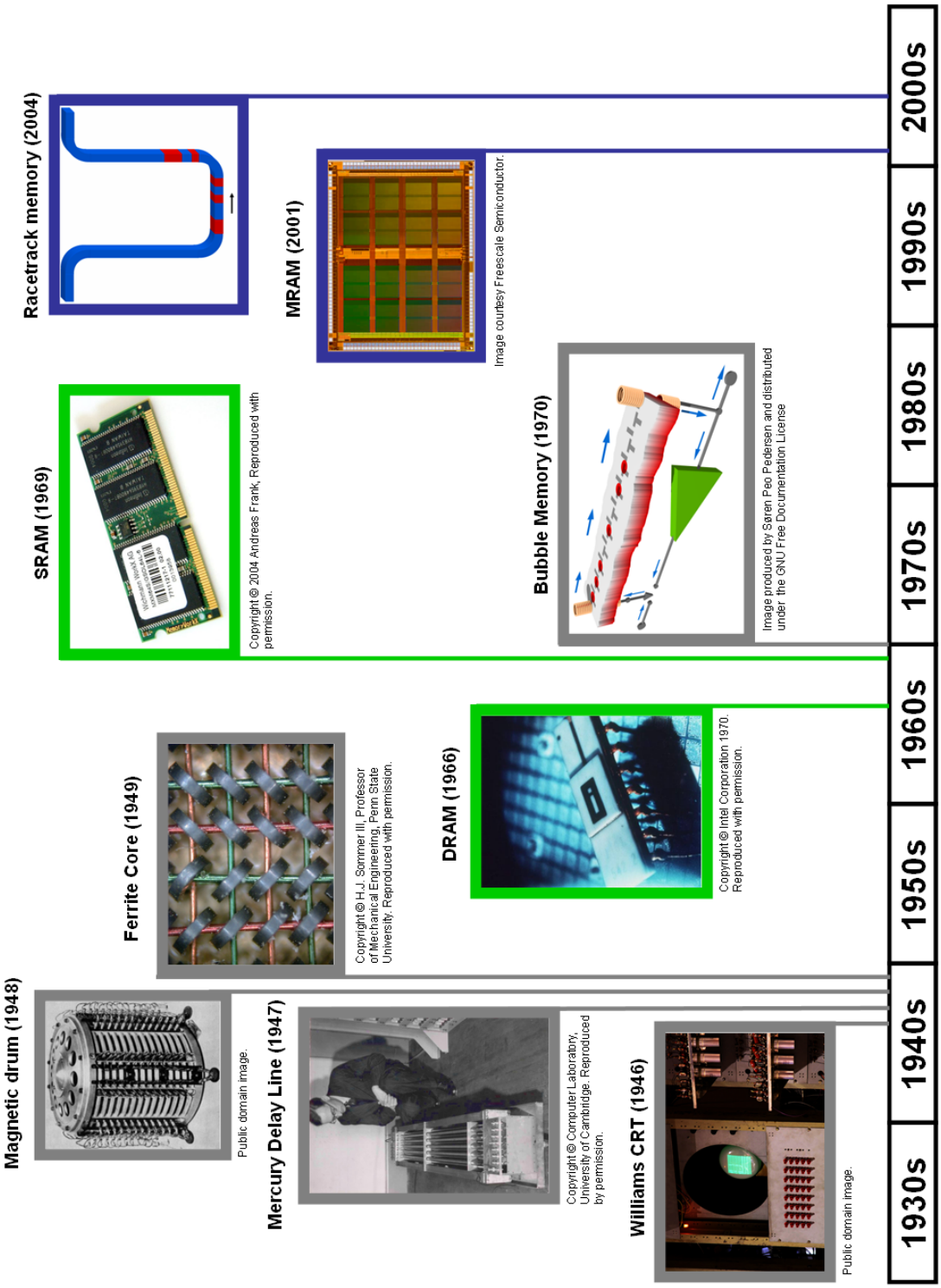

FIGURE A-1.4. Time-line of major technologies for main system memory in computers. Given are important historic memories (grey outline), current predominant technologies (green outline) and some of the memories that will potentially replace them in the future (blue outline).

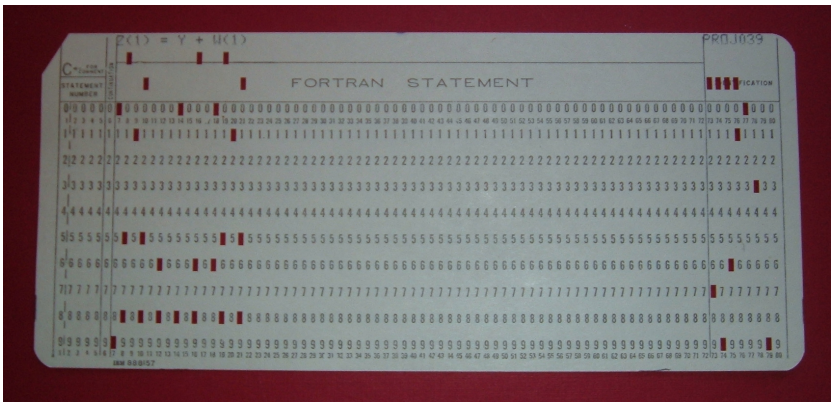

FIGURE A-1.5. A punch card containing a single instruction for a computer program written in the Fortran programming language. The programmer was required to punch holes by hand or using a punching machine in the correct positions, and helped by the printed numbers on the card (Public domain image licensed under the Creative Commons Share Alike (CC-SA) scheme by Arnold Reinhold).

use of punch cards for many years (Figure A-1.5). A typical punch card reading device used wire brush contacts to detect the holes, while others shone a light source at the card and used light sensors. The use of punch cards phased out around the time when IBM introduced the IBM 4331 system in 1979, which had on-line electronic data entry and CRT display units.

Floppy disks (Figure A-1.6) proved to be a very successful method for storing data. The 8 inch floppy disk and drive were invented in 1969 and smaller versions were introduced in 1976 ($5\frac{1}{4}$ inch) and 1984 ($3\frac{1}{2}$ inch). They quickly became the de facto method of data transfer between personal computers, and were only superseded in popularity by the much more recent USB flash drive. They were also used to store the operating system (OS) for many computers in the years before HDDs became affordable. The standard amount of storage was limited to 1.44 MB for the $3\frac{1}{2}$ inch "HD" version. The format itself contained a spinning magnetic disk that was housed in a hard plastic casing. Many attempts to increase the capacity of the technology were made but largely failed in the marketplace, mainly down to cost.

FIGURE A-1.6. Floppy disk drive for 8 inch floppy disks, introduced in 1978, next to a $3\frac{1}{2}$ inch diskette from 1984 (Image: Public domain).

Appendix B: History of processors

The first purely electronic computers, with no mechanical elements, appeared in the 1940s. The idea for using electronic means to perform iterative calculations was utilized in the 1940s by John Mauchly as a way of solving projectile range tables for the military [**177**]. He realised that vacuum tubes could be used as electronic switches that would be inherently faster than the mechanical analytical machines of the day.

An early example of such a computer is the Atanasoff-Berry Computer (ABC), built in 1941. This design was only partially successful and was actually non-programmable. It was an Englishman, Tommy Flowers, who in 1934 first used vacuum tubes in automated telephone exchanges and later went on to design and build the Colossus computers at Bletchley Park that decoded German military secrets during WWII [**178, 179, 180, 181**]. These were the first computers to successfully use vacuum tubes as electronic switches. Mauchly finally unveiled his ENIAC computer in 1946 [**16, 182, 183**]. This was the first 'Turing-complete' computer, which is a measure of a computer's universality. A Turing-complete computer is able, in theory, to perform any possible calculation from any other existing computer [**184, 185**].

In 1926, J.E. Lilenfeld patented the idea for a field effect transistor (FET), where application of an electric current to a poorly conducting material would increase its conductivity [**8**]. It wasn't until much later that the idea was used in a real device. The driving force for research into vacuum tube replacements partially came from the need for devices that worked at higher frequencies than had been previously available, in the GHz range and above, to improve on the precision of radar systems during WWII [**1**].

In November 1947, John Bardeen and Walter Brattain managed to make the first working transistor [**8**]. They were later awarded the Nobel prize for physics along with their co-worker William Shockley, who developed large parts of the theory to explain semiconductor and transistor physics.

Transistors have two main uses. They can amplify a weak electrical signal by outputting a signal factors of ten larger in amplitude. They are also used as switches, where the presence

of a sufficient current at the base terminal increases the conductivity of the semiconductor junction allowing a separate current to flow across it. The smaller size, improved reliability and lower power consumption of transistors quickly made vacuum tube technology obsolete for most applications. Now vacuum tubes have only a few niche uses such as in audio equipment [**186**]. A type of vacuum tube called a magnetron tube is also used as the high power radiation source in microwave ovens [**187**].

A crucial advantage of transistors is that many can be produced lithographically on a single silicon chip to make an integrated circuit (IC). The first integrated circuit was made with discrete wire connections by Jack Kilby at Texas Instruments in 1957 [**8**]. Then the planar process [**188, 189**] was utilized in 1959 to make the first IC using vapour deposited metal connections. Some of the early ICs were used in embedded computer systems for ballistic missile guidance systems and for the Apollo Guidance Computer (AGC) that helped take man to the moon [**1**].

In 1965 Gordon Moore of Fairchild Semiconductor penned his famous law, which stated that the number of transistors that could be included on a single chip would double every year [**190**]. This statement and the implied trend has held true not only for IC design but can be applied more generally throughout the semiconductor industry as device complexity increases, minimum feature size decreases and cost per semiconductor falls [**191**] (Figure B-1.7). Over the years manufacturers, driven by demand for faster, more powerful microprocessors, have been able to decrease the feature sizes of the MOS circuitry by many orders of magnitude.

An important step was the transition from n-type metal-oxide-semiconductor (NMOS) to complimentary metal-oxide-semiconductor (CMOS), which occurred in the 1980s [**10, 192**]. Current state of the art chips can contain around 376 million transistors. Compare this to the first Intel microprocessor on major release, the 4004, with just 2300 transistors in 1971 and it is clear how quickly the technology has progressed (Figure B-1.7).

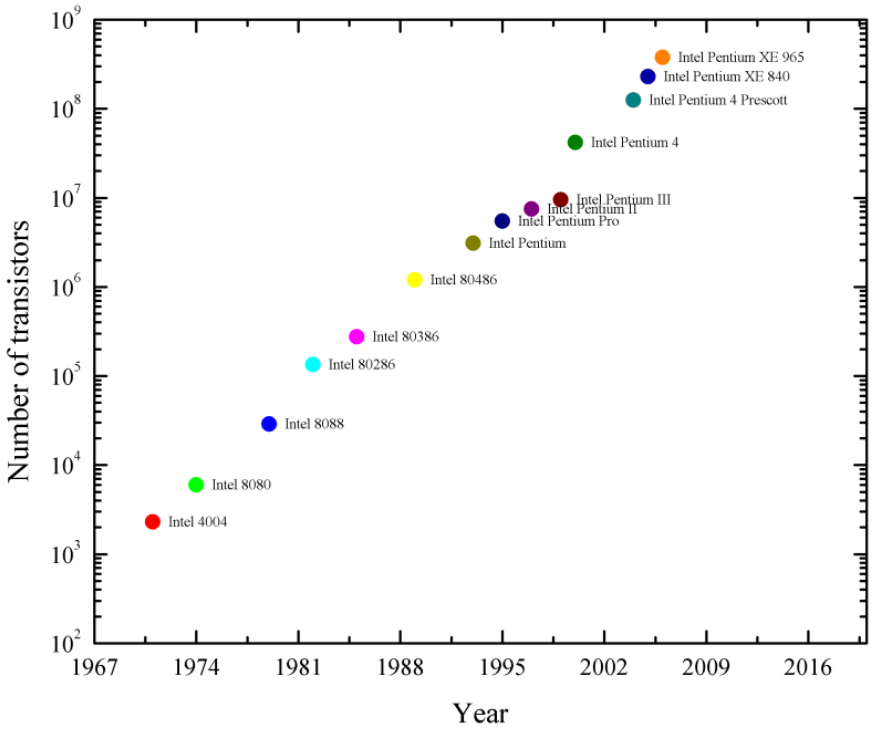

FIGURE B-1.7. The increasing number of transistors on individual Intel® microprocessors throughout their years of development.

Bibliography

[1] A. E. Cooper and W. T. Chow, "Development of on-board space computer systems," *IBM Journal of Research and Development*, vol. 20, no. 1, p. 5, 1976.

[2] H. M. Deitel and P. J. Deitel, *C++ how to program*. Prentice-Hall, Inc., 1994.

[3] S. Tom and A. Don, *PCI System Architecture*. Addison-Wesley Longman, 1995.

[4] A. Don and D. Dave, *Universal Serial Bus System Architecture*. Addison-Wesley Longman, 2001.

[5] I. J. Wickelgren, "The facts about firewire [serial communication bus]," *Spectrum, IEEE*, vol. 34, no. 4, pp. 19–25, 1997.

[6] S. Friedhelm, *The SCSI Bus and IDE Interface: Protocols, Applications and Programming*. Addison-Wesley Longman, 1997.

[7] D. Anderson, J. Dykes, and E. Riedel, "More than an interface—scsi vs. ata," *USENIX Association*, pp. 245–257, 2003.

[8] W. F. Brinkman, D. E. Haggan, and W. W. Troutman, "A history of the invention of the transistor and where it will lead us," *Solid-State Circuits, IEEE Journal of*, vol. 32, no. 12, pp. 1858–1865, 1997.

[9] R. C. Jaeger, *Microelectronic Circuit Design*. McGraw-Hill, 2004.

[10] A. S. Sedra and K. C. Smith, *Microelectronic Circuits*. Oxford University Press, 2004.

[11] S. Tehrani, J. M. Slaughter, E. Chen, M. Durlam, J. Shi, and M. DeHerren, "Progress and outlook for mram technology," *Magnetics, IEEE Transactions on*, vol. 35, no. 5, pp. 2814–2819, 1999.

[12] P. Miller, "Consumer electronics," *Spectrum, IEEE*, vol. 36, no. 1, pp. 41–45, 1999.

[13] Y. Hirai and Y. Ohtani, "Compact flash card," *US Patent D416,886*, 1999.

[14] G. Lawton, "Improved flash memory grows in popularity," *Computer*, vol. 39, no. 1, pp. 16–18, 2006.

[15] E. Grochowski and R. F. Hoyt, "Future trends in hard disk drives," *Magnetics, IEEE Transactions on*, vol. 32, no. 3, pp. 1850–1854, 1996.

[16] N. B. Stern, *From ENIAC to UNIVAC: An Appraisal of the Eckert-Mauchly Computers*. Digital Press, 1981.

[17] B. Hill, R. Pepperl, and J. Kruger, "Optical storage disk system with disk track guide sectors," *US Patent 4,094,013*, 1978.

[18] T. Kobota, "Hd dvd - overview of next generation optical disc format," in *IT to HD: Visions of Broadcasting in the 21st Century, The IEE 2-Day Seminar on (Ref. No. 2004/10760)*, pp. 213–224, 2004.

[19] N. Flaherty, "Battle of the blues," *IEE Review*, vol. 50, no. 4, pp. 48–50, 2004. 0953-5683.

[20] M. Fischetti, "Working knowledge: Blu-ray vs. hd dvd," *Scientific American*, vol. 297, no. 2, pp. 98–99, 2007.

[21] C. Arthur, "The rise of the all-conquering liliputer," *The Guardian*, 28th August, 2008.

[22] C. E. Herdt, "Nonvolatile sram - the next generation," in *Nonvolatile Memory Technology Review, 1993*, pp. 28–31, 1993.

[23] H. V. Tran, D. B. Scott, P. K. Fung, R. H. Havemann, R. H. Eklund, T. E. Ham, R. A. Haken, and A. H. Shah, "An 8-ns 256k ecl sram with cmos memory array and battery backup capability," *Solid-State Circuits, IEEE Journal of*, vol. 23, no. 5, pp. 1041–1047, 1988.

[24] D. Bondurant, "Ferroelectronic ram memory family for critical data storage," *Ferroelectrics*, vol. 112, no. 1, pp. 273 – 282, 1990.

[25] G. R. Fox, F. Chu, and T. Davenport, "Current and future ferroelectric nonvolatile memory technology," *Journal of Vacuum Science and Technology B Microelectronics and Nanometer Structures*, vol. 19, no. 5, pp. 1967–1971, 2001.

[26] M. Hosomi, H. Yamagishi, T. Yamamoto, K. Bessho, Y. Higo, K. Yamane, H. Yamada, M. Shoji, H. Hachino, C. Fukumoto, H. Nagao, and H. Kano, "A novel nonvolatile memory with spin torque transfer magnetization switching: spin-ram," in *Electron Devices Meeting, 2005. IEDM Technical Digest. IEEE International*, pp. 459–462, 2005.

[27] S. S. P. Parkin, M. Hayashi, and L. Thomas, "Magnetic domain-wall racetrack memory," *Science*, vol. 320, pp. 190–194, April 2008.

[28] M. J. Morant, *Integrated circuit design and technology*. Chapman and Hall, 1990.

[29] A. Khitun and K. L. Wang, "Nano scale computational architectures with spin wave bus," *Superlattices and Microstructures*, vol. 38, no. 3, pp. 184–200, 2005.

[30] Y. Taur, "Cmos design near the limit of scaling," *IBM Journal of Research and Development*, vol. 46, no. 2/3, p. 213, 2002.

[31] Y. Trouiller, "From 120 to 32 nm cmos technology: development of opc and ret to rescue optical lithography," *Comptes Rendus Physique*, vol. 7, no. 8, pp. 887–895, 2006.

[32] J. D. Meindl, "Interconnect opportunities for gigascale integration," *Micro, IEEE*, vol. 23, no. 3, pp. 28–35, 2003.

[33] A. K. Goel, *High-speed VLSI interconnections*. Wiley-IEEE, 2007.

[34] L. W. Kang, "Issues of nanoelectronics: A possible roadmap," *Journal of Nanoscience and Nanotechnology*, vol. 2, pp. 235–266, 2002.

[35] V. Dominique, "Nanometer-scale organic thin film transistors from self-assembled monolayers," *Journal of Nanoscience and Nanotechnology*, vol. 2, pp. 267–279, 2002.

[36] A. V. Pohm, J. S. T. Huang, J. M. Daughton, D. R. Krahn, and V. Mehra, "The design of a one megabit non-volatile m-r memory chip using 1.5 x 5 micron cells," *Magnetics, IEEE Transactions on*, vol. 24, no. 6, pp. 3117–3119, 1988.

[37] T. M. Maffitt, J. K. DeBrosse, J. A. Gabric, E. T. Gow, M. C. Lamorey, J. S. Parenteau, D. R. Willmott, M. A. Wood, and W. J. Gallagher, "Design considerations for mram," *IBM Journal of Research and Development*, vol. 50, no. 1, pp. 25–39, 2006.

[38] M. Motoyoshi, I. Yamamura, W. Ohtsuka, M. Shouji, H. Yamagishi, M. Nakamura, H. Yamada, K. Tai,

T. Kikutani, T. Sagara, K. Moriyama, H. Mori, C. Fukamoto, M. Watanabe, R. Hachino, H. Kano, K. Bessho, H. Narisawa, M. Hosomi, and N. Okazaki, "A study for 0.18 um high-density mram," in *VLSI Technology, 2004. Digest of Technical Papers. 2004 Symposium on*, pp. 22–23, 2004.

[39] C. Tannous and J. Gieraltowski, "The stoner-wohlfarth model of ferromagnetism," *European Journal of Physics*, no. 3, p. 475, 2008.

[40] T. Schrefl and J. Fidler, "Reversal modes and reversal times in submicron sized elements for mram applications," *Computational Materials Science*, vol. 17, no. 2-4, pp. 490–495, 2000.

[41] D. C. Worledge, "Single-domain model for toggle mram," *IBM Journal of Research and Development*, vol. 50, no. 1, pp. 69–79, 2006.

[42] X. Zhu, P. Grütter, V. Metlushko, and B. Ilic, "Magnetic force microscopy study of electron-beam-patterned soft permalloy particles: Technique and magnetization behavior," *Physical Review B*, vol. 66, no. 2, p. 024423, 2002.

[43] L. Savtchenko, A. A. Korkin, B. N. Engel, N. D. Rizzo, M. F. Deherrera, and J. A. Janesky, "Method of writing to a scalable magnetoresistance random access memory element," *US Patent 6531723*, 2003.

[44] J. I. Martín, J. Nogués, K. Liu, J. L. Vicent, and I. K. Schuller, "Ordered magnetic nanostructures: fabrication and properties," *Journal of Magnetism and Magnetic Materials*, vol. 256, no. 1-3, pp. 449–501, 2003.

[45] R. D. McMichael, J. Eicke, M. J. Donahue, and D. G. Porter, "Domain wall traps for low-field switching of submicron elements," *Journal of Applied Physics*, vol. 87, p. 7058, 2000.

[46] C. Brownlie, S. McVitie, J. N. Chapman, and C. D. W. Wilkinson, "Lorentz microscopy studies of domain wall trap structures," *Journal of Applied Physics*, vol. 100, no. 3, pp. 033902–9, 2006.

[47] D. Jiles, *Introduction to Magnetism and Magnetic Materials*. CRC Press, 1998.

[48] M. Kläui, "Head-to-head domain walls in magnetic nanostructures," *Journal of Physics Condensed Matter*, vol. 20, no. 31, pp. 1–20, 2008.

[49] C. Brownlie, *Lorentz microscopy, transmission electron microscopy, magnetic materials, electron beam lithography, micromagnetic simulations*. PhD thesis, University of Glasgow, 2007.

[50] A. Hubert and R. Schäfer, *Magnetic Domains: The Analysis of Magnetic Microstructures*. Springer, 1998.

[51] H. Barkhausen, "Zwei mit hilfe der neuen verstarker entdeckte erscheinungen," *Phys. Zeitschrift*, vol. 20, pp. 401–403, 1919.

[52] F. Bloch, "Zur theorie des austauschproblems und der remanenzerscheinung der ferromagnetika," *Zeitschrift für Physik A Hadrons and Nuclei*, vol. 74, no. 5, pp. 295–335, 1932.

[53] L. Landau and E. Lifshitz, "On the theory of the dispersion of magnetic permeability in ferromagnetic bodies," *Physik Zeitschrift Sowjetunion*, vol. 8, pp. 153–169, 1935.

[54] L. Néel, "Les lois de l'aimantation et de la subdivision en domaines élémentaires d'un monocristal de fer," *Journal de Physique et le Radium*, vol. 5, no. 12, pp. 265–276, 1944.

[55] C. Kittel, "Physical theory of ferromagnetic domains," *Reviews of Modern Physics*, vol. 21, no. 4, p. 541, 1949.

[56] T. Trunk, M. Redjdal, A. Kakay, M. F. Ruane, and F. B. Humphrey, "Domain wall structure in permalloy

films with decreasing thickness at the bloch to neel transition," *Journal of Applied Physics*, vol. 89, no. 11, pp. 7606–7608, 2001.

[57] R. D. McMichael and M. J. Donahue, "Head to head domain wall structures in thin magnetic strips," *Magnetics, IEEE Transactions on*, vol. 33, no. 5, pp. 4167–4169, 1997.

[58] M. J. Donahue and D. G. Porter, "Oommf users guide, version 1.2 alpha 3," 2002.

[59] Y. Nakatani, A. Thiaville, and J. Miltat, "Head-to-head domain walls in soft nano-strips: a refined phase diagram," *Journal of Magnetism and Magnetic Materials*, vol. 290-291, no. Part 1, pp. 750–753, 2005.

[60] A. P. Malozemoff and J. C. Slonczewski, *Magnetic Domain Walls in Bubble Materials*. New York: Academic Press, 1979.

[61] L. R. Walker, "Bell telephone laboratories memorandum," *Unpublished memorandum*, 1956.

[62] J. F. Dillon Jr, ed., *Domains and domain walls*, vol. 3 of *A Treatise on Modern Theory and Materials: Magnetism*. New York: Academic Press, 1963.

[63] N. L. Schryer and L. R. Walker, "The motion of 180[degree] domain walls in uniform dc magnetic fields," *Journal of Applied Physics*, vol. 45, no. 12, pp. 5406–5421, 1974.

[64] S. Glathe, R. Mattheis, and D. V. Berkov, "Direct observation and control of the walker breakdown process during a field driven domain wall motion," *Applied Physics Letters*, vol. 93, no. 7, pp. 072508–3, 2008.

[65] M. Hayashi, L. Thomas, C. Rettner, R. Moriya, and S. S. P. Parkin, "Direct observation of the coherent precession of magnetic domain walls propagating along permalloy nanowires," *Nature Physics*, vol. 3, no. 1, pp. 21–25, 2007.

[66] G. S. D. Beach, C. Nistor, C. Knutson, M. Tsoi, and J. L. Erskine, "Dynamics of field-driven domain-wall propagation in ferromagnetic nanowires," *Nat Mater*, vol. 4, no. 10, pp. 741–744, 2005.

[67] J.-Y. Lee, K.-S. Lee, and S.-K. Kim, "Remarkable enhancement of domain-wall velocity in magnetic nanostripes," *Applied Physics Letters*, vol. 91, no. 12, pp. 122513–3, 2007.

[68] S. Glathe, I. Berkov, T. Mikolajick, and R. Mattheis, "Experimental study of domain wall motion in long nanostrips under the influence of a transverse field," *Applied Physics Letters*, vol. 93, no. 16, pp. 162505–3, 2008.

[69] L. Berger, "Generation of dc voltages by a magnetic multilayer undergoing ferromagnetic resonance," *Physical Review B*, vol. 59, no. 17, p. 11465, 1999.

[70] L. Berger, "Emission of spin waves by a magnetic multilayer traversed by a current," *Physical Review B*, vol. 54, no. 13, p. 9353, 1996.

[71] J. C. Slonczewski, "Current-driven excitation of magnetic multilayers," *Journal of Magnetism and Magnetic Materials*, vol. 159, no. 1-2, pp. L1–L7, 1996.

[72] J. C. Slonczewski, "Excitation of spin waves by an electric current," *Journal of Magnetism and Magnetic Materials*, vol. 195, no. 2, pp. 261–268, 1999.

[73] G. Meier, M. Bolte, R. Eiselt, B. Kruger, D.-H. Kim, and P. Fischer, "Direct imaging of stochastic domain-wall motion driven by nanosecond current pulses," *Physical Review Letters*, vol. 98, no. 18, pp. 187202–4, 2007.

[74] M. Kläui, C. A. F. Vaz, W. Wernsdorfer, E. Bauer, S. Cherifi, S. Heun, A. Locatelli, G. Faini, E. Cambril,

L. J. Heyderman, and J. A. C. Bland, "Domain wall behaviour at constrictions in ferromagnetic ring structures," *Physica B: Condensed Matter*, vol. 343, no. 1-4, pp. 343–349, 2004.

[75] M. Kläui, H. Ehrke, U. Rudiger, T. Kasama, R. E. Dunin-Borkowski, D. Backes, L. J. Heyderman, C. A. F. Vaz, J. A. C. Bland, G. Faini, E. Cambril, and W. Wernsdorfer, "Direct observation of domain-wall pinning at nanoscale constrictions," *Applied Physics Letters*, vol. 87, no. 10, pp. 102509–3, 2005.

[76] M. Kläui, C. A. F. Vaz, J. Rothman, J. A. C. Bland, W. Wernsdorfer, G. Faini, and E. Cambril, "Domain wall pinning in narrow ferromagnetic ring structures probed by magnetoresistance measurements," *Physical Review Letters*, vol. 90, no. 9, p. 097202, 2003.

[77] D. Backes, C. Schieback, M. Klaui, F. Junginger, H. Ehrke, P. Nielaba, U. Rudiger, L. J. Heyderman, C. S. Chen, T. Kasama, R. E. Dunin-Borkowski, C. A. F. Vaz, and J. A. C. Bland, "Transverse domain walls in nanoconstrictions," *Applied Physics Letters*, vol. 91, no. 11, pp. 112502–3, 2007.

[78] J. G. Deak and R. H. Koch, "The effect of edge roughness on magnetization reversal in micron-sized permalloy thin films," *Journal of Magnetism and Magnetic Materials*, vol. 213, no. 1-2, pp. 25–31, 2000.

[79] Y. Nakatani, A. Thiaville, and J. Miltat, "Faster magnetic walls in rough wires," *Nature Materials*, vol. 2, no. 8, pp. 521–523, 2003.

[80] H. Asada, Y. Hyodo, J. Yamasaki, M. Takezawa, and T. Koyanagi, "Micromagnetic study of domain wall-pinning characteristics with step-like thickness change in thin films," *Magnetics, IEEE Transactions on*, vol. 40, no. 4, pp. 2110–2112, 2004.

[81] D. A. Allwood, G. Xiong, and R. P. Cowburn, "Domain wall diodes in ferromagnetic planar nanowires," *Applied Physics Letters*, vol. 85, no. 14, pp. 2848–2850, 2004.

[82] D. A. Allwood, G. Xiong, M. D. Cooke, C. C. Faulkner, D. Atkinson, N. Vernier, and R. P. Cowburn, "Submicrometer ferromagnetic not gate and shift register," *Science*, vol. 296, no. 5575, pp. 2003–2006, 2002.

[83] D. A. Allwood, G. Xiong, C. C. Faulkner, D. Atkinson, D. Petit, and R. P. Cowburn, "Magnetic domain-wall logic," *Science*, vol. 309, no. 5741, pp. 1688–1692, 2005.

[84] M. T. Bryan, T. Schrefl, and D. A. Allwood, "Symmetric and asymmetric domain wall diodes in magnetic nanowires," *Applied Physics Letters*, vol. 91, no. 14, pp. 142502–3, 2007.

[85] C. Kittel, "Introduction to solid state physics," *7th Edition*, 1996.

[86] D. C. Mattis, *The Theory of Magnetism Made Simple*. World Scientific, 2006.

[87] A. I. M. Rae, *Quantum Mechanics*. CRC Press, 4th ed., 2002.

[88] A. Aharoni, *Introduction to the Theory of Ferromagnetism*. Clarendon Press, 2000.

[89] M. N. Baibich, J. M. Broto, A. Fert, F. N. Van Dau, F. Petroff, P. Etienne, G. Creuzet, A. Friederich, and J. Chazelas, "Giant magnetoresistance of (001)fe/(001)cr magnetic superlattices," *Physical Review Letters*, vol. 61, no. 21, p. 2472, 1988.

[90] P. Grünberg, "Magnetic field sensor with ferromagnetic thin layers having magnetically antiparallel polarized components," *US patent 4949039*, August 14, 1990 1990.

[91] P. Grünberg, "Magnetfeldsensor mit ferromagnetischer, dünner schicht," *EU Patent 3820475*, 1988.

[92] G. A. Prinz, "Magnetoelectronics," *Science*, vol. 282, no. 5394, pp. 1660–1663, 1998.

[93] E. Y. Tsymbal and D. G. Pettifor, *Perspectives of Giant Magnetoresistance*, vol. 56 of *Solid State Physics*. New York: Academic Press, 2001.

[94] A. Thiaville, Y. Nakatani, J. Miltat, and Y. Suzuki, "Micromagnetic understanding of current-driven domain wall motion in patterned nanowires," *Europhysics Letters*, no. 6, p. 990, 2005.

[95] B. A. Kalinikos and A. N. Slavin, "Theory of dipole-exchange spin wave spectrum for ferromagnetic films with mixed exchange boundary conditions," *J. Phys. C: Solid State Phys.*, no. 35, p. 7013, 1986.

[96] F. Bloch, "Zur theorie des ferromagnetismus," *Zeitschrift für Physik A Hadrons and Nuclei*, vol. 61, no. 3, pp. 206–219, 1930.

[97] S. V. Vasiliev, V. V. Kruglyak, M. L. Sokolovskii, and A. N. Kuchko, "Spin wave interferometer employing a local nonuniformity of the effective magnetic field," *Journal of Applied Physics*, vol. 101, no. 11, pp. 113919–4, 2007.

[98] L. K. Brundle and N. J. Freedman, "Magnetostatic surface waves on a y.i.g. slab," *Electronics Letters*, vol. 4, no. 7, pp. 132–134, 1968. 0013-5194.

[99] P. C. Fletcher and C. Kittel, "Considerations on the propagation and generation of magnetostatic waves and spin waves," *Physical Review*, vol. 120, no. 6, p. 2004, 1960.

[100] M. Chen, M. A. Tsankov, J. M. Nash, and C. E. Patton, "Backward-volume-wave microwave-envelope solitons in yttrium iron garnet films," *Physical Review B*, vol. 49, no. 18, p. 12773, 1994.

[101] B. A. Kalinikos, N. G. Kovshikov, and A. N. Slavin, "Experimental observation of magnetostatic wave envelope solitons in yttrium iron garnet films," *Physical Review B*, vol. 42, no. 13, p. 8658, 1990.

[102] M. Chen, M. A. Tsankov, J. M. Nash, and C. E. Patton, "Microwave magnetic-envelope dark solitons in yttrium iron garnet thin films," *Physical Review Letters*, vol. 70, no. 11, p. 1707, 1993.

[103] G. Srinivasan, C. E. Patton, and P. R. Emtage, "Brillouin light scattering on yttrium iron garnet films in a magnetostatic wave device structure," *Journal of Applied Physics*, vol. 61, no. 6, pp. 2318–2326, 1987.

[104] W. S. Ishak, "Magnetostatic wave technology: a review," *Proceedings of the IEEE*, vol. 76, no. 2, pp. 171–187, 1988.

[105] V. V. Kruglyak and R. J. Hicken, "Magnonics: Experiment to prove the concept," *Journal of Magnetism and Magnetic Materials*, vol. 306, no. 2, pp. 191–194, 2006.

[106] S. Choi, K.-S. Lee, and S.-K. Kim, "Spin-wave interference," *Applied Physics Letters*, vol. 89, no. 6, p. 062501, 2006.

[107] R. Hertel, W. Wulfhekel, and J. Kirschner, "Domain-wall induced phase shifts in spin waves," *Physical Review Letters*, vol. 93, no. 25, p. 257202, 2004.

[108] J. P. Park, P. Eames, D. M. Engebretson, J. Berezovsky, and P. A. Crowell, "Spatially resolved dynamics of localized spin-wave modes in ferromagnetic wires," *Physical Review Letters*, vol. 89, no. 27, p. 277201, 2002.

[109] J. Jorzick, S. O. Demokritov, B. Hillebrands, M. Bailleul, C. Fermon, K. Y. Guslienko, A. N. Slavin, D. V. Berkov, and N. L. Gorn, "Spin wave wells in nonellipsoidal micrometer size magnetic elements," *Physical Review Letters*, vol. 88, no. 4, p. 047204, 2002.

[110] Y. Zhu, *Modern Techniques for Characterizing Magnetic Materials*. Springer, 2005.

[111] K. T. Hecht, *Quantum Mechanics*. Springer, 2000.

[112] M. P. Kostylev, A. A. Serga, T. Schneider, B. Leven, and B. Hillebrands, "Spin-wave logical gates," *Applied Physics Letters*, vol. 87, no. 15, pp. 153501–3, 2005.

[113] A. Khitun and K. L. Wang, "Nano logic circuits with spin wave bus," in *Information Technology: New Generations, 2006. ITNG 2006. Third International Conference on*, pp. 747–752, 2006.

[114] A. Khitun, M. Bao, J. Y. Lee, K. L. Wang, D. W. Lee, and S. Wang, "Cellular nonlinear network with spin wave bus," *International Conference on Information Technology (ITNG'07)*.

[115] L. O. Chua and L. Yang, "Cellular neural networks: theory," *Circuits and Systems, IEEE Transactions on*, vol. 35, no. 10, pp. 1257–1272, 1988.

[116] L. O. Chua and L. Yang, "Cellular neural networks: applications," *Circuits and Systems, IEEE Transactions on*, vol. 35, no. 10, pp. 1273–1290, 1988.

[117] T. Roska and A. Rodriguez-Vazquez, "Toward visual microprocessors," *Proceedings of the IEEE*, vol. 90, no. 7, pp. 1244–1257, 2002.

[118] T. Matsumoto, L. O. Chua, and T. Yokohama, "Image thinning with a cellular neural network," *Circuits and Systems, IEEE Transactions on*, vol. 37, no. 5, pp. 638–640, 1990.

[119] K. R. Krieg, L. O. Chua, and L. Yang, "Analog signal processing using cellular neural networks," in *Circuits and Systems, 1990., IEEE International Symposium on*, pp. 958–961 vol.2, 1990.

[120] T. Roska, T. Boros, P. Thiran, and L. O. Chua, "Detecting simple motion using cellular neural networks," in *Cellular Neural Networks and their Applications, CNNA-90 Proceedings, 1990 IEEE International Workshop on*, pp. 127–138, 1990.

[121] K. L. Wang, K. Galatsis, R. Ostroumov, A. Khitun, Z. Zhao, and S. Han, "Nanoarchitectonics for heterogeneous integrated nanosystems," *Proceedings of the IEEE*, vol. 96, no. 2, pp. 212–229, 2008.

[122] G. Hrkac, J. Dean, A. Goncharov, S. Bance, D. Allwood, T. Schrefl, D. Suess, and J. Fidler, "Micromagnetics of single and double point contact spin torque oscillators," *Arxiv preprint arXiv:0804.2119*.

[123] J. H. Collins, D. M. Hastie, J. M. Owens, and J. C. V. Smith, "Magnetostatic wave terminations," *Journal of Applied Physics*, vol. 49, no. 3, pp. 1800–1802, 1978.

[124] W. Faber, "Terminations for magnetostatic waves," *Electronics Letters*, vol. 16, no. 12, pp. 452–453, 1980.

[125] V. L. Taylor, J. C. Sethares, and C. V. Smith, "Msw terminations," in *1980 Ultrasonics Symposium*, pp. 562–570, 1980.

[126] J. Krug and P. Edenhofer, "Broadband terminations for magnetostatic surface waves," *Electronics Letters*, vol. 19, no. 23, pp. 971–972, 1983.

[127] J. D. Joannopoulos, S. G. Johnson, J. N. Winn, and R. D. Meade, *Photonic Crystals*. Princeton University Press, 2nd edition ed., 2008.

[128] S. Maier, *Plasmonics: Fundamentals and Applications*. Berlin: Springer, 2007.

[129] S. M. Sze and K. K. Ng, *Physics of Semiconductor Devices*. Wiley InterScience, 3rd edition ed., 2006.

[130] M. Krawczyk and H. Puszkarski, "Magnonic excitations versus three-dimensional structural periodicity in magnetic composites," *Crystal Research and Technology*, vol. 41, no. 6, pp. 547–552, 2006.

[131] M. Krawczyk, J.-C. Lévy, D. Mercier, and H. Puszkarski, "Forbidden frequency gaps in magnonic spectra of ferromagnetic layered composites," *Physics Letters A*, vol. 282, no. 3, pp. 186–194, 2001.

[132] V. V. Kruglyak, R. J. Hicken, A. N. Kuchko, and V. Y. Gorobets, "Spin waves in a periodically layered magnetic nanowire," *Journal of Applied Physics*, vol. 98, no. 1, pp. 014304–4, 2005.

[133] Y. Gorobets and S. Reshetnyak, "Reflection of spin waves from a ferromagnetic multilayer with interfacial coupling of finite strength (reflection of spin waves from multilayer)," *Central European Journal of Physics*, vol. 6, no. 1, pp. 7–13, 2008.

[134] D. Fleisch, *A Studen't Guide to Maxwell's Equations*. Cambridge, 1st ed., 2008.

[135] W. F. Brown, *Micromagnetics*. Interscience Publishers New York, 1963.

[136] H. Kronmueller and M. Fähnle, *Micromagnetism and the Microstructure of Ferromagnetic Solids*. Cambridge University Press, 2003.

[137] M. T. Johnson, P. J. H. Bloemen, F. J. A. d. Broeder, and J. J. d. Vries, "Magnetic anisotropy in metallic multilayers," *Reports on Progress in Physics*, no. 11, p. 1409, 1996.

[138] P. Hunter and A. Pullan, *FEM/BEM Notes*. Department of Engineering Science, University of Auckland, 2001.

[139] D. C. Scott and C. H. Alan, "Cvode, a stiff/nonstiff ode solver in c," *Computers in Physics*, vol. 10, no. 2, pp. 138–143, 1996.

[140] B. W. Kernighan and D. M. Ritchie, *The C programming language*. Prentice-Hall, Inc., 1978.

[141] L. F. Shampine, *Numerical Solution of Ordinary Differential Equations*. CRC Press, 1994.

[142] B. Gear, "Backward differentiation formulas," *Scholarpedia*, vol. 2, p. 3162, 2007.

[143] D. Fredkin and T. Koehler, "Hybrid method for computing demagnetizing fields," *Magnetics, IEEE Transactions on*, vol. 26, pp. 415–417, March 1990.

[144] T. R. Koehler, "Hybrid fem-bem method for fast micromagnetic calculations," *Physica B: Condensed Matter*, vol. 233, no. 4, pp. 302–307, 1997.

[145] T. Schrefl, J. Fidler, K. Kirk, and J. Chapman, "A higher order fem-bem method for the calculation of domain processes in magnetic nano-elements," *Magnetics, IEEE Transactions on*, vol. 33, pp. 4182–4184, Sep 1997.

[146] D. Suess, V. Tsiantos, T. Schrefl, J. Fidler, W. Scholz, H. Forster, R. Dittrich, and J. J. Miles, "Time resolved micromagnetics using a preconditioned time integration method," *Journal of Magnetism and Magnetic Materials*, vol. 248, no. 2, pp. 298–311, 2002.

[147] W. Rave, K. Ramstöck, and A. Hubert, "Corners and nucleation in micromagnetics," *Journal of Magnetism and Magnetic Materials*, vol. 183, no. 3, pp. 329–333, 1998.

[148] D. G. Porter and M. J. Donahue, "Velocity of transverse domain wall motion along thin, narrow strips," *Journal of Appled Physics*, vol. 95, no. 11, pp. 6729–6731, 2004.

[149] *GiD - The personal pre and postprocessor*. International Center for Numerical Methods in Engineering (CIMNE), http://gid.cimne.upc.es/ (accessed 10th June, 2009).

[150] S. Bance, T. Schrefl, G. Hrkac, D. Suess, C. Brownlie, S. McVitie, J. N. Chapman, and D. A. Allwood,

"Transitions between vortex and transverse walls in nife nano-structures," *Magnetics, IEEE Transactions on*, vol. 42, no. 10, pp. 2966–2968, 2006.

[151] S. Bance, T. Schrefl, G. Hrkac, A. Goncharov, D. A. Allwood, and J. Dean, "Micromagnetic calculation of spin wave propagation for magnetologic devices," *Journal of Applied Physics*, vol. 103, pp. 07E735–3, 2008.

[152] R. Li, Z. Chen, and W. Wu, *Generalized difference methods for differential equations: Numerical Analysis of Finite Volume Methods*. CRC Press, 2000.

[153] C. Garcia-Cervera and A. Roma, "Adaptive mesh refinement for micromagnetics simulations," *Magnetics, IEEE Transactions on*, vol. 42, pp. 1648–1654, June 2006.

[154] M. Donahue and R. McMichael, "Micromagnetics on curved geometries using rectangular cells: Error correction and analysis," *Magnetics, IEEE Transactions on*, vol. 43, pp. 2878–2880, June 2007.

[155] P. Lendecke, R. Eiselt, G. Meier, and U. Merkt, "Temperature dependence of domain-wall depinning fields in constricted permalloy nanowires," *Journal of Applied Physics*, vol. 103, no. 7, p. 073909, 2008.

[156] R. Dittrich, *Finite element calculations of energy barriers in magnetic systems*. PhD thesis, Vienna Institute of Technology, 2003.

[157] G. Henkelman, G. Jóhannesson, and H. Jónsson, "Methods for finding saddle points and minimum energy paths," in *Theoretical Methods in Condensed Phase Chemistry*, pp. 269–302, 2001.

[158] G. Van Rossum, *Python Language Website*. http://www.python.org/ (accessed 9th June 2009).

[159] M. Diegel, R. Mattheis, and E. Halder, "360° domain wall investigation for sensor applications," *Magnetics, IEEE Transactions on*, vol. 40, pp. 2655–2657, July 2004.

[160] M. Diegel, "Sensor element for a revolution counter," *US patent 324207250*.

[161] R. Dittrich, T. Schrefl, D. Suess, W. Scholz, H. Forster, and J. Fidler, "A path method for finding energy barriers and minimum energy paths in complex micromagnetic systems," *Journal of Magnetism and Magnetic Materials*, vol. 250, pp. 12–19, 2002.

[162] K. K. Mei and J. Fang, "Superabsorption-a method to improve absorbing boundary conditions [electromagnetic waves]," *IEEE Transactions on Antennas and Propagation*, vol. 40, no. 9, pp. 1001–1010, 1992.

[163] G. Mur, "Absorbing boundary conditions for the finite-difference approximation of the time-domain electromagnetic-field equations," *Electromagnetic Compatibility, IEEE Transactions on*, vol. 4, pp. 377–382, 1981.

[164] D. V. Berkov and N. L. Gorn, "Micromagnetic simulations of the magnetization precession induced by a spin-polarized current in a point-contact geometry (invited)," *Journal of Applied Physics*, vol. 99, no. 8, p. 08Q701, 2006.

[165] W. Bailey, P. Kabos, F. Mancoff, and S. Russek, "Control of magnetization dynamics in ni81fe19 thin films through the use of rare-earth dopants," *Magnetics, IEEE Transactions on*, vol. 37, no. 4, pp. 1749–1754, 2001.

[166] C. Kittel, "Excitation of spin waves in a ferromagnet by a uniform rf field," *Physical Review*, vol. 110, no. 6, p. 1295, 1958.

[167] M. Kaltenbacher, *Numerical Simulation of Mechatronic Sensors and Actuators*. Springer, 2004.

[168] Y. Roussigné, S. M. Chérif, and P. Moch, "Spin waves calculations in magnetic stripes," *Journal of Magnetism and Magnetic Materials*, vol. 263, no. 3, pp. 289–294, 2003.

[169] R. P. Cowburn, D. K. Koltsov, A. O. Adeyeye, and M. E. Welland, "Lateral interface anisotropy in nanomagnets," *Journal of Applied Physics*, vol. 87, no. 9 III, pp. 7067–7069, 2000.

[170] J. Gadbois, J. Zhu, W. Vavra, and A. Hurst, "The effect of end and edge shape on the performance of pseudo-spin valve memories," *IEEE Transactions on Magnetics*, vol. 34, no. 4 PART 1, pp. 1066–1068, 1998.

[171] M. T. Bryan, D. Atkinson, and R. P. Cowburn, "Edge roughness and coercivity in magnetic nanostructures," *Journal of Physics: Conference Series*, vol. 17, no. 1, pp. 40–44, 2005.

[172] M. T. Bryan, D. Atkinson, and R. P. Cowburn, "Experimental study of the influence of edge roughness on magnetization switching in permalloy nanostructures," *Applied Physics Letters*, vol. 85, no. 16, pp. 3510–3512, 2004.

[173] *400-metre race*. Encyclopedia Britannica, Encyclopedia Britannica, Inc., 2009.

[174] I. L. Auerbach, J. Eckert, J. P., R. F. Shaw, and C. B. Sheppard, "Mercury delay line memory using a pulse rate of several megacycles," *Proceedings of the IRE*, vol. 37, no. 8, pp. 855–861, 1949.

[175] H. D. Huskey and V. R. Huskey, "Chronology of computing devices," *Computers, IEEE Transactions on*, vol. C-25, no. 12, pp. 1190–1199, 1976.

[176] S. H. Lavington, "The manchester mark i and atlas: a historical perspective," *Communications of the ACM*, vol. 21, no. 1, pp. 4–12, 1978.

[177] N. Stern, "John william mauchly, 1907-1980," *Annals of the History of Computing, IEEE*, vol. 2, no. 2, pp. 100–103, 1980.

[178] P. Gannon, *Colossus: Bletchley Park's Greatest Secret*. Atlantic, 2006.

[179] E. S. Anthony, "The colossus of bletchley park - the german cipher system," in *The first computers: history and architectures*, pp. 351–364, MIT Press, 2000.

[180] B. J. Copeland, "Colossus: its origins and originators," *Annals of the History of Computing, IEEE*, vol. 26, no. 4, pp. 38–45, 2004.

[181] T. Sale, "The colossus of bletchley park," *IEE Review*, vol. 41, no. 2, pp. 55–59, 1995.

[182] S. McCartney, *ENIAC, the Triumphs and Tragedies of the World's First Computer*. Walker, 1999.

[183] A. W. Burks, *From ENIAC to the Stored-Program Computer: Two Revolutions in Computers*. Academic Press, 1980.

[184] M. Davis, *The Universal Computer: The Road from Leibniz to Turing*. Norton, 2000.

[185] A. M. Turing, *Parsing the Turing Test: Computer machinery and intelligence*. Springer.

[186] E. Barbour, "The cool sound of tubes [vacuum tube musical applications]," *Spectrum, IEEE*, vol. 35, no. 8, pp. 24–35, 1998.

[187] P. L. Spencer, "Method of treating foodstuffs," *US Patent 2,495,429*, 1950.

[188] J. A. Hoerni, "Planar silicon diodes and transistors," *Electron Devices, IEEE Transactions on*, vol. 8, no. 2, pp. 178–178, 1961.

[189] J. A. Hoerni, "Method of manufacturing semiconductor devices," *US Patent 3,025,589*, 1962.

[190] G. E. Moore, "Cramming more components onto integrated circuits," *Proceedings of the IEEE*, vol. 86, no. 1, pp. 82–85, 1998.

[191] S. E. Thompson and S. Parthasarathy, "Moore's law: the future of si microelectronics," *Materials Today*, vol. 9, no. 6, pp. 20–25, 2006.

[192] R. H. Krambeck, C. M. Lee, and H. F. S. Law, "High-speed compact circuits with cmos," *Solid-State Circuits, IEEE Journal of*, vol. 17, no. 3, pp. 614–619, 1982.

List of publications

- S. Bance, G. Hrkac, D. Suess, C. Brownlie, S. McVitie, and T. Schrefl, "Transition from vortex to transverse walls in NiFe nano-structures", IEEE Trans. Mag. , 2006. 42 (10), p.2966-2968.
- G. Hrkac, S. Bance, A. Goncharov, T. Schrefl, and D. Suess, "Thermal stability of bubble domains in ferromagnetic discs", Journal of Physics D: Applied Physics, 2007. 40 (9), p. 2695-2698.
- A. Goncharov, T. Schrefl, G. Hrkac, J. Dean, S. Bance, D. Suess, O. Ertl, F. Dorfbauer, and J. Fidler, "Recording simulations on graded media for area densities of up to 1 Tbit in.2.", Applied Physics Letters, 2007. 91 (22).
- S. Bance, T. Schrefl, G. Hrkac, A. Goncharov, D. A. Allwood, and J. Dean, "Micromagnetic calculation of spin wave propagation for magnetologic devices", Journal of Applied Physics, 2008. 103 (7).
- J. Dean, M. A. Bashir, A. Goncharov, G. Hrkac, S. Bance, T. Schrefl, A. Cazacu, M. Gubbins, R. W. Lamberton, and D. Suess, "Thermally induced adjacent track erasure in exchange spring media", Applied Physics Letters, 2008. 92(14).
- A. Goncharov, T. Schrefl, G. Hrkac, and S. Bance, "Effect of shields in perpendicular recording", Physica B: Condensed Matter, 2008. 403(2-3): p. 278-281.
- G. Hrkac, T. Schrefl, S. Bance, D. A. Allwood, A. Goncharov, J. Dean, and D. Suess, "Mutual phase locking in high-frequency microwave nano-oscillators as a function of field angle", Journal of Magnetism and Magnetic Materials, 2008. 320 (17).
- J. Dean, M. A. Bashir, A. Goncharov, G. Hrkac, S. Bance, T. Schrefl, A. Cazacu, M. Gubbins, R. W. Lamberton, and D. Suess, "Thermally induced adjacent track erasure in exchange spring media", Applied Physics Letters, 2008. 92, p. 142505.
- M. A. Bashir, T.Schrefl, J. Dean, A. Goncharov, G. Hrkac, S. Bance, D. Allwood, D. Suess, "Microwave-assisted magnetization reversal in exchange spring media", IEEE Trans. Mag. , 2008. 44 (11) Part 2, p. 3519-3522.

- M.A. Bashir, T. Schrefl, D. Suess, J. Dean, A. Goncharov, G. Hrkac, S. Bance, D. Allwood and J. Fidler "Exchange coupled bit patterned media under the influence of RF-field pulses", Accepted for IEEE Trans. Mag. 6th of March 2009.
- G. Winkler, D. Suess, J. Lee, J. Fidler, M.A. Bashir, J. Dean, G. Hrkac, A. Goncharov, S. Bance and T. Schrefl "Microwave-assisted 3D multilayer magnetic recording", Accepted for Applied Physics Letters 5th of March 2009.
- T. Schrefl, G. Hrkac, A. Goncharov, J. Dean, S. Bance, M.A. Bashir, et al., "Finite element/boundary element simulation of future hard disk recording", Proceedings of the WSEAS International Conference on Applied Computing Conference, Istanbul, Turkey, World Scientific and Engineering Academy and Society (WSEAS), 2008: pp. 430-435. (Invited)
- Thomas Schrefl, Gino Hrkac, Simon Bance, Dieter Suess, Otmar Ertl, Josef Fidler, "Numerical Methods in Micromagnetics (Finite Element Method)", in Handbook of Magnetism and Advanced Magnetic Materials, Helmut Kronmueller, Stuart Parkin (eds.), ISBN: 978-0-470-02217-7, Wiley InterScience.

Presentations

Here follows a list of the major presentations made during my time as a PhD student.

"Transitions between vortex and transverse walls in NiFe nano-structures", Intermag 2006, San Diego, USA (Poster).

"Limiting spin wave reflections in magnetic nanostructures", CRIMS 2006, Imperial College London, UK (Poster).

"Reducing spin-wave reflections in micromagnetic simulations", MMM 2007, Baltimore, USA (Oral).

"Spin-wave reflections in magnetic microstructures", HMM 2007, Naples, Italy (Poster).

"Micromagnetic calculation of spin wave propagation for magneto-logic devices", FE-03, MMM/Intermag 2007, Tampa, USA (Oral).

"Spin wave roughness in strip nanowires", Intermag 2008, Madrid, Spain (Oral).

"Thermal stability of domain wall memory", BB-05, MMM 2008, Austin, USA (Oral).

"Domain wall phase diagram with transverse field and anisotrpy", Intermag 2009, Sacramento, USA (Oral).

"Hysteresis asymmetry in domain wall trap memory", HMM 2009, Gaithersburg, USA (Oral).